The Dissertation Committee for Thomas Alexander Gomez
certifies that this is the approved version of the following dissertation:

Improving Calculations of the Interaction Between Atoms and Plasma Particles and its Effect on Spectral Line Shapes

Committee:

Donald E. Winget, Supervisor

Michael H. Montgomery, Co-Supervisor

Taisuke Nagayama

David P. Kilcrease

Chris Sneden

John C. Wheeler

Improving Calculations of the Interaction Between Atoms and Plasma Particles and its Effect on Spectral Line Shapes

by

Thomas Alexander Gomez

DISSERTATION

Presented to the Faculty of the Graduate School of

The University of Texas at Austin

in Partial Fulfillment

of the Requirements

for the Degree of

DOCTOR OF PHILOSOPHY

THE UNIVERSITY OF TEXAS AT AUSTIN

August 2017

I dedicate this dissertation to my grandparents, Elma and Eugene Longoria, and the late Mae (who passed 6 days before I defended) and Francisco Gómez (who passed when I was a baby); they taught me the value of hard work. I also dedicate this to my kids, Sabian, Raphael, and Inara, whom I hope will give their life's pursuits with dedication.

Acknowledgments

I want to recognize the multitude of people who helped me along this journey to my Ph.D. I especially want to thank Taisuke Nagayama, who has been invaluable to this work; as far as I am concerned, the calculations that come out of this work are as much his as they are mine. I also want to thank Don Winget and Mike Montgomery for their continuing support and enthusiasm. I want to thank Greg Rochau for his guidance, support, and for taking me on as an intern before I even started graduate school. I want to recognize Ross Falcon, Marc Schaeuble, and Jim Bailey, these are the best experimenters I know and I have learned so much about experiments and how to think from them. I also want to recognize the line-broadening theorists who have guided me throughout the years. First and foremost, Dave Kilcrease, for his guidance throughout this thesis. Second and maybe most importantly, Roberto Mancini, for without him, this project would not have gotten started. Also, thanks to Evgeny Stambulchik and Spiros Alexiou for very engaging suggestions, discussions, and ideas that helped move this project forward. Also I want to thank Carlos Iglesias, Dick Lee, Sandrine Ferri, Annette Calisti, and Joel Rosato for their explanations, discussions, brainstorming, and encouragement in this project.

Improving Calculations of the Interaction Between Atoms and Plasma Particles and its Effect on Spectral Line Shapes

Publication No. _____

Thomas Alexander Gomez, Ph.D.

The University of Texas at Austin, 2017

Supervisor: Donald E. Winget
Co-Supervisor: Michael H. Montgomery

Spectral line broadening has many applications in astrophysics and plasma physics. Calculations of line broadening are used in nearly all opacity models, which are then folded into atmosphere or radiative-transfer models, or used as density diagnostics in laboratory plasmas. However, there is evidence to suggest that spectral models are incomplete. For example, the experiment designed to measure the iron opacity at solar interior conditions has revealed significant discrepancies between measured and modeled opacities. Additionally, the determination of masses in white dwarfs using spectroscopic methods does not agree with other opacity-model-independent methods. Due to the challenging nature of line-broadening calculations, approximations are often employed in order to keep the calculation tractable. One approximation that will be examined in this thesis is how charged plasma particles (electrons, ions, and atoms) are assumed to interact with each other. These charged plasma particles interact via a Coulomb potential; in low-density plasmas, this can be approximated by a second-order Taylor expansion, and the plasma particles are assumed to be always

outside the radiator (dipole approximation). The dipole approximation is used extensively throughout spectral line-broadening calculations—even beyond its validity criteria. In this dissertation, I am improving the treatment of the interaction between the radiator and the plasma particles for close interactions and will focus on an accurate treatment of penetrating collisions of plasma particles with the radiator. The first improvement is to examine when the higher-order Taylor terms become important and when the dipole-only approximation breaks down. I further explore the effects of penetrating collisions due to electrons and ions. At extremely high densities, the wave behavior of quantum electrons starts to become important. As a first test of the quantum theory of electron collisions with penetration, I attempted to create correspondence between the new quantum calculation and semi-classical calculations in a regime where quantum effects aren't important. However, I could not create correspondence without the Pauli exclusion (which has been neglected in previous calculations): since electrons exist in both the plasma and the atom, the quantum repulsion of electrons (due to being spin-1/2 particles) needed to be included explicitly. There are also additional terms present in the broadening operator which have been previously neglected and considered for the first time here. I also explore the effect of penetrating collisions due to ions, for it is this treatment that is important for calculations of line merging and continuum lowering (sometimes called ionization potential depression)—a hotly debated physical effect. While I include many improvements in this thesis, it is in no way complete; there are many other untested effects that are commonly used in spectral-line broadening calculations. I conclude by showing some of the astrophysical implications specifically to white dwarfs.

Table of Contents

Acknowledgments **v**

Abstract **vi**

List of Tables **xiv**

List of Figures **xv**

Part I Introduction **1**

Chapter 1. Behavior of Atoms in Astrophysical Objects **2**

1.1 Opacity 4

1.2 Problems with the Opacity in White Dwarf Photospheres 6

1.3 Broader Impact 8

Chapter 2. Overview of Spectral Line Broadening **11**

2.1 Stark Broadening and Profiles 12

2.2 The Coulomb Interaction 14

2.2.1 Taylor Expansion of the Coulomb Operator 15

2.2.2 Dipole Approximation 16

2.3 Validity of the Dipole Approximation 17

Part II Line Broadening Formalism, Techniques, and Approximations **20**

Chapter 3. Spectral-Line-Broadening Formalism **21**

3.1 Liouville Representation 22

3.2 The Hamiltonian 23

3.3 Methods for Calculating Line Shapes 25

Chapter 4. Technical Challenges and Approximations used in Spectral Line Broadening Calculations **27**

4.1 Incomplete Basis Sets 27

4.2 Use of Screening to Approximate N-body Effects 29

4.3 Single-Perturber (Binary Collision) Approximation 31

4.4 Quasi-Static Ions 32

4.5 Separation of the Motion of Electrons and Ions 32

4.6 Neglect of Off-Diagonal Density Matrix Elements 33

Chapter 5. Simulation Methods **35**

5.1 The Plasma Simulation 35

5.2 Time Evolution of the Atom 37

5.3 History of Simulation Calculations 39

Chapter 6. Semi-Analytical Method **42**

6.1 The Various Formalisms 44

6.1.1 Impact Formalism 45

6.1.2 Fano's Relaxation Theory 48

6.1.3 Kinetic Theory 51

6.1.4 Second-Order Broadening Operators 53

6.2 Implementation of Theories 53

6.2.1 Impact Theory 53

6.2.2 Relaxation Theory Calculations at the University of Florida 56

6.2.3 Unified Theory 59

6.2.4 Kinetic Theory 62

Part III Improvements **65**

Chapter 7. Improvements over the Dipole Approximation: Higher-Order Multipoles[1] **69**

7.1 Screening for Higher-Order Multipoles 70

[1]Gomez, T. A. and Nagayama, T. and Kilcrease, D. P. and Montgomery, M. H. and Winget, D. E. *Effect of Higher-Order Multipole Moments on the Stark Line Shape* (2016) Phys. Rev. A. 94, 022501; T. Nagayama helped with writing and quantitative analysis, the remaining authors assisted in writing and provided critique of the work.

7.2 The Impact of the Electron-Quadrupole Term on the Hβ Asymmetry . . . 72
7.3 Convergence of the Multipole Expansion 75
7.4 Density Diagnostics 78

Chapter 8. Penetrating Collisions and Quantum Effects of Plasma Electrons 82

8.1 Semi-Analytic Methods with Quantum-Mechanical Electrons 83
8.2 Comparison of Semi-Classical Calculations with Current Theory & Critique of Past Calculations 85
8.3 Distorted Wave 87
8.3.1 Modification of $T(\omega)$ 92
8.3.2 Changes in the Line Shape due to Distorted Waves 94
8.4 Exchange 97
8.4.1 Illustration of Exchange 101
8.4.2 Changes in Line Shape due to Exchange 103
8.5 Correlated Collisions 109
8.5.1 Physical Interpretation of the Different Terms of $\mathcal{H}$ 111
8.5.2 Implementation 115
8.5.3 Impact on Multi-Electron Radiators 118
8.6 Comparison with Other Calculations 119
8.6.1 Comparison with Semi-classical Calculations of Neutral Radiators . 119
8.6.2 Comparison with Previous Calculations (Ionized Radiators) 122
8.6.3 Comparison with Experiment for Charged Radiators 124
8.7 Future Work 126

Chapter 9. Line Merging/Continuum Lowering (Penetration of Ions) 127

9.1 Overview of Occupation Probability 128
9.1.1 Perturbations from Charged Particles 129
9.1.2 Incorporation of Occupation Probability into Opacities 132
9.1.3 Critique 133
9.2 Direct Solutions of the Atomic Structure 135
9.2.1 Parabolic States: Electric Field-dependent Basis 136
9.2.2 Direct Solution 137
9.3 Perturbation Theory 141

9.3.1 Matrix Elements in Spherical vs Parabolic Representation 141
9.3.2 Line Broadening calculated with Spherical and Parabolic Representations 142
9.3.3 When is Penetration Important? 143
9.3.4 Convergence 145
9.4 Comparison with Occupation Probability 146

Part IV Implicatons and Conclusions 148

Chapter 10. Impact on White Dwarf Mass Determination 149
10.1 Detailed Balance 150
10.2 Modified Occupation Probability 154

Chapter 11. Conclusions 158
11.1 Multipoles 159
11.2 Penetrating Collisions 160
11.2.1 Electrons 160
11.2.2 Ions 161
11.3 Errors & Completeness 161
11.4 Future Work 162

Appendices 164

Appendix A. Matrix Mechanics 165
A.1 Basics of Matrix Mechanics 166
A.2 Solving the Time-Dependent Schrödinger Equation and Matrix Diagonalization 168
A.2.1 Evaluating the Matrix Exponential 169
A.2.2 Time-Dependent Schrödinger Equation with Explicit Time Dependence 170
A.3 Using Matrix Mechanics to Solve the Schrödinger Equation 171
A.3.1 Two-electron Solutions 173
A.3.2 Free-electron Solutions 174
A.3.3 Exchange 174

Appendix B. Wigner nj symbols **176**
B.1 3j Symbols . . . 176
B.1.1 Symmetry . . . 176
B.1.2 Sum Rules . . . 177
B.1.3 Special Values . . . 177
B.1.4 Relationship to spherical harmonics . . . 177
B.2 6j Symbols . . . 178
B.2.1 Symmetry . . . 178
B.2.2 Sum rules . . . 178
B.3 9j symbol . . . 179

Appendix C. Calculational Details of Electron Broadening **180**
C.1 The "T"-matrix . . . 180
C.2 Derivation of the Relaxation Theory . . . 183
C.2.1 The Scattering "T"-matrix . . . 183
C.3 The Electron-Broadening Operator . . . 185
C.3.1 Simultaneous Multiple-Particle Collisions . . . 185
C.3.2 The Matrix Structure of T & $\mathcal{H}$ . . . 187
C.4 Evaluation of Matrix Elements . . . 190
C.4.1 Matrix Elements of the Coulomb Operator . . . 190
C.4.2 Distorted Wave Treatment . . . 192
C.4.3 Distorted Wave + Exchange . . . 193
C.4.3.1 Thermal Average . . . 196
C.5 Spectral Line Shape Assuming Coulomb/Plane Waves . . . 197
C.5.1 Plasma Polarization Term . . . 197
C.5.2 Dynamic Width and Shift term . . . 199
C.6 Evaluation of $T(\omega)$ with Exchange . . . 201
C.6.1 Plasma Polarization with Exchange . . . 202
C.6.2 Dynamic Width and Shift with Exchange . . . 203
C.6.3 Interference Broadening Terms . . . 206
C.6.3.1 Direct Term . . . 207
C.6.4 Dynamic Width and Shifts: Distorted Wave with Exchange . . . 208
C.7 Correlated Collisions . . . 209
C.8 Off-diagonal Density Matrix Elements on Plasma Polarization . . . 210

Appendix D. Parabolic States **213**

D.1 Separation of the Schrödinger Equation in Parabolic Coordinates 213

D.2 With an Electric Field 216

D.2.1 Quadratic Stark Effect 216

D.2.2 Direct Solution 217

D.2.3 Selection Rules with an Electric Field 218

Bibliography **229**

List of Tables

7.1 Percent Error in Line Shape 78
7.2 $\sum(data - model)^2$ (Intensity Units) 81

List of Figures

2.1 Typical Stark profiles in hydrogen-like lines. Left: Lyβ line ($n = 3 \rightarrow n = 1$), right: Lyγ line ($n = 4 \rightarrow n = 1$). Lines with $\Delta n =$ even (like Lyβ) have no central component and usually have a central dip. Lines with $\Delta n =$ odd (like Lyγ) have an unshifted central component; other shifted components usually give rise to "shoulders." 13

2.2 The charge density distribution of the $n = 4$ state of hydrogen. Drawn are spheres of influence, where far away, dipole terms dominate; nearer quadrupole terms become important; and when plasma particles enter the wavefunction of the radiator—inside the red sphere—then penetration needs to be considered explicitly. Depending on the type of particle that enters the red sphere, different physical effects need to be considered. 18

7.1 The double-peaked Hβ line shape. The asymmetry of the core is defined as the fractional difference of the intensity of the blue peak and red peak, $(I_b - I_r)/I_b$, where the subscripts b and r denote the blue ($\Delta E > 0$) and red peak ($\Delta E < 0$), respectively. 73

7.2 Asymmetry calculations (lines) with different approximations: dipole-only interaction (black); dipole + ion-quadrupole (blue); dipole + electron- *and* ion-quadrupole moment (red). The dipole-only calculation agrees well with the data (various points) below 3×10^{17} e/cc. Including only ion-quadrupole created discrepancy at these densities. Calculations including both electron- and ion-quadrupole terms created agreement with the data between 10^{17} and 10^{18} e/cc. Models assume 1eV temperature. 74

7.3 Area-normalized Hβ profiles at various levels of approximation over several different conditions. Profiles calculated at electron densities of 10^{17}, 10^{18}, and $10^{19} e$/cc are shown (all at 1-eV temperature). All moments include contributions from both ions and electrons. The green line shows the dipole approximation of Eq. (7.1); blue line shows up to the quadrupole term, orange line shows up to octupole term; lastly, red shows up to the sedecapole ($k \leq 4$) term, indistinguishable from the octupole profile. The profiles that include up to the quadrupole term match reasonably well to the sedecapole profile. . 76

7.4 a) the highest-density measured spectrum from the Wiese et al. (1972) experiment, focused on Hβ (dots). The fits for the calculated dipole, quadrupole, and sedecapole profiles are identical, yielding fit differences less than the fit errors. b) the measured Hβ spectrum measured by Carlhoff et al. (1986) (dots). The fits for the calculated dipole, quadrupole, and sedecapole profiles yield differences in density of 12%, which is greater than the fit errors. 80

8.1 The Lyman series of neutral hydrogen (at $T_e = 1eV$ and $n_e = 10^{17}e/\mathrm{cm}^3$) that compares the plane-wave treatment (black-dotted) and the Semi-classical calculations of the previous chapter. Reproduction of the Junkel et al. (2000) calculations applied to neutral hydrogen have no correspondence with the semi-classical results in a regime where these classical results are reliable. . . 86

8.2 The monopole term (Eq 8.12) for the 4p state of hydrogen is shown in black. The wavefunction of the bound electron (red) is shown in red for reference. The monopole term of the radiator wavefunction goes to a finite value, and is subtracted by $1/r_p$, this second-term causes the potential to go to negative infinity; this is large and can be included in the solution of the free-electron wavefunction (Eq 8.13). 89

8.3 The changes in the free-electron radial wavefunction when the solving for plane wave (Eq 8.9) vs distorted wave (Eq 8.13) for neutral hydrogen ($Z = 1$). The top-left panel has the smallest k value and the bottom-right panel has the largest k value. Plane-wave solutions are dotted black lines, while the distorted-wave solutions are solid red. 90

8.4 Same as figure 8.3, but for hydrogen-like magnesium ($Z = 12$). Coulomb-wave solutions are dotted black lines, while the distorted-wave solutions are solid red. 91

8.5 The Lyman series of neutral hydrogen (at $T_e = 1eV$ and $n_e = 10^{17}e/\mathrm{cm}^3$) that compares the plane-wave treatment (black-dotted) and distorted-wave treatments (red-dotted) of the colliding electron wavefunction. The distorted-wave treatment becomes more important with the increasing size of the wavefunction and affects the higher-order members of the series. 96

8.6 Leading up to the collision 101

8.7 During the collision 102

8.8 After the collision 103

8.9 The Lyman series of neutral hydrogen that compares the plane-wave treatment (black-dotted), distorted-wave (red-dotted), and distorted-wave with exchange (solid red) treatment of the colliding electron wavefunction. Exchange is important for all transitions. Lyα (left) to Lyδ (right). 104

8.10 Wavefunctions of the bound electron (denoted with ψ and colored red) and the free electron (ϕ, dotted black) as a function of nuclear charge; the exchange charge density ($\psi(r)\phi(r)$) is shown in blue. All wavefunctions are s ($l = 0$) states; the bound electron is in the $n = 3$ state. 106

8.11 Matrix elements of the second-order $T(\omega)$ operator for the various processes. The direct-direct (DD), exchange-exchange (EE), and direct-exchange (DE) processes are shown. Exchange processes are significant compared to the direct processes in hydrogen; not so for magnesium. Additional exchange processes, such as monopole exchange, can increase the importance of exchange (total exchange contribution is shown in dotted red). 108

8.12 Comparison different approximations for Mg^{+11} Lyβ: Coulomb-wave calculation (CW; dashed black) with distorted-wave (DW; dotted green), and distorted-wave-with exchange (DWE; solid red). Each modification, (distorted-waves and exchange) results in about a 15% narrowing of the width. 110

8.13 Feynman diagram of $\mathcal{H}$, where the paths of the atom are shown in black; the path of electrons one, two, and three are denoted by green, blue, and violet colors, respectively; the different Coulomb interactions—though non-relativistic—are shown as the squiggles; time increases from left to right, while the vertical space corresponds to physical space. The additional terms that arise from the projection operator in Eq (8.35), correspond to collisions that happen in quick succession. 114

8.14 Comparison of the binary-collision calculation (DWE-BC) with the calculation with the correlated collision using only up to second-order terms (DWE-CC2). The calculation adds significant broadening to the line in a way that is not seen by experimenters. Comparison with some of the other projection operator terms of Eq (8.32) shows that this calculation is not yet converged (this calculation does not include the fourth term of Eq 8.32). 116

8.15 Comparison of the Coulomb-wave binary-collision calculation (CW-BC) with the binary-collision Distorted-Waves with Exchange calculation (DWE-BC), and our modified correlated collision Distorted-Waves with Exchange calculation (DWE-CCM). The DWE-CCM calculation is slightly narrower than the original version 117

8.16 Comparison of the binary-collision assumption and correlated collision calculation for the spectrum of Li-like carbon. The electron-broadening details are only approximate at this point, treating only the valence electron, not the complicated exchange processes between all 4 electrons considered (3 bound, 1 free). Even at only a moderate density, the effect of correlated collisions seems to increase the width of the lines substantially. 119

8.17 Comparison of DWE with the semi-classical calculations of *Xenomorph* and Vidal et al. (1973). The predictions differ for the Lyα line, but there is excellent agreement for the higher-n lines. 120

8.18 Attempting to replicate past calculations; all past calculations are dotted. The blue dots on the top panel represent the Woltz & Hooper (1984) calculation. My new Lyα agrees with Woltz & Hooper, but Lyβ, but my distorted-wave calculation agrees well with Kepple's distorted-wave calculation. The bottom panel has a compassion with Gunderson et al. (2001) and Kepple (1972); these semi-classical calculations agree well with my Coulomb-wave calculations. 123

8.19 Comparison of the different approximations with the experiment by Musielok et al. (1987). The plasma conditions have been determined by Thomson scattering, so this is not a reduced χ^2 fit. The semi-classical calculation of Kepple (1972) is too wide for the profile; this is relatively consistent with the Coulomb-wave calculation. Only the calculation that includes the effects of exchange and distorted waves can match the data. 125

9.1 A diagram of the isolated-atom potential and the atom with a constant electric field, shown is the saddle point. The electric field value is the saddle point (given by Eq 9.5) of $n = 3$. The true ionization threshold will be slightly less than this value due to quantum tunneling. 131

9.2 2-dimensional surface plot of the potential to be solved by matrix diagonalization. Only two protons are shown for this example. The nucleus is set at the origin and labeled with a red arrow, the nearest neighbor is set at a radius of 100 and in the z-direction, denoted with a blue-arrow. 138

9.3 2-dimensional surface plot of solutions to the potential in figure 9.2. 9.3a has the lowest energy and 9.3c has the highest energy. 139

9.4 This comparison of methods is to verify that for small perturbations, then the spherical and parabolic representations give the same answer (Lyβ in 9.4a). Comparison 9.4b shows that for high-values of electric field, where lines start to overlap, that differences start to emerge between calculations between the two representations 142

9.5 Eigenvalue evolution of various states of hydrogen due to a single perturber as a function of that perturber's distance from the nucleus. The right panel ignores penetration, the left panel includes penetration. Penetration reduces the size of the perturbation and creates a blue shift. 143

9.6 Comparison of spectra with and without penetration. Here we can see that for these conditions, the effects of penetration are fairly minor. 144

9.7 A convergence test of the continuum calculation for the Lyman (left) and the Balmer (right) series of neutral hydrogen at high density. The different lines do not denote the transition, rather they denote which states are included in the calculation; for example, the violet line includes states $n = 3$ and $n = 4$, while the blue line includes n=3,4, and 5, and so on for the other colors. . . . 145

9.8 Comparison of the high-n lines of hydrogen as measured by the Wiese experiment ($T_e = 1eV$ and $n_e = 10^{17} e/\mathrm{cm}^3$). The occupation probability with the VCS line shape overestimates the opacity between lines, but the TB09 profiles seem to do better, but underestimate the width of the line. Only Neomorph (this work) accurately matches both the line width and the continuum levels between lines. 147

10.1 The effect of detailed balance on the Lyα line of hydrogen for $T_e = 0.5eV$ and $n_e = 10^{17} e/\mathrm{cm}^3$, which is a typical density for white dwarf photospheres. The panel on the left shows an extended frequency range, while the right panel zooms into the core, showing that the profiles are nearly the same in the middle. At this low temperature, we see substantial decrease of the Lyα red wing. This decrease in the opacity can be important in determining opacity because Lyα is the dominant opacity source in the atmosphere. 151

10.2 Synthetic spectrum of a white dwarf star at $T_{\text{eff}} = 16,000K$ and log g =8.5. The left panel focuses on the Lyman series, while the right panel shows the Balmer series—what is in the visible spectrum and where most analysis is done. Green lines indicate using Tremblay & Bergeron (2009) profiles, while the red has only the Lyα line switched out for the new calculations here. The percent difference between the two calculations are shown on the bottom panel. 152

10.3 Same as Fig 10.2, but for T_{eff} = 40,000K. The differences between these two models are much reduced where the only discrepancy is near the middle of the Lyα profile. 153

10.4 Comparisons of different occupation probability models with the most detailed Neomorph calculation. The red line is with individual profiles (IP) of Neomorph (N), with a saddle-point criteria; the dashed-blue line is the same as the red, but with Hummer & Mihalas (HM) criteria; and the green-dotted line is the Tremblay & Bergeron profiles (TB) with HM criteria. 154

10.5 Comparison with the different line-shape theories and occupation probability criteria. Differences in gravity can vary substantially. The Keplerian log g is determined to be 8.629±0.007, which means that the only model to match this is the VCS/Xenomorph calculation with the saddle-point occupation probability criteria. 157

C.1 Interaction diagram of the "S"-matrix 182

D.1 The charge-density distribution of the $n = 2$ states of hydrogen. Panel D.1a shows the $2s$ state of hydrogen, while panel D.1b shows the $2p$ state of hydrogen; these states are the solution to the Schrödinger equation in spherical coordinates. Panel D.1c shows the solution of an $n = 2$ state in the parabolic representation, which can be built from spherical states via Eq (D.3); parabolic states have no spherical symmetry and are polarized on one side of the atom. 214

Part I

Introduction

Chapter 1

Behavior of Atoms in Astrophysical Objects

This thesis is going to be largely concerned with atomic processes in plasmas. Understanding the physics of atoms is essential for the study of astronomical objects.

Almost everything we know about astronomical objects comes from the light they emit. There are two primary methods to measure the light from astronomical objects: taking images (photometry), and splitting the light and examining the intensity as a function of wavelength (spectroscopy). To properly interpret the spectra measured from astronomical objects, we need to understand how the radiation interacts with the matter in the object, travels through space, and goes through our detectors. Therefore, the spectra originating from an astronomical object depends on the state of matter of that object. Nearly all astronomical objects have a thin layer of matter from which light can escape known as its atmosphere; this is usually the last bit of matter that radiation escaping the object will interacts with before reaching our detectors.

Most astronomical objects with an atmosphere, such as a star, are hot enough for the matter to be in gaseous form. The radiation will interact with atoms in the atmosphere before it reaches our detectors. Measured spectra of astronomical objects show discrete atomic features. Interpretation of the atomic spectral features gives us clues about the behavior of these objects. However, the accuracy of our interpretation is dependent on our understanding of the atoms in the atmospheres.

One such example is the shifts in spectral lines due to the motion of the atoms (known as the Doppler effect). We can use this to study the motion of stars and determine whether an observed star is actually a binary or has planets. Edwin Hubble studied the kinematic properties of nearby galaxies using the Doppler effect. He determined that, on the largest scales, galaxies that are further from Earth are moving faster away from Earth; this has led us to conclude that the Universe is expanding.

The strength of atomic lines provides information about a given object. The temperature and abundance of the atoms determine the strength of the atomic lines. The strength of hydrogen lines has led to the spectral classification of stars (O,B,A,F,G,K,M). A-stars have the largest hydrogen features, while M- and O-stars have the weakest hydrogen features. The study of the metal abundance in stars provides information about their age and evolution, and gives clues to how these elements are created (nucleosynthesis). For example, calculations of fusion of atomic nuclei, coupled with the carbon abundance in stars led Salpeter (1952) to determine that stars can fuse helium to make carbon later in their evolution.

Observed intensities of atomic lines vary as a function of frequency—known as the line shape. The shape and broadening of atomic lines is different depending on how the environment affects the atom. The thermal distribution of velocities of atoms gives rise to a Gaussian line shape, whose width is determined by the element mass and the temperature (thermal Doppler broadening). Rotation of an unresolved object, such as a star, also broadens lines. Atoms on one side of the star travel toward Earth (Doppler shifting the transition to the blue), while the atoms on the other side travel away from Earth (Doppler shifting the transition to the red), and the distribution of all possible velocities due

to rotation broadens lines. Atomic lines are also broadened by their environment—known as pressure broadening. The pressure broadening of lines can give an estimate of the surface gravity of stars (higher surface gravity stars have broader lines than lower gravity stars). Using this, we can determine which stars are dwarfs (high gravity) and which are giants (low gravity).

1.1 Opacity

Understanding astronomical objects in more detail—such as modeling the emergent spectrum or determining the structure of the object—is limited by our ability to accurately model the opacity of matter. Opacity determines how radiation interacts with the matter it is passing through. For example, high opacity regions tend to trap radiation, while low opacity regions let radiation pass through. How easily radiation can escape an object is determined by its optical depth (τ), which is determined by the opacity and the length of material through which it travels,

$$\tau = \int dL\kappa(L),$$

where κ is used to denote opacity. The optical depth is a measure of the number of interactions the radiation has with the medium before escaping.

The emergent spectrum of stars is determined by the optically thin material of the atmosphere of the stars; this is the part of the star we observe because the optical depth is low ($\tau < 1$). Understanding the opacity of the atoms in the atmosphere is necessary in order to accurately model the strength and shapes of the lines we observe. In high gravity objects, such as white dwarfs, the opacity is dictated by the pressure broadening of spectral

lines. Matching a modeled spectrum to an observed spectrum allows astronomers to infer a surface gravity.

Opacity determines how radiation is transported out of stars. The structure of the solar interior, for example, has three distinct regions: core, radiative zone, and the convection zone. The core is where energy is produced through fusion of atomic nuclei. In the radiative zone, the opacity is low enough that it passes through the medium uninhibited—though it may be millions of years before those photons escape the solar interior due to the high optical depth of the interior ($\tau >> 1$). At some point in the star, the temperature drops, and the opacity increases and prevents the radiation from escaping. When the temperature drops, convection of solar material becomes more efficient to transport the energy out of the sun than radiation.

Calculations of opacity are complicated because of the multi-discipline aspect of the problem. First, an accurate model of the atoms in the medium is required. Second, a model for the statistical properties of the atoms is also needed.

A variety of atomic data is needed for calculating opacity. The energy level structure determines the wavelength of a given transition. Wavefunction solutions of the atomic structure determine oscillator strength, which is proportional to the transition rate. The ionization energy can determine which ionization state is most likely to be observed. Finally, the broadening of spectral lines strongly determines the opacity of the atomic transition.

The statistical properties of the atoms in the plasma can be determined by the equation of state (which relates quantities such as temperature, pressure, and density to each other). This can give information about the probability that atoms occupy certain states, or are ionized, etc. For example, the $n = 2$ state of hydrogen (lower-level of the

Balmer series) is strongly occupied and reaches a maximum around 11,000 Kelvin, which is the temperature of an A-star. Below this threshold, then the population of $n = 2$ is reduced because the temperature is not high enough (M-stars), and above this threshold, hydrogen becomes more ionized and there aren't enough electrons in $n = 2$ to create strong lines (O-stars). The statistical properties of atoms are *required* in order to determine the abundance of that atom in the atmosphere.

1.2 Problems with the Opacity in White Dwarf Photospheres

White dwarf stars (hereafter WDs) are interesting because they are the end-point of 97% of all stars, so studying WDs gives clues about the stars that made them. WDs are also relatively simple objects at extreme conditions (the star is supported by electron degeneracy), which makes it easy to study certain phenomenon (crystallization, equation of state). Because WDs come from other stars, the oldest white dwarf will have been made from the first generation of stars and can therefore help constrain the age of the Universe (Winget et al., 1987). Some WDs pulsate, and their pulsation allows astronomers to probe the interiors of WDs and determine their structure (asteroseismology).

Any study of WDs, whether it is asteroseismology or cosmochronology, requires accurate determination of mass. For a select few WDs that are in binaries, their masses can be determined by applying a Keplerian model to the observed orbit. Most WDs, however, are in single-star systems and there is no direct method of determining their mass (the average mass, however, can be determined by gravitational redshift; see Falcon et al., 2010). The most common method for determining mass is by fitting a model spectrum to an observed spectrum and inferring the star's temperature and gravity.

The gravitational acceleration at the surface of the star is a function of the mass and the radius of the object,

$$g \propto \frac{M}{R^2}.$$

Because WDs have degenerate electrons in the core, an equation of state describing degenerate matter can provide a mass-radius relationship (Chandrasekhar, 1931, 1933), allowing astronomers to derive mass from the inferred gravity and temperature (Bergeron et al., 1991). The spectroscopic method is extremely precise; reported error estimates are at the one-percent level. While the spectroscopic method is precise, it may not be accurate; the true error is much larger and systematic. Unknown errors due to inaccuracies in atmosphere models can affect the estimate of masses.

There is evidence that the opacity model for WD atmospheres is incomplete; the derived masses from spectroscopy and other methods do not agree. In a study of Sirius B (a WD in a binary system and closest to Earth), Barstow et al. (2005), Barstow et al. (2017), and Bond et al. (2017), found that the spectroscopic mass underestimated the mass determined by the Keplerian orbit. The measured log g from the Keplerian orbit (Bond et al., 2017) is 8.629±0.007, while the spectroscopic fits of Barstow et al. (2017) gives 8.591±0.016—discrepant by 2.4σ. In addition, Falcon et al. (2010) determined the average mass of hundreds of WDs and found it to be discrepant with the average mass as determined by the spectroscopic method. The discrepancies here are of order 10-12%; many astronomers would consider this to be an acceptable error, but in the field of WDs, this error is large. This level of error can change the estimates of the age of the Milky Way Galaxy by more than half a billion years—larger than the error estimates for the age of the universe.

There are many sources of uncertainty in the calculation of atmosphere models,

some of which have already been treated (including the 3-D aspects of the atmosphere and NLTE effects; see Tremblay et al., 2013; Hubeny & Lanz, 1995, respectively). The accuracy of the opacities of neutral hydrogen has not been fully explored. Tremblay & Bergeron (2009) have shown that small changes in the hydrogen opacities have significant impact on mass determinations.

Hydrogen opacity is strongly affected by the broadening and merging of spectral lines. The current models for the line broadening and the merging of lines is the unified theory of Vidal et al. (1971) and the occupation probability formalism of Hummer & Mihalas (1988), respectively. Tremblay & Bergeron (2009) merged the unified theory with occupation probability. While, no theory is complete, the theories of both the unified theory and occupation probability formalism are missing some key physics for strong plasma perturbations.

Modeling line broadening and merging is complicated by the multi-disciplinary aspects of solving a quantum-mechanical N-body problem; approximation must be made to keep the calculations tractable. This thesis, inspired by the WD problem, will examine certain problems in the calculation of opacities in one-electron atoms. The focus is on improving the modeled interaction between the radiator and the plasma particles. Charged particles in a plasma interact through a Coulomb interaction, but this is often simplified for low-density plasmas; I will explore when this low-density approximation breaks down.

1.3 Broader Impact

The work I do here has impact on other fields besides white dwarf stars. Whenever opacity is used, detailed atomic processes are needed to understand the object of interest,

whether it be a star or a plasma formed in the laboratory. However, I want to make clear that I am not claiming that all opacities are incorrect, rather, there is a point where the models will break down due to missing or incomplete physics.

One such example of incomplete opacities is in the solar interior; there is evidence that opacity in the interiors of stars is incorrect. The placement of the convection-zone boundary of the sun as predicted by the standard solar model differs with the measured boundary from helioseismology by $> 10\sigma$. This discrepancy between helioseismology and the standard-solar model can be rectified by a 14% increase in the Rosseland-mean opacity—an average opacity often used in stellar structure. Bailey et al. (2015) set out to measure the opacity of iron at solar interior conditions and found that the models contained inaccuracies at the highest-density condition explored: the measured bound-free continuum level was 50-100% higher than the models, and the spectral lines were much broader than the models predicted. When the opacity of the other elements in the sun are considered, then the increase in the iron opacity as measured by the experiment resulted in an increase of the Rosseland-mean opacity by 7%. If similar discrepancies persist in other elements in the solar mixture, such as oxygen (which dominates the opacity at the solar convection zone), then it is not unlikely that the Rosseland-mean opacity of the solar interior could be increased by 14%. A complete understanding of the atomic processes involved in complicated spectra is required to solve this problem; this thesis will not explore this problem, but it does have bearing on the calculations of spectra.

Understanding spectroscopy is valuable in laboratory experiments as well. Many experiments involving plasmas, such as those used for fusion experiments, do not have measurements of density and temperature, or their experimental setup does not allow for

one, such as Thomson scattering. But some experiments can use trace elements such as argon (Woltz & Hooper, 1984) or magnesium (Bailey et al., 2015), and comparisons of modeled and measured argon line shapes determine the temperature and density of the plasma. However, Nagayama et al. (2016) and Iglesias (2016), who performed a cross-comparison analysis of theoretical line shapes of helium-like magnesium lines, found large variability between calculated line shapes; inferred density varied by 50% depending on which calculation was used. This thesis briefly explores the broadening mechanisms of highly charged atoms and I show that more work is needed in order to accurately model these lines.

This work also affects equation of state models. In chapter 9, I look into the physics of line merging and continuum lowering—or ionization potential depression. Equation-of-state calculations need the modified ionization potential due to density effects in order to accurately calculate such quantities as atomic opacities. Past models assume that the ionization is a digital phenomenon, grouping states into either ionized or bound (Stewart & Pyatt, 1966; Ecker & Kröll, 1963). Some models used in astrophysics have a more statistical approach (e.g. Hummer & Mihalas, 1988), but these models need to be refined. The Hummer & Mihalas (1988) formalism is widely used in the astrophysical community (it was designed for stellar interiors), so the work I present here can lead to improvements in this model.

Chapter 2

Overview of Spectral Line Broadening

There are many different mechanisms that can broaden lines beyond their natural widths. These include, but are not limited to, rotational, thermal, and pressure (or density) broadening.

In astrophysical objects, fast-rotating objects can substantially broaden spectral lines. The material at one edge of the object creates a large Doppler shift—a shift in frequency due to motion—and the opposite edge also has a large Doppler shift in the opposite direction, but since most astrophysical objects are round, there is a continuum of shifts, which leads to a broadening. Thermal Doppler broadening arises due to the random motion of atoms having a non-zero temperature; this results in a Gaussian profile. There is also an intrinsic, or natural, broadening of spectral lines due to the lifetime of the states and is dependent on the atomic structure of the observed atom.

Pressure broadening arises due to collisions with nearby particles; it often—but not always—results in a Lorentzian profile. The importance of the collisions from the various species in the plasma is dependent on the environment, namely the ionization level, temperature, and density. Pressure broadening can include collisions from neutral atoms (sometimes called Van der Waals broadening), identical atoms (resonance broadening), and charged particles—which is often called "Stark broadening" because the electric-field interaction is the largest contribution to the broadening. Stark profiles are NOT Lorentzian, but

rather have their own distinct profiles.

The work in this thesis focuses entirely on Stark broadening, i.e., the broadening that arises from charged particles such as electrons and ions.

2.1 Stark Broadening and Profiles

It is common practice to separate the effects of ions and electrons. Electrons and ions have different masses and therefore move with different speeds and will affect line shapes differently. Because electrons move much faster than ions, electrons usually produce a Lorentzian line shape. Ions on the other hand, which are nearly static compared to the electrons, induce a constant electric field on the atom and a Stark spectral pattern emerges; the ensemble average of the ion configurations give rise to what is known as a "Stark profile".

Different transitions will have different Stark profiles. The details of the how the Stark splitting affects transitions are in appendix D.2.3; the various patterns are outlined here and examples are shown in figure 2.1. Transitions with Δn =odd (where n is the principle quantum number) have central unshifted components; examples include Lyα, Lyγ, Hα, Hγ, Hϵ. The other shifted components of Δn =odd transitions give rise to "shoulders." Transitions with Δn =even have no central component and show dips in the middle of the profile; examples include Lyβ, Lyδ, Hβ, Hδ. Examples of Stark profiles are shown in figure 2.1, which demonstrate one without an unshifted component (Lyβ) and one with an unshifted component (Lyγ). Also shown in figure 2.1 are the transition energies and intensities when altered by a typical value of electric microfield.

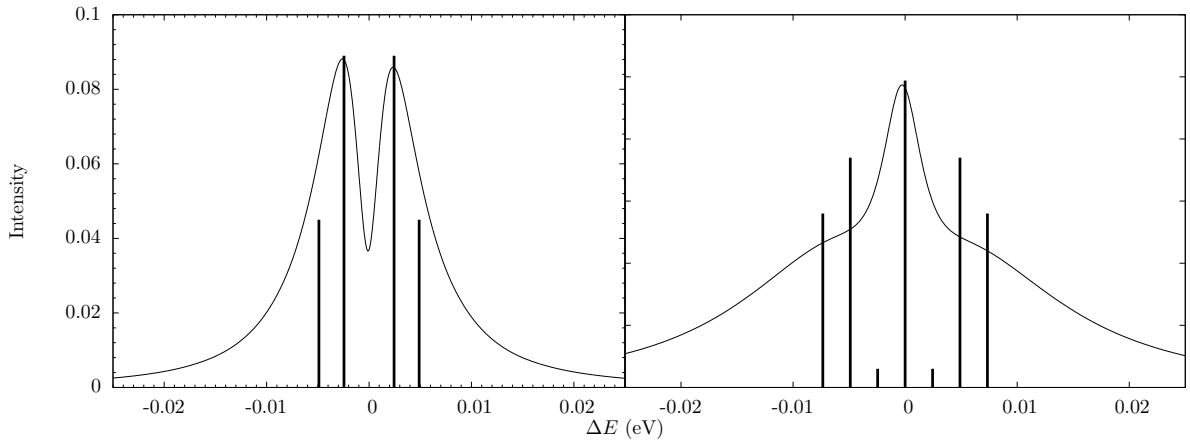

Figure 2.1: Typical Stark profiles in hydrogen-like lines. Left: Lyβ line ($n = 3 \rightarrow n = 1$), right: Lyγ line ($n = 4 \rightarrow n = 1$). Lines with $\Delta n =$ even (like Lyβ) have no central component and usually have a central dip. Lines with $\Delta n =$ odd (like Lyγ) have an unshifted central component; other shifted components usually give rise to "shoulders."

2.2 The Coulomb Interaction

Calculations of line broadening are complicated and involved. Practical calculations of line broadening require many simplifying assumptions, and many of these assumptions are often used beyond their regime of validity. The formalism for spectral line shapes was developed in the late 1940's and practical calculations were presented in the early 1960's by Griem et al. (1959). A list of some of the common approximations used by many are given in chapter 4, though the list is far from complete.

While there have been improvements in spectral-line broadening calculations (Kepple & Griem, 1968; Vidal et al., 1971), and even new techniques developed (Stamm et al., 1984; Stehle, 1994), many of the approximations used by Griem, namely the dipole approximation for radiator-plasma interaction and the semi-classical approximation (where the atom is treated quantum mechanically and the plasma particles are treated classically), are still commonly used. Since the plasma particles that I am considering (electrons and ions) are charged, they interact via a Coulomb interaction. The Coulomb interaction between any two particles is

$$V(\vec{r}_a, \vec{r}_j) = \frac{q_a q_j}{|\vec{r}_a - \vec{r}_j|}, \tag{2.1}$$

where $\vec{r}_j$ and q_j are the position and charge of particle j, while $\vec{r}_a$ and q_a are the position and charge of the electron in the radiating atom. For simplicity, I am only showing the interaction between two particles (the atomic electron and some unspecified particle j). In a plasma, interaction between all particles should be considered, and Eq (2.1) should include a sum over all N particles; this sum would also include contributions of the nucleus, but it is omitted for now. Equation (2.1) is difficult to evaluate for a many-body problem, and an approximate formula is often used in line-shape calculations.

2.2.1 Taylor Expansion of the Coulomb Operator

The most common approach used in atomic structure to evaluate Eq (2.1) is to use a Taylor expansion (Bethe & Salpeter, 1957; Cowan, 1981). We begin by re-writing Eq (2.1) as

$$|\vec{r}_a - \vec{r}_j|^{-1} = \left(\sqrt{r_j^2 + r_a^2 - 2r_a r_j \cos\gamma_{aj}}\right)^{-1} \tag{2.2}$$

where $\cos\gamma_{aj}$ is the angle between the positions of the atomic electron and perturbing particle j, defined as

$$\cos\gamma_{aj} = \cos\theta_a \cos\theta_j + \sin\theta_a \sin\theta_j \cos(\varphi_a - \varphi_j),$$

where θ_a and φ_a are the angular components of coordinate $\vec{r}_a$; similar for θ_j, φ_j, and $\vec{r}_j$ Assuming that $r_j > r_a$, a Taylor series of Eq (2.2) can be written as

$$\sum_{x=0}^{\infty} \frac{r_a^x}{r_j^{x+1}} P_x(\cos\gamma_{aj}), \tag{2.3}$$

with the aid of Legendre polynomials[1] (denoted as P_x). The $x = 0, 1, 2, 3$ terms are known as the monopole, dipole, quadrupole, and octupole terms, respectively.

For $r_a > r_j$, the positions of the perturber and atomic coordinates in Eq (2.3) are switched: r_j is in the numerator and r_a is in the denominator,

$$\sum_{x=0}^{\infty} \frac{r_j^x}{r_a^{x+1}} P_x(\cos\gamma_{aj}). \tag{2.4}$$

The Coulomb potential (Eq 2.1) can be re-written in a more compact form,

$$V(\vec{r}_a, \vec{r}_j) = \sum_x \frac{r_<^x}{r_>^{x+1}} P_x(\cos\gamma_{aj}), \tag{2.5}$$

[1]This can be re-written as a product of spherical harmonics,

$$P_x(\cos\gamma) = \sqrt{\frac{4\pi}{2x+1}} \sum_q Y_{xq}^*(\theta_j, \varphi_j) Y_{xq}(\theta_a, \varphi_a)$$

where $r_>$ and $r_<$ represent the lesser and greater of r_a and r_j, respectively.

2.2.2 Dipole Approximation

Many authors perform calculations in the low-density, high temperature regime. Two simplifications are often made in this regime: assume that perturbing particle is always outside the atom, and evaluate Eq (2.3) only up to the second term:

$$V_{aj} \approx \frac{q_a q_j}{r_j} + q_a q_j \frac{r_a}{r_j^2} \cos\gamma_{aj}. \tag{2.6}$$

We note that the first term of Eq (2.6) is partially canceled by the Coulomb potential between the radiator nuclear charge and perturber,

$$V_{nuc,j} = \frac{Z q_j}{r_j},$$

where Z is the charge of the radiator nucleus. If only one-electron atoms are considered (and replacing $q_a = -1$ for the atomic electron), then the total interaction between the radiator and the plasma particle is

$$V = V_{a,j} + V_{nuc,j} \approx -q_j \frac{r_a}{r_j^2} \cos\gamma_{aj} + q_j \frac{Z-1}{r_j}.$$

The monopole nuclear charge, which uniformly shifts all the levels, does not contribute to broadening, the dipole term, which shifts levels differently, contributes to the broadening of lines. The dipole approximation is one of the most commonly used approximations in calculating spectral line shapes (Kepple & Griem, 1968; Vidal et al., 1971; Gigosos & Cardenoso, 1987; Stambulchik & Maron, 2006; Gomez, 2013, etc.).

The monopole nuclear term is taken into account in the plasmas particle trajectory and is not considered in the evaluation of the broadening. Since the unscreened nuclear

charge affects the particles trajectories, the potential under the dipole approximation which contributes to broadening can be written compactly as

$$\begin{aligned} V_{aj} &\approx (\vec{r}_a) \cdot \left(\frac{\vec{r}_j}{r_j^3} \right) \\ &\approx \vec{D}_a \cdot \vec{F}_j, \end{aligned} \tag{2.7}$$

where $\vec{D}_a$ is the dipole moment of the atom (which is easily obtained with any atomic structure code), and $\vec{F}_j$ is the electric field due to the dynamic plasma particles,

$$\vec{F}_j = \int d\vec{r} \rho_j(\vec{r}) \frac{\vec{r}}{|r|^3}, \tag{2.8}$$

where $\rho_j(\vec{r})$ is the charge density of perturbing particle j.

Equation 2.8 applies to both quantum and classical treatments of the plasma electrons. For quantum electrons, then ρ is defined as the square of the absolute value of the plasma-electron wavefunctions ($\rho(\vec{r}) = |\psi(\vec{r})|^2$). But if the particles are treated within a classical approximation, ρ is approximated with a Dirac delta function, $\delta(\vec{r} - \vec{r}_j)$, where $\vec{r}_j$ is the position of a point-like particle, such that the electric field generated by a point particle is

$$\vec{F}_j = q_j \frac{\vec{r}_j(t)}{|\vec{r}_j(t)|^3}. \tag{2.9}$$

2.3 Validity of the Dipole Approximation

The dipole approximation makes two major assumptions: the plasma particles are *always* outside of the radiator, and higher-order terms are negligible. When the density becomes higher, these two assumptions break down. Figure 2.2 shows an $n = 4$ wavefunction with circles indicating where the higher-order terms are non-negligible (green) and where plasma particles can enter the wavefunction (red).

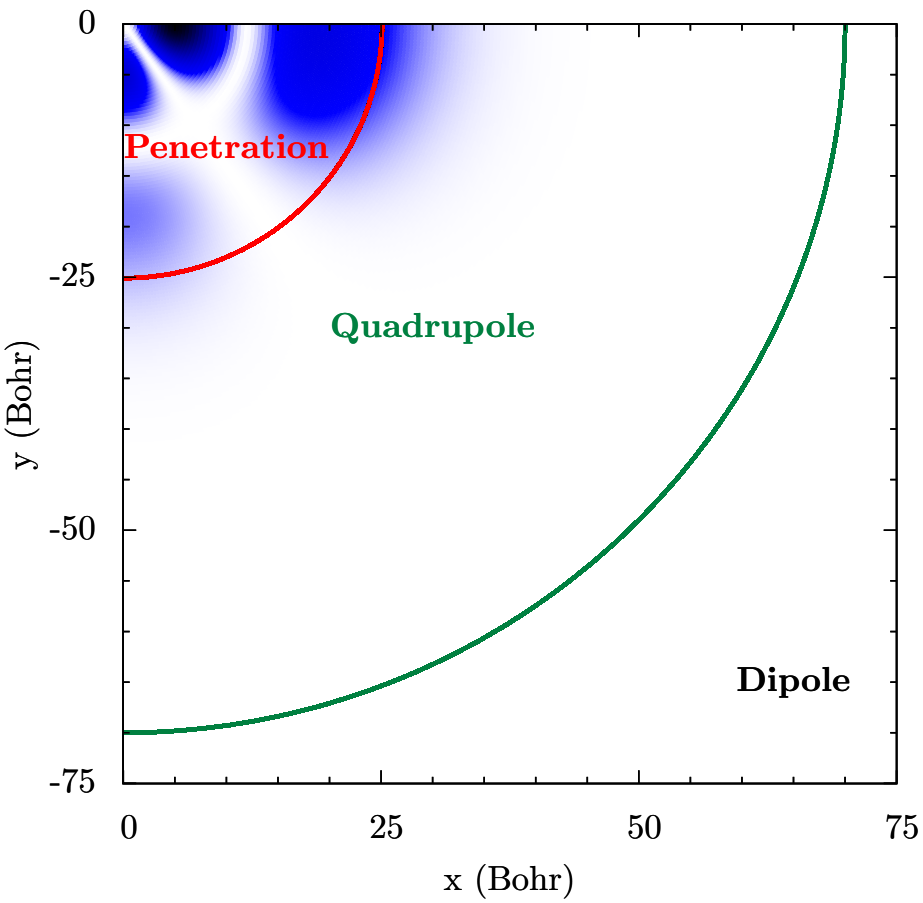

Figure 2.2: The charge density distribution of the $n = 4$ state of hydrogen. Drawn are spheres of influence, where far away, dipole terms dominate; nearer quadrupole terms become important; and when plasma particles enter the wavefunction of the radiator—inside the red sphere—then penetration needs to be considered explicitly. Depending on the type of particle that enters the red sphere, different physical effects need to be considered.

Some work has been done to examine the importance of higher-order terms as well as penetrating collisions. Higher-order terms of the Coulomb expansion have been considered in some extent (e.g., Griem, 1974; Joyce et al., 1987; Kilcrease et al., 1993), but only including contributions from plasma ions and not from the electrons. Penetration effects have also been considered by Woltz & Hooper (1984) and Junkel et al. (2000), but they neglected exchange effects—a quantum effect that occurs when two identical particles occupy the same space, it is sometimes known as Pauli exclusion. To my knowledge, only Nguyen et al. (1986) has included exchange in line-broadening calculations.

This thesis will build off the work that has already been done on higher-order multipole moments and penetration. In chapter 7, I perform a systematic investigation on the effect of including both ion and electron quadrupole terms as well as a convergence study. Chapter 8 explores penetrating collisions and exchange effects of electrons, while chapter 9 investigates penetrating collisions of ions. A review of spectral line broadening formalism will be the subject of Part II. The improvements I make to line-broadening calculations will be presented in Part III.

Part II

Line Broadening Formalism, Techniques, and Approximations

Chapter 3

Spectral-Line-Broadening Formalism

Anderson (1949) first showed the fundamental equation of spectral line broadening. Anderson defined the line shape, $I(\omega)$, is defined as the real part of the Fourier transform of the average dipole-dipole autocorrelation function,

$$I(\omega) = Re \int_0^\infty dt\ e^{i\omega t} \left\langle \vec{D}_{lu} \cdot \vec{D}_{ul}(t) \right\rangle, \tag{3.1}$$

where the dipole moment, D, connects the upper and lower states (denoted by the subscripts u and l, respectively) of the transition of interest, and $\langle\rangle$ denotes a statistical average of the radiator and perturbing plasma configurations. While there is no formal proof for this derivation, Zwanzig (2001) can motivate its use, who described autocorrelation functions as a measure of relaxation processes.

Thermal/statistical averages of quantum operators are defined as the trace over the operator weighted by the density matrix,

$$\langle O \rangle = Tr\{O\rho\},$$

where O is any quantum operator. The density matrix is defined as

$$\rho = \frac{e^{-H/k_B T}}{Tr\{e^{-H/k_B T}\}}, \tag{3.2}$$

where H is the Hamiltonian of the system (which can be evaluated as a matrix, see appendix A); evaluation of a matrix exponential is given in appendix A.2.1.

The time evolution of the dipole moment is defined in the Heisenberg picture,

$$\vec{D}_{ul}(t) = U_u(t)\vec{D}_{ul}U_l^\dagger(t). \tag{3.3}$$

where $U(t)$ is the time-evolution operator; the subscripts u and l on $\vec{D}$ and U indicate that they operate only on a subset of states that make up the upper- and lower-states of the transition, respectively. The time evolution operators are defined by the time-dependent Schrödinger equation,

$$i\frac{d}{dt}U_u(t) = H_u(t)U_u(t) \tag{3.4}$$

$$i\frac{d}{dt}U_l(t) = H_l(t)U_l(t), \tag{3.5}$$

where the time-evolution initial conditions defined as the identity matrix,

$$U_u(t=0) = I \tag{3.6}$$

$$U_l(t=0) = I. \tag{3.7}$$

The subscripts on the Hamiltonians in Eq (3.5) indicate that the Hamiltonian operates only on the set of states spanning the upper (u) or lower (l) states.

3.1 Liouville Representation

The Liouville operator is used extensively in spectral line broadening; it offers a convenient way to incorporate the broadening of the upper and lower levels of the transition. We start with the time evolution of the dipole moment in the Heisenberg picture, which is

$$-i\frac{d}{dt}D_{ul}(t) = [H(t), D_{ul}(t)] = H_u(t)D_{ul}(t) - D_{ul}(t)H_l(t) \tag{3.8}$$

where $D_{ul}(t)$ is the dipole moment of the transition This equation can be written in a short-hand:

$$L(t)D_{ul} = [H(t), D_{ul}],$$

where the elements of the Liouville operator will have four indices (as opposed to the Hamiltonian which has two indices):

$$\langle u; l \,|L(t)|\, u'; l' \rangle = \langle u \,|H(t)|\, u' \rangle \, \delta_{ll'} - \delta_{uu'} \, \langle l \,|H(t)|\, l' \rangle \,. \tag{3.9}$$

More information about Liouville operators are given in appendix A.

3.2 The Hamiltonian

The Hamiltonian is used to evaluate both the density matrix as well as the time-evolution operator. It is therefore one of the critical elements in calculating spectral line broadening.

The Hamiltonian is an energy operator that contains kinetic-energy, potential-energy, and interaction-energy terms,

$$H = \sum_i K_i + \sum_i U_i + \sum_{ij} V_{ij}.$$

These different terms are often abbreviated further by including the kinetic-energy and potential-energy terms into a single operator,

$$H = \sum_i H_0^i + \sum_{ij} V_{ij},$$

so that we have part of a system that is solvable and the effects of the interaction is solved perturbatively. These different energy terms constrain the motion of the particles (classical

or quantum particles) of the system, which for the problem of Stark broadening is limited to the radiator and perturbing plasma electrons and ions,

$$H = \sum_A H_0^A + \sum_E H_0^E + \sum_I H_0^I + \sum_{AE} V_{AE} + \sum_{E \neq E'} V_{EE'} + \sum_{AI} V_{AI} + \sum_{I \neq I'} V_{II'} + \sum_{EI} V^{IE}, \quad (3.10)$$

where the first three terms represent the isolated atom (denoted with an "a"), free electron (denoted with an "e"), and perturbing ion (denoted with an "i"); the remaining terms are the interactions between all the various particles. The various interactions can be split into two categories: interactions between plasma particles ($V^{ii'}$, $V^{ee'}$, V^{ie}), and the interaction of the plasma particles with the radiator (V^{ae} and V^{ai}). The former terms are rarely treated explicitly and will be discussed more in section 4.2. Improvements in the evaluation of the latter terms are the focus of the thesis and were discussed more explicitly in chapter 2.2.

In this thesis, I will focus only on one-electron radiators, so $H^{(a,0)}$ represents the Hamiltonian of a hydrogen (or hydrogen-like) atom. If the plasma particles were treated quantum-mechanically, then the different isolated-particle Hamiltonians have eigenvalues (atomic units used throughout; $\hbar = 1, m_e = 1, e = 1$),

$$H_0^A = -\frac{1}{2}\nabla_A^2 - \frac{Z}{r_A} \quad \rightarrow \quad E_A = -\frac{1}{2}\frac{Z^2}{n^2} \quad (3.11)$$

$$H_0^E = -\frac{1}{2}\nabla_A^2 \quad \rightarrow \quad E_E = \frac{1}{2}k_E^2 \quad (3.12)$$

$$H_0^I = -\frac{1}{2m_I}\nabla_I^2 \quad \rightarrow \quad E_I = \frac{1}{2m_i}k_I^2, \quad (3.13)$$

where the energy for the isolated atom depends on the charge of the nucleus, Z, and the principle quantum number, n, while the free particles depend on the wavenumbers, denoted as k, where k is related to the momentum of the particle ($\vec{p} = \hbar\vec{k}$).

There is no line-broadening treatment that includes all of the N-body quantum effects of Eq (3.10). Practical evaluation of the time-evolution of the system requires some

simplifying assumptions to keep the problem tractable and different methods can treat some aspects of the problem better than others.

3.3 Methods for Calculating Line Shapes

There are two primary methods for solving Eq (3.1): simulation and semi-analytic approaches. Both simulation and semi-analytic methods have their own advantages and disadvantages.

If the plasma particles are assumed to be classical, their motion can be simulated. The motion of the plasma particles can provide a time-dependent perturbation on the atom, $V(t)$, and the time-evolution operator of the atomic states can be solved with the time-dependent Schrödinger equation,

$$i\frac{d}{dt}U(t) = [H_0 + V(t)]\,U(t). \tag{3.14}$$

This procedure is repeated for many different simulations of the plasma particles, each having a different set of initial conditions (positions and velocities). The average $U(t)$ is used to calculate the line shape in Anderson's equation.

Simulation methods are advantageous because certain details of the plasma particle motion can be treated explicitly. For example, simulations can easily treat the effects of ion dynamics as well as overlapping collisions. However, simulations have thus-far been limited to a semi-classical treatment where the atom is treated quantum-mechanically, while the plasma particles are treated classically (see chapter 5 for more details). No simulation-based line-shape calculation so far has treated the plasma particles quantum mechanically.

The semi-analytical method puts all of the effects of the plasma into a single oper-

ator, $\mathcal{H}(t)$, such that the time-evolution is evaluated as

$$i\frac{d}{dt}U(t) = [H_0 + \mathcal{H}(t)]\,U(t). \tag{3.15}$$

The electron broadening operator, $\mathcal{H}(t)$, is evaluated with a variety of degrees of complexity, which can include a semi-analytic treatment of the problem, similar to simulations, or $\mathcal{H}$ can be evaluated to include quantum effects of the plasma. One advantage of using semi-analytic methods is speed: the time required to calculate line shapes with semi-analytic methods is much less than it is with simulation, and semi-analytic methods do not have issues with numerical noise, so the resulting calculated spectrum is much cleaner. However, semi-analytic methods treat ion dynamics effects only approximately and such effects as multiple collisions have been completely neglected. Exact evaluation and different methods for approximating $\mathcal{H}(t)$ are presented in chapter 6.

Chapter 4

Technical Challenges and Approximations used in Spectral Line Broadening Calculations

Solving for the detailed motion and interaction of N-particles in some finite volume makes line-broadening calculations challenging. Detailed treatment of N-body effects is not feasible or practical for implementation. Simplifying assumptions must be made to approximate the set of eigenvalue solutions of Eq (3.10). This chapter shows a list of many of the commonly-used approximations; this list is not comprehensive.

Most of the approximations discussed here are valid in the limit of weak perturbations, which happen in low-density (or weakly-coupled) plasmas. For example, plasma particles in low-density plasmas travel along roughly straight-path trajectories and a small correction can be made to account for correlated motion between plasma particles. In the approximations I discuss here, only one—the incomplete basis set—is an approximation of the atomic perturbations; all other approximations are related to plasma-particle motion and how the plasma particles interact with the radiating atom.

4.1 Incomplete Basis Sets

There are only a few systems for which the energy eigenvalues and wavefunction eigenvectors are known. To solve more complicated systems, we must resort to using matrix mechanics (appendix A). When calculating the Hamiltonian of these more complicated

systems, the Hamiltonian is often split into two parts, $H = H_0 + V$, where H_0 is the part of the Hamiltonian that has known solutions:

$$H_0 \left|\psi_0\right\rangle = E_0 \left|\psi_0\right\rangle . \tag{4.1}$$

Often times for spectral-line-broadening calculations, then H_0 is the atomic Hamiltonian and E_0 is the energy of a given atomic state. To solve for the total Hamiltonian, H, matrix mechanics can be used. The unperturbed matrix of H_0 will have (in general) diagonal terms,

$$\left\langle \psi_0 \left| H_0 \right| \psi_0' \right\rangle = 0,$$

whose matrix elements are

$$\left\langle \psi_0 \left| H_0 \right| \psi_0 \right\rangle = E_0.$$

The interaction term, V, will in general be off-diagonal,

$$\left\langle \psi_0 \left| V \right| \psi_0' \right\rangle \neq 0.$$

Energy eigenvalues of the total Hamiltonian can be found by diagonalizing the H matrix, such that

$$T^\dagger H T = T^\dagger \left[H_0 + V\right] T = E$$

where T is a unitary transformation matrix and E is a diagonal matrix containing all of the energy solutions of the total Hamiltonian. The wavefunctions of the total system would be defined as a linear combination of the unperturbed states:

$$\left|\psi\right\rangle_i = \sum_j T_{i,j} \left|\psi_0\right\rangle_j , \tag{4.2}$$

where $\left|\psi\right\rangle_i$ is the ith solution of the total Hamiltonian and $\left|\psi_0\right\rangle_j$ is the jth solution to H_0. The new states are a "mixture" of the unperturbed states.

The accuracy of the wavefunctions of the total Hamiltonian depends on the number of states included in the sum in Eq 4.1; the basis set is the number of states considered in this sum. In principle, the sum would be over all eigenstates that satisfy Eq (4.1), but the number of states that span this space is infinite; this is not practical. Therefore, a decision has to be made about the number of possible states considered (the basis size).

In non-degenerate perturbation theory, the "mixing coefficients" of Eq (4.2) can be roughly evaluated as (Griffiths, 1995)

$$T_{ij} \approx \frac{\langle i\,|V|\,j\rangle}{E_i - E_j}. \tag{4.3}$$

This rough functional form for the mixing coefficients scales linearly with the size of the perturbation and inversely with the energy separation. Therefore, when the perturbation is small, or the energy separation is large, matrix elements that connect different n states can be neglected. The size of the perturbation is small at low-densities and most calculations include only the states of the same principle quantum number n as the upper and lower states of the transition. For example, for Hβ, which is $n = 4 \rightarrow n = 2$ then only the substates $2s$, $2p$, $4s$, $4p$, $4d$, and $4f$ are included. However, at higher densities, the matrix elements that connect the $n = 4$ states to the $n = 5$ states are no longer small and the $n = 5$ shell (i.e., $5s$, $5p$, $5d$, $5f$, and $5g$) needs to be included in Eq (4.2). When the perturbation becomes stronger, then additional states (beyond the state of nearest energy) need to be considered. The importance of this extended basis set has been confirmed previously (Kilcrease et al., 1993; Stambulchik et al., 2007; Djurović et al., 2009).

4.2 Use of Screening to Approximate N-body Effects

Stambulchik et al. (2007) may be the only published line-shape calculation in exis-

tence that uses explicit N-body effects; all other calculations employ some kind of screening function to describe correlations between plasma particles. In this approximation, the plasma particles follow straight-path trajectories (or plane waves) for the case of neutrals or hyperbolic-trajectories (or Coulomb waves) for charged radiators. The interaction between plasma particles and the radiator is screened to account for the presence of the other $N-1$ particles in the volume surrounding the atom (the density is defined as $n = N/V$). Use of a screening function—like Debye-Huckel theory—is valid for low-coupled plasma regimes and will break down for high-coupled regimes (Stambulchik et al., 2007), but it is used nearly universally in spectral-line-shape calculations.

Debye screening is derived from the Poisson-Boltzmann equation, which models the reaction of a neutral plasma to the presence of a test charge,

$$\nabla^2 V_{scr}(\vec{r}) \approx 4\pi\rho(\vec{r}) + 4\pi n e^{V_{scr}/k_B T}, \tag{4.4}$$

where V_{scr} is the screened potential, n is the density of plasma particles, k_B is the Boltzmann constant, and T is the temperature; the second term is the thermal distribution of the plasma reacting to the presence of the a test-charge $\rho(\vec{r})$. A second-order Taylor expansion of the exponential term yields

$$\nabla^2 V_{scr,Deb}(\vec{r}) \approx 4\pi\rho(\vec{r}) + \lambda_{Debye}^2 V(\vec{r}), \tag{4.5}$$

where λ_{Debye} is the Debye length ($\lambda_{Debye} = \sqrt{4\pi n/k_B T}$). The Green's function solution gives the formula for the Debye-screened potential:

$$\begin{aligned} V_{scr,Deb}(\vec{r}_a, \vec{r}_p) &= V(\vec{r}_a, \vec{r}_p) e^{-|\vec{r}_a - \vec{r}_j|/\lambda_{Debye}} \\ &= \frac{q_a q_j}{|\vec{r}_a - \vec{r}_j|} e^{-|\vec{r}_a - \vec{r}_j|/\lambda_{Debye}}. \end{aligned} \tag{4.6}$$

The screened potential can be evaluated by using Taylor expansion of Eq (4.6)—similar to the Taylor expansion in Eq (2.5)—or a numerical integration of Eq (4.5).

Some screening functions other than Debye exist for use in line broadening, such as dielectric functions (Dufty & Boercker, 1976), where

$$V_{scr,diel}(\vec{r}_a, \vec{r}_j) = \epsilon^{-1} V(\vec{r}_a, \vec{r}_j)$$

The accuracy of screening is important and can affect the accuracy of the collision rates.

4.3 Single-Perturber (Binary Collision) Approximation

In low-density plasmas, the time between electron collisions is long enough that they can be assumed to happen one-at-a-time; this approximation is used extensively by semi-analytical methods (simulations do not need to make this approximation). This neglects the possibility that two plasma particles could impact the atom simultaneously. This simplification allows for detailed interaction between plasma particles and the radiator, as I do in this thesis for chapter 8.

The way that this method is implemented is by solving for the detailed collision of a single-particle interaction and multiplying this interaction by the N electrons in the volume (Baranger, 1958c; Fano, 1963). However, the electron moves in the presence of the other plasma particles, and much work has been done to correct for this effect. The most common method to correct for the other plasma particles is to screen the interaction of a single particle, such effects, I will refer to as "correlations" (Hussey et al., 1975; Dufty & Boercker, 1976). As I will show in chapter 8 that correlated collisions by electrons—while they may not be simultaneous collisions—can substantially change the line shape of highly charged ions.

4.4 Quasi-Static Ions

In many line-shape calculations the ions are assumed to be static over the time it takes the autocorrelation function to decay (due to the mass difference between electrons and ions); this is especially common in semi-analytic calculations. For heavy ions, this is a valid approximation, but for neutral hydrogen, and to some extent helium, the ions can move substantially and contribute to the width of the line. This is especially important for the hydrogen Lyα line ($n = 2 \rightarrow n = 1$). Since Lyα is a narrow line, that means that the autocorrelation function takes a long time to decay; ions can move substantially over the characteristic time scales of the Lyα line.

The effect of ion motion has been determined experimentally by Wiese et al. (1975), who performed experiments and found differences in the spectral line shape that are dependent on the perturber mass. Lighter ions, such as H^+ broaden lines more than heavy ions, such as Ar^+. By the 1980's simulation methods were developed and could include ion dynamics in their calculations (Stamm et al., 1984). Later, the ion-dynamic corrections are introduced to semi-analytic calculations (Boercker et al., 1987; Ferri et al., 2014).

4.5 Separation of the Motion of Electrons and Ions

It is common to assume that the motion of the electrons and ions is uncorrelated; this assumption is almost universally made with the exception of Stambulchik et al. (2007). The reasoning is similar to that of the jellium model (Giuliani & Vignale, 2008), where the ion charge has been replaced by a background potential (a "jelly"); this is used extensively in solid-state physics. Because the plasma is net-neutral, the other $N - 1$ electrons in the plasma neutralize the uniform positively-charged ion background, allowing the plasma

electron to move about as if it were free; the correlations between plasma particles can be treated in a screening model (section 4.2). As a result, many calculations assume that the correlations between plasma ions and electrons can be neglected. This is most apparent in semi-analytic methods.

Only a few calculations have attempted to quantify this effect. Oks (2000) tried to show that the nearest ion can accelerate the path of electrons near the radiator so that it travels in a hyperbolic rather than straight-path trajectory. However, the simulated results Griem et al. (2005) and analytical arguments of Alexiou et al. (2006) show that the effect had the wrong sign and is much less important than Oks (2000) claimed. My own treatment of this problem, by assuming an additional monopole contribution in the free-electron trajectory, also shows a small increase in the widths. Further examination of the dependence of correlated electron and ion motion was explored by Stambulchik et al. (2007). One critique of these published calculations of ion-electron correlated motion is that they are all classical models; no treatment thus far treats this effect with quantum particles.

4.6 Neglect of Off-Diagonal Density Matrix Elements

The density matrix is used to weight states when performing a thermal average (Eq 3.2) and contains a matrix exponential of a Hamiltonian,

$$\rho = e^{-H\beta}/\mathrm{Tr}\left\{e^{-H\beta}\right\}.$$

As in Eq (3.10), the Hamiltonian contains information about the entire system. A common approximation used in weakly-coupled plasmas is to assume that the density matrix contains no coupling between the plasma and the radiator. This approximation assumes that the density matrix is diagonal, and therefore separable so that the density matrix of the entire

system is re-written as

$$\begin{aligned} \rho &\approx \rho_A \rho_E \\ &\approx \frac{e^{-H_A\beta}}{\mathrm{Tr}\left\{e^{-H_A\beta}\right\}} \frac{e^{-H_A\beta}}{\mathrm{Tr}\left\{e^{-H_A\beta}\right\}}. \end{aligned} \tag{4.7}$$

The kinetic theory of line broadening (see chapter 6.1.3) do not immediately assume the separation of the density matrix. Calculations of effect of off-diagonal matrix elements are not practical due to the large number of states involved in the calculation.

Boercker & Iglesias (1984) estimated the size of these effects by performing a Taylor expansion of the density matrix and examining the effects of the second-order term on plasma shifts (details are in appendix C.8). The study of Boercker & Iglesias (1984) is limited only to the static shifts (which is purely real and gives no width). For neutral hydrogen and ionized helium, the second-order static-shift term can be large compared to the first-order static-shift term.

Off-diagonal corrections to the density matrix can affect the other terms of the broadening operator and thus the width of lines can also be coupled to the plasma. Other than the second-order effects studied by Boercker & Iglesias (1984), off-diagonal matrix elements of ρ are largely unexplored.

Chapter 5

Simulation Methods

This chapter summarizes the different simulation calculations; it will be short because the simulation models all use roughly the same techniques, unlike the semi-analytic methods where different authors have different methods. Simulation calculations are split into two parts: the simulation of the plasma particles, and the time evolution of the atom.

5.1 The Plasma Simulation

The simulated plasma particles are assumed to be classical and obey a Newtonian equation of motion. The complexity of the simulations vary depending on the density and temperature of the plasma. Section 4.2 discusses a low-density simplification for simulation methods. It is common practice to assume that the plasma particles travel on straight-path trajectories (or hyperbolic trajectories for charged radiators) and account for the particle-particle correlations with screened interactions. Only Stambulchik et al. (2007) has treated the full N-body interactions of the plasma.

Simulations that use straight-path trajectories randomly sample the positions of the plasma particles according to the distribution of impact parameter distribution for a finite-sized box (Gigosos et al., 1986):

$$P(b)db = \frac{3}{R_{box}^3} b \sqrt{R_{box}^2 - b^2} db. \tag{5.1}$$

When plasma particles leave the simulation sphere, they must be re-injected with the same impact parameter; if they were re-injected randomly, the particles would drift to the edge of the simulation sphere. Stambulchik & Maron (2006) on the other hand uses both a re-injection technique and periodic boundary conditions.

Non-interacting simulation calculations of neutral hydrogen usually define a time-step that is of order 1% of the particle crossing time, defined to be r_{typ}/v_{th}, defined as

$$\begin{aligned} r_{typ} &= \left(\frac{3n_e}{4\pi}\right)^{1/3} \\ v_{th} &= \sqrt{\frac{2k_BT}{m}}. \end{aligned}$$

This criteria for time resolution works well for neutral hydrogen, but more highly-coupled systems require a different criteria for the time step.

Assuming the plasma particles do not interact with each other and correcting for correlations with Debye-screened interactions (with the radiator) is quite common. It should be noted that the plasma particles do interact with the radiator, where their trajectories are either straight-path (for neutral radiators) or hyperbolic (for charged particles). The simulation code *Xenomorph* that I will be using for chapter 7, uses the same approximations as Gigosos et al. (1986) for the plasma particles: straight-path trajectories with Debye-screened plasma-radiator interactions, and numerical sampling according to the impact parameter.

Simulations that account for the detailed N-body interaction often use periodic boundary conditions. Care must be taken when performing these detailed simulations. If two point particles (whose Lorentz force scales as the inverse distance squared) get too close, then they may accelerate each other. Too many of such interactions can lead to an unphysical heating of the plasma; this is one advantage of the non-interacting plasma where

numerical heating need not be considered. A variety of methods can be used to correct for this, including an adaptive time-step, or a cutoff for the Lorentz force. The fully interacting method must use a much smaller time-step than the non-interacting simulation to avoid numerical jumps in the Lorentz force between plasma particles.

Plasma simulations can produce microfield distributions and a comparison of the different methods is a good check of their accuracy. Independent-particle simulations with Debye-screened fields can reproduce the microfield distributions calculated analytically by Hooper (1968). The detailed fully interacting simulations can also reproduce Hooper's calculations at low coupling/density. However, as shown by Stambulchik et al. (2007), this breaks down for higher-coupled plasmas. In these higher-coupled (or high-density) plasmas, the ions can "drag" the electrons around, changing the effective screening length, which will disagree with previously established calculations of microfield distributions.

The various details of the simulations—the randomness, size of the box, or the way the motion of plasma particles is altered by the presence of other particles—can affect the resulting line shape.

5.2 Time Evolution of the Atom

The simulated motion of the collective plasma particles provides a time-dependent potential, $V_{AE}(t)$ for electrons, and V_{AI} for ions. The interaction potential is usually assumed to be the atomic dipole moment times the plasma electric field, where the total interaction of the plasma with the radiator is

$$V(t) = \sum_E V_{AE}(t) + \sum_I V_{AI}(t) = \vec{D}_A \cdot \left\{ \sum_E \vec{F}_E(t) + \sum_I \vec{F}_I(t) \right\}.$$

Plasma electric fields, $\vec{F}_{AE}(t)$ and $\vec{F}_{AI}(t)$ are sensitive to the simulation details about screening and correlations and will become more so for higher coupling.

The total interaction potential, $V(t)$ is inserted into the time-dependent Schrödinger equation,

$$i\frac{d}{dt}U(t) = \left[H_0^A + V(t)\right]U(t). \tag{5.2}$$

This process of simulating a field history, then solving the time-dependent Schrödinger equation is repeated over many simulations with different initial conditions. The time-evolution operators of the different simulated time histories are averaged to produce the autocorrelation function used in Anderson's equation (Eq 3.1).

In some calculations (such as Stambulchik & Maron, 2006), the interaction picture is used for the time-dependent Schrödinger equation,

$$i\frac{d}{dt}U_I(t) = V_I(t)U_I(t),$$

where both the wavefunctions and the interaction potential shares the time dependence,

$$\begin{aligned} |\psi_I(t)\rangle &= e^{iH_0^A t}\,|\psi\rangle \\ V_I(t) &= e^{iH_0^A t}V(t)e^{-iH_0^A t}. \end{aligned}$$

This has the advantage of removing the known high-frequency part of the calculation and only the modulation due to the plasma perturbation is in $U_I(t)$. The technique of removing the known high-frequency part can also be achieved with $U(t)$ by multiplying by $e^{i\omega_0 t}$:

$$\tilde{U}(t) = e^{i\omega_0 t}U(t).$$

Using either $\tilde{U}(t)$ or $U_I(t)$ results in numerically clean autocorrelation functions, which is handy for the performing the final Fourier transform to get the final line-shape.

There are different available numerical techniques for solving Eq (5.2), including, but not limited to explicit (Stambulchik & Maron, 2006) and implicit (Calisti et al., 1990) Runge Kutta integrators, as well as matrix exponential methods (Gomez, 2013, ; see also appendix A.2), and for the special case of hydrogen, Euler-Rodriguez parameters can be used (Gigosos & Cardenoso, 1987). Care must be taken when integrating the time-dependent Schrödinger equation. If plasma particles are too close to the radiator, the interaction potentials become large and the differential equations become "stiff," and numerically unstable. Certain techniques, such as the matrix exponential, or the implicit Runge-Kutta methods (such as backward Euler or implicit midstep), handle the stiffness of the differential equations quite nicely. The explicit methods, however, do not. One remedy is to use an adaptive time-step integrator, where the time-step used when numerically integrating Eq (5.2) is modified so that $V(t)\Delta t$ remains small. A recent study at the 3rd spectral line shape workshop showed that given an electric field history (at sufficiently high time resolution) all four methods give the same spectral line shape.

5.3 History of Simulation Calculations

This section gives a brief overview of simulation calculations and its successes in explaining experimental data. I also discuss the improvements of the simulation methods over the years.

The first simulation calculations emerged in the early 1980's, with the first published result (of which I am aware) is Stamm et al. (1984). These simulations were built to explain the discrepancies between calculated and measured line profiles of low-n transitions (factors of two in the width) of the Lyα line of neutral hydrogen. Stamm et al. (1984) used a

semi-analytic method of electron broadening and simulated the ions. The ions traveled on straight-path trajectories and the interaction between the radiator and the ions is a screened Debye potential (see chapter 4.2). Incorporation of ion motion is one of the major successes of the simulation method and Stamm et al. (1984) was the first of many studies to show that ion motion is necessary to include in calculations in order to accurately reproduce measured line profiles (e.g. Calisti et al., 1990; Ferri et al., 2014; Luque et al., 2003; Djurović et al., 2009).

Gigosos et al. (1985) provided some simplifying tools for his future work on simulation-based line-shape calculations of neutral hydrogen. Gigosos & Cardenoso (1987) simulated both ion and electron motion, which traveled along the straight-path trajectories with Debye-screened interactions with the radiator—same as Stamm et al. (1984). In hydrogen, where the states are degenerate with principle quantum number n, then a mathematical simplification can be made to evaluate the time-evolution operator: Euler-Rodriguez parameters. Euler-Rodriguez parameters are related to rotation angles; this is useful because the electric fields provided by the plasma particles are stochastic and move randomly in all directions. The simplification of the time-evolution operator to Euler-Rodriguez parameters made it easy to calculate a grid of line-profiles for use in experiments (Gigosos et al., 2003). However, the method of Euler-Rodriguez parameters only works when the field-free eigenstates considered for the upper or lower states are degenerate in energy. This method cannot be used when $\Delta n \neq 0$ interactions (chapter 4.1) become important; the grids in Gigosos et al. (2003) are limited due to this limitation. Using Euler-Rodriguez parameters are valid only for plasma conditions where $\Delta n \neq 0$ interactions can be safely ignored. The calculations published with the asymmetry study by Djurović et al. (2009) included an

expanded basis set, but used a matrix exponential solver rather than the Euler-Rodriguez parameters.

The last major publication before my master's simulation code (Gomez, 2013) was Stambulchik & Maron (2006). In their simulation, they modeled more complex atoms, using an explicit adaptive-time-step Runge-Kutta integration of the time-evolution operator, so it is therefore not limited to degenerate systems. Also, the explicit N-body interaction of the plasma particles is treated in the simulation. This provided a good test for the Debye-screened approximation (Stambulchik et al., 2007).

Simulations (because they can isolate certain effects) have been used to validate—or invalidate—claims by other calculations. For example Oks (2000) claimed narrowing of hydrogen lines due to the acceleration of electrons by the nearest ion to the radiator. Simulation methods, which can isolate the effect, showed this effect to be much smaller than was claimed and has the opposite sign (Griem et al., 2005; Stambulchik et al., 2007).

Chapter 6

Semi-Analytical Method

Semi-analytic methods separate the effects of the ions and electrons:

$$I(\omega) = \int_0^\infty W(F_{\rm ion}) J(\omega, F_{\rm ion}) dF_{\rm ion}, \tag{6.1}$$

where the average perturbation due to the ions is evaluated with an integration over plasma microfields, and J is an average electron broadening function; W is the microfield probability distribution function.

$$\begin{aligned} J(\omega, F_{\rm ion}) &= {\rm Re}\frac{1}{\pi}\int dt\ e^{i\omega t} \times \\ &\quad \left\langle D_{lu} \exp\left[-i(H_0^A + H_0^E + V_{AE} + \vec{D}\cdot\vec{F}_{\rm ion})_u t\right] \vec{D}_{ul} \exp\left[i(H_0^A + H_0^E + V_{AE} + \vec{D}\cdot\vec{F}_{\rm ion})_l t\right]\right\rangle. \\ &= {\rm Re}\frac{1}{\pi}\int dt\ e^{i\omega t} \left\langle D_{lu} \exp\left[-i(L_0^A + L_0^E + L_{AE} + (\vec{D}_u - \vec{D}_l)\cdot\vec{F}_{\rm ion})t\right] \vec{D}_{ul}\right\rangle. \end{aligned}$$

The electron broadening operator is derived from Eq (3.3); it takes the many-body effects of the Hamiltonian and puts it in an effective collision operator, $\mathcal{H}(t)$:

$$Tr_e\left\{\exp\left[-i(L_0^A + L_0^E + L_{AE})t\right] \vec{D}_{ul}\rho_{AE}\right\} = e^{-iL_0^A t}\vec{D}_{ul} e^{-i\mathcal{H}(t)t}\rho_A, \tag{6.2}$$

where the interaction of only one electron is shown (and the ion term neglected) for simplicity but should contain the effects from all of the electrons in the plasma. The real part of the Fourier transform of Eq 6.2 gives a Lorentz shape with a frequency-dependent width,

$${\rm Re}\ \mathcal{F}\{e^{-iL_0^A t}\vec{D}_{ul} e^{-i\mathcal{H}(t)t}\rho_a\}(\omega) = {\rm Im}\frac{-1}{\omega - L_0^A - \mathcal{H}(\omega)}\rho_a. \tag{6.3}$$

which combined with Anderson's equation, the atomic Hamiltonian results in the standard formula for spectral line shapes.

$$J(\omega, F_{ion}) = \frac{-1}{\pi} \mathbb{I}\mathrm{m}\ D \left[\omega - L_0^A - \mathcal{H}(\omega)\right]^{-1} D, \tag{6.4}$$

which has become the "standard-theory" equation used for spectral-line-shape calculations.

The collision operator, $\mathcal{H}(\omega)$, is a complex-valued operator, where the real-part contributes to shifts, while the imaginary part gives a width. Practical evaluation of the $\mathcal{H}(\omega)$ requires the use of many approximations to keep the problem tractable, many of these approximations are discussed in chapter 4. Derivations of a functional form of $\mathcal{H}(\omega)$ varies between different approaches.

Even though only approximate forms of $\mathcal{H}$ exist, semi-analytic methods can treat some effects that simulations cannot, such as quantum effects of the plasma electrons. Semi-analytic methods do have limitations; no calculation so far has included the effects of multiple collisions, though this is handled trivially in simulation.

In this chapter, I go through the developments of semi-analytic electron broadening. I warn the reader that the rest of this chapter is technical, and the derivations may be tedious or lacking explanation. There should be sufficient references if more details are required; this is intended as an introduction, overview, and comparison of the different methods. One of the main take-away points of this section is the relation of the electron-broadening operator to scattering processes. Section 6.1.4 gives a summary of the quantum-mechanical methods showing the similarities between the different derivations.

6.1 The Various Formalisms

There are many different methods to evaluate $\mathcal{H}$; I feel it is necessary to discuss the various approaches used to solve the line-broadening equations. In the following, I will discuss the foundations and approximations used by the different formalisms. First is the impact formalism, as derived by Baranger and Griem in the late 1950s. Second, the relaxation theory was developed by Fano in the early 1960s. This was a re-derivation of Baranger's work, but with more a general treatment of line broadening, especially with respect to ensemble effects. The third method is the kinetic theory of Hussey, which is derived from the BBGKY hierarchy; this theory has not been used as widely as the impact, relaxation, or unified theories.

In the discussion below, I will use V to denote all plasma-radiator interactions. I will not make any assumptions about the form of V. It should be noted that most of the implementations of the theories use the dipole approximation (see chapter 2.2). Sometimes the interaction picture is used in this chapter, which uses a combination of both the Heisenberg and Schrödinger pictures for time evolution. This formalism only applies when there is a reference Hamiltonian, H_0 and a time-dependent perturbation $V(t)$ that is additive, such that

$$H = H_0 + V(t).$$

The time-dependent Schrödinger equation is redefined so that

$$i\frac{d}{dt}U(t) = [H_0 + V(t)]\,U(t) \Rightarrow i\frac{d}{dt}U_I(t) = V_I(t)U_I(t) \tag{6.5}$$

where the wavefunctions have Schrödinger time-dependence,

$$|\psi_I(t)\rangle = e^{iH_0 t}\,|\psi\rangle \tag{6.6}$$

and operators have Heisenberg time evolution:

$$V_I(t) = e^{iH_0 t} V(t) e^{-iH_0 t}, \tag{6.7}$$

where $V(t)$ is the usual interaction between the radiator and plasma particles. In this picture, both the states and the operators have time-evolution. The three pictures (Heisenberg, Schrödinger, and interaction) are identical in their implementation (i.e. matrix elements come out the same).

6.1.1 Impact Formalism

The formulation by Baranger (1958a) focuses only on the electron contribution to the line shape, therefore neglecting the ion contribution (i.e., neglecting all terms with "i" superscript in Eq 3.10). In the first quantum electron broadening theory, Baranger (1958c) simplified the problem so that only binary collisions are considered. The binary-collision approximation reduces the many-body interaction to a series of binary-collisions:

$$\mathcal{H} \approx Nh,$$

where h is the average interaction between the atom and one electron. This is called the impact approximation, which is accurate only for weak collisions and when the time between collisions is long compared to the duration of a collision.

Baranger writes the time evolution as (neglecting lower-state collisions with the plasma electron):

$$\left\langle \vec{k} \right| \left(e^{-iH_0^A t} e^{i(H_0^A + H_0^E)t} \right)_l \left(e^{-i(H_0^A + H_0^E + V_{AE})t} \right)_u \left| \vec{k}' \right\rangle \tag{6.8}$$

where u and l labels indicate which set of atomic states (upper or lower) the operators act on, $\vec{k}$ denotes the free-electron state; the energy of the free electron is $k^2/2$ (see chapter

3.2). The thermal average is evaluated with a trace over the free-electron states weighted by the density matrix. This trace from the thermal average forces $\vec{k}$ to be equal to $\vec{k}'$, so this is why $\vec{k}$ appears on both sides of the matrix element in Eq (6.8).

The evaluation of the average interaction with the electrons is not in a convenient form, so Baranger used the transformation,

$$e^{-i(H_0^A+H_0^E+V_{AE})t} = e^{-i(H_0^A+H_0^E)t} - i\int_0^t dt' e^{-i(H_0^A+H_0^E)(t-t')} V_{AE} e^{-i(H_E^A+H_0^E+V_{AE})t'}, \quad (6.9)$$

to simplify the matrix exponential in Eq (6.8) for a single perturber (Baranger, 1958a). If we look closely at the last time evolution term and use it to evolve a ket, then we see that this is an outgoing scattered wave,

$$e^{-i(H_0^A+H_0^E+V_{AE})t'}|u'\vec{k}\rangle = e^{i(E_A+\epsilon^k)t'}|\phi^+_{u'\vec{k}}\rangle.$$

The scattered wave is an eigenvalue of the total two-particle Hamiltonian, and whose solution is obtained by an integral equation (Lippmann & Schwinger, 1950),

$$|\phi^+_{u'\vec{k}}\rangle = |u'\vec{k}\rangle + \lim_{\eta\to 0}\frac{1}{E_A+\epsilon-H_0^A-H_0^E-V_{AE}+i\eta}V_{AE}|\phi^+_{u'\vec{k}}\rangle. \quad (6.10)$$

With this definition, Baranger related electron broadening to scattering. The quantity that defines the electron width and shift is the transition "T"-matrix, defined as

$$\left\langle u\vec{k}\,|T|\,u'\vec{k}\right\rangle = \frac{2m_e}{\hbar^2}\left\langle u\vec{k}\,|V_{AE}|\,\phi^+_{u'\vec{k}}\right\rangle. \quad (6.11)$$

One can use Eq (6.10) to evaluate this to some perturbation order, but this perturbation expansion, coupled with the definition (Eq 6.11), can also be written in an exact form,

$$\left\langle u\vec{k}\,|T|\,u'\vec{k}\right\rangle = \frac{2m_e}{\hbar^2}\left\langle u\vec{k}\left|\frac{1}{1-V^{AE}G}V^{AE}\right|u'\vec{k}\right\rangle, \quad (6.12)$$

where G is the inverse operator in Eq (6.10):

$$G = \lim_{\eta \to 0} \frac{1}{E_A + \epsilon - H_0^A - H_0^E - V_{AE} + i\eta}.$$

To bring this back to line-shapes, then Eq (6.9) can be rewritten in terms of a "T"-matrix

$$e^{-i(H_0^A + H_0^E + V_{AE})t} = e^{-i(H_0^A + H_0^E)t} - i \int_0^t dt' e^{-i(H_0^A + H_0^E)(t-t')} T e^{-i(H_0^A + H_0^E)t'}. \tag{6.13}$$

It is at this point that we average over the free-electron states since all the relevant terms are linearized. The total scattering "T"-matrix, by use of a time-ordered integral over the various collisions (see Baranger, 1958a), becomes h; when multiplied by N particles becomes the broadening operator,

$$\begin{aligned} e^{-iH_0^A t} \left\langle e^{i(H_0^A + H_0^E)t} e^{-i(H_0^A + H_0^E + V_{AE})t} \right\rangle_e &= \exp\left[-i(H_0^A + N\langle T\rangle)t\right] \\ &= \exp\left[-i(H_0^A + \mathcal{H})t\right]. \end{aligned} \tag{6.14}$$

Therefore, the electron broadening operator is assumed to be time-independent and is related simply to the "T"-matrix

$$\mathcal{H} = N\langle T\rangle. \tag{6.15}$$

If the lower-state broadening is included, then the electron broadening operator also includes the "T"-matrix of the lower state, and an interference term,

$$\mathcal{H} = N\langle T_u\rangle + N\langle T_l\rangle - N\langle T_u T_l\rangle. \tag{6.16}$$

These equations were also derived indecently by Kolb & Griem (1958), who also used similar binary-collision approximations.

6.1.2 Fano's Relaxation Theory

Fano (1963) re-derived Baranger's results, but took a different approach, using elements of Zwanzig (1960) theory of irreversibility. Fano referred to spectral line broadening as a "prototype for relaxation"; a relaxation process describes the return to equilibrium of the radiator with its environment (relaxation of the radiator to a thermal bath). Therefore, the line shape is a measure of how long it takes for a radiating atom to equilibrize with its surroundings (Zwanzig, 2001).

The Fourier transform of Anderson's equation (Eq 3.1) is immediately performed, giving

$$I(\omega) = Im\ Tr\left\{\vec{D}\frac{1}{\omega - H_u + H_l}(\rho\vec{D})\right\}, \tag{6.17}$$

where the Hamiltonians contain all terms from all particles, the subscript u and l denote the upper and lower states of the transition. I will now introduce some short-hand notation for the following derivation:

$$\hat{H}_0 = H_0^A + \sum_E H_0^E + \sum_I H_0^I \tag{6.18}$$

$$\hat{V} = \sum_E V_{AE} + \sum_{E\neq E'} V_{EE'} + \sum_I V_{AI} + \sum_{I\neq I'} V_{II'} + \sum_{EE} V_{IE}, \tag{6.19}$$

where the hats on the operator indicate that it acts on more than one particle and the total Hamiltonians appearing in Eq (6.17) is

$$H = \hat{H}_0 + \hat{V}.$$

I then move to a Liouvillian notation such that

$$L = [H,]$$

$$L_0 = [\hat{H}_0,]$$

$$L_1 = [\hat{V},]$$

Fano then does the following algebraic manipulations:

$$\begin{aligned}
\frac{1}{\omega - L_0 - L_1} &= \frac{(\omega - L_0)^{-1}}{(\omega - L_0)^{-1}} \frac{1}{\omega - L_0 - L_1} \\
&= (\omega - L_0)^{-1} \frac{1}{1 - (\omega - L_0)^{-1} L_1} \\
&= (\omega - L_0)^{-1} \frac{1}{1 - (\omega - L_0)^{-1} L_1} \times \\
&\quad \left[1 - (\omega - L_0)^{-1} L_1 + (\omega - L_0)^{-1} L_1\right] \\
&= (\omega - L_0)^{-1} \left[1 + T(\omega) \frac{1}{\omega - L_0}\right] \qquad (6.20) \\
T(\omega) &= \frac{1}{1 - L_1 (\omega - L_0)^{-1}} L_1 \\
&= L_1 + L_1 (\omega - L_0)^{-1} L_1 + \cdots . \qquad (6.21)
\end{aligned}$$

This form separates the effects of the "bath" into a single operator, $T(\omega)$. When the trace is performed over perturber coordinates, Eq (6.20) will become

$$(\omega - L_0^A)^{-1} \left[1 + \langle T(\omega) \rangle \frac{1}{\omega - L_0^A}\right].$$

The operator $T(\omega)$ is now the exact same "T"-matrix formula as in Baranger's impact formula, but is not in the denominator as expressed by Baranger. In order to evaluate an operator that is in the denominator,

$$\frac{1}{\omega - L_0^A - \mathcal{H}(\omega)}, \qquad (6.22)$$

we do a similar transformation as in Eq (6.20),

$$\begin{aligned}\frac{1}{\omega - L_0^A - \mathcal{H}(\omega)} &= (\omega - L_0^A)^{-1}\left[1 + \langle T(\omega)\rangle \frac{1}{\omega - L_0^A}\right] \\ \langle T(\omega)\rangle &= \frac{1}{1 - \mathcal{H}(\omega)(\omega - L_0^A)^{-1}}\mathcal{H}(\omega).\end{aligned}$$

With some algebraic manipulation,

$$\langle T(\omega)\rangle = \frac{1}{1 - \mathcal{H}(\omega)(\omega - L_0^A)^{-1}}\mathcal{H}(\omega)$$

$$\left[1 - \mathcal{H}(\omega)(\omega - L_0^A)^{-1}\right]\langle T(\omega)\rangle = \mathcal{H}(\omega)$$

$$\langle T(\omega)\rangle = \mathcal{H}(\omega) + \mathcal{H}(\omega)(\omega - L_0^A)^{-1}\langle T(\omega)\rangle$$

$$\langle T(\omega)\rangle = \mathcal{H}(\omega)\left[1 + (\omega)(\omega - L_0^A)^{-1}\langle T(\omega)\rangle\right]$$

The electron broadening operator is defined as

$$\begin{aligned}\mathcal{H}(\omega) &= \frac{1}{1 + \langle T(\omega)\rangle(\omega - L_0^A)^{-1}}\langle T(\omega)\rangle \\ &= \langle T(\omega)\rangle - \langle T(\omega)\rangle(\omega - L_0^A)^{-1}\langle T(\omega)\rangle + \cdots . \qquad (6.23)\end{aligned}$$

The relaxation theory has this additional transformation not present in Baranger's impact theory. I also note that $\mathcal{H}(\omega)$ contains a frequency dependence; this will be important for the wings of the line.

Fano simplified the problem further by reducing the complicated N-body interaction into powers of the gas density n. The total "T"-matrix is rewritten as

$$\langle T\rangle = n\, Tr_{e_1}\{T^{(a,e_1)}\rho\} + \frac{1}{2}n(n - 1/V)Tr_{e_1,e_2}\{T^{(a,e_1,e_2)}\rho + \cdots\} \qquad (6.24)$$

where the first term contains all the information about one electron interacting with the radiator (two-body collision; denoted as $T^{(A,E_1)}$ where plasma electron 1 interacting with atom), while the second term contains information about two electrons interacting with the

radiator (three-body collision; denoted as $T^{(A,E_1,E_2)}$ where both electron 1 and electron 2 interact with the atom):

$$T^{(A,E_1)} = \frac{1}{1 - L_{A,E_1}\left(\omega - L_0^A - L_0^{E_1}\right)^{-1}} L_{A,E_1} \tag{6.25}$$

$$\begin{aligned} T^{(A,E_1,E_2)} = & \Big[1 - \left(L_{A,E_1} + L_{A,E_2} + L^{E_1E_2}\right) \times \\ & \left(\omega - L_0^A - L_0^{E_1} - L_0^{E_2}\right)^{-1}\Big]^{-1} \times \\ & (L_{A,E_1} + L_{A,E_2} + V_{E_1E_2}) - T^{(A,E_1)} - T^{(A,E_2)}. \end{aligned} \tag{6.26}$$

The first term of Eq (6.24) corresponds to the binary collision term, the second term is 3-body collision process. Higher-order terms capture the physics of collisions involving at least 4 particles.

6.1.3 Kinetic Theory

The kinetic theory is based on Hussey et al. (1975) who derived and line-broadening operator from the BBGKY hierarchy and uses some kind of closure relationship. The time-evolution operator in Hussey et al. (1975) is defined as F, and there is a time evolution for each particle in the system (electrons only),

$$-i\tfrac{d}{dt}F^a(t) \quad +L_0^A F^a(t) + n_e Tr_1\{L_{A,E_1}F^{A,E_1}(t)\} = 0 \tag{6.27}$$

$$\begin{aligned} -i\tfrac{d}{dt}F^{A,E_1}(t) \quad & +(L_0^A + L_0^{E_1})F^A(t) \\ & +n_e Tr_2\{(L_{A,E_1} - L_{E_1,E_2})F^{A,E_1,E_2}(t)\} = 0. \end{aligned} \tag{6.28}$$

The operator F has the density matrix, ρ, built into its solution. It is at this point that I would like to pause to explain that, in Fano's derivation, he assumed that the density matrix, ρ, contained only diagonal elements of the Hamiltonian; this made ρ separable

into ρ_A and a ρ_E. In the kinetic theory, this assumption is not made, and the interaction potential is included in the evaluation of ρ.

Through operator manipulation, Hussey et al. (1975) derived a closed form equation for $F^A(t)$,

$$-i\frac{d}{dt}F^A(t) + L_0^A F^A(t) = -BF^A(t) - \int_0^t d\tau\ M(t-\tau)F^A(\tau) \tag{6.29}$$

where B is defined as $n_e Tr_1\{L^{A,E_1}\rho^{(A,E_1)}\rho^{(A)^{-1}}\}$. The M operator is more difficult to evaluate since it contains the many-body effects of the problem. A Fourier transform provides an equation for the spectral line shape as

$$I(\omega) = \frac{-1}{\pi}D\frac{1}{\omega - L_0^A - B - M(\omega)}D,$$

where the electron broadening operator is defined as

$$\mathcal{H}(\omega) = B + M(\omega)$$

in the kinetic theory.

I will not provide a detailed derivation here, I will simply show the results for the different terms of $\mathcal{H}(\omega)$ as defined by Hussey et al. (1975):

$$\begin{aligned}
B &= n_e Tr_1\left\{L_{A,E_1}\rho_{A,E_1}\right\}\rho_A^{-1} \\
M(\omega) &= n_e Tr_1\left\{L_{A,E_1}\frac{1}{\omega - L_0^A - L_0^{E_1} - L_{A,E_1} - \mathfrak{V}^{a,1}(\omega)}\mathcal{L}_{A,E_1}\right\} \\
\mathcal{L}_{A,E_1} &= L_{A,E_1} + n_e\rho_A^{-1}Tr_2\{(\rho_{A,E_1,E_2} - \rho_{A,E_2})L_{A,E_2}\} \\
\mathfrak{V}^{A,E_1}(\omega) &= \rho_A^{-1}n_e Tr_2\{\rho_{A,E_2}L_{A,E_2}\} + \rho_{A,E_1}^{-1}n_e Tr_2\{\rho_{A,E_1,E_2}L_{E_1,E_2}\} + \Delta,
\end{aligned}$$

where Δ takes into account multiple simultaneous collision interactions.

6.1.4 Second-Order Broadening Operators

The equations derived in the previous subsections are too complicated to solve. Evaluation of the various terms requires large matrix inversions and is usually not done except for simple systems and even then with limited basis sets. Calculations often employ a second-order Taylor expansion to simplify the problem. The second-order equations are listed here for convenience, starting with the impact theory, followed by the relaxation theory, and finally the kinetic theory:

$$\mathcal{H}_{impact} = Tr_1\{L_{A,E_1}\rho_{E_1}\} + Tr_1\{L_{A,E_1}GL_{A,E_1}\rho_{E_1}\} \tag{6.30}$$

$$\begin{aligned}\mathcal{H}_{relax}(\omega) &= Tr_1\{L_{A,E_1}\rho_{E_1}\} + Tr_1\{L_{A,E_1}(\omega - L_0^A - L_0^{E_1})^{-1}L_{A,E_1}\rho_{E_1}\} \\ &\quad -Tr_1\{L_{A,E_1}\rho_{E_1}\}(\omega - L_0^A)^{-1}n_e Tr_1\{L_{A,E_1}\rho_{E_1}\}\end{aligned} \tag{6.31}$$

$$\begin{aligned}\mathcal{H}_{kinetic}(\omega) &= Tr_1\{L_{A,E_1}\rho_{A,E_1}\} + Tr_1\{L_{A,E_1}(\omega - L_0^A + L_0^{E_1})^{-1}L_{A,E_1}\rho_{A,E_1}\} \\ &\quad +Tr_1\{L_{A,E_1}\rho_{A,E_1}\}(\omega - L_0^A)^{-1}n_e Tr_2\{L_{A,E_2}\rho_{E_1,E_2}\} \\ &\quad -Tr_1\{L_{A,E_1}\rho_{A,E_1}\}(\omega - L_0^A)^{-1}n_e Tr_2\{L_{A,E_2}\rho_{A,E_2}\}.\end{aligned} \tag{6.32}$$

6.2 Implementation of Theories

In this section, I will outline some of the important calculations and what approximations are used. I would like to warn the reader that some of the notation may change because this is a summary of many different works; I will try to keep it similar to the above sections.

6.2.1 Impact Theory

The first practical use of the impact theory was by Hans Griem, and he has used it throughout his career. Griem's treatment of line broadening in hydrogen assumes clas-

sical particles moving along straight-path trajectories. Griem approximates the Coulomb interaction with the dipole interaction (Eq 2.7), where the time-dependent electric field of a plasma particle, whose closest approach is b,

$$V(t) = \vec{r} \cdot \vec{r}_i \frac{1}{|\vec{r}_i|^3} = \frac{\vec{D} \cdot \left(\vec{b}_i + \vec{v}_i t\right)}{(b_i^2 + v_i^2 t^2)} \tag{6.33}$$

where r_i and v_i are the position and velocity of particle i. Griem et al. (1959) use a Dyson series to solve the time-dependent Schrödinger equation and stop at second-order in the interaction picture (Eq 6.5)

$$U_I(t) \approx 1 - i \int_{-\infty}^{\infty} V(t) dt + (-i)^2 \int_{-\infty}^{\infty} dt \int_{-\infty}^{\infty} dt' V(t) V(t'). \tag{6.34}$$

In a plasma, the average electric field in a plasma is zero, therefore the second term of Eq (6.34) is zero. After averaging out the different possible angles for b_i in Eq (6.33), then the time-evolution operator simplifies to

$$U_i(t) = 1 - \frac{2}{3} \frac{\vec{D} \cdot \vec{D}}{(bv)^2}, \tag{6.35}$$

where $f(v)$ is a Maxwellian distribution, and as usual, N is the number of electrons in the volume. Griem et al. (1959) used an effective operator, which they called ϕ to describe the average interaction.

$$\begin{aligned} \phi &= 2\pi \int \int dbdv \; bf(v)(U_i(t) - 1) \\ &= -2\pi N \int \int db \; dv \; bf(v) \frac{2}{3} \frac{\vec{D} \cdot \vec{D}}{(bv)^2}, \end{aligned} \tag{6.36}$$

where $f(v)$ is the velocity distribution,

$$f(v) = \sqrt{\frac{2}{\pi}} \left(\frac{m}{k_B T}\right)^{2/3} v^2 e^{-mv^2/2k_B T} \tag{6.37}$$

and the impact parameter distribution is simply b.

The integral diverges at small impact parameter, which is unphysical; this is a result of not using the full-Coulomb interaction (Eq 2.5). To avoid this divergence and mimic the effect of penetrating collisions, Griem et al. (1959) employ an impact parameter cut-off derived from the Lorentz-Weisskopf collision frequency. The final equation for the collision operator is

$$\phi = \frac{1}{3}\left(\frac{8\pi m_e}{kT}\right)^{1/2} N\ \vec{D}\cdot\vec{D}\int_{y_{min}}^{\infty} dy \frac{e^{-y}}{y} \tag{6.38}$$

$$y_{min} = \frac{4\pi N}{3m}\left(\frac{n^2}{kT}\right)^2, \tag{6.39}$$

where n is the principle quantum number of the upper state of the transition. Kepple & Griem (1968) expanded on the work of Griem et al. (1959) by supplying better corrections for the close interactions and strong collisions as well as including lower state broadening. Kepple & Griem (1968) also truncated the impact parameter integral to stop at some maximum impact parameter, chosen to be the Debye length to mimic N-body effects.

The fundamental work of Griem et al. (1959) and Kepple & Griem (1968) became the basis for the line broadening calculations that came later, such as the He II electron broadening treatment (Kepple, 1972) or the semi-classical calculations of highly-charged ions (Griem et al., 1979).

There were several quantum-mechanical calculations that Griem performed, where the scattering "T"-matrix for the line-shape was calculated other established codes used by the scattering community. In these papers, few details of the calculation are provided, making his work less transparent (e.g. Bely & Griem, 1970; Griem et al., 1979; Griem & Ralchenko, 2000). In some cases, Griem used the quantum mechanical calculations to

calibrate the semi-classical calculations, for example, Griem et al. (1979) used the results of Davis et al. (1976) to calibrate the strong-collision cutoffs and corrections.

Nguyen et al. (1986), who also equated $\mathcal{H}$ to the "T"-matrix, also provided some impact approximation calculations for charged one-electron radiators, examining the effects of ionization and strong plasma perturbations. The details of the evaluation of the "T"-matrix in Nguyen et al. (1986) were provided and they included effects such as exchange; this is an all-order evaluation of the "T"-matrix. As with all impact-theory calculations, $\mathcal{H}$ is assumed to be frequency independent and will be inaccurate at the wings of the line; $\mathcal{H}_{impact}$ also ignores multiple collision effects.

6.2.2 Relaxation Theory Calculations at the University of Florida

The implementation of the relaxation theory of line broadening was done at the University of Florida under the supervision of Prof. Hooper. Earl Smith, Professor Hooper's first student to work on line broadening, used the relaxation theory of Smith & Hooper (1967) to calculate hydrogen line shapes. The calculations by Smith & Hooper (1967) assumed the dipole approximation and assumed the perturbing electrons were quantum-mechanical plane waves. However, these calculations were incomplete and gave unphysical answers; for example, the hydrogen Lyα line had a double-peak structure when it is supposed to have an unshifted central component (see chapter 2.1). A follow-up publication (Smith, 1968) corrected the Lyα line by including the effects of plasma correlations. Plasma correlations are accounted for with screening, which reduces the size of the interaction and eliminated the double peak structure of Lyα.

The relaxation theory was continued under the supervision of Prof. Hooper with

a number of students working on its development or on developing improved microfield distributions. In the following theories, as with the previous calculations, the dipole approximation is made unless otherwise stated.

O'Brien & Hooper (1974) started with the second-order calculations of Smith & Hooper (1967) and applied it to a charged-radiator system, namely He II. It is practically the same calculation as Smith & Hooper (1967) but with Coulomb waves instead of plane waves. Since O'Brien & Hooper (1974) were evaluating the behavior of quantum electrons scattering off of a charge, they were able to relate the electric field of the plasma to the free-free Gaunt factor; this technique has been used by the line-shape code MERL (Woltz & Hooper, 1988; Mancini et al., 1991). Unlike Smith & Hooper (1967), O'Brien & Hooper (1974) did not use an impact parameter cutoff because there was no need due to the lack of divergence of the electric field for close interactions. While the lack of a divergence is desirable from a numerical point of view, the accuracy of the calculation is not guaranteed due to improper treatment of penetration (Iglesias, 2016). The collision operator (denoted as M) was written in a form very similar to Griem,

$$M = -in_e\lambda_T^3\vec{D}\cdot\vec{D}G(\omega), \tag{6.40}$$

where $G(\omega)$ includes the free-free Gaunt factor for the electrons.

Woltz & Hooper (1984) improved upon O'Brien & Hooper (1974) by using the full-Coulomb interaction (Eq 2.5), which includes penetration as well as higher-order multipoles. The full-Coulomb interaction softens the interaction and the potential goes to zero at the origin—as opposed to infinity in the dipole approximation. Woltz & Hooper (1984) found that at low densities, the line shapes calculated with the dipole approximation gives similar

answers to the line shapes calculated with the full-Coulomb treatment. This is because other terms which are non-zero, such as the monopole and quadrupole terms, add to the broadening and coincidentally agree with the dipole approximation. At higher densities, though, line shapes that use the dipole approximation were much wider than line shapes that used the full-Coulomb treatment.

Future students of Prof. Hooper developed techniques for charged radiators, and continued the use of the dipole approximation for electron broadening as calculated by O'Brien & Hooper (1974). Joyce et al. (1987) investigated the effects of higher-order multipole moments of ion perturbations up to and including the octupole interaction. Kilcrease et al. (1993), examined the importance of using an exact treatment of environment-dependent atomic basis (where the electric field was included in the atomic data; see appendix D), which showed that the accuracies of the eigenvalue evolution as a function of electric field broke down using field-free atomic data, and additional shifts and asymmetries were present that were not reproduced by field-free atomic data.

Prof. Hooper's last students, Don Haynes, Mark Gunderson, and Gweneth Junkel, investigated continuum-lowering and line-merging effects (Haynes & Hooper, 1997; Haynes et al., 2000), all-order treatment of the collision operator (without the third term of Eq 6.31; Gunderson et al., 2001), and plasma polarization shifts using a full-Coulomb quantum-mechanical electron broadening treatment (Junkel et al., 2000). The focus of this dissertation is further improvements on the relaxation theory.

6.2.3 Unified Theory

Earl Smith, after his work on the relaxation theory, worked with Vidal and Cooper to create what is known as the VCS theory of spectral line broadening (Smith et al., 1969; Vidal et al., 1971, 1973). The VCS calculations, similar to Kepple & Griem (1968), assume classical-path electrons that travel on straight-path trajectories, and correlations are corrected with Debye screening. Their formalism is a re-derivation of Zwanzig (1960) and is very similar in form to the relaxation theory.

They begin by defining the time-evolution of the atomic states with $F(t)$, which is an integral over the time-evolution of the entire system (electron and atom),

$$F(t) = \iint d^3\vec{r}d^3\vec{v}\; Q(\vec{v},\vec{r})U(\vec{r},t), \tag{6.41}$$

where $Q(\vec{v},\vec{r})$ is the velocity and position distribution function, while $U(\vec{r},t)$ is the time evolution operator of the whole system. From this, the time evolution operator can be written (in the interaction picture)

$$i\frac{\partial}{\partial t}F(\vec{r},t) = V_I F(\vec{r},t). \tag{6.42}$$

Then using the projection operator technique of Zwanzig (1960), they separate the "relevant" part of F,

$$F_1 = PF,$$

and the "irrelevant" part of F,

$$F_2 = (1-P)F,$$

where $F = F_1 + F_2$. The projection operator performs an average over the plasma perturbations. In the relaxation theory, the projection operator performs a trace over the plasma

coordinates on quantum operators,

$$PA\rho = \rho Tr_p\{A\rho\}.$$

In the unified theory, the projection operator is a classical analog of what is used in the quantum projection operator used in the relaxation theory,

$$Pf(\vec{r}) = Q(\vec{r}) \int d\vec{r}' f(\vec{r}),$$

where $f(\vec{r})$ is an arbitrary function dependent on plasma particle variables, and $Q(\vec{r})$ is a normalized probability function, analogous to the density matrix.

Using the projection operators to separate the time-evolution function, $F(t)$, then the problem is simplified to solving two differential equations for $F_1(t)$ and $F_2(t)$:

$$i\frac{\partial}{\partial t}F_1(\vec{r},t) = PV_I\left[F_1(\vec{r},t) + F_2(\vec{r},t)\right] \tag{6.43}$$

$$i\frac{\partial}{\partial t}F_2(\vec{r},t) = (1-P)V_I\left[F_1(\vec{r},t) + F_2(\vec{r},t)\right]. \tag{6.44}$$

The solution for F_2 is obtained with the use of a Green's function, which is chosen to be a time-ordered exponential integral of the interaction potential,

$$G(t,t') = \mathfrak{T}exp(-i\int_{t'}^{t}(1-P)V_I(\vec{r},s)ds).$$

Using the solution for F_2 in the equation for F_1, the problem is reduced to solving the differential equation,

$$i\frac{\partial}{\partial t}F_1(\vec{r},t) = PV_IF(\vec{r},t) - i\int_0^t PV_I(\vec{r},t)G(t,t')\left[1-P\right]V_I(\vec{r},t')F_1(\vec{r},t)dt', \tag{6.45}$$

under the assumption that $F_2(\vec{r},0) = 0$ and $F(\vec{r},0) = Q(\vec{r})$. After averaging over the spatial coordinates, the differential equation of the total time evolution $F(t)$ is defined by

$$i\frac{\partial}{\partial t}F(\vec{r},t) = \langle V_I\rangle F(t) - i\int_0^t \langle V_I(\vec{r},t)G(t,t')\left[1-P\right]V_I(\vec{r},t')\rangle F(t)dt', \tag{6.46}$$

where now some of the projection terms have dropped out (except from the Green's function) and all the interaction potential operators are averaged. This solution by VCS is still general, but using the dipole approximation for the interaction potential causes the first term to go to zero and the projection operator in the integrand to also go to zero. The final line shape is equivalent in form to that used by Kepple & Griem (1968), where the broadening operator is simply the Fourier transform of Eq (6.46),

$$\mathcal{H}(\omega) = -iN \int_0^\infty e^{i\Delta\omega t} \langle V_I(t) U_I(t) V_I(0) \rangle \, dt, \tag{6.47}$$

except the time-dependence of the problem is retained. Then through operator manipulation and the unified theory approximation, VCS transforms $V_I(t)U_I(t)V_I(0)$ to $U(t) - 1$, which in the impact limit (t$\rightarrow \infty$) turns into $(S - 1)$, where S is the scattering "S"-matrix (which is related to the "T"-matrix by $T = 1 - S$).

VCS made the binary-collision approximation, just like in Kepple & Griem (1968), where the collisions are assumed to happen one at a time and the particles are statistically independent of each-other. As before, the problem is simplified by using Debye screened interaction to account for the other N electrons in the plasma and the average interaction is multiplied by N electrons. Because the interest is in neutral hydrogen, the particles travel on straight-path trajectories.

The calculations done by VCS are called the "unified theory," which unifies the Kepple & Griem (1968) theory in the core of the line with the one-electron static limit in the wings of the line. Early times correspond to large detunings ($\Delta\omega$) of the line, while long times correspond to small detunings of the line; at early times, the particles have barely moved (even the electrons), while at late times, the electrons have moved appreciably and several collisions have taken place.

The original theory published by Smith et al. (1969) included only the broadening of the upper-state of the transition; this was extended by Vidal et al. (1971) to include the lower-state and interference broadening terms. Because VCS theory includes the time-dependence of the electron broadening operator, it compared better with the experimental of Wiese et al. (1972) than Kepple & Griem (1968) especially in the wings. Vidal et al. (1973) tabulated the profiles, which made for easy access for the astronomical community. Later, the unified theory foundation was extended to neutral helium lines (Barnard et al., 1974, 1975) The electron broadening model of VCS is the one implemented by Tremblay & Bergeron (2009), but with modifications to the ion contribution of the line-shape.

The lack of generality of the unified theory was pointed out by Lee (1971), where the removal of the projection operator and the assumption of the impact approximation in the core of the line were points of criticism. Lee (1971) also points out that VCS does not justify the use a static microfield for the far-wing contribution to the line, nor unifying this limit with the impact limit in the core.

6.2.4 Kinetic Theory

There were few developments after the kinetic theory of Hussey et al. (1975). The main developments were by Dufty & Boercker (1976), who laid down the foundation for electron correlations, simplifying some of the results of Hussey et al. (1975) to keep the problem tractable. Dufty & Boercker (1976) derived a quantum mechanical screening function, which reduces to Debye screening in limit that the plasma is classical. Hussey et al. (1977) used this foundation to calculate correlations for the Lyα line of neutral hydrogen; this calculation was done within the dipole approximation.

One advantage of the kinetic theory is that the assumption of the separation of the density matrix is never made. It is common to assume that the off-diagonal elements of the Hamiltonian are zero so that the density matrix can be separated as such:

$$\begin{aligned}
\rho &= e^{-H\beta} && (6.48)\\
&= e^{-(H^{(a,0)}+H^{(e,0)}+V)\beta} && (6.49)\\
&\approx e^{-(H^{(a,0)}+H^{(e,0)})\beta} && (6.50)\\
&\approx \rho^{(a,0)}\rho^{(e,0)}; && (6.51)
\end{aligned}$$

this approximation breaks down, especially if V becomes large. Boercker & Iglesias (1984) provided a second-order expansion to the density matrix. Because H and V do not commute, then an expansion would NOT be a simple Taylor expansion of V. The expansion is an integral equation for V (Zwanzig, 2001),

$$e^{-(H^{(a,0)}+H^{(e,0)}+V)\beta} = e^{-(H^{(a,0)}+H^{(e,0)})\beta} \times \sum_{n=0}^{\infty} (-1)^n \frac{1}{n!} \int_0^\beta d\tau_1 \cdots \int_0^\beta d\tau_n \mathfrak{T}\left\{V_I(\tau_1)\cdots V_I(\tau_n)\right\}, \tag{6.52}$$

where $V_I(\tau) = e^{(H^{(a,0)}+H^{(e,0)})\tau} V e^{-(H^{(a,0)}+H^{(e,0)})\tau}$, making the second-order estimate of the density matrix:

$$\begin{aligned}
e^{-(H^{(a,0)}+H^{(e,0)}+V)\beta} &\approx e^{-(H^{(a,0)}+H^{(e,0)})\beta} - \\
&\quad e^{-(H^{(a,0)}+H^{(e,0)})\beta} \int_0^\beta d\tau\ e^{(H^{(a,0)}+H^{(e,0)})\tau} V e^{-(H^{(a,0)}+H^{(e,0)})\tau}. \qquad (6.53)
\end{aligned}$$

The screening results of Dufty & Boercker (1976), the second-order shifts from Boercker & Iglesias (1984), combined with a multi-electron formalism from Woltz & Hooper (1988), and a full-Coulomb interaction of Woltz & Hooper (1984) became the thesis work of Junkel et al. (2000). Junkel et al. (2000) was mostly concerned about plasma polarization

shifts of diagnostic lines, and found rough agreement between the measurements (which were now good enough to accurately measure these shifts) and her calculations.

Part III

Improvements

My work focuses on using a more accurate interaction potential. Since most calculations assume the dipole approximation, then the first step (chapter 7) is to examine the importance of the higher-order multipole moments. One particularly important investigation in the multipole expansion is to determine how high in the expansion is needed to achieve convergence. The next step is to include the effects of penetration; this is substantially different for electrons and ions. Since plasma electrons are identical with those in the atom, then quantum effects such as exchange need to be included; this is the subject of chapter 8. Lastly, chapter 9 explores the importance of penetrating collisions due to ions.

This work uses a variety of techniques, for example, the multipole study is using a classical simulation method, while the work on electron broadening uses the semi-analytical relaxation theory. Chapter 9 uses both simulation and semi-analytic methods.

Higher-Order Multipoles In Chapter 7, I perform several comparisons of line shapes calculated using the dipole-only interaction and including higher-order multipoles. Higher-order multipoles due to ions have long been thought to explain asymmetries in the Hβ line of hydrogen. Strangely, these higher-order terms have been evaluated from only the plasma ions. I examine how quadrupole terms affect the asymmetry by including only ion quadrupole terms and then ion *and* electron quadrupole terms and compare with measured asymmetries. Most importantly, I perform a convergence test, examining how the line shape changes with increasing multipole orders. The importance of the different multipole orders varies with density and I quantify the errors in the line shape when calculated using dipole-only interactions, vs using up to quadrupole interactions, etc. Lastly, I study how the differences in the line shape using dipole-only and the various higher-order terms affect

density diagnostics.

Penetrating Collisions of Electrons I examine the effects of penetration of plasma electrons in Chapter 8. The first change I make is to use a quantum-mechanical treatment of the plasma electrons. At low densities, quantum effects are not important and the classical-path approximation is valid; however, this limits the range of validity of the calculations and there may be quantum behavior that is important even in the classical regime. For example, when the wavefunctions of identical particles overlap, then Pauli-exclusion effects must be taken into account. Quantum mechanical calculations electron broadening with penetrating collisions already exist: Woltz & Hooper (1984) and Junkel et al. (2000), but both papers use some simplifying assumptions about the interaction between radiator and plasma electrons. I build off the work of Junkel et al. (2000), who included a quantum treatment of plasma electrons and used Eq (2.5) to describe the interactions. Junkel et al. (2000) studied high-Z elements where the radiator wavefunction occupies an extremely small volume and it is assumed that the effect of Pauli exclusion are not important; I test this assumption for a variety of hydrogen-like ions. For cases of neutral hydrogen, this effect is very important, but becomes less important as the charge of the atom increases since the size of the atomic wavefunction decreases. With penetrating collisions, certain terms of the evaluation of the broadening, which have been historically neglected, are no longer zero; I examine the effects of these forgotten terms.

Penetrating Collisions of Ions Close-range interactions of plasma ions with the radiator have not been previously modeled in detail. At high densities, the ion broadening is so large that lines start to merge and disappear into a continuum. There have been several attempts

to quantify this phenomenon (e.g. Inglis & Teller, 1939; Hummer & Mihalas, 1988) and is closely related to ionization potential depression (Stewart & Pyatt, 1966; Ecker & Kröll, 1963). Many approximate methods exist for estimating how the lines merge, but no detailed calculations exist. In chapter 9, I perform these calculations in detail. Computing power has advanced to the point where large-scale calculations are now possible. The calculations presented in chapter 9 will have a more complete basis set and treat penetrating collisions by using Eq (2.5). At the end of chapter 9, I will have a model for spectral line broadening that properly includes penetration from both plasma ions and plasma electrons.

Chapter 7

Improvements over the Dipole Approximation: Higher-Order Multipoles[1]

I update the simulation line-broadening code *Xenomorph* to include higher-order multipole moments. Since *Xenomorph* assumes classical particles, then the charge density of particle j is represented by a well-defined position as a function of time ($\vec{R}_j(t)$). The interaction of the plasma with a one-electron radiator (including contributions from both nucleus and electron) by particle j is defined as (setting $q_a = -1$):

$$\begin{aligned}\frac{q_j}{|\vec{R}_j(t)|} - \frac{q_j}{|\vec{r}_a - \vec{R}_j(t)|} &\approx \frac{q_j}{R_j(t)} - \left[\frac{q_j}{R_j(t)} + \frac{q_j r_a}{R_j^2(t)}\cos\gamma_j(t) + \frac{q_j r_a^2}{R_j^3(t)}(3\cos^2\gamma_{aj}(t) - 1)\cdots\right] \\ &\approx -\sum_{x=1}^{\infty} q_j \frac{r_a^x}{R_j^{x+1}(t)} P_x(\cos\gamma_{aj}(t)), \end{aligned} \tag{7.1}$$

where $P_x(y)$ are Legendre polynomials and $\cos\gamma_{aj}$ is the angle between the radiator and plasma particle. Most calculations will stop at the dipole term ($x = 1$) term of Eq (7.1). There has been no systematic study of the importance of the higher-order lines beyond dipole; I explore their effects in this chapter.

There have been a limited number of studies that have included terms higher than the dipole term. Moreover, those studies investigated the effect of the higher-order terms

[1]Gomez, T. A. and Nagayama, T. and Kilcrease, D. P. and Montgomery, M. H. and Winget, D. E. *Effect of Higher-Order Multipole Moments on the Stark Line Shape* (2016) Phys. Rev. A. 94, 022501; T. Nagayama helped with writing and quantitative analysis, the remaining authors assisted in writing and provided critique of the work.

only due to either ions (Kilcrease et al., 1993; Demura et al., 1997; Olchawa, 2002) or electrons (Woltz & Hooper, 1984; Junkel et al., 2000). To my knowledge, this is the first calculation to simultaneously include higher-order multipole contributions from both species (See Gomez et al., 2016).

I only evaluate Eq. (7.1) for neutral hydrogen, but these results could be extended to any atom. The perturbation potential due to nearby charged particles can always be expressed as multipole expansion for any radiator (i.e., neutral or charged, single or multiple bound electrons).

7.1 Screening for Higher-Order Multipoles

For the study of the higher-order multipoles, I use my simulation-line-shape code *Xenomorph*. *Xenomorph* uses straight-path trajectories with screened interactions. To implement this, we include a Debye screening factor in the Coulomb potential:

$$V_{\rm ext}(\vec{r},t) = \sum_j q_{ij} \left[\frac{q_j}{|\vec{R}_j(t)|} e^{-|\vec{R}_j(t)|/\lambda_{\rm D}} \frac{q_j}{|\vec{r}-\vec{R}_j(t)|} e^{-|\vec{r}-\vec{R}_j(t)|/\lambda_{\rm D}} \right], \tag{7.2}$$

where $\lambda_{\rm D} = \sqrt{k_B T/4\pi n_e}$ is the electron Debye length. The resulting Taylor expansion this potential is given by a modified version of Eq. (7.1):

$$\begin{aligned} V_{\rm ext}(\vec{r},t) &= -\sum_j \sum_{x=1}^{\infty} q_j \frac{r^x}{R_j^{k+1}(t)} P_x(\cos\gamma_j(t)) \times \\ &\quad S_x(R_j(t)/\lambda_{\rm D}) e^{-R_j(t)/\lambda_{\rm D}}, \end{aligned} \tag{7.3}$$

where $S_k(x)$ comes from the Debye screening factor:

$$\begin{aligned}
S_0(x) &= 1 \\
S_1(x) &= 1 + x \\
S_2(x) &= 1 + x + \frac{1}{3}x^2 \\
S_3(x) &= 1 + x + \frac{2}{5}x^2 + \frac{1}{15}x^3 \\
S_4(x) &= 1 + x + \frac{1}{9}x^2 + \frac{4}{81}x^3 + \frac{1}{81}x^4 \\
&\vdots
\end{aligned} \tag{7.4}$$

There are additional terms that are of lower-order angular dependence and they are ignored. For example, the Taylor expansion for $x = 2$ is

$$\left[P_2(\cos\gamma) r^2 S_2(R/\lambda_{\mathrm{D}})/R^3 + r^2 (R/\lambda_{\mathrm{D}})^2/6R^3\right] \exp(-R/\lambda_{\mathrm{D}}),$$

and we are ignoring the second term in brackets, which is the divergence term; this is commonly assumed to be zero inside the radiator wavefunction (Olchawa, 2002).

At higher coupling parameters, the trajectories of classical particles are no longer accurately described by Debye-screened straight paths and perturber motions need to be computed in detail taking into account Coulomb interactions. Stambulchik et al. (2007) demonstrated how this alters the effective screening length of the electrons, increasing it beyond what is predicted by the Debye theory, thus reducing the screening. However, the errors in the effective screening length mostly influence long-range interaction, which is dominated by the lowest-order terms (e.g., dipole term). Thus, we expect that detailed treatment of perturber motions would mostly impact the accuracy of the dipole term and not our conclusions on the importance of the higher-order terms.

One advantage in using the screened Coulomb potential is that particles beyond a few Debye lengths are completely screened and do not contribute to the line shape. Therefore, the total number of particles in our simulation (Eq. 7.2) is determined by the conditions of our plasma. We performed a study of the sensitivity of the line shape to the size of the simulation box; we chose the simulation box to be at least 5 Debye lengths. The number of the particles used in the simulation is based on the box size and the particle number density. If, however, we perform a fully-interacting simulation (as opposed to the non-interacting simulation), then we may require several thousand particles in a much larger box.

7.2 The Impact of the Electron-Quadrupole Term on the Hβ Asymmetry

Griem (1974) considered the quadrupole term due to the ions (denoted as Q_i and often referred to as the ion quadrupole in the literature) as a primary source of asymmetry in Hβ. More recent studies have shown that the mixing of state n with state $n+1$ (i.e., an expanded basis; see appendix 4.1) is also a source of asymmetry (Kilcrease et al., 1993; Stambulchik et al., 2007). Djurović et al. (2009) studied extensively the effects of asymmetry in the Hβ line using experiment and two different line-broadening theories: one simulation and one semi-analytic method, The simulation method used an extended basis set (using $n = 1$ up to $n = 6$) but maintained the dipole approximation. The semi-analytic model kept a limited basis set (only $n = 4$) and included quadratic-Stark effect (appendix D.2.1) as well as ion quadrupole terms; the electron broadening was kept in the dipole approximation. The simulation model was able to reproduce the measured asymmetry for densities below a few 10^{17} e/cc, but over-predicted the asymmetry above this threshold. On the other hand,

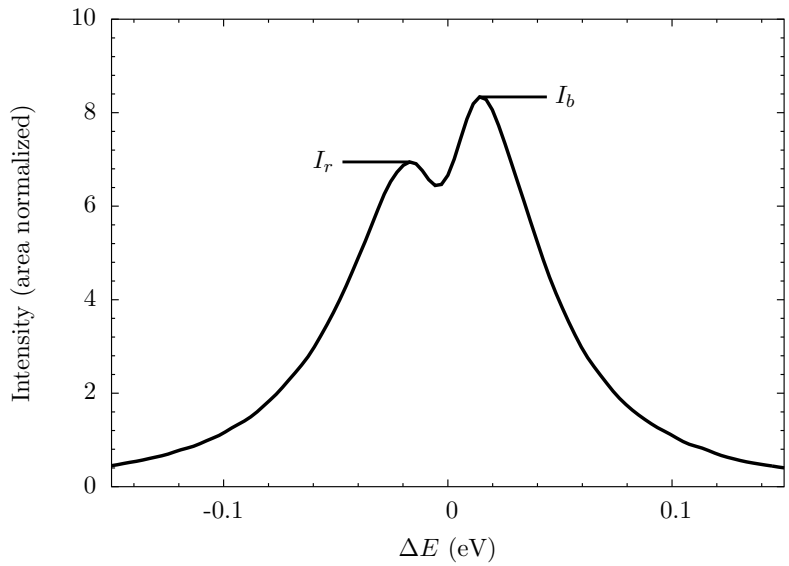

Figure 7.1: The double-peaked Hβ line shape. The asymmetry of the core is defined as the fractional difference of the intensity of the blue peak and red peak, $(I_b - I_r)/I_b$, where the subscripts b and r denote the blue ($\Delta E > 0$) and red peak ($\Delta E < 0$), respectively.

the semi-analytic model was able to match the measurements above this same threshold, but not below. No single calculation was able to match the data over the entire density range presented in Djurović et al. ($1 \times 10^{16} - 1.2 \times 10^{18}$ e/cc).

Here, we revisit this study of Hβ asymmetry with the simulation-based model developed in my master's thesis (Gomez, 2013) and expanded as described in Eq (7.1). Because the extended basis set is important for asymmetry calculations (Kilcrease et al., 1993), we use it by default throughout the chapter. We then test the importance of the higher-order terms by comparing three different levels of approximation: dipole only (denoted as D_i+D_e), dipole and ion quadrupole term ($Q_i + D_i + D_e$), and finally dipole and quadrupole terms from both ions and electrons ($Q_i + Q_e + D_i + D_e$). I focus on a smaller range of densities, $n_e = 1 \times 10^{17} - 1.2 \times 10^{18}$ e/cc, where there is discrepancy with the simulation calculation

of Djurović et al. (2009). The asymmetry of the calculated line shape is defined in the same way as in Djurović et al. (2009), as the ratio of the difference of the blue ($\Delta E > 0$, where $\Delta E = 0$ is the unshifted Hβ photon energy) and red peak ($\Delta E < 0$) intensities, $(I_b - I_r)/I_b$ (Fig. 7.1).

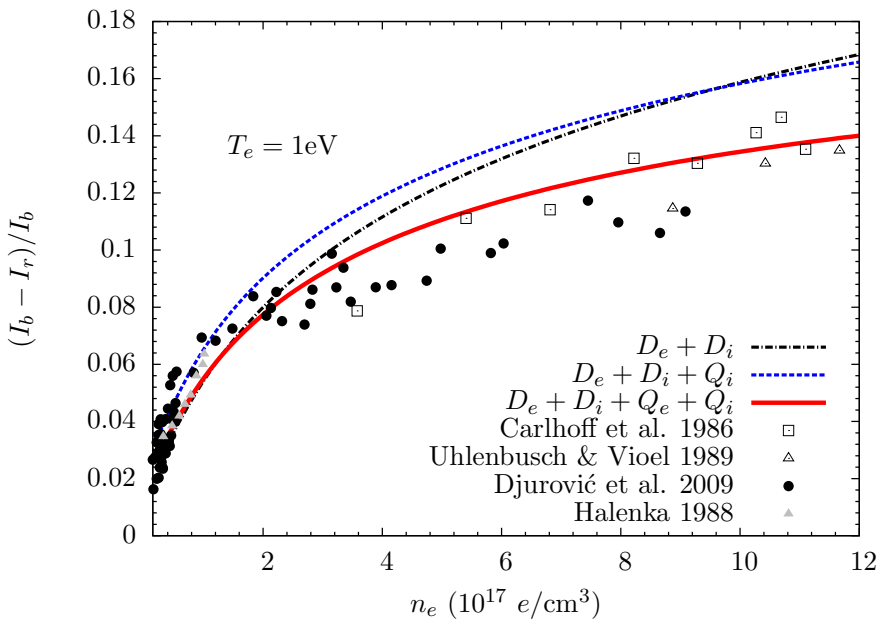

Figure 7.2: Asymmetry calculations (lines) with different approximations: dipole-only interaction (black); dipole + ion-quadrupole (blue); dipole + electron- *and* ion-quadrupole moment (red). The dipole-only calculation agrees well with the data (various points) below 3×10^{17} e/cc. Including only ion-quadrupole created discrepancy at these densities. Calculations including both electron- and ion-quadrupole terms created agreement with the data between 10^{17} and 10^{18} e/cc. Models assume 1eV temperature.

Figure 7.2 includes several measurements of the Hβ asymmetry, from Carlhoff et al. (1986), Halenka (1988), Djurović et al. (2009), and Uhlenbusch & Vioel (1989). I then compare the asymmetry simulated with different degrees of completeness in the higher-order terms (i.e., $D_e + D_i$, $D_e + D_i + Q_i$, and $D_e + D_i + Q_e + Q_i$) against the measured asymmetry.

The dipole-only calculation ($D_i + D_e$) compares well with the measured asymmetry at densities below $\sim 2 \times 10^{17}$ e/cc but over-predicts the asymmetry above this threshold, in agreement with the results of the simulation-based line-shape models presented in Djurović et al. (2009). Including Q_i increases the asymmetry compared with the dipole-only calculation, showing less agreement with the data. When we include both Q_i and Q_e, the calculated asymmetry improved and successfully reproduced the measured asymmetry throughout the whole range of available n_e data.

We repeated this calculation at 2 eV because the experiments (Carlhoff et al., 1986; Uhlenbusch & Vioel, 1989; Djurović et al., 2009; Halenka, 1988) have reported temperatures between 1 and 2 eV. All of the calculated asymmetries based on the listed approximations ($D_e + D_i$, $D_e + D_i + Q_i$, and $D_e + D_i + Q_e + Q_i$) systematically increase with temperature. Thus, the calculation with $D_e + D_i + Q_e + Q_i$ at 2 eV temperature still more accurately reproduces the trend seen in the measurements than the other theories do.

This improvement can be explained by the fact that the shape around the line center is more susceptible to rapid microfield fluctuations (Alexiou, 2009). Inclusion of higher order terms from electrons is therefore important to get an accurate calculation near the line center. Thus, to model the line shape accurately throughout the line profile, it is important to consistently include higher-order terms from both ions (Q_i) and electrons (Q_e).

7.3 Convergence of the Multipole Expansion

We include multipole terms consistently from both ions and electrons and study how the Hβ line shape converges with higher-order terms. We only explore the line shapes

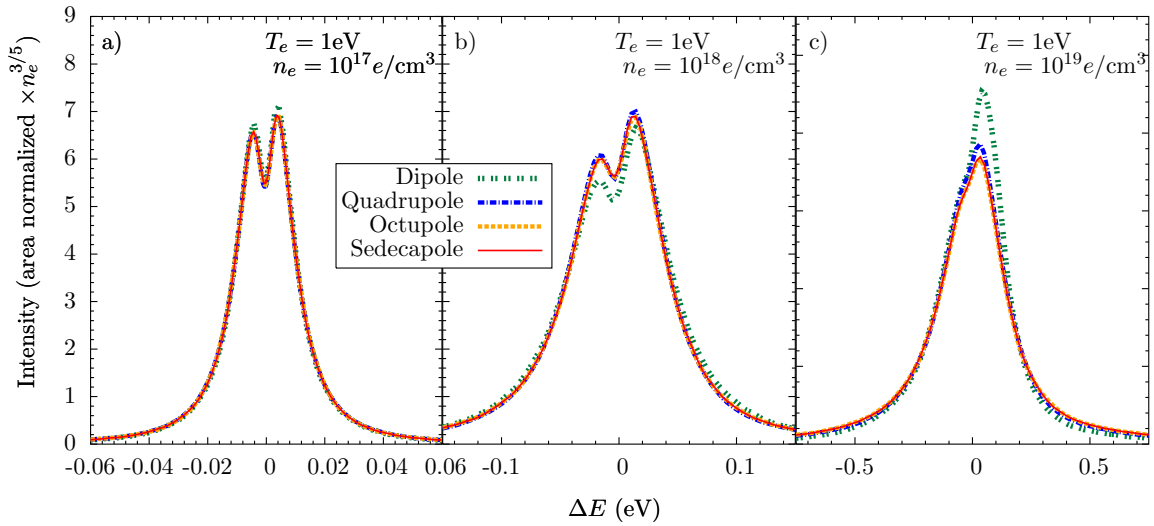

Figure 7.3: Area-normalized Hβ profiles at various levels of approximation over several different conditions. Profiles calculated at electron densities of 10^{17}, 10^{18}, and $10^{19} e/\mathrm{cc}$ are shown (all at 1-eV temperature). All moments include contributions from both ions and electrons. The green line shows the dipole approximation of Eq. (7.1); blue line shows up to the quadrupole term, orange line shows up to octupole term; lastly, red shows up to the sedecapole ($k \leq 4$) term, indistinguishable from the octupole profile. The profiles that include up to the quadrupole term match reasonably well to the sedecapole profile.

at 1 eV because the relative importance of the higher order multipole terms is not sensitive to temperature.

In Figure 7.3, we compare the Hβ line shapes calculated with different multipole terms at a) 10^{17}, b) 10^{18}, and c) 10^{19} e/cc. The green, blue, orange, and red represent Hβ line shapes computed with the terms up to the dipole ($k \leq 1$), the quadrupole ($k \leq 2$), the octupole ($k \leq 3$), and the sedecapole ($k \leq 4$), respectively. Figure 7.3-a) shows all profiles having nearly identical shapes, indicating that the line shape computed with the dipole term is sufficiently accurate at this lower density. In Figure 7.3-b), the dipole line shape is systematically wider and shorter than the line shape with more-complete calculations. Figure 7.3-c) shows the opposite trend; the dipole line shape is systematically narrower and taller and shows larger asymmetry. In either case, the quadrupole line shape is consistent with more-complete octupole and sedecapole line shapes.

To quantify the goodness of the dipole and quadrupole line shapes, we compute the average percent error in the line shapes, assuming that the sedecapole profile is the correct one:

$$\text{Percent Error} = \frac{1}{n}\sum_{i=1}^{n}\frac{|\phi(E_i) - \psi(E_i)|}{\psi(E_i)} \times 100\%, \tag{7.5}$$

where ψ is the sedecapole profile, ϕ is either the dipole or quadrupole profile, and the sum of i is only over points within the energy range of interest. We compare the line-shape accuracy over two energy ranges: the core and wings. The core is defined as the photon-energy range inside the full width at half maximum ($|\Delta E| <$ FWHM), and the wings are defined to have the energy ranges between that and twice the full width at half maximum (FWHM $< |\Delta E| < 2 \times$ FWHM).

Table 7.1 summarizes the percent errors of the dipole, quadrupole, and octupole line shapes for the core and wings, respectively. As electron density increases, the error in the dipole line shape significantly increases from less than 1% to nearly 10%, while the quadrupole line shapes are accurate within a few percent throughout the tested densities. The percent error in the octupole line shape is less than 1% across all densities. It is important to include at least up to quadrupole terms to accurately calculate the line shapes within 2% error.

Table 7.1: Percent Error in Line Shape

n_e (e/cc)	Dipole	Quadrupole	Octupole	Region
10^{17}	0.53	0.52	0.40	
10^{18}	5.20	0.88	0.58	Core
10^{19}	8.68	2.10	0.89	
10^{17}	0.78	0.80	0.81	
10^{18}	9.2	1.1	0.81	Wings
10^{19}	5.05	1.7	0.80	

7.4 Density Diagnostics

Plasma electron density is often diagnosed by fitting a modeled line shape to the measured line shape. However, many line-shape models used for this purpose employ up only to the dipole term (known as the dipole approximation) for the perturber-radiator interaction potential in Eq. 7.1. Since we find the quadrupole terms are important for accurate line-shape calculation (section 7.3), here we investigate the impact of including higher-order multipole terms on density diagnostics.

The black dots in Figure 7.4-a) and b) are Hβ line profiles measured by Wiese et al. (1972) and by Carlhoff et al. (1986), respectively. We fit these measured profiles with dipole, quadrupole, and sedecapole line shapes to infer the electron density of the source plasmas.

Since the sedecapole line shape includes the most higher-order multipole terms, we consider the diagnostics with this line shape to be the most accurate. Based on our sedecapole line-shape diagnostics, the inferred conditions are $n_e = 9.2 \times 10^{16}$ e/cc and 1.5×10^{18} e/cc, respectively. Our determination for Figure 7.4-a agrees well with the conditions published in Wiese et al. (1972), which was determined to be 9.3×10^{16} e/cc). However, we note that our inferred density is slightly different for the Carlhoff et al. (1986) data (determined to be 1.1×10^{18} e/cc from Lorentz fitting) since they only compared the FWHM with a calculation from Griem (1964).

When we use the dipole and quadrupole line shapes, the inferred conditions are not always consistent with the values inferred using the sedecapole line-shape model even though the fits always look reasonable. For Figure 7.4-a), the percent difference in inferred density is small, i.e., 1.6% and 0.5% for dipole and quadrupole, respectively. This is consistent with the expectation that the dipole approximation is accurate at low density.

In Figure 7.4-b), we compare a case where the electron density is above 10^{18} e/cc. The densities inferred with the dipole and quadrupole line shapes are 1.3×10^{18} e/cc and 1.5×10^{18} e/cc, respectively.

For a quantitative discussion we use $\sum(data - model)^2$, which is similar to the variance, as a measure of the goodness of the fit because the uncertainties on the individual data points are not available; the results are shown in Table 7.2. For the Wiese experiment, our χ^2 decreases for each of the higher-order approximations, while the for Carlhoff experiment, the χ^2 varies between the different approximations rather than steadily decreasing. The trends reported are not conclusive. There could be other sources of error due to neglect of high-density effects, such as the overlapping Hγ line, changes in the relative line intensity,

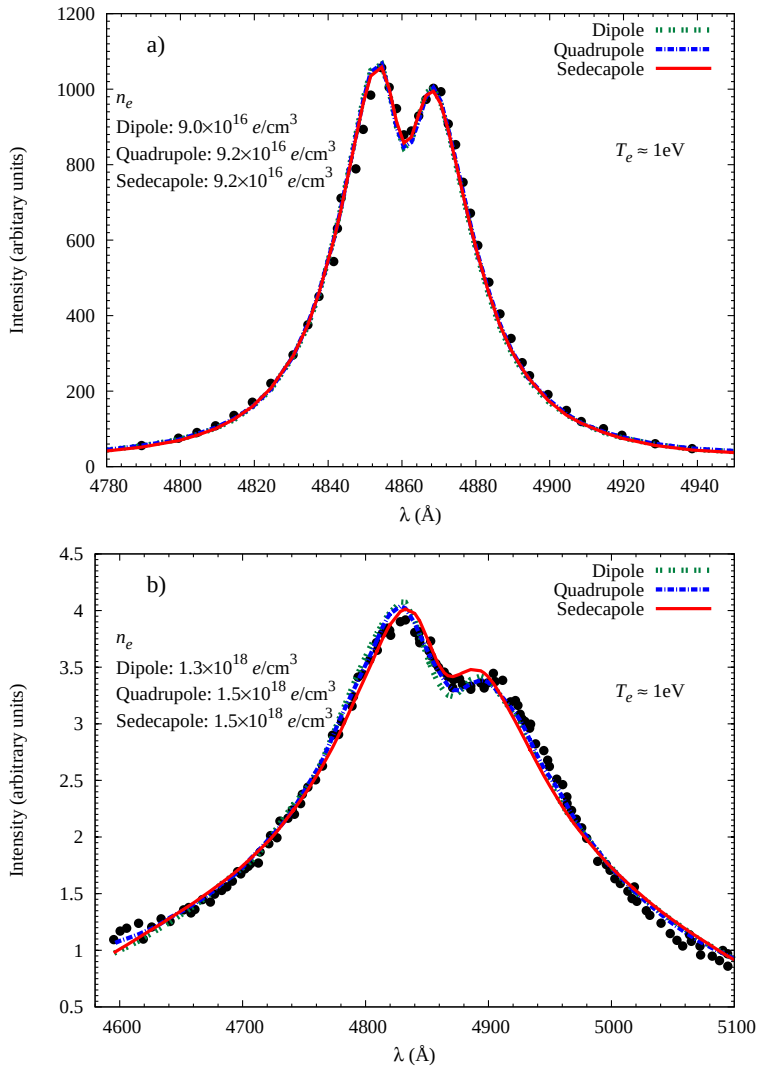

Figure 7.4: a) the highest-density measured spectrum from the Wiese et al. (1972) experiment, focused on Hβ (dots). The fits for the calculated dipole, quadrupole, and sedecapole profiles are identical, yielding fit differences less than the fit errors. b) the measured Hβ spectrum measured by Carlhoff et al. (1986) (dots). The fits for the calculated dipole, quadrupole, and sedecapole profiles yield differences in density of 12%, which is greater than the fit errors.

the lowered continuum, and the disappearance of substates; these effects are beyond the scope of this chapter.

Table 7.2: $\sum(data - model)^2$ (Intensity Units)

Approximation	Wiese	Carlhoff
Dipole	1166	9.9×10^{-3}
Quadrupole	860	5.1×10^{-3}
Sedecapole	829	9.5×10^{-3}

At these high densities, the dipole line shape becomes inaccurate as discussed in Sec. 7.3 and underestimates the density by 12%, while the quadrupole line shape still infers the correct density. At these densities, including quadrupole terms is necessary for accurate electron-density diagnostics and for accurate line-shapes used in white dwarf atmospheres.

Chapter 8

Penetrating Collisions and Quantum Effects of Plasma Electrons

The inclusion of higher-order multipoles in Chapter 7 is an improvement over the dipole approximation, but has limited range of validity. In order to extend to higher densities, penetrating collisions is necessary for accurate calculations. It is easiest to evaluate matrix elements of the Coulomb using a Taylor expansion; Eq (2.5) is repeated here for convenience,

$$V(\vec{r}_a, \vec{r}_j) = \sum_x \frac{r_<^x}{r_>^{x+1}} P_x(\cos\gamma). \tag{8.1}$$

The previous chapter has informed us that x needs to go up to at least 2 for an accurate spectrum calculation.

When particles overlap in space, quantum effects become important, therefore I will treat the free electron motion with quantum mechanics, rather than classical mechanics; this is a more general treatment for electron broadening. The correspondence principle states that in the limit of high quantum number, quantum systems can be approximated as classical particles—this corresponds to high temperatures. At cooler temperatures and higher densities, however, the plasma electrons do not behave classically. When quantum-particle wavefunctions of identical species overlap, then the way that quantum particles interact is more complicated (e.g. Bethe & Salpeter, 1957) and this effect is generally not treated in spectral-line-shape models.

According to Griem (1974), it is desirable to perform calculations that treat the plasma particles quantum mechanically as both a check on the classical calculations and for when the classical particle assumption break down. In this chapter I will use Equation (8.1) with quantum electrons. As we learned from the previous chapter, evaluating Eq (8.1) up to quadrupole is sufficient for 2% accuracy, even at conditions near the continuum threshold; the rest of this chapter will only evaluate Eq (8.1) for up to quadrupole for electron broadening unless otherwise specified.

8.1 Semi-Analytic Methods with Quantum-Mechanical Electrons

As shown in chapters 6, specifically Eq (6.4), semi-analytic methods put all the effects of the perturbing electrons into a single complex-valued (and frequency-dependent) broadening operator, $\mathcal{H}$,

$$J(\omega) = \frac{-1}{\pi}\mathbb{I}\mathrm{m}\ D\left[\omega - L_0^A - \mathcal{H}(\omega)\right]^{-1} D, \tag{8.2}$$

where $J(\omega)$ is the intensity of the spectrum as a function of frequency due to electron broadening.

I will be using the relaxation theory of Fano to evaluate $\mathcal{H}$. Fano (1963) defines the electron broadening operator as (a more rigorous derivation is given in chapter 6 and appendix C)

$$\begin{aligned} \mathcal{H}(\omega) &= \frac{1}{1 + \langle T(\omega)\rangle\,(\omega - L_0^A)^{-1}}\,\langle T(\omega)\rangle \qquad (8.3)\\ &\approx \langle T(\omega)\rangle - \langle T(\omega)\rangle\,(\omega - L_0^A)^{-1}\,\langle T(\omega)\rangle + \cdots \\ T(\omega) &= \frac{1}{1 - L_1(\omega - L_0^A - L_0^E)^{-1}}L_1 \qquad (8.4)\\ &\approx L_1 + L_1(\omega - L_0^A - L_0^E)^{-1}L_1 + \cdots, \end{aligned}$$

where L_0^A and L_0^E are the Liouville (Tetradic) operators associated with the atomic and free Hamiltonians, $H^{(a,0)}$ and $H^{(e,0)}$, respectively; L_1 is Liouville operator associated with the interaction potential, V, defined by Eq (8.1). For more details on Liouville operators, see section 3.1. The various operators are defined here, where atomic states are denoted with Latin letters and perturbing electron coordinates with Greek letters:

$$\begin{aligned}
\left\langle ab \left| L_0^A \right| a'b' \right\rangle &= \left\langle a \left| H_0^A \right| a' \right\rangle \delta_{bb'} - \delta_{aa'} \left\langle b \left| H_0^A \right| b' \right\rangle && (8.5)\\
\left\langle \alpha\beta \left| L_0^E \right| \alpha'\beta' \right\rangle &= \left\langle \alpha \left| H_0^E \right| \alpha' \right\rangle \delta_{\beta\beta'} - \delta_{\alpha\alpha'} \left\langle \beta \left| H_0^E \right| \beta' \right\rangle && (8.6)\\
\left\langle ab; \alpha\beta \left| L_1 \right| a'b'; \alpha'\beta' \right\rangle &= \left\langle a; \alpha \left| V \right| a'; \alpha' \right\rangle \delta_{bb'}\delta_{\beta\beta'} - \delta_{aa'}\delta_{\alpha\alpha'} \left\langle b; \beta \left| V \right| b'; \beta' \right\rangle , && (8.7)
\end{aligned}$$

where a and a' represent the upper state of the atom, while b and b' represent the lower state of the atom; likewise, α and α' belong to an upper state of the plasma electron, while β and β' are lower-states of the plasma electron.

The form of the electron broadening operator, $\mathcal{H}$, and $T(\omega)$ strongly resemble scattering "T"-matrices (see appendix C.1 for details on the "T"-matrix). The $T(\omega)$ operator, is the Liouville equivalent of the "T"-matrix with the usual Green's function propagators (Eq 6.10) replaced by a frequency-dependent propagator and with the interaction potential, V, replaced by L_1. A second-order calculation of $\mathcal{H}$ will be used throughout the rest of the chapter (Smith & Hooper, 1967):

$$\mathcal{H} \approx \langle L_1 \rangle + \left\langle L_1 (\omega - L_0^A - L_0^E)^{-1} L_1 \right\rangle - \langle L_1 \rangle \left(\omega - L_0^A\right)^{-1} \langle L_1 \rangle ; \qquad (8.8)$$

this is obtained by a Taylor expansion of both Eq (8.3) and Eq (8.4) and retaining terms that are only second-order in L_1

The calculations by Junkel et al. (2000) are considered the state-of-the art calculations due to the use of quantum electrons and the full-Coulomb interaction (Eq 8.1); this

calculation is my starting point for calculations of hydrogenic spectra.

8.2 Comparison of Semi-Classical Calculations with Current Theory & Critique of Past Calculations

As a first step, I tried to reproduce the calculations of Woltz & Hooper (1984) and Junkel et al. (2000) for highly-charged argon, with limited success. I was able to reproduce the Lyα line of Woltz & Hooper (1984), but not the Lyβ line and using some simplifying approximations I was able to reproduce the He-β calculations from Junkel et al. (2000).

With some success reproducing past calculations, I applied my results to the neutral hydrogen case. In figure 8.1, these calculations are compared with the semi-classical calculations from the previous chapter at conditions where these semi-classical calculations are known to be accurate. The accuracy of these semi-classical calculations is justified due to the comparison with experiment with reasonably well known conditions. These new quantum calculations, as published by Junkel et al. (2000) result in line shapes that are much broader than the semi-classical calculations. Therefore, I can conclude that the line-shape theory as it is already published is incomplete; there must be some missing processes.

Junkel et al. (2000) used the second-order calculation of $\mathcal{H}$, but omit the third term. Because $\mathcal{H}$ is approximated with a Taylor expansion, the accuracy of the second-order calculation depends on the smallness of L_1. There are two ways with one can remedy this problem: include higher-order terms, or use a distorted-wave treatment. Higher-order terms are more complicated to evaluate and become computationally expensive, I therefore choose to use a distorted-wave treatment. The distorted-wave approximation separates the

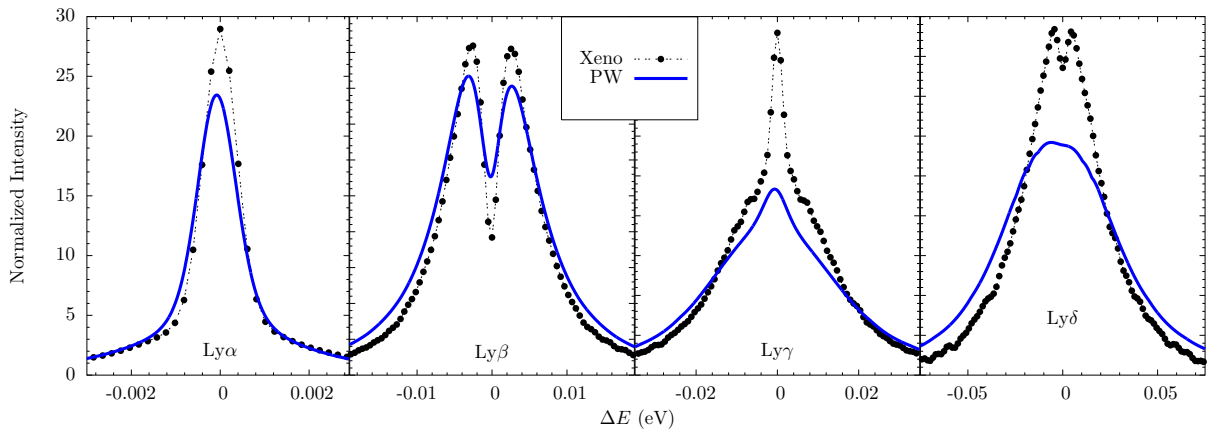

Figure 8.1: The Lyman series of neutral hydrogen (at $T_e = 1eV$ and $n_e = 10^{17} e/\mathrm{cm}^3$) that compares the plane-wave treatment (black-dotted) and the Semi-classical calculations of the previous chapter. Reproduction of the Junkel et al. (2000) calculations applied to neutral hydrogen have no correspondence with the semi-classical results in a regime where these classical results are reliable.

interaction potential into two parts:

$$L_1 = L_1' + L_1^\dagger$$

where L_1' can be solved by the Schrödinger equation and incorporated into the wavefunction, and then $L_1^\dagger$ will be solved using Eq (8.8); this will be explored in section 8.3. Quantum-particle exchange has been neglected in the line-shape calculations of Prof. Hooper's students (Smith & Hooper, 1967; O'Brien & Hooper, 1974; Woltz & Hooper, 1984; Junkel et al., 2000) assuming the attractive force of the nucleus of charged radiators dominates the interaction. An examination of exchange effects will be in section 8.4. The third term in Eq (8.8) has been neglected assuming $\langle L_1 \rangle = 0$, which is true under dipole approximation. In section 8.5, we re-evaluate the importance of the third term. These improvements will be compared with other calculations and some experimental results toward the end of the chapter.

The rest of the chapter investigates the changes in line shapes using a distorted-wave treatment (Sec 8.3), including exchange (Sec. 8.4), and these missing terms of the electron-broadening operator (Sec. 8.5). The chapter concludes with a comparison with past calculations and experiment and a discussion about those comparisons.

8.3 Distorted Wave

The electron broadening operator, $\mathcal{H}$ is valid only when the interaction potential, V is small. Therefore, to improve the approximation, part of V can be incorporated directly into the solution of the free-electron wavefunction.

The free electron wavefunction, $\phi(r_p)$ is the solution to

$$\left[\frac{1}{2}\nabla_p^2 + \frac{1}{2}k^2 + \frac{Z-1}{r_p}\right]\phi(r_p) = 0 \tag{8.9}$$

where we have assumed that the atom is hydrogenic—one unit of charge of the atom has been screened by the one bound electron. For neutral hydrogen, the bound electron completely screens the charge so that Eq (8.9) becomes

$$\left[\frac{1}{2}\nabla_p^2 + \frac{1}{2}k^2\right]\phi(r_p) = 0,$$

and $\phi(r_p)$ is a plane wave,

$$\phi(r_p) = \sqrt{\frac{2}{\pi}}e^{i\vec{k}\cdot\vec{r}_p}. \tag{8.10}$$

In this approximation, which is what is assumed by Woltz & Hooper (1984) and Junkel et al. (2000), then the motion of the free electron is only dependent on the net charge of the radiator.

The Coulomb operator is in practice evaluated with a Taylor expansion (Eq 8.1) with the first, second, and third terms denoted as the monopole, dipole, and quadrupole terms, respectively. The largest contribution to the Coulomb interaction is the monopole term due to the potential going to negative infinity at the origin (see figure 8.2). Because the various term (monopole, dipole, etc) are additive, I can re-define V as the monopolar interaction plus the higher-order terms of the interaction,

$$V = V_{mon} + V_{HO}. \tag{8.11}$$

The monopolar interaction contains contributions from *both* the bound electron and the nucleus:

$$V_{mon}(r_p) = \int_0^\infty d^3\vec{r}_r\psi_a^*(\vec{r}_r)\psi_a'(\vec{r}_r)\left[\frac{1}{r_>} - \frac{1}{r_p}\right], \tag{8.12}$$

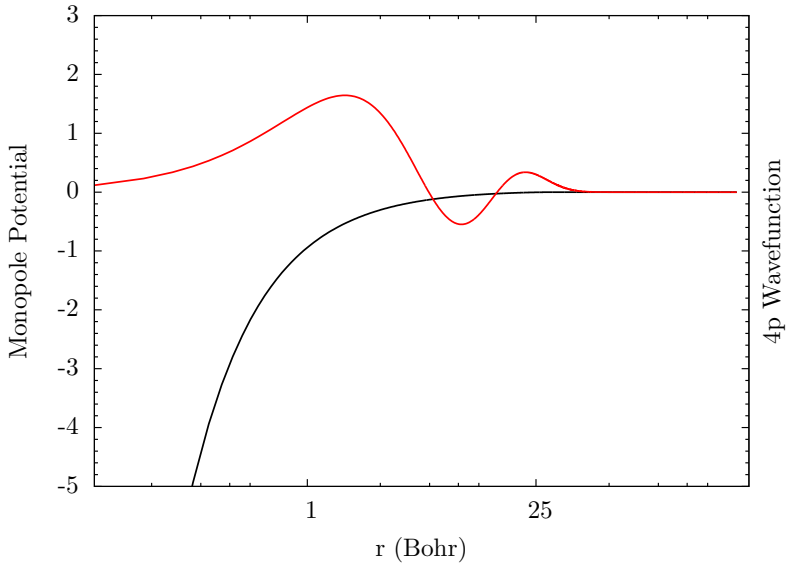

Figure 8.2: The monopole term (Eq 8.12) for the 4p state of hydrogen is shown in black. The wavefunction of the bound electron (red) is shown in red for reference. The monopole term of the radiator wavefunction goes to a finite value, and is subtracted by $1/r_p$, this second-term causes the potential to go to negative infinity; this is large and can be included in the solution of the free-electron wavefunction (Eq 8.13).

which is shown is figure 8.2 in black, with the atomic wavefunction shown in red as a reference. Because V_{mon} is spherically symmetric, it is easy to include it in Eq (8.9),

$$\left[\frac{1}{2}\nabla_p^2 + \frac{1}{2}k^2 + \frac{Z-1}{r_p} - V_{mon}(r_p)\right]\phi(r_p) = 0. \tag{8.13}$$

Figure 8.3 shows the perturbing-electron wavefunction solutions, $\phi(r_p)$, for different values of wavenumber k where (red) and without (black) the monopole term. The changes in the wavefunctions—going from Eq (8.9) to Eq (8.13)—for neutral hydrogen and hydrogen-like magnesium are shown in figures 8.3 and 8.4, respectively. These figures show a variety of wavenumbers for comparison. For neutral hydrogen, the changes are drastic near the nucleus, creating additional Coulomb-wave-like oscillations. Once the waves are outside the

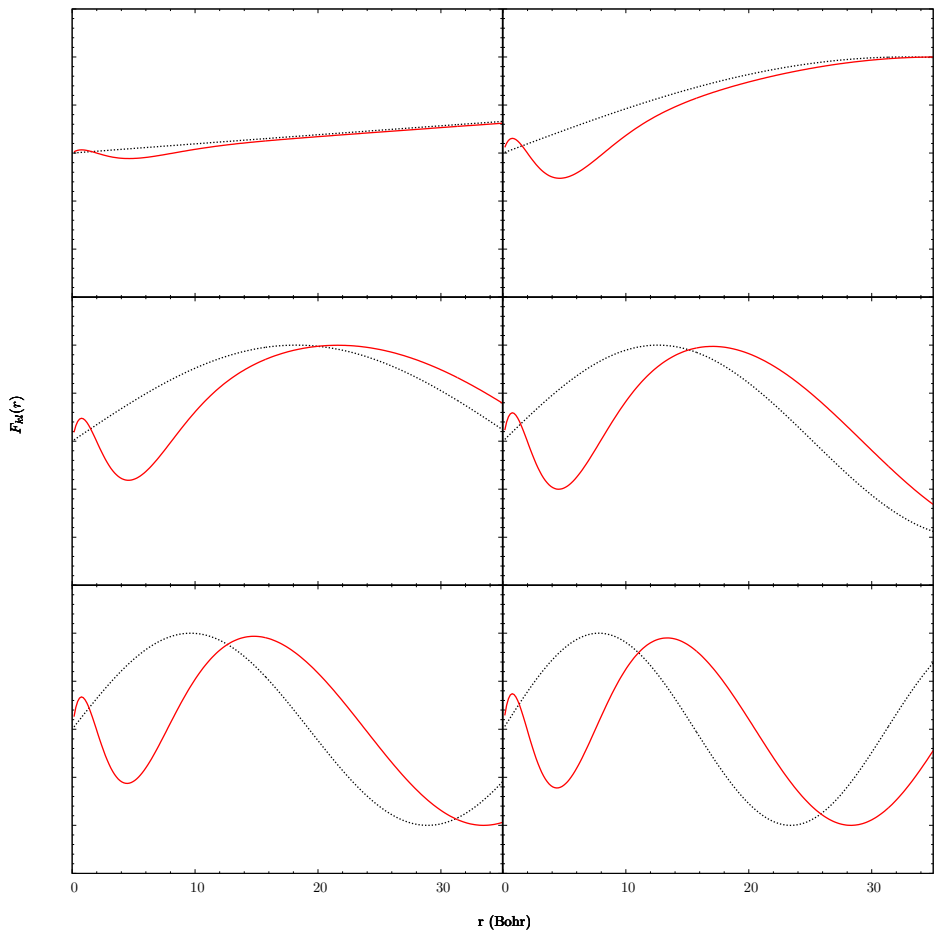

Figure 8.3: The changes in the free-electron radial wavefunction when the solving for plane wave (Eq 8.9) vs distorted wave (Eq 8.13) for neutral hydrogen ($Z = 1$). The top-left panel has the smallest k value and the bottom-right panel has the largest k value. Plane-wave solutions are dotted black lines, while the distorted-wave solutions are solid red.

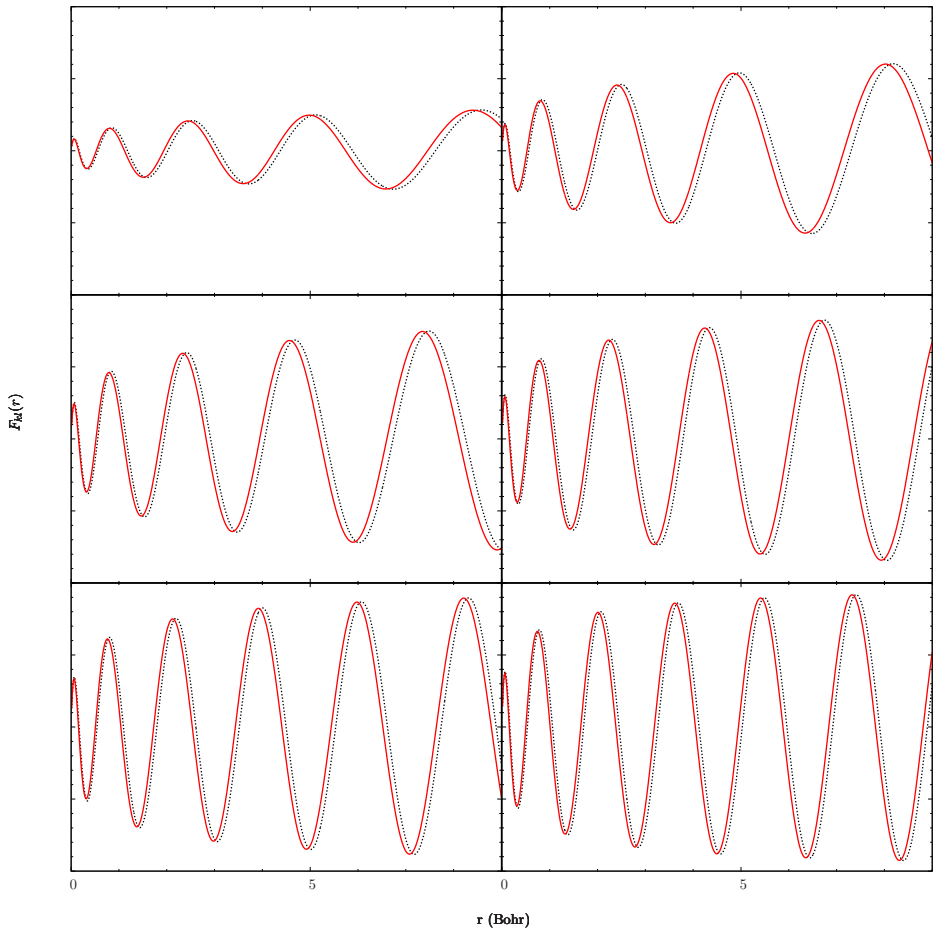

Figure 8.4: Same as figure 8.3, but for hydrogen-like magnesium ($Z = 12$). Coulomb-wave solutions are dotted black lines, while the distorted-wave solutions are solid red.

radiator, then the behavior is the same as the plane-waves, but offset by a phase. The highly-charged magnesium case is different, the changes in the wavefunction are not nearly as drastic and the distorted-wave solution still resembles the Coulomb-wave calculation, but is off by a phase.

These changes near the nucleus are large for hydrogen because far away, the free-electron sees no charge; the free electron starts to react to the imperfection of bound-electron screening as it approaches to the nucleus. However, if we look at a case for a highly-charged hydrogen ion, such as magnesium, the free-electron already experiences a charge of +11, then once it gets inside the radiator, it sees a charge of +12; this is not a drastic change in the electron motion.

8.3.1 Modification of $T(\omega)$

Incorporating the monopole term in the motion of the free-electron in the perturbing particle wavefunction, $T(\omega)$ will have to be evaluated slightly differently. Because $T(\omega)$ is a "T"-matrix—

$$\begin{aligned} T(\omega) &= \frac{1}{1 - L_1(\omega - L_0^A + L_0^E)^{-1}} L_1 \\ &\approx L_1 + L_1(\omega - L_0^A + L_0^E)^{-1} L_1 + \cdots \end{aligned} \tag{8.14}$$

$$\begin{aligned} \mathrm{T} &= \frac{1}{1 - VG} V \\ &\approx V + VGV + \cdots \end{aligned} \tag{8.15}$$

where G is a Green's function and the operator products can be evaluated using matrix mechanics[1]—I can use some of the evaluation tricks used by the scattering community.

[1]see Eqs A.2 and A.3 in appendix A, more details on "T"-matrices in appendix C

Now, using the state vectors (Appendix A), the "T"-matrix can be evaluated as

$$\begin{aligned} \mathrm{T} &= \left\langle \psi\phi \left| \frac{1}{1-VG} V \right| \psi'\phi' \right\rangle \\ &= \left\langle \psi\phi \left| V \right| \psi'\phi'^{+} \right\rangle \end{aligned} \tag{8.16}$$

where the atomic-electron wavefunction is denoted by ψ, and the free-electron is denoted by ϕ. The outgoing scattered wave is denoted by ϕ^{+} and is the exact solution to the electron moving in the presence of the atom; it can be evaluated using the following integral equation, (Lippmann & Schwinger, 1950; Gell-Mann & Goldberger, 1953):

$$\left|\psi\phi^{+}\right\rangle = \left|\psi\phi\right\rangle + GV\left|\psi\phi^{+}\right\rangle \tag{8.17}$$

$$\approx \left|\psi\phi\right\rangle + GV\left|\psi\phi\right\rangle . \tag{8.18}$$

When Eq (8.18) is multiplied on the left by $\langle\psi\phi| V$, it is exactly the Taylor expansion of the "T"-matrix in Eq (8.15).

We can also write $\left|\phi^{+}\right\rangle$ as a function of the distorted wavefunctions,

$$\left|\psi\phi^{+}\right\rangle = \left|\psi\phi^{(DW)}\right\rangle + GV_{HO}\left|\psi\phi^{+}\right\rangle \tag{8.19}$$

$$\approx \left|\psi\phi^{(DW)}\right\rangle + GV_{HO}\left|\psi\phi^{(DW)}\right\rangle . \tag{8.20}$$

If we insert this definition to Eq (8.16), then we can re-write the "T"-matrix as

$$\begin{aligned} \mathrm{T} &= \left\langle \psi\phi \left| V_{mon} + V_{HO} \right| \psi'\phi'^{+} \right\rangle \\ &= \left\langle \psi\phi \left| V_{mon} \right| \psi'\phi'^{(DW)} \right\rangle + \left\langle \psi\phi \left| V_{HO} \right| \psi'\phi'^{+} \right\rangle . \end{aligned} \tag{8.21}$$

The distorted-wave can be written in an integral form of plane waves

$$\left|\psi\phi^{(DW)}\right\rangle = \left|\psi\phi\right\rangle + GV\left|\psi\phi^{(DW)}\right\rangle ,$$

which can be re-arranged so that the plane-wave is written as a function of distorted waves,

$$|\psi\phi\rangle = \left|\psi\phi^{(DW)}\right\rangle - GV\left|\psi\phi^{(DW)}\right\rangle. \tag{8.22}$$

Combining Eq (8.22) and Eq (8.21), then the "T"-matrix can be approximated to second order as

$$\mathrm{T} \approx \left\langle \psi\phi \left|V_{mon}\right| \psi'\phi'^{(DW)}\right\rangle + \left\langle \psi\phi^{(DW)} \left|V_{HO}\right| \psi'\phi'^{(DW)}\right\rangle + \left\langle \psi\phi^{(DW)} \left|V_{HO}GV_{HO}\right| \psi'\phi'^{(DW)}\right\rangle.$$

I can extend this logic to the Liouvillian $T(\omega)$ operator and evaluate it (in matrix element form):

$$\begin{aligned} T(\omega) \quad &\approx \quad \left\langle \psi\phi \left|L_{mon}\right| \psi'\phi^{(DW)}\right\rangle + \left\langle \psi\phi^{(DW)} \left|L_{HO}\right| \psi'\phi^{(DW)}\right\rangle \\ &+ \quad \left\langle \psi\phi^{(DW)} \left|L_{HO}(\omega - L_0^A + L_0^E)^{-1}L_{HO}\right| \psi'\phi^{(DW)}\right\rangle. \end{aligned} \tag{8.23}$$

There is an interesting difference between these calculations and semi-classical calculations. Semi-classical calculations of Vidal et al. (1971), Tremblay & Bergeron (2009), and *Xenomorph* assume straight-path trajectories—even when the plasma particles enter the wavefunction of the radiator. This distorted-wave calculation accounts for the modification of the trajectory of the perturbing electron when it enters the radiator wavefunction in a way that the semi-classical calculations do not—and cannot—model.

8.3.2 Changes in the Line Shape due to Distorted Waves

The changes in the line shape of hydrogen are shown in figure 8.5. The condition here ($T_e = 1eV$, $n_e = 10^{17}e/\mathrm{cm}^3$) is typical of conditions achieved at laboratories, and is relevant to the line-forming region of white dwarf photosphere. Because the $n = 2$ wavefunction is small, the changes in the Lyα ($n = 2 \rightarrow n = 1$) line should be small. More

highly-excited states have extended wavefunctions, and the free-electron behavior inside the atomic wavefunction becomes more important. Thus, the lines from excited states like Lyγ and Lyδ benefits more from the detailed distorted-wave calculation are much larger physically than the $n = 2$ states, so we expect the distorted-wave calculations to become more important for higher-n lines.

The fundamental quantity determining the importance of the distorted-wave treatment is the number of waves inside the atomic wavefunction. For neutral hydrogen, this is a strong function of temperature since the average size of the free-electron wave is the thermal de Broglie wavelength,

$$\lambda_T = \sqrt{\frac{2\pi\hbar}{m_e k_B T}}.$$

When the radiating atomic wavefunction is larger than the thermal deBroglie wavelength, the distorted waves tend to decrease the width of the line. Hydrogen Lyman α FWHM is smaller by 10%, 15%, and 20% for electron temperatures of 2eV, 4eV, and 8eV, respectively. When λ_T is larger than the atomic wavefunction, then the distorted-waves results in a slightly wider electron width. For example, at $T_e = 0.5eV$, the distorted-wave treatment gives a FWHM that is 3% larger than the plane wave treatment. At this low temperature, the plane wave has a small amplitude near the origin, however, the distorted wave has several oscillations in the region of the atom, which will create a larger matrix element, thus increasing the width. In figure 8.3 the $l = 0$ solutions of the free electron are shown with plane waves and distorted waves at different values of wavenumber. Additional oscillations of the wavefunction near the nucleus are present in the distorted-wave solution. For high values of k, additional oscillations are near the nucleus, but the amplitude of the oscillations are reduced.

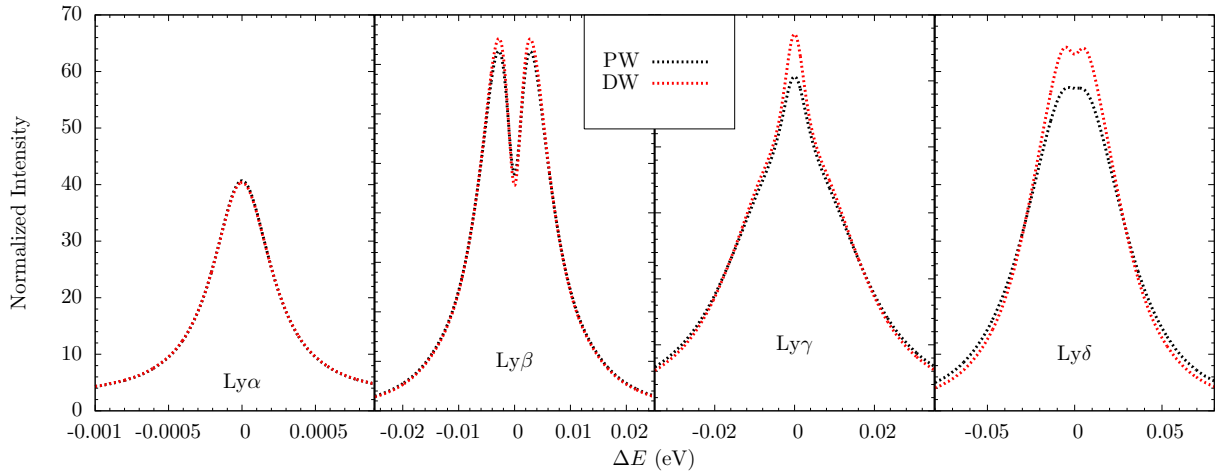

Figure 8.5: The Lyman series of neutral hydrogen (at $T_e = 1eV$ and $n_e = 10^{17} e/\mathrm{cm}^3$) that compares the plane-wave treatment (black-dotted) and distorted-wave treatments (red-dotted) of the colliding electron wavefunction. The distorted-wave treatment becomes more important with the increasing size of the wavefunction and affects the higher-order members of the series.

Distorted waves treatments of highly-charged radiators will always result in a decrease in the width. In this case, the number of waves near the atom is dictated by the charge of the nucleus and is insensitive to temperature. Junkel et al. (2000) showed that a factor of two change in temperature is required to see any appreciable changes in the amount of plasma shifts. The Coulomb waves and Distorted waves are nearly identical in figure 8.4. We can also see that the frequency of the waves inside a 2 Bohr radius from the nucleus are nearly identical in the spread of k. This is indicates that near the nucleus, the wavefunction behavior is dominated by the Coulomb potential.

8.4 Exchange

The second physical effect I will explore is the indistinguishability of electrons. The Hamiltonian of a two-electron system (one labeled r and one labeled e) moving around a nucleus of charge Z (atomic units),

$$H(r_r, r_e) = -\frac{1}{2}\nabla_r^2 - \frac{1}{2}\nabla_e^2 - \frac{Z}{r_r} - \frac{Z}{r_e} + \frac{1}{|\vec{r}_r - \vec{r}_e|}; \tag{8.24}$$

this Hamiltonian is symmetric between the two particles such that

$$H(r_r, r_e) = H(r_e, r_r).$$

Therefore any wavefunction solution to the two-electron Hamiltonian should have the following property:

$$\Psi(r_r, r_e) = \pm\Psi(r_e, r_r), \tag{8.25}$$

where a permutation of the coordinates is also a solution of the Hamiltonian with the same eigenvalue; the positive sign corresponds to Bosons (integer-spin particles), while the

negative sign corresponds to Fermions (half-integer spin particles, such as electrons and protons).

This permutation of coordinates does not apply if the particles that are not identical, for example, if we have an electron and a proton (labeled r and p, respectively), then the Hamiltonian is

$$H(r_r, r_p) = -\frac{1}{2}\nabla_r^2 - \frac{1}{2m_p}\nabla_p^2 - \frac{1}{|r_r - r_p|}. \tag{8.26}$$

This Hamiltonian is no longer symmetric under permutation of coordinates and the wavefunction symmetry requirement (Eq (8.25)) does not apply. Therefore for ion perturbations, we do not need to consider ion-electron exchange, but we do need to consider electron-electron exchange and proton-proton exchange, the latter has never been considered in line-broadening calculations. Since the thermal de Broglie wavelength of ions is much smaller, the probability of overlap is small, compared to the relatively large overlap of waves seen for electrons and it is this effect that we will consider here.

A common assumption in previous line-broadening calculations is to ignore exchange (Smith & Hooper, 1967; O'Brien & Hooper, 1974; Junkel et al., 2000)[2]. This approximation assumes a wavefunction of the form

$$\Psi(r_r, r_p) \approx \psi(r_r)\phi(r_p), \tag{8.27}$$

where as before, ψ is the bound-electron wavefunction and ϕ is the colliding-electron wavefunction. This form does not satisfy the symmetry requirement of Eq (8.25). In order to satisfy the symmetry requirement, we need to include a permutation of coordinates:

$$\Psi(r_r, r_p) = \frac{1}{\sqrt{2}}\left[\psi(r_r)\phi(r_p) - \phi(r_r)\psi(r_p)\right] \tag{8.28}$$

[2]only a handful of calculations have included it (Nguyen et al., 1986; Griem et al., 1997).

As we saw in the previous section, electron broadening is closely related to scattering, and the exchange has been deemed important since Oppenheimer (1928). The Born-Oppenheimer approximation evaluates the first term of the T-matrix,

$$\langle \psi\phi | T | \psi'\phi' \rangle \approx \langle \psi\phi | V | \psi'\phi' \rangle - \langle \psi\phi | V | \phi'\psi' \rangle \,, \tag{8.29}$$

where the first term is the direct term and the second term is known as the exchange term; the labels ψ and ψ' denote a set of atomic states, while ϕ and ϕ' denote a set of free-electron states. In the exchange term, the wavefunctions of the free and bound states are switched.

A second-order distorted-wave-with-exchange "T"-matrix calculation has already been evaluated by Madison et al. (1991):

$$\begin{aligned}
\langle \psi\phi | \mathrm{T} | \psi'\phi' \rangle \approx\ & \left\langle \psi\phi | V_{mon} | \psi'\phi'^{(DW)} \right\rangle + \left\langle \psi\phi^{(DW)} | V_{HO} | \psi'\phi'^{(DW)} \right\rangle - \left\langle \psi\phi^{(DW)} | V_{HO} | \phi'^{(DW)}\psi' \right\rangle + \\
& \frac{1}{2} \sum_{\psi''\phi''} \left[\left\langle \psi\phi^{(DW)} | V_{HO} | \psi''\phi''^{(DW)} \right\rangle - \left\langle \psi\phi^{(DW)} | V_{HO} | \phi''^{(DW)}\psi'' \right\rangle \right] G \times \\
& \left[\left\langle \psi''\phi''^{(DW)} | V_{HO} | \psi'\phi'^{(DW)} \right\rangle - \left\langle \psi''\phi''^{(DW)} | V_{HO} | \phi'^{(DW)}\psi' \right\rangle \right] \\
\approx\ & \left\langle \psi\phi | V_{mon} | \psi'\phi'^{(DW)} \right\rangle + \left\langle \psi\phi^{(DW)} | V_{HO} | \psi'\phi'^{(DW)} \right\rangle - \left\langle \psi\phi^{(DW)} | V_{HO} | \phi'^{(DW)}\psi' \right\rangle + \\
& \frac{1}{2} \sum_{\psi''\phi''} \sum_{S=0}^{1} \frac{2S+1}{4} \Bigg[\left\langle \psi\phi^{(DW)} | V_{HO} | \psi''\phi''^{(DW)} \right\rangle G \left\langle \psi''\phi''^{(DW)} | V_{HO} | \psi'\phi'^{(DW)} \right\rangle + \\
& \left\langle \psi\phi^{(DW)} | V_{HO} | \phi''^{(DW)}\psi'' \right\rangle G \left\langle \phi''^{(DW)}\psi'' | V_{HO} | \psi'\phi'^{(DW)} \right\rangle + \\
& +(-1)^S \left\langle \psi\phi^{(DW)} | V_{HO} | \psi''\phi''^{(DW)} \right\rangle G \left\langle \psi''\phi''^{(DW)} | V_{HO} | \phi'\psi'^{(DW)} \right\rangle \\
& +(-1)^S \left\langle \psi\phi^{(DW)} | V_{HO} | \phi''^{(DW)}\psi'' \right\rangle G \left\langle \phi''^{(DW)}\psi'' | V_{HO} | \phi'^{(DW)}\psi' \right\rangle \Bigg],
\end{aligned} \tag{8.30}$$

where S is the different spin states.

And we can translate this into our second-order $T(\omega)$ for the upper-state broadening (and after performing the sum over the spin states, and evaluating the trace on the free-

electron states):

$$
\begin{aligned}
T(\omega) \approx\ & \left\langle \psi\phi \left| V_{mon} \right| \psi'\phi'^{(DW)} \right\rangle + \left\langle \psi\phi^{(DW)} \left| V_{HO} \right| \psi'\phi'^{(DW)} \right\rangle - \left\langle \psi\phi^{(DW)} \left| V_{HO} \right| \phi^{(DW)}\psi' \right\rangle + \\
& \frac{1}{2} \sum_{\psi''\phi''} \left[\left\langle \psi\phi^{(DW)} \left| V_{HO} \right| \psi''\phi''^{(DW)} \right\rangle \frac{1}{\Delta\omega - \frac{1}{2}(k''^2 - k^2)} \left\langle \psi''\phi''^{(DW)} \left| V_{HO} \right| \psi'\phi^{(DW)} \right\rangle + \right. \\
& \left\langle \psi\phi^{(DW)} \left| V_{HO} \right| \phi''^{(DW)}\psi'' \right\rangle \frac{1}{\Delta\omega - \frac{1}{2}(k''^2 - k^2)} \left\langle \phi''^{(DW)}\psi'' \left| V_{HO} \right| \psi'\phi^{(DW)} \right\rangle + \\
& -\frac{1}{2} \left\langle \psi\phi^{(DW)} \left| V_{HO} \right| \psi''\phi''^{(DW)} \right\rangle \frac{1}{\Delta\omega - \frac{1}{2}(k''^2 - k^2)} \left\langle \psi''\phi''^{(DW)} \left| V_{HO} \right| \phi^{(DW)}\psi' \right\rangle \\
& \left. -\frac{1}{2} \left\langle \psi\phi^{(DW)} \left| V_{HO} \right| \phi''^{(DW)}\psi'' \right\rangle \frac{1}{\Delta\omega - \frac{1}{2}(k''^2 - k^2)} \left\langle \phi''^{(DW)}\psi'' \left| V_{HO} \right| \phi^{(DW)}\psi' \right\rangle \right], \qquad (8.31)
\end{aligned}
$$

likewise terms exist for the lower-state and interference broadening terms.

Madison et al. (1991) defines the additional terms in the "T"-matrix as the direct-direct, exchange-exchange, direct-exchange, and exchange-direct terms. The first two terms of the second-order term denote a process where the two electrons (supposing that you can actually track them), end up in the same place they started after the collision, whether its by a direct process, or a double-exchange process. The last two terms of Eq (8.30) denote a process that includes one direct interaction and one exchange interaction, which results in an exchange after the collision. Bethe & Salpeter (1957) define the rate of exchange simply as the exchange matrix element. The exchange matrix element contributes to the total Hamiltonian and the Hamiltonian is directly related to time evolution (appendix A.2).

Previous calculations that have ignored the effects of exchange (such as O'Brien & Hooper, 1974; Junkel et al., 2000), evaluate only the average potential, $\langle \psi\phi \left| V \right| \psi'\phi' \rangle$, and the direct-direct interaction term,$\langle \psi\phi \left| V \right| \psi''\phi'' \rangle \langle \psi''\phi'' \left| V \right| \psi'\phi' \rangle$. However, if exchange is included, we see from Eq (8.30), that there are an additional four processes to consider when exchange is included, which makes the calculation of spectral line shapes much more

complicated. The various angular and radial integrals are evaluated in appendix C. We will see later that including the effects of exchange is quite important.

8.4.1 Illustration of Exchange

To illustrate the effect that exchange has on an electron collision, I show pictures of a quantum-electron collision with an atom with and without exchange in figures 8.6 and 8.7. In these figures, I show only two spatial dimensions (x and z) on the horizontal axis; the vertical axis is the absolute values of the wavefunctions,

$$|\psi(\vec{r})|,$$

which are are also color-coded: black corresponds to low values of $|\psi(\vec{r})|$, and yellow corresponds to high values of $|\psi(\vec{r})|$. For the sake of the illustration, I will assume that I can prepare the system so that electron 1 is the free electron and that electron 2 is the bound state at the starting time (figure 8.6).

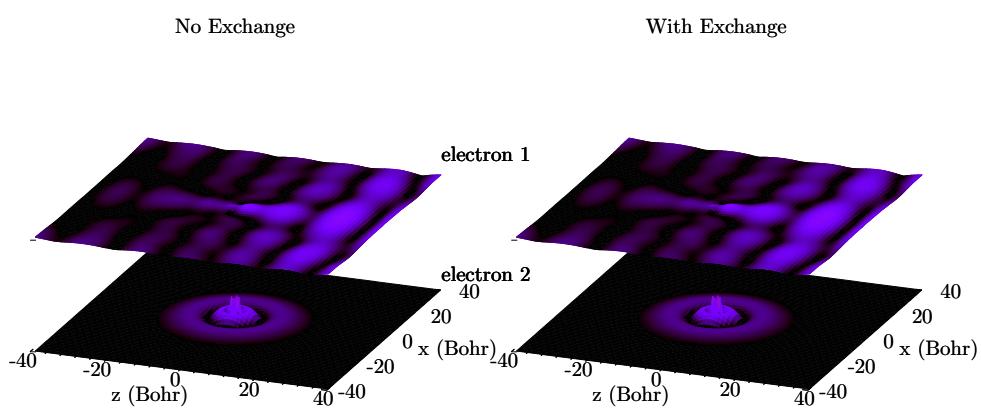

Figure 8.6: Leading up to the collision

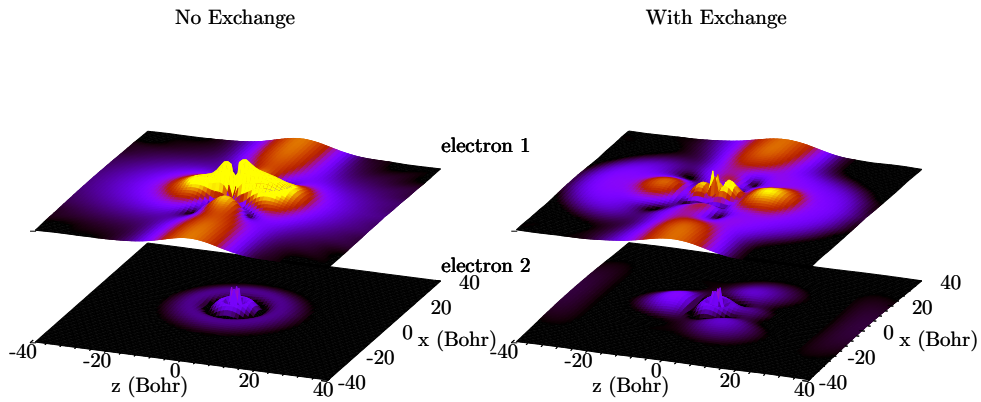

Figure 8.7: During the collision

Figure 8.7 shows the wavefunctions at a later time in the collision when the free electron occupies the same space as the atom. It is immediately evident that the electron 2 is distorted compared to its unaffected counterpart. The intensity of electron 1 is much reduced (the height of the wavefunction is not as large, nor is it as solidly yellow) in the exchange panel vs the no-exchange panel; this is a repulsion effect present in Fermions known as Pauli exclusion. Identical Fermions repel each other due to this quantum effect. To be clear, this is not due to electrostatic repulsion, but rather to the nature of the particles; this has no classical analog. As a result, the intensity of the wavefunction of electron 1 is significantly reduced near the origin, where the bound-electron and free-electron wavefunctions overlap. We can therefore expect that the broadening will be much reduced with the inclusion of exchange.

Figure 8.8 shows how the wavefunctions are affected after the collision. In the exchange panel, most of electron 1 is leaving the atom behind, but some of electron 1 remains near the nucleus, having properties of a bound electron. Similar behavior is also

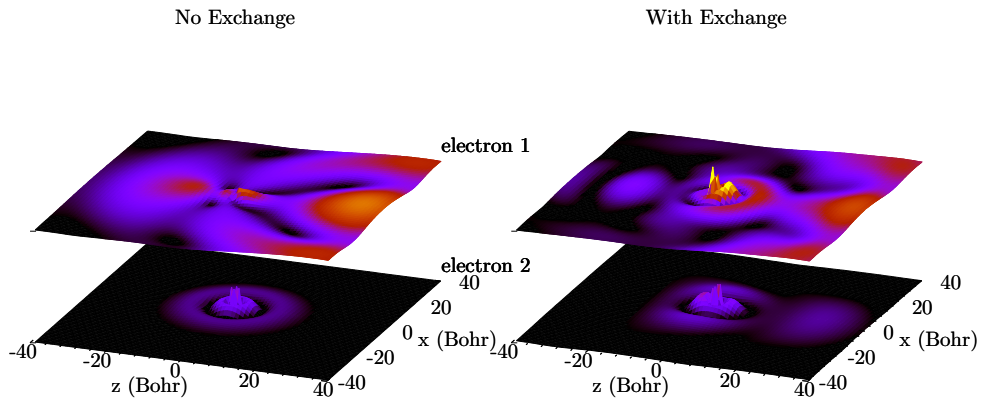

Figure 8.8: After the collision

seen in electron 2, where some of the wavefunction is leaving and some of it is left behind. After the collision, both electron 1 and electron 2 have bound- and free-electron behavior; they are a mixture of the different wavefunction solutions. This is in contrast to the no-exchange case. Electron 1 does have some charge left over on the nucleus, but it does not show bound-electron behavior as the exchange case does. Also, electron 2 is undisturbed since before the collision.

The rate of exchange is greater for high-n lines than it is for low-n lines. This is because the wavefunctions of high-n states are much larger than and the space that is shared by the electrons is larger.

8.4.2 Changes in Line Shape due to Exchange

Exchange is extremely important for the electron broadening calculation of hydrogen, as is shown in figure 8.9; exchange significantly reduces the widths of the lines compared to the no-exchange case. At the conditions explored here, ($T_e = 1eV$ and $n_e = 10^{17} e/\text{cm}^3$),

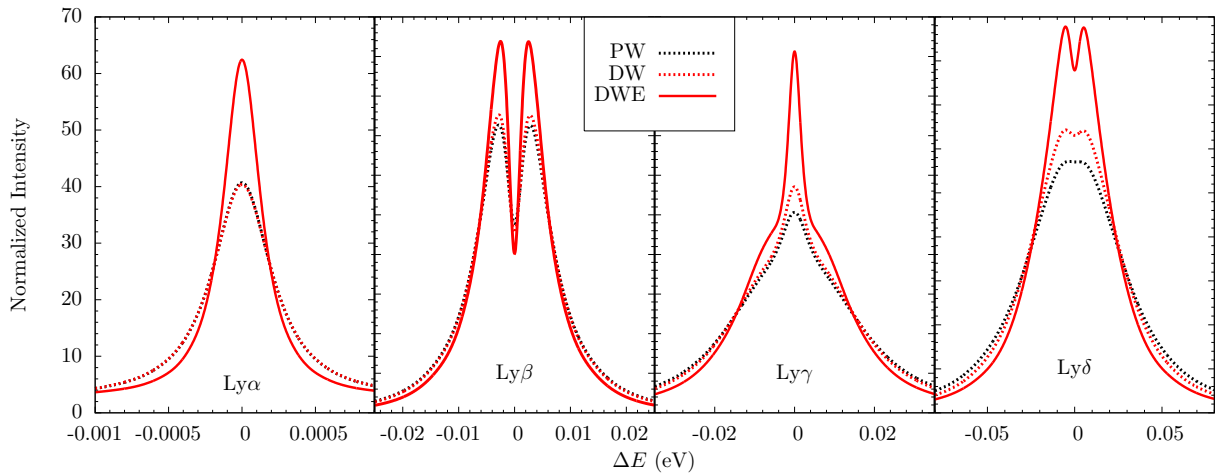

Figure 8.9: The Lyman series of neutral hydrogen that compares the plane-wave treatment (black-dotted), distorted-wave (red-dotted), and distorted-wave with exchange (solid red) treatment of the colliding electron wavefunction. Exchange is important for all transitions. Lyα (left) to Lyδ (right).

the line widths are reduced by nearly a factor of two.

Evaluation of exchange matrix elements creates correspondence of the quantum multipole expansion convergence with the semi-classical results in chapter 7. Including only direct terms results in an increase in the electron width when higher-order Coulomb terms are included. However, at this moderate density, as we saw from chapter 7 (see figure 7.3), profiles calculated using only dipole terms are nearly identical with those calculated with higher-order terms. When exchange is included, then this quantum treatment is accurate when only the dipole term is used.

The importance of exchange depends on the overlap of the two wavefunctions; Bethe & Salpeter (1957) discuss this when talking about the helium atom. In helium, the most common configuration is to have one electron in the $1s$ state and the other electron in an excited nl state. Excited s states of helium have the most charge overlap with the $1s$ ground electron and is therefore most susceptible to exchange. The excited p states are further way from the nucleus (due to having a non-zero angular momentum) and the charge overlap with the $1s$ state is reduced and the effect of exchange is reduced. The difference in energy of the spin-aligned and spin-anti-aligned states is 0.76eV and 0.49eV for the $2s$ and $2p$ states, respectively.

We can therefore gain some intuition about the importance of exchange for higher-charged elements. Figure 8.10 shows the bound electron (ψ) in dashed red and the free-electron (ϕ) in dotted black; also plotted is the exchange charge density,

$$\psi(r)\phi(r),$$

in blue. The wavefunctions of neutral hydrogen ($Z = 1$) and the free electron are similar

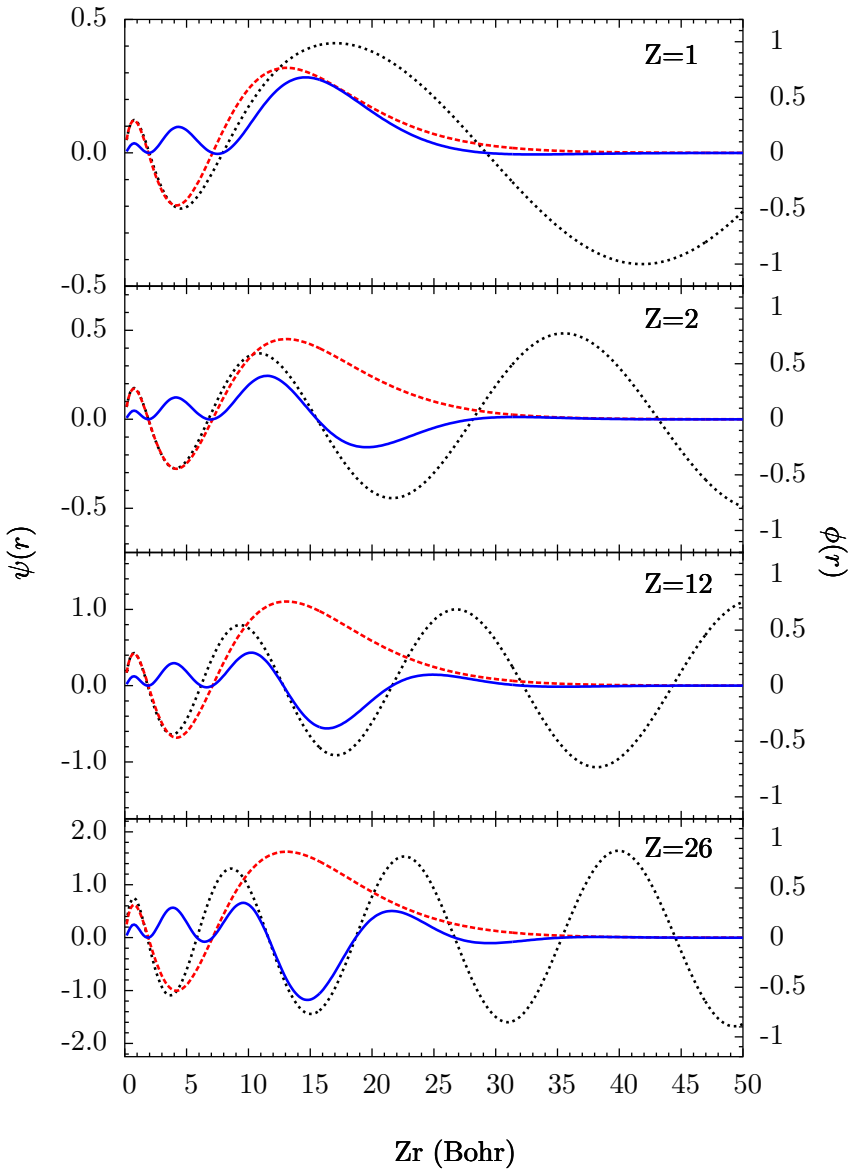

Figure 8.10: Wavefunctions of the bound electron (denoted with ψ and colored red) and the free electron (ϕ, dotted black) as a function of nuclear charge; the exchange charge density ($\psi(r)\phi(r)$) is shown in blue. All wavefunctions are s ($l = 0$) states; the bound electron is in the $n = 3$ state.

in behavior up to about 12 Bohr; at higher radii, the wavefunctions are both positive, thus leading to a large charge overlap. The exchange charge density is almost all positive, so when the integral is performed, then this will be a comparable to the atomic charge density. This is different for ionized helium ($Z = 2$); there are additional oscillations of the free-electron wavefunction, so there is cancellation in the exchange charge at larger distances and the charge overlap is reduced. There is a significant negative portion to the exchange charge density, which means that the integral will not be as large as it is in hydrogen. This effect is happens at smaller and smaller radii as the charge increases. For both magnesium ($Z = 12$) and iron ($Z = 26$), the only charge overlap is very close to the radiator ($Zr = 4$ Bohr and $Zr = 3$ Bohr, respectively). The exchange charge density has larger negative components as Z increases, thus the exchange matrix elements will be smaller for higher Z elements. We therefore do not expect that exchange will not be as important for magnesium and iron as it will for neutral hydrogen and helium.

To demonstrate this, I compare the different processes of $T(\omega)$ for neutral hydrogen and ionized magnesium in figure 8.11; these different processes are shown as a function of k of the free electron. These processes are:

$$T^{DD} = \langle 3s; ks \,|V|\, 3p; kp\rangle \langle 3p; kp \,|V|\, 3s; ks\rangle$$

$$T^{EE} = \langle 3s; ks \,|V|\, kp; 3p\rangle \langle kp; 3p \,|V|\, 3s; ks\rangle$$

$$T^{DE} = \langle 3s; ks \,|V|\, 3p; kp\rangle \langle 3p; kp \,|V|\, ks; 3s\rangle \,,$$

where T^{DD}, T^{EE}, and T^{DE}, are the direct-direct, exchange-exchange, and direct-exchange matrix elements. In this example, the direct-direct process has the atomic state starting in the $3p$ state, going to $3s$, then back to $3p$, while the free electron does something similar,

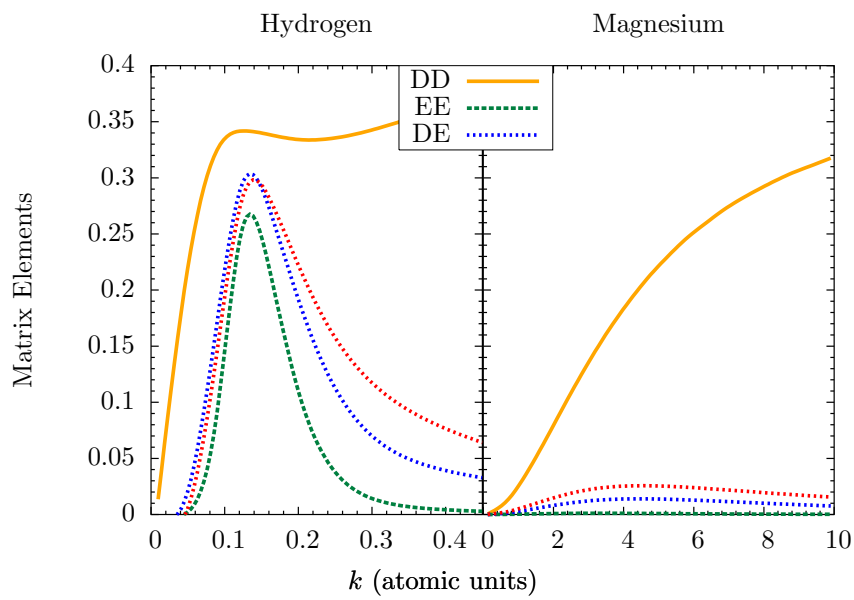

Figure 8.11: Matrix elements of the second-order $T(\omega)$ operator for the various processes. The direct-direct (DD), exchange-exchange (EE), and direct-exchange (DE) processes are shown. Exchange processes are significant compared to the direct processes in hydrogen; not so for magnesium. Additional exchange processes, such as monopole exchange, can increase the importance of exchange (total exchange contribution is shown in dotted red).

going from $kp \to ks \to kp$. The exchange-exchange process, has two exchange processes,

$$3p \to ks \to 3p; kp \to 3s \to kp,$$

leaving the bound-electron bound and the free-electron free after the process. The direct exchange can be written as

$$3p \to 3s \to kp; kp \to ks \to 3p$$

where after the process, the electrons have switched places. All three processes for hydrogen are comparable at low values of k; at high values of k, the exchange processes decrease while the direct process continues to increase. Exchange processes therefore become

unimportant—approaching the classical limit where exchange does not exist—as temperature increases. For magnesium, the size of the exchange matrix elements are much reduced compared to the direct-direct term. Exchange is relatively unimportant for the processes I have listed. There are, however, other processes which will increase the importance of exchange, such as the monopolar interactions (which are about as big as the dipole exchange process shown). The exchange monopole interactions (shown in figure 8.11 in red dotted lines)—which includes the DE process

$$3p \to 3s \to ks; ks \to kp \to 3p$$

—increase the high k exchange process in hydrogen, and brings the total exchange interaction of Mg to 18% of the direct interaction across a large range of k.

Figure 8.12 shows the results for hydrogen-like magnesium at similar conditions as the solar interior experiment. Due to the overlap of the free-electron wavefunction with the radiator, both the distorted-wave and distorted-wave-with-exchange treatments cause narrowing in the line shape. The changes due to distorted waves are greater than that of neutral hydrogen, but the effects due to exchange are much reduced.

8.5 Correlated Collisions

The third term of the 2nd-order Taylor expansion of $\mathcal{H}$ has been historically ignored due to the dipole approximation (Smith & Hooper, 1967). Because the plasma is isotropic,

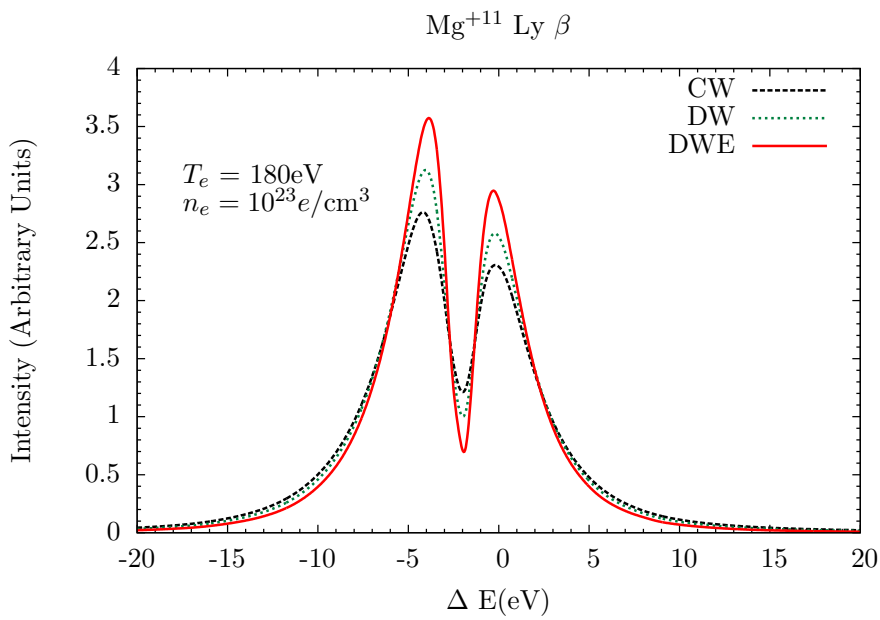

Figure 8.12: Comparison different approximations for Mg^{+11} Lyβ: Coulomb-wave calculation (CW; dashed black) with distorted-wave (DW; dotted green), and distorted-wave-with exchange (DWE; solid red). Each modification, (distorted-waves and exchange) results in about a 15% narrowing of the width.

the average direct dipole interaction, $\langle L_1 \rangle$, is zero. As a result, the third-order terms of $\mathcal{H}$,

$$\begin{aligned}\mathcal{H} \approx \langle L_1 \rangle + \left\langle L_1(\omega - L_0^a - L_0^E)^{-1} L_1 \right\rangle - \langle L_1 \rangle (\omega - L_0^A)^{-1} \langle L_1 \rangle + \\ \left\langle L_1(\omega - L_0^A - L_0^E)^{-1} L_1(\omega - L_0^A - L_0^E)^{-1} L_1 \right\rangle \\ - \langle L_1 \rangle (\omega - L_0^A)^{-1} \left\langle L_1(\omega - L_0^A - L_0^E)^{-1} L_1 \right\rangle \\ - \left\langle L_1(\omega - L_0^A - L_0^E)^{-1} L_1 \right\rangle (\omega - L_0^A)^{-1} \langle L_1 \rangle \\ + \langle L_1 \rangle (\omega - L_0^A)^{-1} \langle L_1 \rangle (\omega - L_0^A)^{-1} \langle L_1 \rangle , \quad (8.32)\end{aligned}$$

are also zero (the 4th term of Eq (8.32) is also zero because it has an odd number of dipole transitions; only even powers of dipole terms survive). Therefore, under the dipole approximation, the second-order formula of Smith & Hooper (1967) is accurate out to third

order,

$$\mathcal{H} \approx \left\langle L_1(\omega - L_0^A - L_0^E)^{-1} L_1 \right\rangle \tag{8.33}$$

which gives justification for the continued use of the second-order single-particle "T"-matrix.

The third-term on the right-hand side of Eq (8.32) also exists in the kinetic theory of Hussey et al. (1975), but gets lumped in with a screening term, which is approximated with a dielectric function (Dufty & Boercker, 1976), or in the low-density case, Debye screening (Hussey et al., 1977). Because of how common the dipole approximation is, the additional terms that arise due to Eq (8.3) have not been explicitly treated since the original derivation of Fano (1963), and it has no correspondence in the impact theory of Griem or Baranger. In other treatments where $\langle L_1 \rangle$ is not assumed to be zero, such as Woltz & Hooper (1984) or Junkel et al. (2000), this term seems to have been forgotten. As a result, much mystery has surrounded it and many in the community are unsure or unaware of its meaning.

8.5.1 Physical Interpretation of the Different Terms of $\mathcal{H}$

The terms of $\mathcal{H}$ that have a negative sign do not appear in the impact theory of Baranger or Griem due to their use of the binary-collision approximation. These additional terms arise due to the additional transformation of the one-electron "T"-matrix to create the electron-broadening operator (Eqs 8.3 and 8.4; repeated here for convenience),

$$\begin{aligned} \mathcal{H}(\omega) &= \frac{1}{1 + \langle T(\omega) \rangle \, (\omega - L_0^A)^{-1}} \langle T(\omega) \rangle \\ T(\omega) &= \frac{1}{1 - L_1(\omega - L_0^A - L_0^E)^{-1}} L_1 \end{aligned} \tag{8.34}$$

The physical interpretation of these expressions only makes sense in a Taylor expansion:

$$\begin{aligned}
\mathcal{H}(\omega) &= \langle T(\omega)\rangle - \langle T(\omega)\rangle \left(\omega - L_0^A\right)^{-1} \langle T(\omega)\rangle + \cdots \\
T(\omega) &= L_1 + L_1(\omega - L_0^A - L_0^E)^{-1} L_1 + \cdots,
\end{aligned}$$

where the different terms of the expansion of $\mathcal{H}$ are shown in Eq (8.32), and each term from the Taylor expansion corresponds to scattering events (L_1) or propagation (Griffiths, 1995).

These additional terms in $\mathcal{H}$ first appeared in Zwanzig (1960), while deriving a master equation of motion for an ensemble of particles. Zwanzig constructed a "T"-matrix that included an additional term in the propagation—a projection-operator, P.

$$\begin{aligned}
\mathcal{H}(\omega) &= L_1 + L_1 \frac{1-P}{\omega - L_0^A - L_0^E} \mathcal{H}(\omega) \\
&= L_1 + L_1 \frac{1-P}{\omega - L_0^A - L_0^E} L_1 + L_1 \frac{1-P}{\omega - L_0^A - L_0^E} L_1 \frac{1-P}{\omega - L_0^A - L_0^E} L_1 + \cdots
\end{aligned} \tag{8.35}$$

where the only difference between this equation and the more commonly-used single-particle "T"-matrix is the presence of the projection operator,

$$\begin{aligned}
T(\omega) &= L_1 + L_1 \frac{1}{\omega - L_0^A - L_0^E} T(\omega) \\
&= L_1 + L_1 \frac{1}{\omega - L_0^A - L_0^E} L_1 + L_1 \frac{1}{\omega - L_0^A - L_0^E} L_1 \frac{1}{\omega - L_0^A - L_0^E} L_1 + \cdots.
\end{aligned}$$

In Fano (1963), the projection operator is defined as

$$P L_1 \rho_E = \rho_E Tr\{L_1 \rho_E\}, \tag{8.36}$$

which is just a thermal average of the electron states of all the operators to the right of the P operator. In his paper on irreversibility, it allowed him to determine the "relevant" part of the equation of motion, which describe the motion of the "system of interest", from the "irrelevant part", which describe the "noise" of the system. The noise of the system would

be the effect of the thermal bath (or plasma collisions) on the system of interest (Zwanzig, 2001), which in this case is our atom. Fano stated that $\mathcal{H}$ which includes the $(1-P)$ term has the format of a linked-diagram expansion, which adds non-Markovian behavior to the line-broadening and is therefore more general than the impact formalism of Baranger or Griem.

These projection terms introduce memory into the system. The impact theory of Griem and Baranger do not have this projection operator in their formalism; neglect of the projection term assumes that the atom has a negligibly short memory such that the free electrons impact the atom independently of each other. The third term of Eq (8.32) correspond to the a singe-scattering event followed by propagation of the atom, followed by another single-scattering event. This is therefore describing collisions that happen in quick succession.

One way to reinforce this picture is to express these various collision terms as Feynman diagrams (Feynman, 1949b,a), which has been used to describe scattering processes (e.g. Griffiths, 1995). Though to refer these diagrams as Feynman diagrams may be inappropriate; I will refer to them as interaction diagrams. In appendix C.1, interaction diagrams are used to demonstrate the various scattering processes of a single particle. An interaction diagram for the various processes in Eq (8.32) are shown in figure 8.13; here different plasma electrons are shown in colors, while the atom of interest is in black; the squiggles denote the different Coulomb interaction "events." For the first-term, $\langle L_1 \rangle$, an electron collision has only one interaction "event", then propagates away from the atom with no further interaction. The second term, $\left\langle L_1(\omega - L_0^A - L_0^E)^{-1} L_1 \right\rangle$, indicates one collision with two scattering "events": there is an initial scattering "event" followed by propagation of both

$$\left\langle L_1 \right\rangle + \left\langle L_1 \frac{1}{\omega - L_0^A - L0^E} L_1 \right\rangle - \left\langle L_1 \right\rangle \frac{1}{\omega - L_0^A} \left\langle L_1 \right\rangle + \left\langle L_1 \frac{1}{\omega - L_0^A - L0^E} L_1 \frac{1}{\omega - L_0^A - L_0^E} L_1 \right\rangle$$

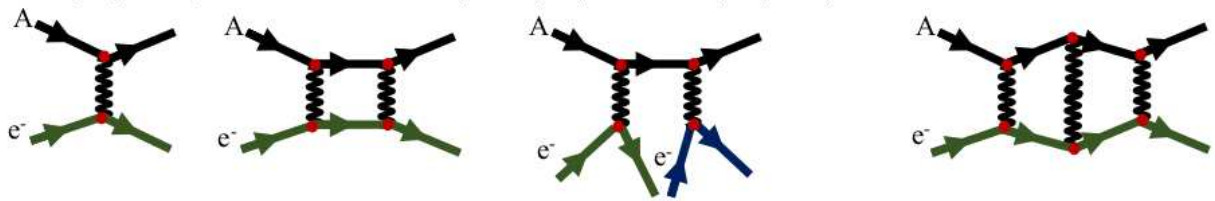

$$-\left\langle L_1 \right\rangle \frac{1}{\omega - L_0^A} \left\langle L_1 \frac{1}{\omega - L_0^A - L_0^E} L_1 \right\rangle - \left\langle L_1 \frac{1}{\omega - L_0^A - L_0^E} L_1 \right\rangle \frac{1}{\omega - L_0^A} \left\langle L_1 \right\rangle + \left\langle L_1 \right\rangle \frac{1}{\omega - L_0^A} \left\langle L_1 \right\rangle \frac{1}{\omega - L_0^A} \left\langle L_1 \right\rangle$$

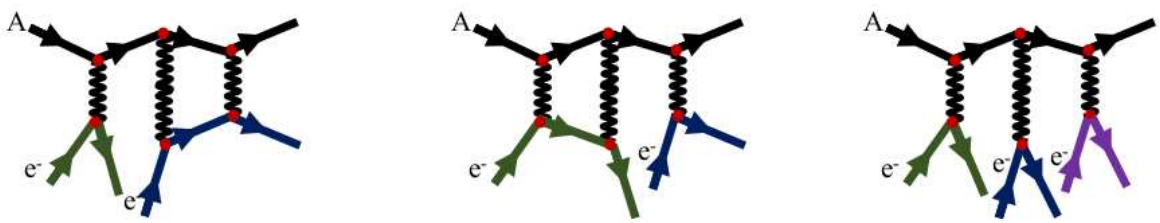

Figure 8.13: Feynman diagram of $\mathcal{H}$, where the paths of the atom are shown in black; the path of electrons one, two, and three are denoted by green, blue, and violet colors, respectively; the different Coulomb interactions—though non-relativistic—are shown as the squiggles; time increases from left to right, while the vertical space corresponds to physical space. The additional terms that arise from the projection operator in Eq (8.35), correspond to collisions that happen in quick succession.

atom and electron, then culminating in a second scattering event before the electron and atom propagate away. Now, the first term that arises from the projection operator has a collision, followed by an *atomic* propagation, and concluding with another scattering event; this is a substantially different interaction than the other second-order term.

I interpret this to be a two-electron process where one electron impacts the atom, then some time passes—but not enough that the atom "forgets" that it was just impacted—and the atom is impacted again by a different electron. This process has non-Markovian behavior in the sense that this second-collision process is dependent on the first-collision process; contrast this with the collision that contains a double scattering-event. This process involves subsequent collisions, which is different than simultaneous collisions.

8.5.2 Implementation

My work in this thesis is the first time that this term is implemented explicitly; some have included it in their formalism, but made simplifications (Dufty & Boercker, 1976) and lumped it into a screening term. This term is not difficult to evaluate and requires only a matrix multiplication of $\langle L_1 \rangle$, which is already evaluated. However Eq (8.32) as written is somewhat awkward to evaluate due to the singularity and having a discrete set of states. If this term is evaluated as is, when $\langle L_1 \rangle$ is large, then the profile will skew badly (figure 8.14). Inclusion of 3rd-order projection operator terms from Eq (8.32)—because they are made up of first- or second-order terms of M and are calculable by matrix multiplication—shows that for the Mg case, the broadening operator is not converged.

Without actually calculating the third- and fourth-order terms of M, I resort to an approximate method of calculating the broadening operator for highly-charged ions. I,

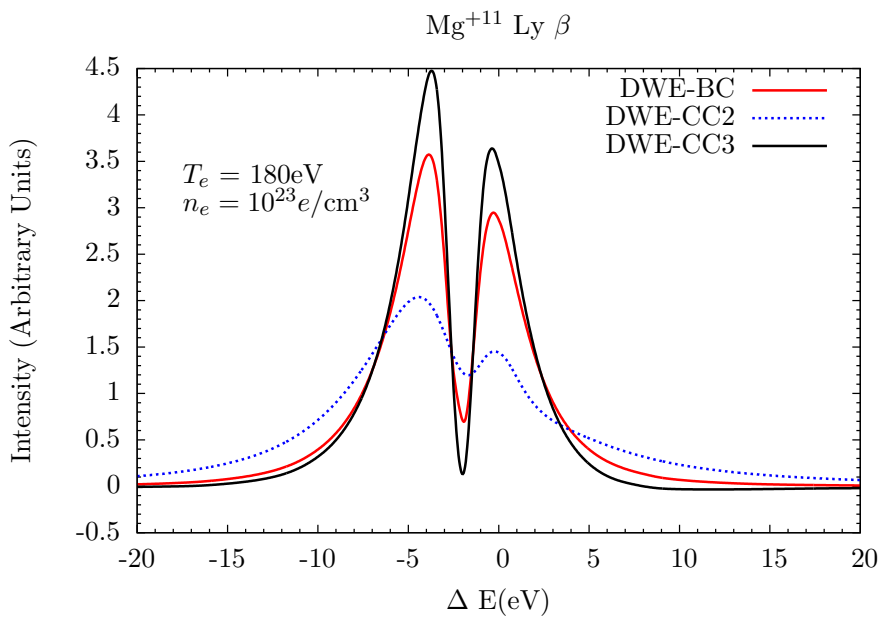

Figure 8.14: Comparison of the binary-collision calculation (DWE-BC) with the calculation with the correlated collision using only up to second-order terms (DWE-CC2). The calculation adds significant broadening to the line in a way that is not seen by experimenters. Comparison with some of the other projection operator terms of Eq (8.32) shows that this calculation is not yet converged (this calculation does not include the fourth term of Eq 8.32).

therefore, chose a form for the correlated collision term that is a little closer to the original derivation. The original form of the broadening operator (Eq 8.3) can be re-written as

$$\mathcal{H} = \langle M \rangle - \langle M \rangle \frac{1}{\omega - L_0^A + \langle M \rangle} \langle M \rangle \tag{8.37}$$

I therefore evaluate the broadening operator as

$$\mathcal{H} \approx \langle L_1 \rangle + \left\langle L_1 (\omega - L_0^A - L_0^E)^{-1} L_1 \right\rangle - \langle L_1 \rangle \frac{1}{\omega - L_0^A + \langle M_2 \rangle} \langle L_1 \rangle \,, \tag{8.38}$$

where M_2 is the second-order term of the M operator,

$$M_2 = L_1 (\omega - L_0^A - L_0^E)^{-1} L_1 \tag{8.39}$$

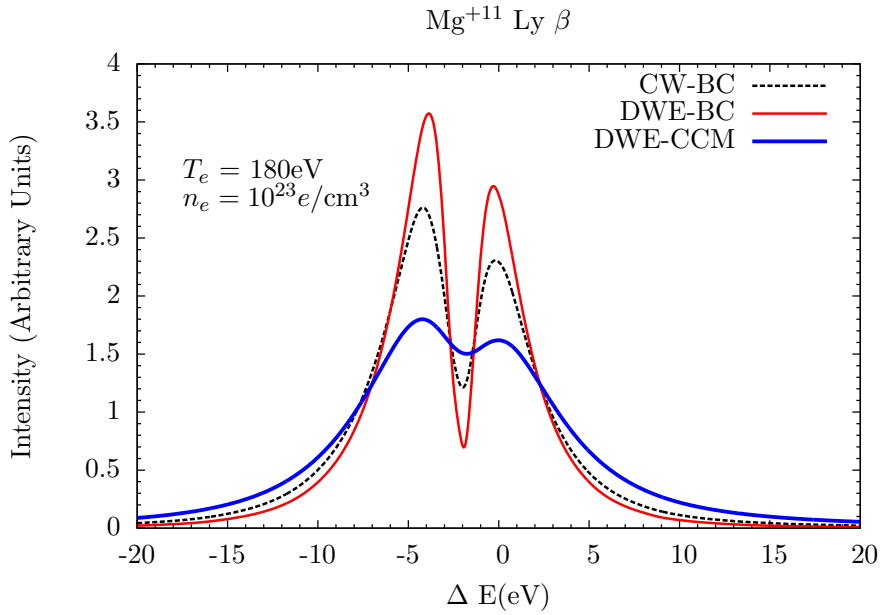

Figure 8.15: Comparison of the Coulomb-wave binary-collision calculation (CW-BC) with the binary-collision Distorted-Waves with Exchange calculation (DWE-BC), and our modified correlated collision Distorted-Waves with Exchange calculation (DWE-CCM). The DWE-CCM calculation is slightly narrower than the original version

Actually, there is no justification for Eq (8.38) other than using different approximations for M in different places in the Eq (8.37), though I can motivate its use. Third-order terms narrow perturbative calculations (figure 8.14), but without contribution from the third-order term of M, it is difficult to quantify exactly how big the changes are between the second- and third-order terms. And these terms will compete, for there will be combinations of terms that are of different orders of density. The implementation of Eq (8.38) reduces the amount of broadening—going in the same direction as the third-order term—due to the complex-valued argument in the denominator. This seems to work well for our

applications, when comparing Eq (8.32) to Eq (8.38).

8.5.3 Impact on Multi-Electron Radiators

The correlated collision term has almost no impact on the hydrogen or ionized helium widths, and takes substantially higher Z (and higher density) before these correlated collisions become important for one-electron radiators. Correlated collisions can become important at lower densities for multi-electron radiators.

The dominant contribution from M will come from the valence electron, though additional exchange terms may become important—this has yet to be determined. In multi-electron radiators, more of the nucleus will be screened by the bound electrons, therefore increasing $\langle L_1 \rangle$ over one-electron radiators. Since the first correlated collision term depends on the square of $\langle L_1 \rangle$, then this is the important quantity. For lithium-like (3 electrons) ions, I have treated the broadening terms approximately, neglecting some exchange processes, and am trying to get an order-of-magnitude estimate of the correlated collision term. Figure 8.16 shows a Li-like carbon transition in the far-UV part of the spectrum; it is not easily observable in an astronomical object, but other transitions that are similar to it are and will show similar changes. The changes in the line-width are not negligible; they are on the order of 30-40% increases for conditions on the surface of hot white dwarfs.

Solving for the detailed interaction of three electron atoms is a monumental task and is outside the scope of this thesis.

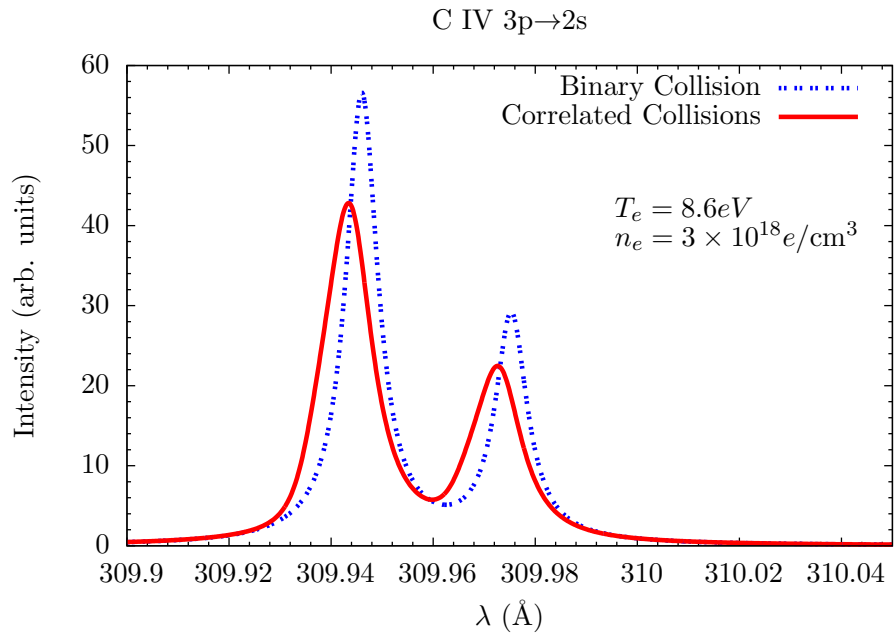

Figure 8.16: Comparison of the binary-collision assumption and correlated collision calculation for the spectrum of Li-like carbon. The electron-broadening details are only approximate at this point, treating only the valence electron, not the complicated exchange processes between all 4 electrons considered (3 bound, 1 free). Even at only a moderate density, the effect of correlated collisions seems to increase the width of the lines substantially.

8.6 Comparison with Other Calculations

With many calculations that treat the electron quantum mechanically, we must compare with the same level of physics to establish reproducibility of past calculations. I also want to compare with semi-classical calculations, which have good comparisons with experiment to at least evaluate that our calculations produce physical results.

8.6.1 Comparison with Semi-classical Calculations of Neutral Radiators

To our knowledge, the only work on quantum-mechanical electron-broadening calculations applied to neutral hydrogen was that of Smith & Hooper (1967). All the other

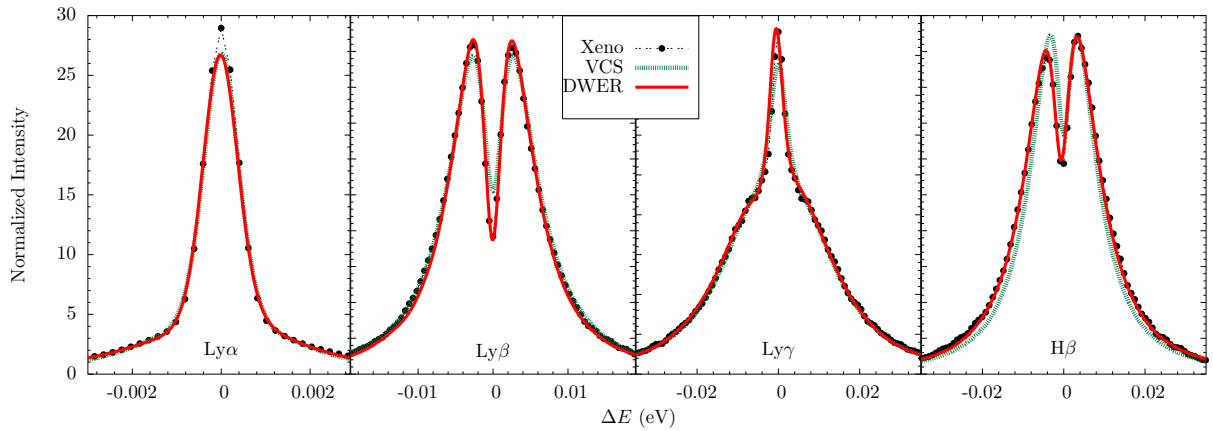

Figure 8.17: Comparison of DWE with the semi-classical calculations of *Xenomorph* and Vidal et al. (1973). The predictions differ for the Lyα line, but there is excellent agreement for the higher-n lines.

line-shape calculations were done in the semi-classical picture, where the atom is treated quantum mechanically and the perturbing particles are treated classically; this approximation is well justified for low density and high temperatures.

For hydrogen, we compare the results of this work with the unified theory calculations of Vidal et al. (1973) and the simulation calculation, *Xenomorph*, built from my masters thesis (Gomez, 2013). Both of these theories rely on the classical-path approximation, which for neutrals is a straight-line trajectory, correlations between electrons are taken into account via Debye screened potentials. *Xenomorph* includes dynamic ions in the simulation, though for this analysis I can freeze the ions, so that the only differences between the work presented here and these other calculations is the electron broadening treatment. The assumptions about the Coulomb interaction between the radiator and free electrons are also different: Vidal et al. (1973) assume the dipole approximation, *Xenomorph* uses higher-order multipoles; no penetration or exchange treatment of any kind is considered in the semi-classical calculations.

The agreement is somewhat puzzling, given the vastly different physics that is going into the different calculations. One could interpret this as the correspondence principle in action.

It should be noted that these semi-classical calculations have compared well with experiment (Wiese et al., 1972; Gomez et al., 2016), so by comparing our new calculations with the past semi-classical calculations in their range of validity, we are in essence comparing with experiment.

8.6.2 Comparison with Previous Calculations (Ionized Radiators)

It is important to compare these results with previous calculations for the same set of approximations. I compared our new calculations with those of Woltz & Hooper (1984) and the calculations by Kepple that were privately communicated with Woltz & Hooper. The argon Lyα calculations were nearly identical with those of Woltz & Hooper (1984), but our Lyβ and Lyγ lines were narrower. However, when we compared our distorted wave calculations with those of Kepple for Lyβ, our profiles were within a couple percent of the FWHM (see top panel of fig 8.18). At this point, I do not understand our disagreement with the Lyβ calculation of Woltz & Hooper (1984); we do not exclude the possibility of errors in my program (even after much rigorous testing). It may be possible that there were errors in the code implemented by Woltz & Hooper (1984), but the program is no longer in use, so examination is not possible.

We do note fairly good agreement *of the Coulomb-wave calculation* with the semi-classical calculation of Gunderson et al. (2001) of H-like carbon and decent agreement with the semi-classical calculation of Kepple (1972) for ionized helium (bottom panel of fig 8.18). The calculation by Kepple (1972) did not include inelastic collisions or interference terms; this may make up the difference between my calculation and his. Both calculations by Gunderson et al. (2001) and Kepple (1972) are semi-classical, which means that the plasma electrons are treated with classical-path trajectories. It seems that this would imply that, at these conditions, the quantum particles behave like classical particles, but without quantum effects such as exchange.

These classical-plasma calculations seem to agree well with the Coulomb-wave calculations *without exchange*; this is an interesting result because it is directly opposite of the

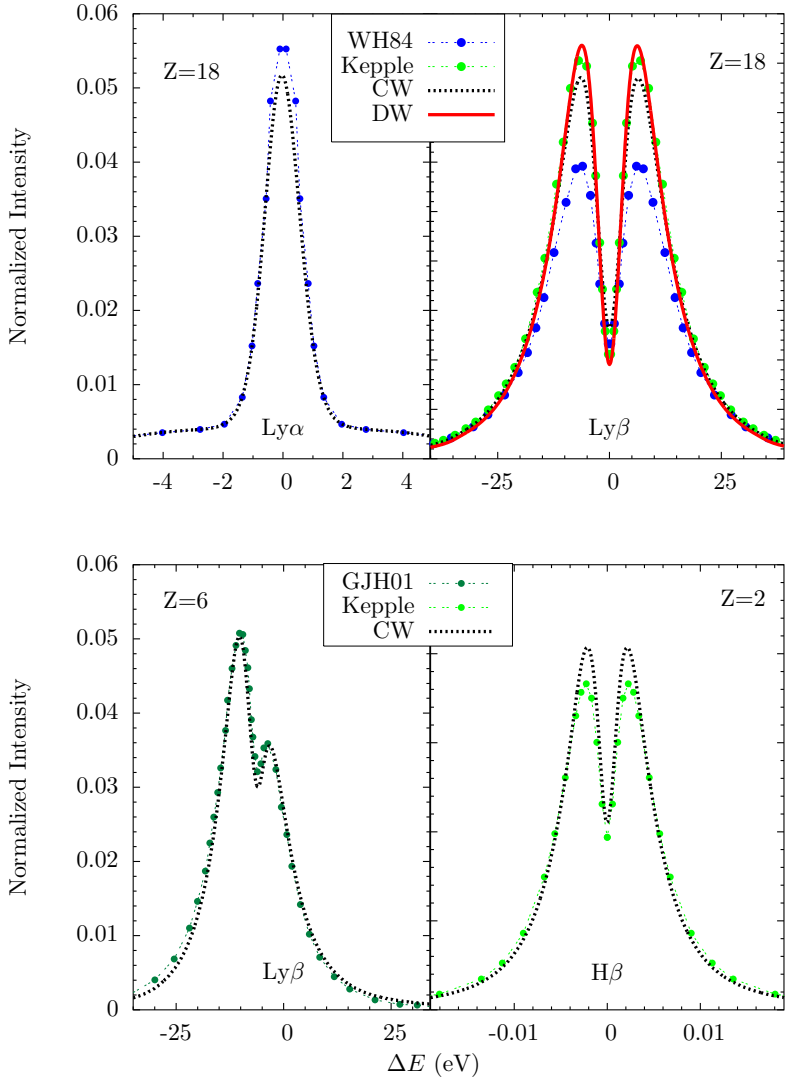

Figure 8.18: Attempting to replicate past calculations; all past calculations are dotted. The blue dots on the top panel represent the Woltz & Hooper (1984) calculation. My new Lyα agrees with Woltz & Hooper, but Lyβ, but my distorted-wave calculation agrees well with Kepple's distorted-wave calculation. The bottom panel has a compassion with Gunderson et al. (2001) and Kepple (1972); these semi-classical calculations agree well with my Coulomb-wave calculations.

results with the neutral hydrogen comparison. In the neutral hydrogen case, then details such as exchange were necessary in order to have correspondence, whereas, inclusion of exchange removes correspondence. Now, it is fair to raise the question: which calculation is correct? To answer this, an experiment is needed to differentiate between the calculations.

The first interesting comparison is that for lines that originate at $n = 3$ and above, the agreement between the best-level calculations (distorted wave with exchange) is extraordinary; this result is contrary to the result for ionized radiators. For the ionized radiators, agreement was reached for the Coulomb-wave treatment which ignored of exchange effects. But for the neutral hydrogen case, then agreement is *only* achieved when both distorted waves and exchange are included.

8.6.3 Comparison with Experiment for Charged Radiators

Few high-fidelity experiments with independent density diagnostics exist for charged H-like species. Hydrogen-like helium lines are the most commonly measured lines.

The semi-classical calculations by Kepple (1972) are the most extensive and commonly used. Kepple's calculations of low-lying states have compared well with experiment (Smith & Burgess, 1978; Pittman & Fleurier, 1986). However, these experiments suffered from large instrumental widths compared to the measured profiles and ion dynamic effects (Wrubel et al., 2001) that can affect the interpretation. Higher-n transitions, such as Balmer-γ, are wider and not quite so affected by ion dynamics, the instrument profile is smaller compared to the width of the profile, and the intensity of the line is much smaller so that optical depth effects do not affect the profile. The experiment by Musielok et al. (1987) shows fair agreement with the Kepple (1972) calculation for the Balmer-α line, but a 30%

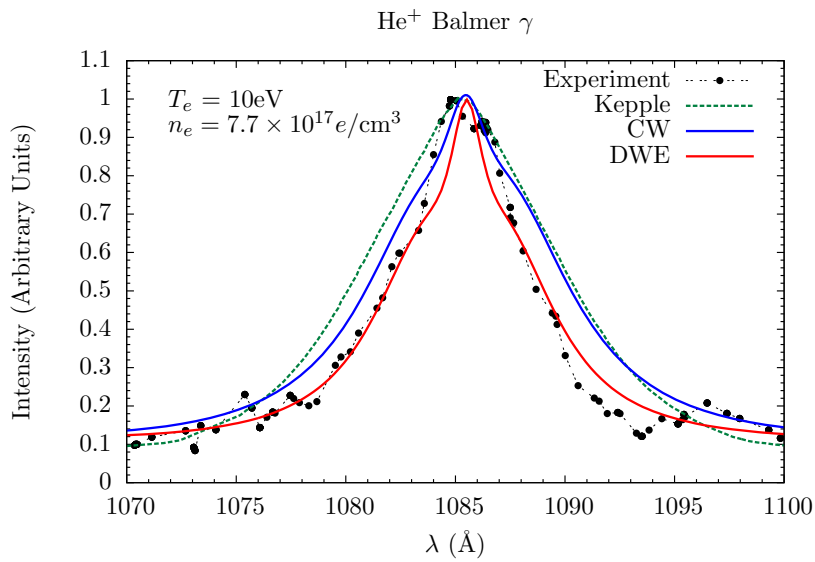

Figure 8.19: Comparison of the different approximations with the experiment by Musielok et al. (1987). The plasma conditions have been determined by Thomson scattering, so this is not a reduced χ^2 fit. The semi-classical calculation of Kepple (1972) is too wide for the profile; this is relatively consistent with the Coulomb-wave calculation. Only the calculation that includes the effects of exchange and distorted waves can match the data.

disagreement for the Balmer-γ line—which is beyond their experimental and the theoretical uncertainties. In fact, the authors reduced the density of the Kepple (1972) calculation to the lower limit of the density estimate (from Thomson scattering) and still found reasonable agreement with the Balmer-α profile.

I have compared the Coulomb-wave calculating (similar to that of Junkel et al., 2000), the new distorted-wave-with-exchange-and-back-reaction calculation (abbreviated to just DWE in the plot), with Kepple's calculation. The Coulomb-wave calculation without exchange effects produces a profile that is too wide compared to the measurement. But the new calculation presented in this chapter, matches the data fairly well—it's not perfect, but it is a substantial improvement over the previous efforts. This result might call into question

the accuracy of semi-classical calculations for charged radiators.

8.7 Future Work

The calculations here represent an important step forward, but they are far from complete. So far, the effect of higher-order terms of the broadening operator have not yet been examined. Also, the effects of multiple collisions have not been investigated; in fact, no semi-analytic method has done this; only simulations can treat it. I would also like to extend these calculations to multi-electron radiators; so far, the treatments I have explored for multi-electron radiators are only approximate, in that I neglect a numerous exchange processes that may (or may not) affect the line shape. I have a hypothesis that these additional exchange processes may account for the discrepancy between theory and experiment simple closed-shell Li-like ions (Glenzer et al., 1992; Glenzer & Kunze, 1996; Ralchenko et al., 2003). So far, the semi-classical calculations (with penetrating collisions) agree with the quantum-mechanical approach (Alexiou & Lee, 2006), where the width is defined as the "T"-matrix. No semi-classical calculation treats the four-way exchange processes that can occur for these Li-like ions.

Work on electron broadening for multi-electron systems is sorely needed.

Chapter 9

Line Merging/Continuum Lowering (Penetration of Ions)

At high density, atomic states are perturbed so much that the width of the spectral line is the same as the energy spacing with the next level; this is when atomic lines begin to overlap and merge to form a featureless continuum. This phenomenon is known as continuum lowering, or ionization potential depression. Continuum lowering is one of the most complicated (and contested) sub-fields within atomic and plasma physics. The first empirical model of this phenomenon was given by Inglis & Teller (1939), whose famous limit describes *when you should observe the last line of a series, but does not make any claim when an atom is ionized due to the plasma or the lines are just too broad to distinguish.*

There are two methods to approach the problem: a chemical picture or a physical picture. Most of the estimates of the lowering of the continuum are through a chemical picture, where an average-atom model gives an estimate for the change in the ionization potential, which then alters the Saha-Boltzmann equations. There are so far no detailed calculations of continuum lowering in the physical picture, where the detailed atomic structure is a function of the plasma environment. It is harder to do these calculations because they are computationally expensive and must be performed many times in order to provide good statistics for the ensemble average.

Ab initio chemical models vary widely, from average atom approach such as Ecker

& Kröll (1963), and Stewart & Pyatt (1966), to a more statistical approach of Däppen et al. (1987) and Hummer & Mihalas (1988). The most widely used model in the astronomical community is the "occupation probability" formalism by Däppen et al. (1987) and Hummer & Mihalas (1988). The occupation probability formalism is a statistical approach to estimate the probability that an electron is still bound to the atom, i.e., that the level still exists as opposed to being dissolved into a continuum. This formalism has several advantages, such as thermodynamically self-consistency and easily implemented to solve NLTE rate equations (Hubeny et al., 1994; Hubeny & Lanz, 1995) and into opacity models (Däppen et al., 1987). However, many approximations are made with the original formalism that require scrutiny and comparison against a more complete method.

There is evidence to suggest that the formalism of occupation probability put forth by Hummer & Mihalas (1988) is incomplete. Bergeron et al. (1992) had to modify the criteria for ionization by a factor of two to get similar gravities between different lines when fitting the spectrum of stars. Additionally, Barstow et al. (2005, 2017) and Falcon et al. (2010) found that the masses of white dwarf stars determined by Keplerian orbits or gravitational redshift are different from the spectroscopic method. Tremblay & Bergeron (2009) merged the occupation probability formalism of Hummer & Mihalas (1988) with the line-broadening model of VCS (which achieves some level of consistency), but disagreement between different spectral lines still persists.

9.1 Overview of Occupation Probability

The partition function is defined as

$$Z = \sum_i g_i e^{-E_i/k_B T}, \tag{9.1}$$

however, there is an infinite number of atomic states, which makes this non-convergent. The model from which the partition function is derived assumes the gas is ideal, meaning non-interacting; this is not a very physical picture when densities are high. At high density, the perturbations from nearby particles are strong enough to destroy states, limiting the number of available states that can contribute to the partition function; this is one example of a departure from an ideal gas, or as it is called by Tremblay & Bergeron (2009), "non-ideal effects."

One way to make the model more realistic is to introduce w_i, the probability that a state is "occupied." The populations can therefore be described by the following equations (Hummer & Mihalas, 1988):

$$\frac{n_i}{n_j} = \frac{g_i w_i}{g_j w_j} e^{-(E_i - E_j)/k_B T} \hat{Z}^{-1} \tag{9.2}$$

$$\hat{Z} = \sum_i g_i w_i e^{-E_i/k_B T} \tag{9.3}$$

This is a very convenient set of equations; Hummer & Mihalas (1988) used them to re-derive the fundamental equations of thermodynamics for a given occupation probability formalism.

The crux of the problem for occupation probability is to define the criteria for when a state is "not occupied" vs when it is "occupied." Hummer & Mihalas discuss various processes that could destroy states, including perturbations by neutral particles and charged particles.

9.1.1 Perturbations from Charged Particles

The first model explored by Hummer & Mihalas is the static-screened Coulomb potential, which describes the atom having a finite range of influence due to the presence of

plasma particles—as opposed to having the nuclear potential go as $1/r$ to infinite lengths. But there are many problems with this model and it is discarded by Hummer & Mihalas.

They move on to electric microfield perturbations, since the dominant interactions in a plasma are not through an average potential, but rather through fluctuations around the average. The occupation probability with electric field perturbations is defined as

$$w_i = \int_0^{F_i} dFW(F) \tag{9.4}$$

where $W(F)$ is the probability distribution of microfields—short range electric fields due to the presence of ions in a plasma—and F_i is the field at which state i is ionized; this is the same probability distribution used by semi-analytic methods (section 6).

The first estimate of the critical value of electric microfield, F_i, is using a saddle point (see figure 9.1). The potential of a nuclear potential, $1/r$ plus a constant uniform electric field (in the z-direction for simplicity), $-zF$, goes to positive infinity as z goes to increasing negative values (the electron runs into the potential and is bound on this side) and goes to negative infinity as z goes to large positive values; since the potential goes to increasing negative values, the atomic electron will have free-electron behavior at large z, which makes the electron *unbound* (I will comment on the accuracy of this picture shortly). There is a high point between the negative infinity at large positive z and the nuclear potential at the origin, which occurs at $z = -\sqrt{1/F}$; this high point is referred to as the "saddle point". If we use the "saddle point" as our ionization criteria, i.e., any state with energy above this threshold is considered "ionized", then the critical value of electric field is

$$F_i = \frac{1}{16n_i^4}, \tag{9.5}$$

where n is the principle quantum number of state i.

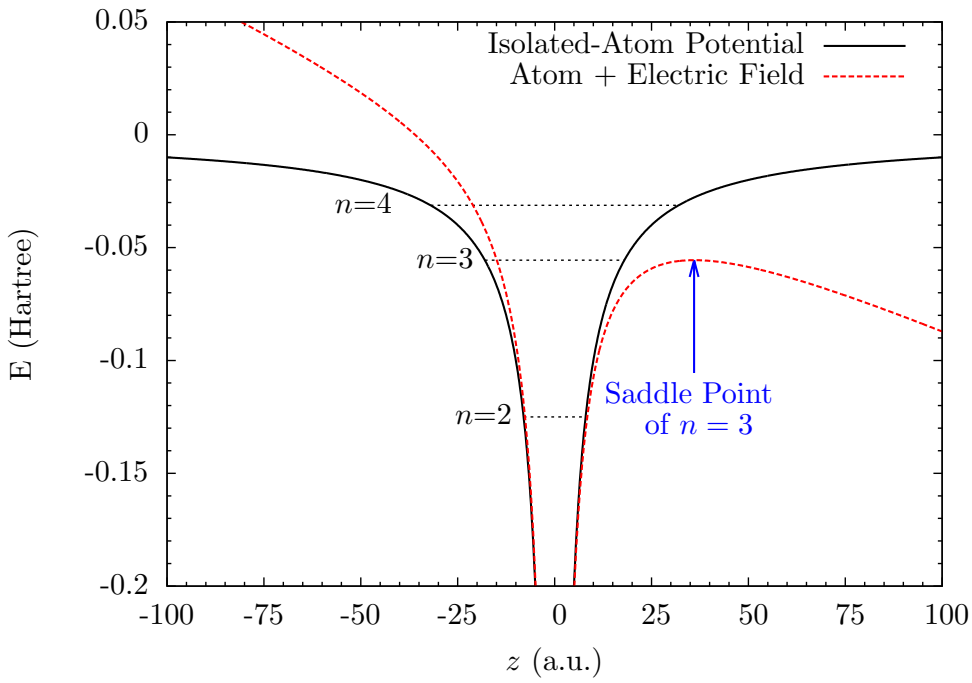

Figure 9.1: A diagram of the isolated-atom potential and the atom with a constant electric field, shown is the saddle point. The electric field value is the saddle point (given by Eq 9.5) of $n = 3$. The true ionization threshold will be slightly less than this value due to quantum tunneling.

Hummer & Mihalas point out several problems with this model, namely that things like quantum tunneling can reduce this value, as well as avoided crossings between the blue states of n and the red states of $n+1$ and the fact that the electric field is actually fluctuating, not constant. The argument, based on high-frequency sodium experiments by Pillet et al. (1984) and van Linden van den Heuvell & Gallagher (1985) show Landau-Zener transitions where an electron starting in state n can transition to state $n+1$, and continue up to $n+2$, etc. until it becomes ionized. They also argue that collisions mix states, which can further change the criteria for ionization. Finally, Hummer & Mihalas arrive at an answer that is identical with the Inglis & Teller (1939) limit. They admit that the physical pictures are

very different, with Inglis & Teller (1939) describing the merging of lines, while Hummer & Mihalas described rapid fluctuations.

A simpler equation for the ionization threshold was adopted by Seaton (1990), which was the formula for the critical electric field when the bluest substate of n is the same energy as the reddest substate of $n+1$,

$$F_i = \frac{2n_i + 1}{6n_i^4(n_i+1)^2} \tag{9.6}$$

in atomic units.

9.1.2 Incorporation of Occupation Probability into Opacities

The occupation probability formalism can be incorporated into the formulae for opacities, as was first done by Däppen et al. (1987). Line opacity is then modified to include the occupation of the upper and lower states (Tremblay & Bergeron, 2009),

$$k_{ij}^{(BB)}(\nu)d\nu = n_i \frac{\pi e^2}{m_e c} \frac{w_j}{w_i} f_{ij}\phi(\nu)d\nu \tag{9.7}$$

where i is the initial state, n_i is the population of the upper state, f_{ij} is the oscillator strength, and ϕ is the frequency-dependent line shape. The continuum is modified in a similar way,

$$k_i^{(BF)}(\nu)d\nu = n_i \left(1 - \frac{w_n^*}{w_i}\right) \frac{64\pi^4 m_e e^{10}}{3\sqrt{3}ch^6} \frac{g_{bf,i}(\nu)}{n_i^5 \nu^3} d\nu \tag{9.8}$$

where there is a fictitious upper level occupation, w_n^*, defined as

$$n^* = \left(\frac{1}{n_i^2} - \frac{E}{13.6eV}\right)^{-1/2}.$$

The intrinsic spectral line shapes should—in principle—include an occupation probability built into the equations. If ion dynamics is ignored and the line shape can be described

by an electron-broadening function, J integrated over a microfield distribution, then the line shape can be described with occupation probability to be

$$L(\omega) = \int_0^{F_i} dF\ W(F) J(\omega, F) \tag{9.9}$$

This was first done by Stehle & Jacquemot (1993) and compared with single-temperature and density data from the Wiese et al. (1972) experiment. A grid was made by Tremblay & Bergeron (2009), who used this to study white dwarfs.

9.1.3 Critique

First, I want to discuss the Stark pattern. Appendix D discusses in detail the pattern of splitting that arises when a constant electric field is applied to an atom. To first order, there is a splitting where some substates of any given n will increase in energy to the blue, while others will decrease in energy toward the red. In figure 9.1, the states that are nearest the unbound side of the atom are the red states, while the blue states are polarized toward the bound-side of the potential. Therefore, the states that will ionize sooner will be lower in energy than the saddle-point electric field defined in Eq (9.5). The claim that the saddle point is too high of an electric field may not be accurate since the energy of the soonest-to-be-ionized red side of the profile is actually below this value.

In figure 9.1, we see that the electric field extends to all space—but this is not an accurate picture. A proton is sitting close to the atom and another $1/r$ potential will be present on the positive z-side of the atom. These two potentials will give different behavior for the atomic electron when the energy is near the saddle point. In a constant electric field, an electron can tunnel out of the atom and leave toward infinity with a vanishing small probability that it will tunnel back; once the electron is free, the electric field will continue

to accelerate the electron away from the atom. However, in the more realistic picture with a nearby proton, the electron can tunnel out, but will still be confined to the space of the two protons and has a relatively high probability of tunneling back in.

Next, lets examine the time-scales. We can think of spectral line shapes as being a property of both time and frequency. For example, if the time-scale for something to happen is long, then it corresponds to small detunings from the line center (large $\Delta t \rightarrow$ small $\Delta\omega$). This can also translate into some intuition about line widths; if a line is narrow, then that means that it takes a long time for the line to lose coherence. The opposite is true of wide lines: it takes a relatively small amount of time for the the states to lose coherence and decay. Near the continuum threshold, where levels are starting to cross, the lines are extremely broad and therefore the timescales are short—so short that ions barely move. The electric field due to the ions is nearly static over the time it takes to form the line. Adopting the model of a high-frequency fluctuating field will not work for spectrum calculation, though it may be relevant for calculating populations.

Lets also take a look at the processes. The atoms and plasma particles in the spectra are in stasis, which means that detailed balance must be taken into account. For example, if one atom can ionize, then another can recombine, conserving the total number of particles, the temperature, etc.—even if the plasma is not in LTE. So Hummer & Mihalas describe electrons tunneling out of the atom, but they do not consider that the reverse process can also take place.

Hummer & Mihalas base their estimates of the ionization criteria on experiments with multi-electron atoms—not neutral hydrogen. Littman et al. (1978) showed that tun-

neling for ionization in neutral hydrogen is different than multi-electron atoms[1] . When the electric field increases, the blue side of a given energy level disappears first due to ionization; in hydrogen, however, the red side disappears first (Littman et al., 1978; Luc-Koenig & Bachelier, 1980a). The astronomical community has used the ionization criteria by Hummer & Mihalas extensively.

There is evidence that the Hummer & Mihalas treatment may not be the right procedure. Stehle & Jacquemot (1993) calculated spectra of neutral hydrogen with and without these cutoffs and compared them with the Wiese et al. (1972) experiment. They showed that using the microfield cutoff (Eq 9.9) resulted in worse comparison with experiment than if the integral bounds were allowed to go to infinity. In addition, Tremblay & Bergeron (2009) compared their new results with the Wiese data, and compared with the Vidal et al. (1973) line shapes (which has no occupation probability built in), and found that their new profiles did not necessarily improve the comparison with experiment.

A more detailed solution is sorely needed and I am going to explore the line-merging continuum lowering phenomenon in the rest of this chapter.

9.2 Direct Solutions of the Atomic Structure

In the previous section, I talked briefly about time scales and showed that ion dynamics is a minor correction when calculating line shapes near the continuum threshold. Therefore for these calculations I can use the static-ion approximation to calculate the atomic data necessary. I want to calculate the behavior of electrons in the presence of

[1] The Hamiltonians of multi-electron atoms contain Coulomb matrix elements between different n levels—hydrogen does not

many protons and the computing power is such that this task can be handled by a desktop computer.

The goal is to try to solve for the atomic structure in the presence of many ions. The accuracy of such a calculation is dependent on the size of my basis set. I can, however use a different basis set and reduce the number of matrix elements I need to use to calculate continuum lowering. Ideally, the potential used in the Schrödinger equation, would also include the protons in the plasma.

9.2.1 Parabolic States: Electric Field-dependent Basis

My first attempts were to try to solve for wavefunctions with a field-dependent basis; the basics of this method are outlined in Bethe & Salpeter (1957) and examination of the properties of such atomic structure were studied by Luc-Koenig & Bachelier (1980a,b). Kilcrease et al. (1993) used this method to obtain more accurate atomic data for lines near the continuum threshold.

In parabolic coordinates, the Schrödinger equation is separable in even with an external field in the z-direction. In this basis, I can solve numerically for the wavefunctions that are dependent on a *constant, uniform* electric field. Additional details are in appendix D. This technique has the advantage of exact numerical solutions.

Critique There is a problem with this technique, both computationally and physically. One side of the wavefunction is bound, but the other is unbounded (i.e. extends to infinity); this is a problem for evaluating matrix elements for electron broadening. Also, the true field in a plasma is NOT uniform. It has gradients as well as sinks due to nearby plasma ions;

this model does not accurately represent the physics of the problem.

9.2.2 Direct Solution

The next method that I tried was to use matrix mechanics to solve for the one-electron Schrödinger equation in the presence of several nearby ions. This is not using Heisenberg's method, but rather is setting up a matrix of finite-difference elements and solving a large matrix. Each point on the vector represents a spatial point on a finite mesh:

$$\psi(r) = \begin{pmatrix} \psi(r_1) \\ \psi(r_2) \\ \psi(r_3) \\ \psi(r_4) \\ \vdots \end{pmatrix} \tag{9.10}$$

where the Hamiltonian is written as a giant matrix (see appendix A.3).

$$H = \frac{1}{(\Delta r)^2} \begin{pmatrix} 2 & -1 & 0 & 0 & \cdots \\ -1 & 2 & -1 & 0 & \cdots \\ 0 & -1 & 2 & -1 & \cdots \\ \vdots & \vdots & \vdots & \vdots & \ddots \end{pmatrix} + \begin{pmatrix} V(r_1) & 0 & 0 & 0\cdots & \\ 0 & V(r_2) & 0 & 0\cdots & \\ 0 & 0 & V(r_3) & 0\cdots & \\ \vdots & \vdots & \vdots & \vdots & \ddots \end{pmatrix}, \tag{9.11}$$

where first term is the derivative term (written as a finite difference element) and the second term is the potential in which the electron is moving. I diagonalize this Hamiltonian as a giant matrix and the eigenvectors that are returned are the values of the wavefunction at the mesh points.

The example above is for one dimension, however, the real problem is three dimensional. I can use some symmetry to reduce this to a two-dimensional problem (see Eq A.15). The electric field is dominated by the nearest neighbor in the plasma; if I rotate my plasma so that the electric field is in the z direction, then the φ dependence of the plasma is small and can be solved with perturbation theory without much loss of accuracy. This simplification means that I need to solve for the wavefunctions in r and θ, and I can retain

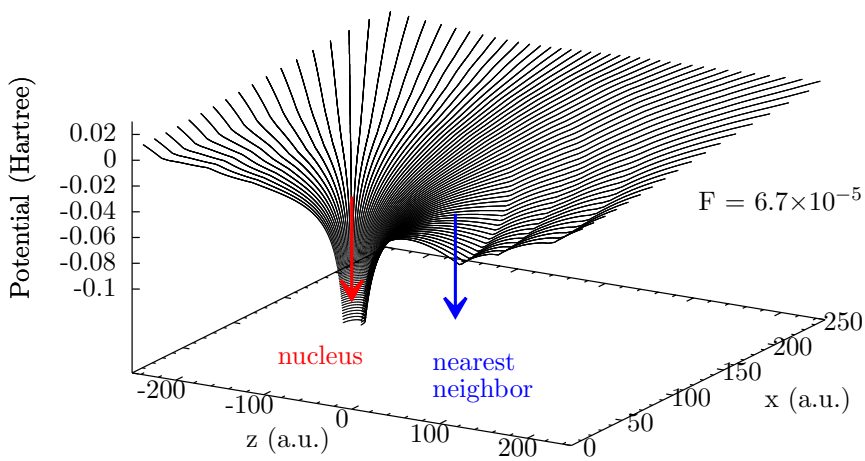

Figure 9.2: 2-dimensional surface plot of the potential to be solved by matrix diagonalization. Only two protons are shown for this example. The nucleus is set at the origin and labeled with a red arrow, the nearest neighbor is set at a radius of 100 and in the z-direction, denoted with a blue-arrow.

the φ symmetry in the atomic wavefunction.

$$\psi(r,\theta,\phi) = \frac{1}{r}R(r,\theta)e^{im\varphi}.$$

To solve such a system, the spatial vector will be a function of r, and θ,

$$R(r,\theta) = \begin{pmatrix} R(r_1,\theta_1) \\ R(r_1,\theta_2) \\ R(r_1,\theta_3) \\ \vdots \\ R(r_2,\theta_1) \\ R(r_2,\theta_2) \\ R(r_2,\theta_3) \\ \vdots \end{pmatrix} \tag{9.12}$$

and the Hamiltonian will contain finite-difference elements that include the θ derivative; this matrix will be large and will require a sparse numerical eigenvalue solver. Fortunately, since

the Hamiltonian is symmetric, the problem is simplified and calculation time reduced with the use of a symmetric/Hermitian matrix solver. The potential will have the nucleus at the origin and several randomly placed protons (See figure 9.2). The wavefunction solutions are illustrated in figure 9.3.

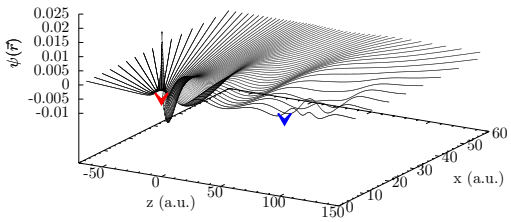

(a) The wavefunction is shared between protons.

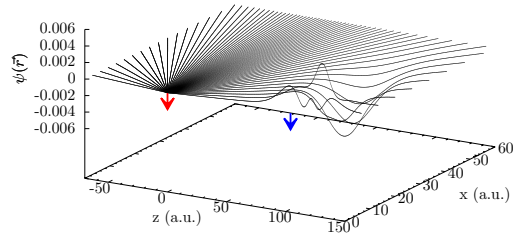

(b) This wavefunction is isolated on the nearest neighbor.

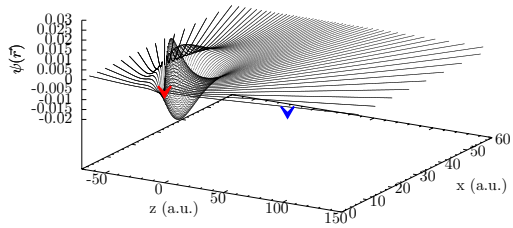

(c) Same as figure 9.3b, but bound to the nucleus.

Figure 9.3: 2-dimensional surface plot of solutions to the potential in figure 9.2. 9.3a has the lowest energy and 9.3c has the highest energy.

With this method, there were in general three types of solutions: states bound to the nucleus, states bound to the nearest proton, and states that are shared between both protons. Figure 9.3a shows an example where the wavefunction is shared between the two

protons; this is the sort of behavior expected for high-energy states in a dense plasma where the effects of protons can "destroy" states. However, this does not apply to all states, even those states whose energies are above the saddle point between the two protons (see figure 9.2 around $z = 50a.u.$) can be isolated to one proton or another, as shown in figures 9.3b and 9.3c.

We can see from this analysis that the simple binary picture of "ionized" or "not-ionized" is inaccurate. There are states that are bound above the ionization threshold—though they never will be observed after averaging over different proton configurations. Other states that are above, but still near the ionization threshold, can be isolated to just two protons and are not truly continuum states. One would have to categorize these different states as having properties of being bound, free, and quasi-bound. These quasi-bound states are extended but finite in size and decay to zero at large radii. In terms of modeling the continuum threshold, the most important element is the nearest neighbor, where quasi-bound states dominate that part of the spectrum.

Critique This method is a fantastic tool for gaining physical intuition of the process of continuum lowering and even obtaining environment-dependent wavefunctions. As great a tool as this is, I have lost the advantages of spherical symmetry to perform the electron broadening calculations developed in chapter 8 and in appendix C—which I will need in order to include exchange, something which has been established as being important for electron broadening. The loss of spherical symmetry means that the effects of exchange become much more difficult (and impractical) to evaluate.

9.3 Perturbation Theory

In order to use the accuracy of the electron-broadening model, while doing continuum lowering, I will be resorting to using matrix methods to diagonalize a state-vector Hamiltonian as described in appendix A. However, there are two approaches that one could take. The first is to use the formulae as presented in chapter 8 and evaluate the intermediate states at the unperturbed energy. The second is to calculate all possible transitions, then transform the basis set from one with spherical symmetry (i.e. using spherical harmonics) to one that does not, such as the parabolic solution to the Schrödinger equation (See Appendix D).

9.3.1 Matrix Elements in Spherical vs Parabolic Representation

In the spherical representation, the second-order broadening term is defined as

$$M^{(2)} = \left\langle 2s\ \vec{k}\,|V|\,2p\ \vec{k}'\right\rangle \left\langle 2p\ \vec{k}'\,|V|\,2s\ \vec{k}\right\rangle$$

In a parabolic representation, a parabolic state can be defined as a linear combination of spherical states. For $n = 2$, the parabolic states are defined:

$$\begin{aligned}
|210\rangle &= \frac{1}{\sqrt{2}}|2s0\rangle + \frac{1}{\sqrt{2.}}|2p0\rangle \\
|2-10\rangle &= \frac{1}{\sqrt{2}}|2s0\rangle - \frac{1}{\sqrt{2.}}|2p0\rangle \\
|201\rangle &= |2p1\rangle \\
|20-1\rangle &= |2p-1\rangle.
\end{aligned}$$

Therefore to calculate the matrix elements of a parabolic state, such as that from a spherical case, the following terms must also be included

$$
\begin{aligned}
M^{(2)} &= \left\langle 210\ \vec{k}\,|V|\,210\ \vec{k}'\right\rangle \left\langle 210\ \vec{k}'\,|V|\,210\ \vec{k}\right\rangle \\
&= \frac{1}{2}\left\langle 2s0\ \vec{k}\,|V|\,2p0\ \vec{k}'\right\rangle \left\langle 2p0\ \vec{k}'\,|V|\,2s0\ \vec{k}\right\rangle \\
&\quad + \frac{1}{2}\left\langle 2s0\ \vec{k}\,|V|\,2p0\ \vec{k}'\right\rangle \left\langle 2s0\ \vec{k}'\,|V|\,2p0\ \vec{k}\right\rangle
\end{aligned}
$$

which includes an additional term that does *not* conserve the l quantum number. The m symmetry, on the other hand is still preserved in this representation.

9.3.2 Line Broadening calculated with Spherical and Parabolic Representations

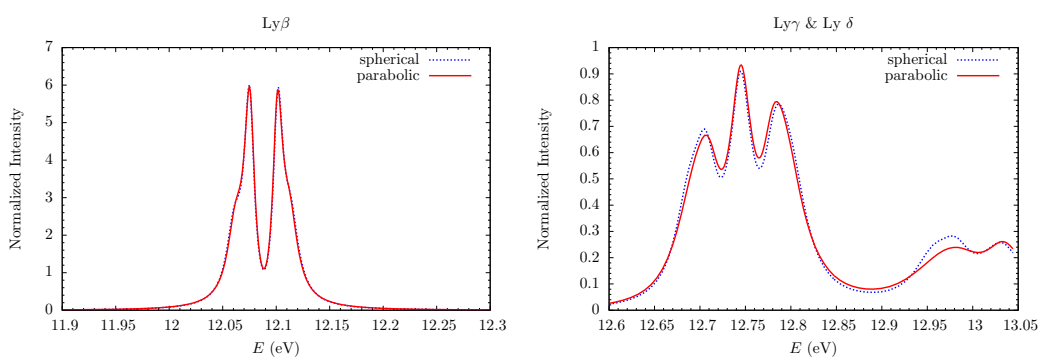

(a) Lyβ line at a single value of electric field. (b) Lyγ and Lyδ at single value of electric field.

Figure 9.4: This comparison of methods is to verify that for small perturbations, then the spherical and parabolic representations give the same answer (Lyβ in 9.4a). Comparison 9.4b shows that for high-values of electric field, where lines start to overlap, that differences start to emerge between calculations between the two representations .

In the low-perturbation limit, calculations using either the spherical and parabolic representations should give similar line shapes. Figure 9.4a shows the Lyman β line at a single value of ion microfield and here we can see that there are marginal differences between the two models. However, in figure 9.4b, the differences are more pronounced. This mainly

has to do with the fact that inelastic collisions are starting to dominate the interactions. Also the energy levels have shifted so much from their original energies that the way they interact with the nearby levels changes. This becomes apparent as an increase in the asymmetry of both the Lyγ and Lyδ lines in figure 9.4b.

If the calculation were performed using a spherical representation, then transforming to a parabolic representation (Eq D.3) makes this calculation fairly simple. Though the number of matrix elements needed for calculation are increased, this additional step, while requiring increased computation time, results in a substantial increase in accuracy. One major difference is the prominence of the features near the continuum. In a spherical basis, the last member of the series is broadened to the point that it is more or less washed out. However, when the parabolic basis is used, the features are more prominent and a distinct continuum begins to appear.

9.3.3 When is Penetration Important?

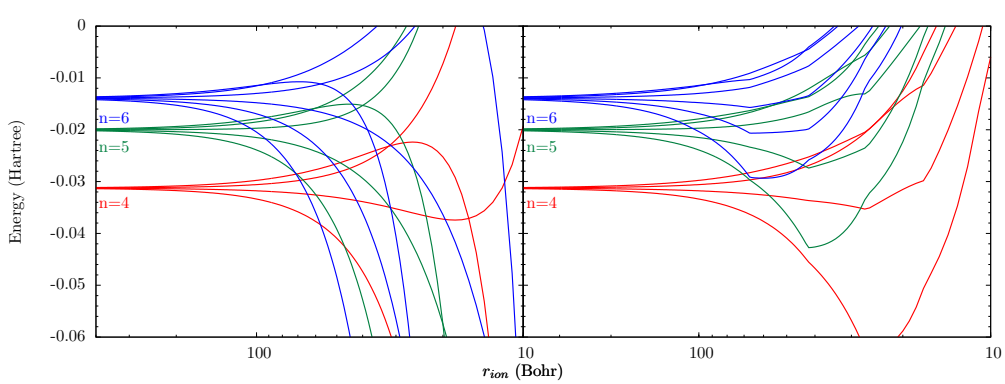

Figure 9.5: Eigenvalue evolution of various states of hydrogen due to a single perturber as a function of that perturber's distance from the nucleus. The right panel ignores penetration, the left panel includes penetration. Penetration reduces the size of the perturbation and creates a blue shift.

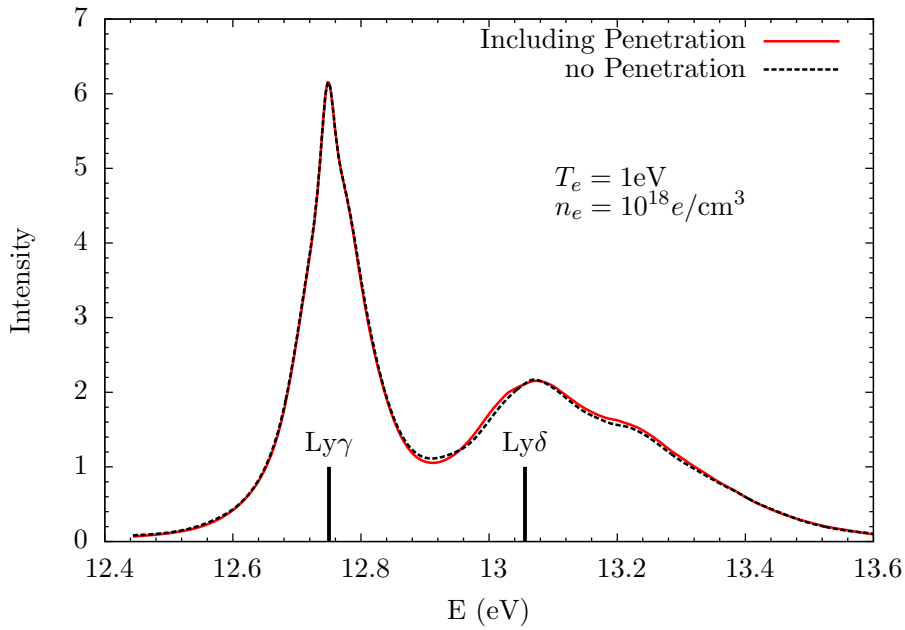

Figure 9.6: Comparison of spectra with and without penetration. Here we can see that for these conditions, the effects of penetration are fairly minor.

This thesis has been focused principally on a more accurate treatment of the interaction of the perturbing-particle and the radiator. One question I would want to examine is when penetration is important. Figure 9.5 illustrates this by plotting the eigenvalue evolution of various n states due to a single perturber as a function of that perturber's distance from the nucleus. The left-panel of figure 9.5 has no penetrating collisions, while the right panel properly includes penetration. A major difference is that the eigenvalues reach a maximum ΔE from the line center and reverse direction. Also, when the perturber is inside the radius of the wavefunction of a state, there is an upturn of the eigenvalues due to monopolar interactions. We see that the effects of penetrating collisions do not happen when n and $n+1$ cross, but at much stronger interactions than that. From this plot, I can

expect the effects of penetration to be fairly minor, affecting the wing behavior more than the core structure.

Figure 9.6 compares high-density hydrogen plasma spectral models; one model includes penetration, while the other does not. As expected from figure 9.5, the differences between the calculation with ion penetration and the one without ion penetration are fairly minor. There is slight decrease in the opacity between Lyγ and Lyδ and we can see that the Lyδ line is slightly broader and the continuum level is slightly raised, but these changes are less than the 10% level.

9.3.4 Convergence

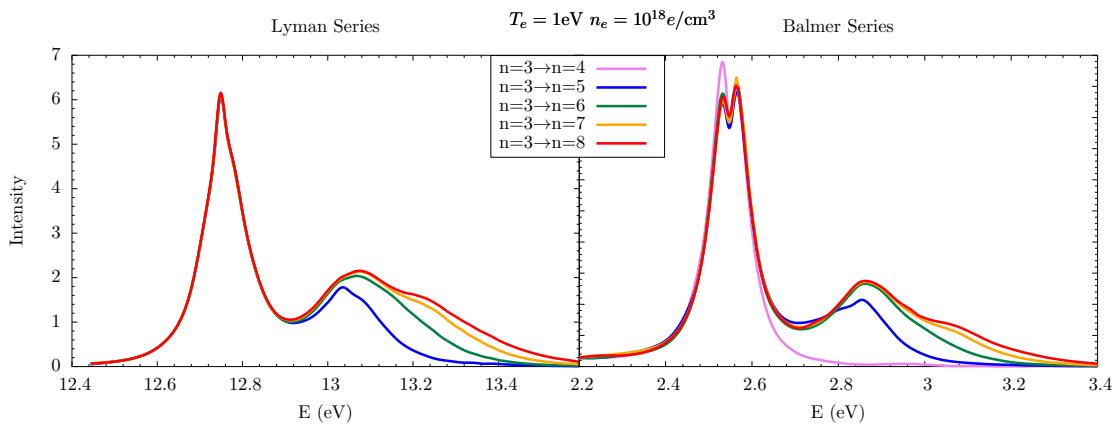

Figure 9.7: A convergence test of the continuum calculation for the Lyman (left) and the Balmer (right) series of neutral hydrogen at high density. The different lines do not denote the transition, rather they denote which states are included in the calculation; for example, the violet line includes states $n = 3$ and $n = 4$, while the blue line includes n=3,4, and 5, and so on for the other colors.

In these calculations, I have to make sure I have a suitable basis set to accurately model the changes in the line shape due to a strong perturbation by nearby protons; see appendix A, specifically the discussion in appendix 4.1. Figure 9.7 compares the different

spectral responses when including different numbers of states; the Inglis-Teller limit indicates that the $n = 5$ state is the last observable state at electron densities of $10^{18} e/\mathrm{cm}^3$.

For the conditions shown in figure 9.7, some level of convergence seems to have been obtained with the $n = 5$ level and the continuum level.

9.4 Comparison with Occupation Probability

I now want to compare these new calculations with experiments. Figure 9.8 compares this new calculation (dubbed "Neomorph") with the Wiese data; the only additional process included is the $n = 3$ bound-free opacity. Also shown in figure 9.8 are the line shape theories of Vidal et al. (1973) and Tremblay & Bergeron (2009)—hereafter VCS and TB, respectively—combined with the occupation probability formalism of Hummer & Mihalas (1988)—hereafter HM.

The Neomorph calculation shown in figure 9.8 includes off-diagonal electron broadening matrix elements with $\Delta n_{max} = 2$ and all off-diagonal elements of the ion perturbation. Only up to $n = 9$ states are included; computational limitations have prevented inclusion of higher-n states.

When VCS is combined with HM, the line intensity does not match the data, and the opacity between lines is also too large. The combination of TB with HM improves the opacity between lines (though the temperature had to be increased in order to fill in the windows), but the line widths are underestimated. Only the new calculation is able to reproduce the Hγ and Hδ widths and intensities, but due to an incomplete basis, the continuum level has not been matched.

Due to the numerical difficulties with such a large-scale calculation, this model is

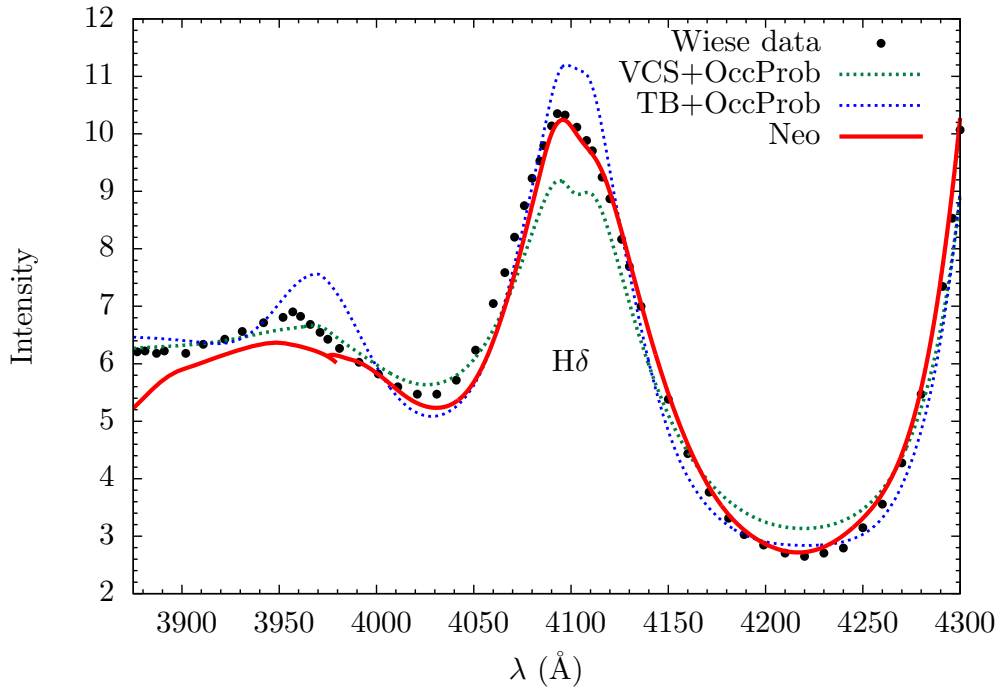

Figure 9.8: Comparison of the high-n lines of hydrogen as measured by the Wiese experiment ($T_e = 1eV$ and $n_e = 10^{17} e/\text{cm}^3$). The occupation probability with the VCS line shape overestimates the opacity between lines, but the TB09 profiles seem to do better, but underestimate the width of the line. Only Neomorph (this work) accurately matches both the line width and the continuum levels between lines.

not convenient for implementation in astrophysical studies. On the other hand, it can be used to calibrate a simpler theory, such as occupation probability formalism. In other words, we can choose an ionization criterion for occupation probability such that it can reproduce these new calculations. This exercise is outside the scope of this thesis.

Part IV

Implicatons and Conclusions

Chapter 10

Impact on White Dwarf Mass Determination

In no way are the full implications of this study presented in this thesis. However, there are some applications—in particular those with white dwarf stars—where we can begin to estimate some of the impacts of this work. First, we examined the importance of detailed balance in electron broadening. Next would be a better informed criteria for occupation probability.

I want to take a moment to note some differences in implementation of the final astrophysical model spectra. First, the tables by Vidal et al. (1973) and Tremblay & Bergeron (2009) are given in terms of a $\Delta\lambda$ and are assumed symmetric in wavelength. However, the broadening is mostly symmetric in energy. Due to the relationship between energy and frequency,

$$E = h\nu,$$

then the line shapes will also be mostly symmetric in frequency. Thanks to the courtesy of Dr. Ivan Hubeny, the model atmosphere code TLUSTY was modified to include asymmetric profiles and the input from the work of this thesis will be given in frequency space, a more natural set of units for these kinds of calculations.

10.1 Detailed Balance

In Appendix C, specifically Eq (C.11), there is a quantum-mechanical effect in spectral line broadening that has no classical analog. This is the evaluation of the frequency dependence of the electron broadening operator,

$$\frac{1}{\omega - L_0} = \frac{PV}{\omega - L_0} - i\pi\delta(\omega - L_0).$$

I want to focus specifically on the delta function, the imaginary part of the expression, which gives rise to widths. This delta function will be integrated over the different energies of the different free-electron states, giving the following evaluation for the imaginary part of the operator M

$$Im\{M^{(2)}\} \propto \int_0^\infty \int_0^\infty dk_1 dk_2 G(k_1, k_2)\delta(\Delta\omega - \frac{1}{2}k_2^2 + \frac{1}{2}k_1^2)e^{-\frac{1}{2}k_1^2/k_BT}, \tag{10.1}$$

where $G(k_1, k_2)$ contains all of the matrix element evaluations and the exponential is the thermal weighting factor. To evaluate positive values of $\Delta\omega$, one needs to integrate over k_2 first, which gives the following solution:

$$Im\{M^{(2)}\} \propto \int_0^\infty dk_1 \frac{G(k_1, \sqrt{k_1^2 + 2\Delta\omega})}{\sqrt{k_1^2 + 2\Delta\omega}} e^{-\frac{1}{2}k_1^2/k_BT}; \Delta\omega > 0. \tag{10.2}$$

Now, for the case of negative values of $\Delta\omega$, it would make sense to integrate over k_1. Because a delta function is an even function, the negative sign of the argument can be factored out and we arrive at the following expression:

$$Im\{M^{(2)}\} \propto \int_0^\infty dk_2 \frac{G(\sqrt{k_2^2 + 2|\Delta\omega|}, k_2)}{\sqrt{k_2^2 + 2|\Delta\omega|}} e^{-\frac{1}{2}k_2^2/k_BT} e^{-|\Delta\omega|/k_BT}; \Delta\omega < 0. \tag{10.3}$$

Now, this differs from the positive values for $Im\{M^{(2)}\}$ by a factor of $\exp\{-\Delta\omega/k_BT\}$. Physically, this is the result of detailed balance and that some free-electron states are not

available. The effect of this exponential damping factor can be seen in Figure 10.1, which showcases the Lyman α line of neutral hydrogen.

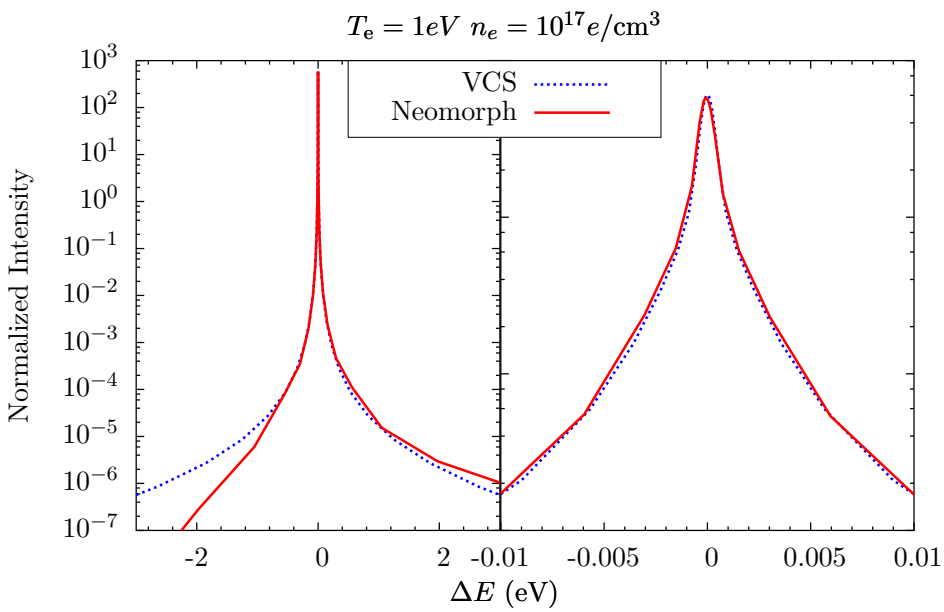

Figure 10.1: The effect of detailed balance on the Lyα line of hydrogen for $T_e = 0.5eV$ and $n_e = 10^{17} e/\mathrm{cm}^3$, which is a typical density for white dwarf photospheres. The panel on the left shows an extended frequency range, while the right panel zooms into the core, showing that the profiles are nearly the same in the middle. At this low temperature, we see substantial decrease of the Lyα red wing. This decrease in the opacity can be important in determining opacity because Lyα is the dominant opacity source in the atmosphere.

Figures 10.2 and 10.3 demonstrate the differences in the model atmosphere, just from switching the Lyα profiles. The first thing that jumps out is the increase of the continuum level between Lyα (at 10.2eV) and Lyβ (at 12.08eV); this is likely due to using frequency-symmetric profiles. However, there is a systematic decrease in the continuum level—even in the visible range. It seems that this decrease in the continuum level decreases with temperature, where in Figure 10.3 it is seen that the differences in continuum between

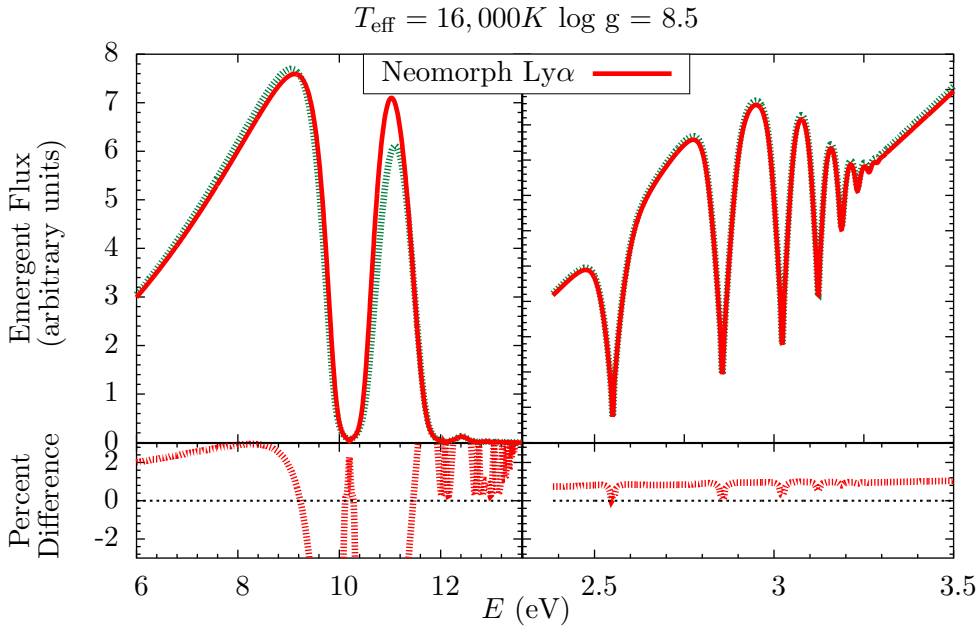

Figure 10.2: Synthetic spectrum of a white dwarf star at $T_{\rm eff} = 16,000K$ and log g =8.5. The left panel focuses on the Lyman series, while the right panel shows the Balmer series—what is in the visible spectrum and where most analysis is done. Green lines indicate using Tremblay & Bergeron (2009) profiles, while the red has only the Lyα line switched out for the new calculations here. The percent difference between the two calculations are shown on the bottom panel.

the two models are nearly non-existent.

However, these results are not because of detailed balance, these are simply the differences between the models. When I switched the blue and red files for the input, there was very little difference between the modeled spectra. So we can say with confidence that detailed balance does not matter in white dwarf spectral models above effective temperatures of 16,000K; the differences we are seeing are simply due to fundamental differences in the models. Quantifying exactly how this will change the log g and $T_{\rm eff}$ determinations is beyond the scope of this work due to the many intricacies involved in the fitting method.

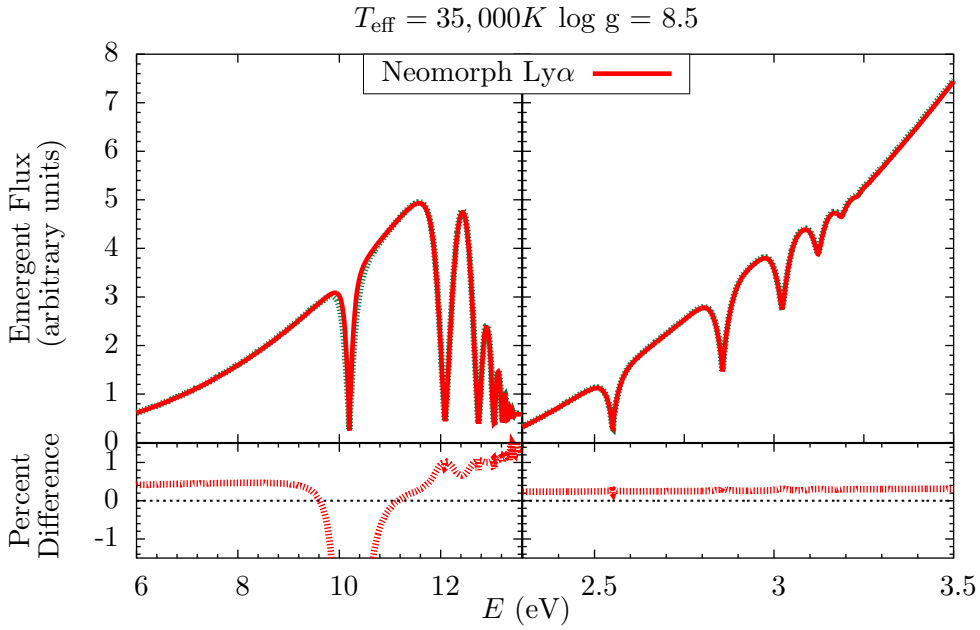

Figure 10.3: Same as Fig 10.2, but for $T_{\rm eff}$ = 40,000K. The differences between these two models are much reduced where the only discrepancy is near the middle of the Lyα profile.

The changes in the visible part of the spectrum are of order the same magnitude as those changes going from Vidal et al. (1973) to Tremblay & Bergeron (2009) models: of order 5% changes in gravity.

There is a systematic change in the location of the continuum of the model white dwarf atmosphere across the entire visible range of the spectrum due to proper treatment of the line asymmetry. White dwarfs are often used as spectroscopic standards to calibrate spectra of other objects. If the flux of the white-dwarf atmosphere model is decreased, then it affects the calibration of other stars; these changes are 1% for the 10,000K case and 0.3% in the 40,000K case and could be potentially larger for stars with temperatures below 10,000K.

10.2 Modified Occupation Probability

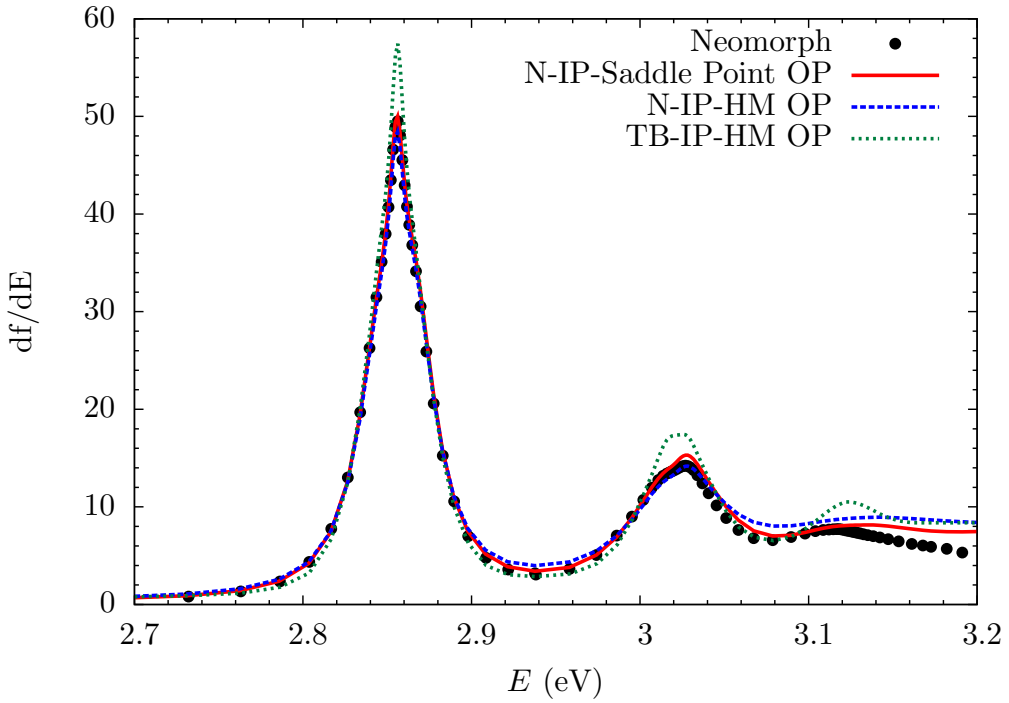

Figure 10.4: Comparisons of different occupation probability models with the most detailed Neomorph calculation. The red line is with individual profiles (IP) of Neomorph (N), with a saddle-point criteria; the dashed-blue line is the same as the red, but with Hummer & Mihalas (HM) criteria; and the green-dotted line is the Tremblay & Bergeron profiles (TB) with HM criteria.

In chapter 9, I introduce Neomorph, which is a calculation that takes into account the penetrating collisions of both ions and electrons. Rather than use an ad-hoc ionization criteria, I include the matrix elements between as many energy levels as is computationally possible. While this will be more accurate than using the occupation probability, it is impractical to make a grid from this method: the calculations are extremely expensive, and occupation probability is already incorporated in atmosphere models. I therefore want to modify the current occupation probability to better match the detailed calculation, for it

compared best with the experiment in figure 9.8.

I will not spend time trying to find the optimum calculation, but will simply use another simpler option: the saddle point criteria. In figure 10.4, I compare past methods with the most detailed calculation (Neomorph) at typical white dwarf conditions. In dots is the Neomorph calculation, while solid red is with individual Neomorph profiles with the saddle point (figure 9.1 in chapter 9). Dotted-blue lines indicate Hummer & Mihalas (HM) criteria for occupation probability, but with Neomorph profiles, while the dotted-green lines show the same criteria for the occupation probability, but with the Tremblay & Bergeron (TB) profiles. In this case, the saddle-point criteria agrees better with the Neomorph calculation modeling the intensity of Hγ and Hδ line and the flux between the lines than the HM criteria. The TB profiles slightly under-predict the intensity between lines, and over-predicts the core intensity and under-predicts the line wings compared to Neomorph. At this point, I would say that the saddle-point theory does better for lines below the continuum (modeling lines) but does worse right at the continuum threshold.

In figure 10.5, I compare the measured Sirius B spectrum with three calculations by reduced χ^2 fitting; the three models are: Vidal, Cooper, & Smith (VCS) profiles with HM, TB with HM, and Xenomorph (chapter 7 simulation calculation for Hβ and Hγ) with the saddle-point occupation probability criteria. The fits are all good. This is similar to the fits of data in chapter 7—but I want to emphasize that small χ^2 is not a guarantee of correct interpretation of data. Only with independent mass determination can we verify models. Bond et al. (2017), using HST astrometry, measured the orbit of Sirius B and determined a Keplerian gravity of 8.629. The spectroscopic fit, using TB profiles was determined to be 8.59, over two sigma disagreement from the measurement. When I re-did the fits, the TB

atmosphere was slightly higher, but still under the Keplerian gravity, beyond the error bars. But when I used the saddle-point criteria with *Xenomorph* and VCS, then the fitted log g was 8.635, which is within the one-sigma errors.

This agreement in log g with data and spectroscopy does not mean that the saddle-point is the correct theory, but it does mean that more work is needed and that the HM criteria is not as accurate and TB, by extension is also not as accurate. Since the occupation probability formalism is used universally in atmosphere models, then a practical course forward would be to modify the theory, rather than to insert the complicated, time-consuming calculations of chapters 8 and 9. This is not to say that these calculations are for naught, these extremely detailed calculations can inform the modification of the occupation probability models.

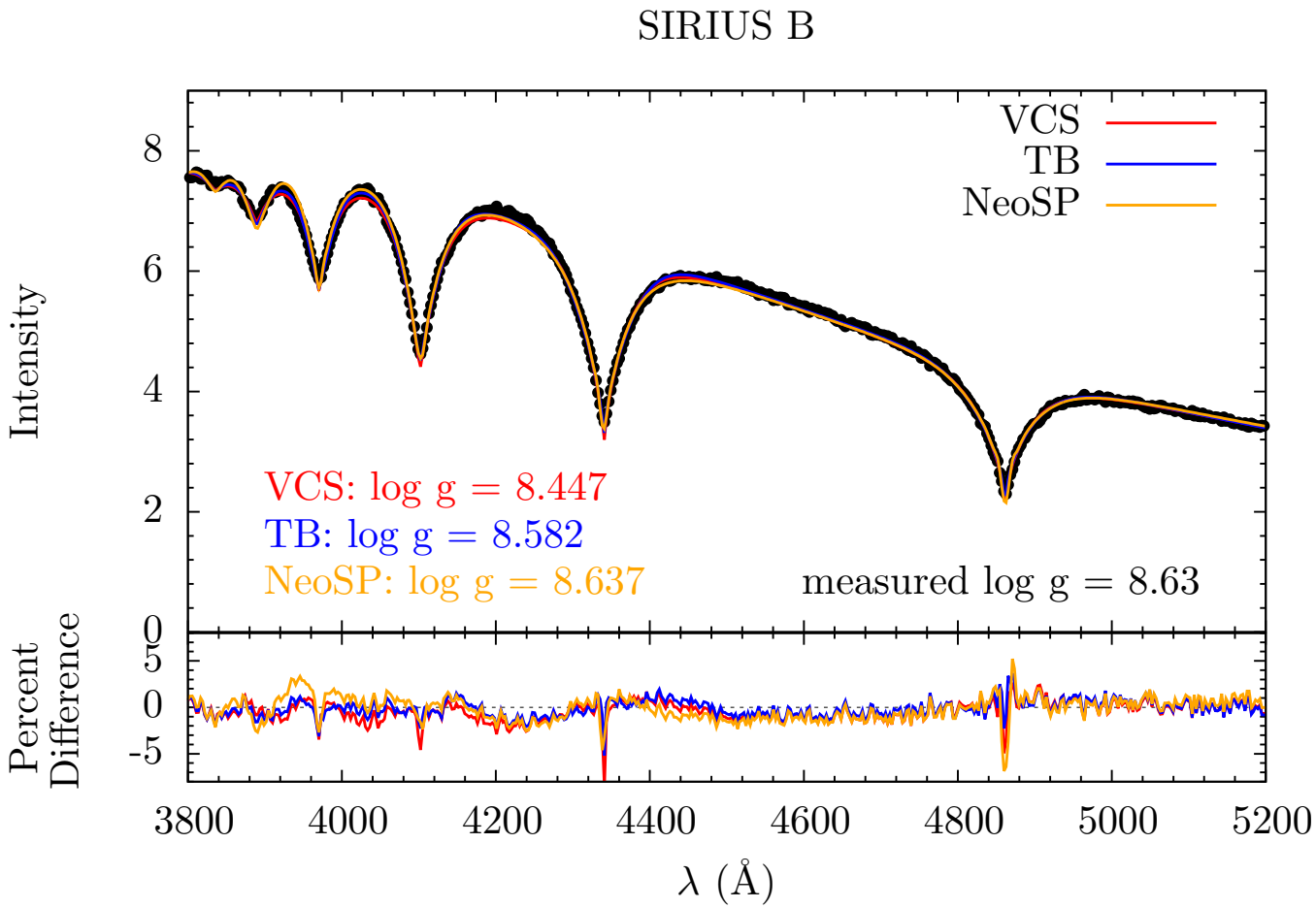

Figure 10.5: Comparison with the different line-shape theories and occupation probability criteria. Differences in gravity can vary substantially. The Keplerian log g is determined to be 8.629±0.007, which means that the only model to match this is the VCS/Xenomorph calculation with the saddle-point occupation probability criteria.

Chapter 11

Conclusions

Accurate models of spectral line broadening are important in many applications. The accuracy of these models rests largely on the approximations used for the interaction between plasma and radiating atom. It is common practice to use a low-density approximation where the plasma particles are always outside of the radiator and only the second term of the Taylor series of the Coulomb interaction is retained; this is known as the dipole approximation. The goal of this thesis is to more accurately model the interaction, by using a better approximation for the Coulomb interaction.

First, I investigated how the terms beyond dipole affect the line shape and at what conditions they become important. Second, I investigated the proper treatment of penetrating collisions; in the dipole approximation a strong collision cutoff is often employed to treat the effects of penetration; here I explicitly treat penetrating collisions and the various interactions that occur as a result. For ions, this is fairly straightforward, because ions can be treated classically, to good approximation, and are a different species than the atomic electron. However, for electrons, this interaction is more complicated: detailed quantum motion should be taken into account explicitly and certain interactions, such as exchange effects—which happen when identical particles interact—become important.

This thesis makes dramatic improvements in the interaction potential, although this is in no way the final set of calculations.

11.1 Multipoles

In chapter 7, I explored the higher-order multipole moments in the Coulomb interaction potential between the radiator and the perturbing particles, focusing on their effect on line shapes. While this is important for all line-shape theory, I focused on the hydrogen Balmer β line ($n = 4 \rightarrow 2$) due to its use as an astrophysical and laboratory diagnostic (Falcon et al., 2015). This is the first line-shape calculation to include higher-order multipole moments from both ions and electrons in the plasma; some past calculations have evaluated the ion quadrupole term or the electron quadrupole term, but not both. In calculations of the asymmetry of the Hβ line, the quadrupole term due to the ions is often included while the quadrupole term due to the electrons is usually neglected. I showed that including just the ions in the quadrupole calculation results in greater disagreement with measurement, while including quadrupole contributions from *both* ions and an electrons brings the asymmetry into agreement with data. I also studied the convergence of the line shapes from using the higher-order multipole moments; at least the quadrupole term should be included for two percent accuracy in the line shape.

The plasma conditions of laboratory experiments are often determined by fitting a theoretical profile to the measure spectrum. If I assume that the density inferred by χ^2 fitting line-shape profile that includes up to the sedecapole (4th-order) term is correct, then the fits using profiles only up to the dipole term results in errors in density greater than 10%. Fits of profiles that include up to the quadrupole term, are in agreement with the sedecapole profile within 2%, even at densities up to to the Inglis-Teller limit of the Hβ line ($\sim 10^{19}$ e/cc). The line-shape inaccuracy due to omitting the quadrupole terms would cause one to underestimate the density inferred from a measured spectrum by $\sim$12% even

at a density as low as 10% of its Inglis-Teller limit. While we focus on the Hβ line-shape calculation, similar impact is expected from other lines.

I therefore find that it is necessary to include up to at least the quadrupole terms due to *both* the ions and electrons for accurate line-shape calculations and accurate electron-density diagnostics.

11.2 Penetrating Collisions

In chapters 8 and 9, the effects of penetrating collisions were examined for electrons and ions, respectively.

11.2.1 Electrons

Past quantum calculations that include penetration do exist, but they are limited in accuracy since they do not include the physical indistinguishability of the electrons. As a result these calculations are not able to provide reliable electron broadening for neutral hydrogen. Here, I have incorporated the effects of exchange, which resolves the discrepancy between quantum calculations and semi-classical calculations for neutral radiators. I have also investigated the importance of a term present in the original relaxation theory derivation, but has been ignored since the late sixties. This missing term, which I have called the correlated collision term, has little-to-no impact on neutral hydrogen and provides a modest broadening of spectral lines of highly-charged radiators. The accuracy of this new theory for neutral radiators is verified with the comparison with semi-classical calculations—which have already been benchmarked against experiment. These calculations, however disagree with semi-classical calculations for charged radiators—where few such benchmark experiments exists. Comparison with experimental measurements of the He^+ Balmer γ line shows

that semi-classical calculations are too wide while this new model matches the width fairly well.

11.2.2 Ions

Penetrating collisions due to ions seem to be relatively unimportant in the core of the line. When the ions are close enough where penetration becomes important, the level splitting is large enough for energies of one state to cross with that of another state. This therefore means that only for large detunings from the line center does penetration become important. Penetration due to ions is important for the opacity between lines and setting the continuum level of the spectra.

Combining an accurate interaction potential with an expanded basis set, I can accurately calculate the merging of lines into a continuum.

11.3 Errors & Completeness

It would be worthwhile to explore the error estimates in spectral line broadening. We will not evaluate the actual size of the errors for these calculations, for there is an ambiguity on how to actually quantify the errors. The spectral line shape workshops (SLSP Stambulchik, 2013; Ferri et al., 2014; Alexiou et al., 2014; Stambulchik et al., 2014) have begun to address these issues.

Errors could result from implementation. For example, I was able to reproduce the Lyα calculation of Woltz & Hooper (1984), but unable to reproduce the Lyβ or Lyγ lines. The code used for the Woltz & Hooper (1984) no longer exists and their possible implementation errors cannot be examined. However, I was able to reproduce the distorted-

wave calculation of Kepple (also presented in Woltz & Hooper, 1984).

Other errors would fall under the category of completeness due to the fact that no one calculation is complete and contains all the physical effects associated with spectral line broadening. For example, calculations performed using the dipole approximation are not complete in that they ignore penetrating collisions and gradients in the plasma field. I have made an effort here to address the errors in this approximation, but the work presented here is in no way complete. The evaluation of the collision operator is an approximation and the effects of multiple collisions are not considered at all. This is not uncommon, since all semi-analytic models ignore the effects of multiple collisions; only simulations can handle this effect. Also, simulations have no treatment of quantum effects, though they can treat overlapping collisions with ease.

11.4 Future Work

There are many areas where spectral line broadening can be improved and these improvements will be more important at lower temperatures and higher densities. One of the most important things that should be done is an exact evaluation of the collision operator, rather than using a Taylor expansion. Previous calculations which have treated the collision operator to all order usually give up certain information, such as the frequency dependence. Such calculations would likely be limited to simple systems and require some clever programming and some large computing power. This thesis has also completely neglected the treatment of multiple collision, where two electrons impact the radiator simultaneously. Inclusion of multiple simultaneous collisions has been hypothesized to bring calculated and measured line shapes into closer agreement (S. Alexiou, private communication). The theory

presented here is limited to only one-electron systems; future work would be to extend this detailed treatment to multi-electron systems. This is no easy task, since treating two electrons in detail is already complicated enough, but it needs to be done. A goal for modeling multi-electron systems with this level of detail is to resolve the disagreement in measured and calculated line shapes of lithium-like isolated lines ($\Delta n = 0$ transitions).

This thesis makes some significant steps forward in improving spectral-line-broadening calculations and has impact on determining the surface conditions of white dwarf stars. In the course of my work, I have realized how many approximations are used in spectral line broadening and I have begun to examine the changes in the line-shape calculations when these approximations are removed. I hope that this work provides a foundation for those new to the field of spectral line broadening. I am excited to see future developments in these calculations.

Appendices

Appendix A

Matrix Mechanics

(or How to be a Quantum Mechanic)

These appendices assumes the reader has had some level of quantum mechanics, namely to have seen the Schrödinger equation. The goal of this appendix is to teach those who might be unfamiliar some of the tricks used for practical calculations of quantum mechanics.

At the very start of quantum mechanics, there were two lines of thinking: E. Schrödinger wanted to use solutions to his equation to describe everything in the system, while W. Heisenberg wanted to use matrix mechanics. The latter is easier conceptually since the formalism for linear algebra had already been fleshed out and could be easily implemented to solve quantum problems. The former is difficult because there are really only a hand full of problems that can be exactly solved by integrating Schrödinger's differential equation. One powerful tool that was developed was the use of perturbation theory. It boils down to this: use Schrödinger's equation to solve a problem that can be solved and then we can use matrix mechanics to solve for the rest; this is common practice in atomic physics and in spectral line shapes.

It is important to note that in Heisenberg's formalism that all quantum operators are linear operators, which mean that operators can be treated as a matrix, and the states can be treated as a vector.

A.1 Basics of Matrix Mechanics

I want to walk the reader through a simple example for those who are unfamiliar with the use of matrix mechanics, for those that are more familiar, they can skip this little section. First, one can devise a set of states as a vector, let's take the $n = 2$ states of hydrogen as an example,

$$\begin{array}{c} \begin{array}{ccc} n & l & m \end{array} \\ \begin{pmatrix} 2 & 0 & 0 \\ 2 & 1 & 0 \\ 2 & 1 & -1 \\ 2 & 1 & 1 \end{pmatrix} \end{array} \tag{A.1}$$

where the different numbers denote the principle quantum number (n), the orbital angular quantum number (l), and the magnetic quantum number (m). Therefore, if we wanted to prepare the atom in the $2s$ state (200), then we can write the vector as

$$|200\rangle = \begin{pmatrix} 1 \\ 0 \\ 0 \\ 0 \end{pmatrix}$$

and so on. We can even prepare the atom to be in a mixture of states, for example,

$$|\psi_{mixed}\rangle = \begin{pmatrix} 1/\sqrt{2} \\ 0 \\ -1/\sqrt{2} \\ 0 \end{pmatrix},$$

a phenomenon that occurs when the atom is subjected to an external electric field. The only requirement for the state vector is that it be normalized: the sum of the squares of the vector must equal unity. Hamiltonians can be written as a matrix such that for the isolated hydrogen atom, where the eigenvectors and eigenvalues are known, is

$$H|\psi\rangle = E|\psi\rangle,$$

where $|\psi\rangle$ is the Dirac notation for the state vector. Using this, then the Hamiltonian can be written as a matrix.

$$\begin{pmatrix} H_{11} & 0 & 0 & 0 \\ 0 & H_{22} & 0 & 0 \\ 0 & 0 & H_{33} & 0 \\ 0 & 0 & 0 & H_{44} \end{pmatrix}$$

Since the eigenvalues and eigenvectors are already known then the corresponding solutions are

$$E_1 \begin{pmatrix} 1 \\ 0 \\ 0 \\ 0 \end{pmatrix}; E_2 \begin{pmatrix} 0 \\ 1 \\ 0 \\ 0 \end{pmatrix}; E_3 \begin{pmatrix} 0 \\ 0 \\ 1 \\ 0 \end{pmatrix}; E_4 \begin{pmatrix} 0 \\ 0 \\ 0 \\ 1 \end{pmatrix}.$$

The real challenge starts when the wavefunction that are sought are not known, i.e. no easy solution to the Schrödinger exists. For example, when a constant electric field is applied on the atom, then the Hamiltonian has off-diagonal elements,

$$\begin{pmatrix} H_{11} & V_{12} & 0 & 0 \\ V_{21} & H_{22} & 0 & 0 \\ 0 & 0 & H_{33} & 0 \\ 0 & 0 & 0 & H_{44} \end{pmatrix}$$

where V_{12} connects states 1 and 2, in the case of the $n = 2$ states, then this would connect the 200 state to the 210 state. In general, there is no analytical solution to this generalized Hamiltonian, so a numerical method of diagonalizing the Hamiltonian is required.

Because of the strong connection between quantum mechanics and linear algebra, then it is conceptually simple to evaluate products of operators. Any product of operators can be evaluated simply through matrix multiplication

$$\langle \psi | AB | \psi' \rangle = \sum_{\psi''} \langle \psi | A | \psi'' \rangle \langle \psi'' | B | \psi' \rangle . \tag{A.2}$$

But if the basis set is over a set of continuous states, then the sum is replaced by an integral:

$$\langle \phi | AB | \phi' \rangle = \int d\phi'' \langle \phi | A | \phi'' \rangle \langle \phi'' | B | \phi' \rangle .. \tag{A.3}$$

When using Liouville representation in matrix mechanics, then the operator A can be mapped onto a vector, where

$$A = \begin{pmatrix} A_{11} & A_{12} & A_{13} \\ A_{21} & A_{22} & A_{23} \\ A_{31} & A_{32} & A_{33} \end{pmatrix} \rightarrow \begin{pmatrix} A_{11} \\ A_{12} \\ A_{13} \\ A_{21} \\ A_{22} \\ \vdots \end{pmatrix} \tag{A.4}$$

then the Liouville operator can be written as an ordinary operator with four indices:

$$LA = \begin{pmatrix} L_{11;11} & L_{11;12} & L_{11;13} & L_{11;21} & \cdots \\ L_{12;11} & L_{12;12} & L_{12;13} & L_{12,21} & \cdots \\ L_{13;11} & L_{13;12} & L_{13;13} & L_{13;21} & \cdots \\ L_{21;11} & L_{21;12} & L_{21;13} & L_{21;21} & \cdots \\ \vdots & \vdots & \vdots & \vdots & \end{pmatrix} \begin{pmatrix} A_{11} \\ A_{12} \\ A_{13} \\ A_{21} \\ A_{22} \\ \vdots \end{pmatrix}. \tag{A.5}$$

A.2 Solving the Time-Dependent Schrödinger Equation and Matrix Diagonalization

For spectral line broadening, it is important to evaluate the time evolution of the system, since the Fourier transform of which dictates the spectral line shape (see chapter 3). If all the perturbations are time independent, then the solution to the time-dependent Schrödinger equation is known:

$$\begin{aligned} i\frac{d}{dt}\psi(t) &= H\psi(t) \\ &= [H_0 + V]\,\psi(t) \\ \psi(t) &= e^{-iHt}\psi(t=0). \end{aligned}$$

Sometimes, this time evolution is written as a single operator, $e^{-iHt} = U(t)$, the time evolution operator.

A.2.1 Evaluating the Matrix Exponential

If the Hamiltonian is diagonal (in a matrix representation), then direct evaluation of the matrix exponential is trivial,

$$e^{-iHt} = \begin{pmatrix} e^{-iH_{11}t} & 0 & 0 & 0 \\ 0 & e^{-iH_{22}t} & 0 & 0 \\ 0 & 0 & e^{-iH_{11}t} & 0 \\ 0 & 0 & 0 & e^{-iH_{44}t} \end{pmatrix}.$$

However, if there are off diagonal elements of the matrix,

$$\begin{pmatrix} H_{11} & V_{12} & 0 & 0 \\ V_{21} & H_{22} & 0 & 0 \\ 0 & 0 & H_{33} & 0 \\ 0 & 0 & 0 & H_{44} \end{pmatrix}$$

then evaluation of the matrix exponential requires a different technique. A Taylor expansion of the matrix exponential gives the following:

$$e^{-iHt} = 1 - iHt + \frac{1}{2!}(-iHt)^2 + \frac{1}{3!}(-iHt)^3 + \cdots,$$

but exactly evaluating this series is tedious and not practical. One possible method to evaluate this is to diagonalize the Hamiltonian. If one can define the Hamiltonian as

$$H = T^\dagger \begin{pmatrix} E_1 & 0 & 0 & 0 \\ 0 & E_2 & 0 & 0 \\ 0 & 0 & E_3 & 0 \\ 0 & 0 & 0 & E_4 \end{pmatrix} T$$

where the E's are the eigenvalue solutions and T is the eigenvector solution, then evaluation of the Taylor expansion becomes

$$e^{-iHt} = 1 - iT^\dagger ETt + \frac{1}{2!}T^\dagger ETT^\dagger ETt^2 + \frac{1}{3!} - iT^\dagger ETT^\dagger ETT^\dagger ETt^3 + \cdots.$$

By the definition of the diagonalization of a Hermitian matrix, the T matrix is unitary, i.e it has the property that $T^\dagger = T^{-1}$, therefore $T^\dagger T = 1$. The matrix exponential simplifies to

$$\begin{aligned} e^{-iHt} &= T^\dagger T - iT^\dagger ETt + \frac{1}{2!}T^\dagger E^2 Tt^2 + \frac{1}{3!} - iT^\dagger E^3 Tt^3 + \cdots \\ e^{-iHt} &= T^\dagger e^{-iEt} T \end{aligned}$$

The matrix exponential is a simple set of matrix multiplications:

$$e^{iHt} = T^\dagger \begin{pmatrix} e^{iE_1 t} & 0 & 0 & 0 \\ 0 & e^{iE_2 t} & 0 & 0 \\ 0 & 0 & e^{iE_3 t} & 0 \\ 0 & 0 & 0 & e^{iE_4 t} \end{pmatrix} T.$$

A.2.2 Time-Dependent Schrödinger Equation with Explicit Time Dependence

In some cases, such as those with a driving radiation field or a simulation with classical particles imposing a fluctuating electric field on the atom, the perturbing potential is variable with time,

$$H(t) = H_0 + V(t)$$

Then the time-dependent Schrödinger equation contains an explicit time dependence and a different method is required to solve for the time evolution operator,

$$i\frac{d}{dt}U(t) = H(t)U(t); \tag{A.6}$$

Solving this equation requires some kind of numerical integration techniques, such as a Runge-Kutta solver. The Runge-Kutta method can vary depending on what is appropriate. For line-broadening simulations, then this can be a stiff differential equation and any explicit method, such as Euler's method or RK4 is accurate only as long as the time step in the integration is small enough. Implicit Runge-Kutta methods (such as backwards Euler or implicit midstep) are more desirable for stiff differential equations since it relies on future information to solve for the next time step.

In my simulation, I choose time-steps that are small enough that the potential, V, is roughly time-independent over one time step. I have then chosen to use the matrix

diagonalization techniques above to evaluate the matrix exponential

$$U(t + \Delta t) \approx e^{iH(t)\Delta t} U(t). \tag{A.7}$$

Then the time-evolution of advancement is simply a matrix multiplication between the exponential Hamiltonian and the previous time-step.

A.3 Using Matrix Mechanics to Solve the Schrödinger Equation

For a select few cases, the Schrödinger equation,

$$-\frac{1}{2}\nabla^2\psi(r) + V(r)\psi(r) = E\psi(r) \tag{A.8}$$

is solvable by analytic techniques. In the case of the hydrogen atom, the potential is a spherically symmetric Coulomb operator ($V = z/r$). For the case of spherically symmetric potentials, the wavefunction can be separated into a radial solution and the angular wavefunction is the well-known spherical harmonics:

$$\psi(r, \theta, \phi) = R(r)Y_{lm} \tag{A.9}$$

where the spherical harmonics is the solution to the eigenvalue problem:

$$\left[\frac{1}{\sin\theta}\frac{\partial}{\partial\theta}\sin\theta\frac{\partial}{\partial\theta} + \frac{1}{\sin^2\theta}\frac{\partial^2}{\partial\phi^2}\right] Y_{lm} = l(l+1)Y_{lm}$$

Therefore, the solution of the radial hydrogen wavefunction is the solution to the following differential equation

$$-\frac{1}{r^2}\frac{d}{dr}r^2\frac{d}{dr}R(r) + \frac{l(l+1)}{r^2}R(r) - \frac{Z}{r}R(r) = ER(r).$$

This equation can be simplified further by defining a quantity

$$R(r) = \frac{1}{r}\hat{R}(r)$$

and the complicated differential is simplified to a relatively simple second-order differential equation.

$$-\frac{d^2}{dr^2}\hat{R}(r) + \frac{l(l+1)}{r^2}\hat{R}(r) - \frac{Z}{r}\hat{R}(r) = E\hat{R}(r). \tag{A.10}$$

There are several methods for solving this equation, there exist analytical methods that give formulae for the radial wavefunctions. The method I want to discuss is a numerical method of solving Eq (A.10).

There are many many methods for solving differential equations, the appropriate boundary conditions are needed. The most numerically stable method for solving Eq (A.10) is to numerical solve the eigenvalue problem.

I will define a state vector as a function of space, rather than as individual solutions to the Hamiltonian in Eq (A.1),

$$|\hat{R}(r)\rangle = \begin{pmatrix} R(\Delta r) \\ R(2\Delta r) \\ R(3\Delta r) \\ R(4\Delta r) \\ R(5\Delta r) \\ \vdots \end{pmatrix} \tag{A.11}$$

where Δr is the step in the spatial grid. The first challenge is how to write the operators in Eq (A.10).

First, the differential operator: a second-order derivative can be written as a finite difference,

$$\frac{d^2}{dr^2}\hat{R}(r) \approx \frac{1}{\Delta r}\left[\hat{R}(r-\Delta r) - 2\hat{R}(r) + \hat{R}(r+\Delta r)\right]. \tag{A.12}$$

A finite difference formula can be written as a matrix:

$$-\frac{d^2}{dr^2}|\hat{R}(r)\rangle = \frac{1}{\Delta r^2}\begin{pmatrix} 2 & -1 & 0 & 0 & 0 & \cdots \\ -1 & 2 & -1 & 0 & 0 & \cdots \\ 0 & -1 & 2 & -1 & 0 & \cdots \\ 0 & 0 & -1 & 2 & -1 & \cdots \\ 0 & 0 & 0 & -1 & 2 & \cdots \\ \vdots & \vdots & \vdots & \vdots & \vdots & \ddots \end{pmatrix}\begin{pmatrix} R(\Delta r) \\ R(2\Delta r) \\ R(3\Delta r) \\ R(4\Delta r) \\ R(5\Delta r) \\ \vdots \end{pmatrix} \tag{A.13}$$

The potential, $V(r)$ is a completely diagonal operator

$$V(r)|\hat{R}(r)\rangle = \begin{pmatrix} V(\Delta r) & 0 & 0 & 0 & 0 & \cdots \\ 0 & V(2\Delta r) & 0 & 0 & 0 & \cdots \\ 0 & 0 & V(3\Delta r) & 0 & 0 & \cdots \\ 0 & 0 & 0 & V(4\Delta r) & 0 & \cdots \\ 0 & 0 & 0 & 0 & V(5\Delta r) & \cdots \\ \vdots & \vdots & \vdots & \vdots & \vdots & \ddots \end{pmatrix}\begin{pmatrix} R(\Delta r) \\ R(2\Delta r) \\ R(3\Delta r) \\ R(4\Delta r) \\ R(5\Delta r) \\ \vdots \end{pmatrix}. \tag{A.14}$$

The eigenvalue solution of the matrix in the form of

$$-\frac{d^2}{dr^2} + V(r)$$

can be found by numerical diagonalization. In this method, then a wavefunction solution can be found for any potential.

Interestingly, this method actually satisfies the boundary conditions for bound states. It assumes that the wavefunction solution at $R(0) = 0$ and $R(r_{max}) = 0$ and therefore only finds solutions that satisfy this criteria.

A.3.1 Two-electron Solutions

This same logic can also be applied to two-electron systems. The differential operator is going to be much more complicated:

$$\left[\frac{d^2}{dr_1^2} + \frac{d^2}{dr_2^2}\right] R(r_1, r_2) \approx \frac{1}{\Delta r_1^2 \Delta r_2^2} \times$$
$$[4R(r_1, r_2) - R(r_1 + \Delta r_1, r_2) - R(r_1 - \Delta r_1, r_2) - R(r_1, r_2 + \Delta r_2) - R(r_1, r_2 - \Delta r_2)] \tag{A.15}$$

and a corresponding matrix must be constructed.

When I diagonalize this giant matrix with a V(r) that includes a Coulomb-repulsion term, then I can calculate the ground-state of helium within 2% with no iterative or approximate-field method.

A.3.2 Free-electron Solutions

For the case of free-electrons, then the eigenvalue is known and the appropriate wavefunction has to be found. Therefore, the eigenvalue is moved to the other side of the Schrödinger equation,

$$\left[\frac{d^2}{dr^2} - \frac{l(l+1)}{r^2} + \frac{Z}{r} + E\right] \hat{R}(r) = 0. \tag{A.16}$$

The matrix of E will be a defined as EI, where I is the identity matrix. Therefore, I need to solve for a system resembling $Ax = b$, where b is set to zero; this is a difficult system to solve. I realized a numerical trick for forcing a numerical matrix solver to solve for the operator ($A = H - E$), by setting the "b"-vector to zero except for the last element in the vector:

$$b = 0 = \begin{pmatrix} 0 \\ 0 \\ \vdots \\ 0 \\ 0 \\ 1 \end{pmatrix}. \tag{A.17}$$

The solutions to this equation correspond exactly with other methods, such as Numerov method.

A.3.3 Exchange

For two- or more-electron systems, the fundamental set of equation to be solved is the Hartree-Fock equation. This is an iterative method, where a guess is given for the

initial wavefunctions, then each electronic wavefunction is solved in the presence of the other electrons, then repeated. The effects of identical particle (i.e. exchange interactions) make the Hartree-Fock equations an integro-differential equation,

$$\left[-\frac{1}{2}\frac{d}{dr^2}+\frac{1}{2}\frac{l(l+1)}{r^2}-\frac{Z}{r}+\sum_{j\neq i}\sum_k\int_0^\infty dr_j\frac{r_<^k}{r_>^{k+1}}P_k(\cos\gamma_{ij})|\psi_j(r_j)|^2\right]\psi_i(r_i)=$$
$$E_i\psi_i(r_i)+\sum_{j\neq i}\psi_j(r_i)\sum_k\int_0^\infty dr_j\frac{r_<^k}{r_>^{k+1}}P_k(\cos\gamma_{ij})\psi_j^*(r_j)\psi_i(r_j)+\sum_{j\neq i}E_{ij} \quad \text{(A.18)}$$

Ordinarily, when these calculations are done, the exchange integral part of the differential equation is treated as an inhomogeneous part and is solved iteratively. In other words, just to do these calculations that two iterations are done: one on set of iterations to solve Eq (A.18) and another, where Eq (A.18) is solved multiple times.

With matrix methods, I can eliminate one of these iterations by writing the entire differential equation as a matrix. I have already written the terms on the right-hand side of Eq (A.18) as a matrix. Since I can write an integral as a sum, then the exchange term can also be written as a matrix:

$$\psi_j(r_i)\int_0^\infty dr_jV(r_i,r_j)\psi_j^*(r_j)\psi_i(r_j)\approx\psi_j(r_i)\Delta r\sum_j V(r_i,r_j)\psi_j^*(r_j)\psi_i(r_j)$$
$$\approx\Delta r\times$$
$$\begin{pmatrix}\psi_j(\Delta r)V(\Delta r,\Delta r)\psi_j^*(\Delta r) & \psi_j(\Delta r)V(\Delta r,2\Delta r)\psi_j^*(2\Delta r) & \cdots\\ \psi_j(2\Delta r)V(2\Delta r,\Delta r)\psi_j^*(\Delta r) & \psi_j(2\Delta r)V(2\Delta r,2\Delta r)\psi_j^*(2\Delta r) & \cdots\\ \psi_j(3\Delta r)V(3\Delta r,\Delta r)\psi_j^*(\Delta r) & \psi_j(3\Delta r)V(3\Delta r,2\Delta r)\psi_j^*(2\Delta r) & \cdots\\ \psi_j(4\Delta r)V(4\Delta r,\Delta r)\psi_j^*(\Delta r) & \psi_j(4\Delta r)V(4\Delta r,2\Delta r)\psi_j^*(2\Delta r) & \cdots\\ \psi_j(5\Delta r)V(5\Delta r,\Delta r)\psi_j^*(\Delta r) & \psi_j(5\Delta r)V(5\Delta r,2\Delta r)\psi_j^*(2\Delta r) & \cdots\\ \vdots & \vdots & \ddots\end{pmatrix}\begin{pmatrix}\psi_i(\Delta r)\\ \psi_i(2\Delta r)\\ \psi_i(3\Delta r)\\ \psi_i(4\Delta r)\\ \psi_i(5\Delta r)\\ \vdots\end{pmatrix}. \quad \text{(A.19)}$$

Appendix B

Wigner nj symbols

In this appendix, we will *list* the different identities that involves the nj symbols that are used for the derivation of angular matrix elements. I will not define the nj symbol, but simply show their usefulness and related them to each-other

B.1 3j Symbols

The derivation for the 3j symbol is shown in Cowan (1981) as a means of coupling the angular momenta together. The derivation is lengthy and complicated and I will not show it here. The coupling of angular momenta can be used as such,

$$|l_1 l_2 LM\rangle = \sum_{m_1 m_2} |l_1 l_2 m_1 m_2\rangle (-1)^{l_1 - l_2 + M} \sqrt{2L+1} \begin{pmatrix} l_1 & l_2 & L \\ m_1 & m_2 & -M \end{pmatrix}, \tag{B.1}$$

and likewise, one can de-couple the angular momenta via a transpose,

$$|l_1 l_2 m_1 m_2\rangle = \sum_{LM} |l_1 l_2 LM\rangle (-1)^{l_1 - l_2 + M} \sqrt{2L+1} \begin{pmatrix} l_1 & l_2 & L \\ m_1 & m_2 & -M \end{pmatrix}. \tag{B.2}$$

B.1.1 Symmetry

The interchange of any two columns of the 3j symbol result in a phase change,

$$\begin{pmatrix} j_1 & j_2 & j_3 \\ m_1 & m_2 & m_3 \end{pmatrix} = (-1)^{j_1+j_2+j_3} \begin{pmatrix} j_2 & j_1 & j_3 \\ m_2 & m_1 & m_3 \end{pmatrix}. \tag{B.3}$$

Negating the m_i results in the same phase change,

$$\begin{pmatrix} j_1 & j_2 & j_3 \\ m_1 & m_2 & m_3 \end{pmatrix} = (-1)^{j_1+j_2+j_3} \begin{pmatrix} j_1 & j_2 & j_3 \\ -m_1 & -m_2 & -m_3 \end{pmatrix}. \tag{B.4}$$

B.1.2 Sum Rules

The following sum rules apply due to the orthonormal set of the 3j symbols,

$$\sum_{JM} \begin{pmatrix} j_1 & j_2 & J \\ m_1 & m_2 & M \end{pmatrix} \begin{pmatrix} j_1 & j_2 & J \\ m_1' & m_2' & M \end{pmatrix} = \frac{\delta_{m_1 m_1'} \delta_{m_2 m_2'}}{2J+1} \tag{B.5}$$

$$\sum_{m_1 m_2} \begin{pmatrix} j_1 & j_2 & J \\ m_1 & m_2 & M \end{pmatrix} \begin{pmatrix} j_1 & j_2 & J' \\ m_1 & m_2 & M' \end{pmatrix} = \frac{\delta_{JJ'} \delta_{MM'}}{2J+1} \tag{B.6}$$

$$\sum_{m} (-1)^{j-m} \begin{pmatrix} j & j & J \\ m & -m & 0 \end{pmatrix} = \delta_{J0} \sqrt{2j+1} \tag{B.7}$$

B.1.3 Special Values

There are some 3j symbols that have simple analytic solutions,

$$\begin{pmatrix} j & j & 0 \\ m & -m & 0 \end{pmatrix} = (-1)^{j-m} \frac{1}{\sqrt{2j+1}} \tag{B.8}$$

B.1.4 Relationship to spherical harmonics

Products of spherical harmonics can be re-written as a sum over 3j symbols,

$$Y_{kq} Y_{lm} = \sum_{LM} (-1)^M \sqrt{\frac{(2L+1)(2k+1)(2l+1)}{4\pi}} \begin{pmatrix} L & k & l \\ 0 & 0 & 0 \end{pmatrix} \begin{pmatrix} L & k & l \\ -M & q & m \end{pmatrix} Y_{LM}; \tag{B.9}$$

this makes it incredibly useful for evaluating integrals that are the product of three spherical harmonics,

$$\int d\theta \, d\phi \, \sin(\theta) \; Y_{lm}^* Y_{kq} Y_{l'm'} = (-1)^m \sqrt{\frac{(2l+1)(2k+1)(2l'+1)}{4\pi}} \begin{pmatrix} l & k & l' \\ 0 & 0 & 0 \end{pmatrix} \begin{pmatrix} l & k & l' \\ -m & q & m' \end{pmatrix}. \tag{B.10}$$

B.2 6j Symbols

The 6j symbol is the result product of four 3j symbols where a sum over all m is performed,

$$\begin{Bmatrix} j_1 & j_2 & j_3 \\ l_1 & l_2 & l_3 \end{Bmatrix} = \sum_{m,m'} (-1)^{l_1+m_1'+l_2+m_2'+l_3+m_3'} \begin{pmatrix} j_1 & j_2 & j_3 \\ m_1 & m_2 & m_3 \end{pmatrix} \times \\ \begin{pmatrix} j_1 & l_2 & l_3 \\ m_1 & m_2' & -m_3' \end{pmatrix} \begin{pmatrix} l_1 & j_2 & l_3 \\ -m_1' & m_2 & m_3' \end{pmatrix} \begin{pmatrix} l_1 & l_2 & j_3 \\ m_1' & -m_2' & m_3 \end{pmatrix}. \quad \text{(B.11)}$$

The 6j symbol can also be defined in an alternate way,

$$\begin{pmatrix} j_1 & j_2 & j_3 \\ m_1 & m_2 & m_3 \end{pmatrix} \begin{Bmatrix} j_1 & j_2 & j_3 \\ l_1 & l_2 & l_3 \end{Bmatrix} = \sum_{m'} (-1)^{l_1+m_1'+l_2+m_2'+l_3+m_3'} \times \\ \begin{pmatrix} j_1 & l_2 & l_3 \\ m_1 & m_2' & -m_3' \end{pmatrix} \begin{pmatrix} l_1 & j_2 & l_3 \\ -m_1' & m_2 & m_3' \end{pmatrix} \begin{pmatrix} l_1 & l_2 & j_3 \\ m_1' & -m_2' & m_3 \end{pmatrix}. \quad \text{(B.12)}$$

B.2.1 Symmetry

The 6j symbol is unchanged if any two columns are interchanged,

$$\begin{Bmatrix} j_1 & j_2 & j_3 \\ l_1 & l_2 & l_3 \end{Bmatrix} = \begin{Bmatrix} j_2 & j_1 & j_3 \\ l_2 & l_1 & l_3 \end{Bmatrix} \quad \text{(B.13)}$$

or if any two top two numbers are switched with its corresponding bottom number,

$$\begin{Bmatrix} j_1 & j_2 & j_3 \\ l_1 & l_2 & l_3 \end{Bmatrix} = \begin{Bmatrix} l_1 & l_2 & j_3 \\ j_1 & j_2 & l_3 \end{Bmatrix}. \quad \text{(B.14)}$$

B.2.2 Sum rules

The 6j symbols also create an orthonormal set such that,

$$\sum_J (2J+1) \begin{Bmatrix} j_1 & j_2 & J \\ l_1 & l_2 & l_3 \end{Bmatrix} \begin{Bmatrix} j_1 & j_2 & J \\ l_1 & l_2 & l_3' \end{Bmatrix} = \frac{\delta_{l_3,l_3'}}{2l_3+1}. \quad \text{(B.15)}$$

The result in Eq (B.15) can simplify these sums,

$$\sum_J (-1)^{J+k+k'} \begin{Bmatrix} j_1 & j_2 & J \\ j_3 & j_4 & k \end{Bmatrix} \begin{Bmatrix} j_1 & j_2 & J \\ j_4 & j_3 & k' \end{Bmatrix} = \begin{Bmatrix} j_1 & j_4 & k \\ j_2 & j_3 & k' \end{Bmatrix} \tag{B.16}$$

$$\sum_J (-1)^{J} \begin{Bmatrix} j_1 & j_1' & J \\ j_2' & j_2 & j_3 \end{Bmatrix} \begin{Bmatrix} l_3 & l_3' & J \\ j_1' & j_1 & l_2 \end{Bmatrix} \begin{Bmatrix} l_3 & l_3' & J \\ j_2' & j_2 & l_1 \end{Bmatrix} =$$

$$(-1)^{j_1+j_2+j_3+j_1'+j_2'+j_3'+l_1+l_2+l_3+l_3'} \begin{Bmatrix} j_1 & j_2 & j_3 \\ l_1 & l_2 & l_3 \end{Bmatrix} \begin{Bmatrix} j_1' & j_2' & j_3 \\ l_1 & l_2 & l_3' \end{Bmatrix}. \tag{B.17}$$

B.3 9j symbol

Unlike the 3j and the 6j symbols, the 9j symbol does not have an explicit form based on sums over factorials; instead, the 9j symbol can only be built up from sums over 3j symbols and 6j symbols,

$$\begin{Bmatrix} j_{11} & j_{12} & j_{13} \\ j_{21} & j_{22} & j_{23} \\ j_{31} & j_{32} & j_{33} \end{Bmatrix} = \sum_{allm} \begin{pmatrix} j_{11} & j_{12} & j_{13} \\ m_{11} & m_{12} & m_{13} \end{pmatrix} \begin{pmatrix} j_{21} & j_{22} & j_{23} \\ m_{21} & m_{22} & m_{23} \end{pmatrix} \begin{pmatrix} j_{31} & j_{32} & j_{33} \\ m_{31} & m_{32} & m_{33} \end{pmatrix} \times$$

$$\begin{pmatrix} j_{11} & j_{21} & j_{31} \\ m_{11} & m_{21} & m_{31} \end{pmatrix} \begin{pmatrix} j_{12} & j_{22} & j_{32} \\ m_{12} & m_{22} & m_{32} \end{pmatrix} \begin{pmatrix} j_{13} & j_{23} & j_{33} \\ m_{13} & m_{23} & m_{33} \end{pmatrix} \tag{B.18}$$

$$= \sum_J (-1)^{2J} (2J+1) \begin{Bmatrix} j_{11} & j_{21} & j_{31} \\ j_{32} & j_{33} & J \end{Bmatrix} \begin{Bmatrix} j_{12} & j_{22} & j_{32} \\ j_{21} & J & j_{23} \end{Bmatrix} \times$$

$$\begin{Bmatrix} j_{13} & j_{23} & j_{33} \\ J & j_{11} & j_{12} \end{Bmatrix} \tag{B.19}$$

I will only show one relationship of the 9j symbol because it is the only one used in this thesis,

$$\sum_J (2J+1) \begin{Bmatrix} j_{11} & j_{12} & J \\ j_{21} & j_{22} & j_{23} \\ j_{31} & j_{32} & j_{33} \end{Bmatrix} \begin{Bmatrix} j_{11} & j_{12} & J \\ j_{23} & j_{33} & j \end{Bmatrix} =$$

$$(-1)^{2j} \begin{Bmatrix} j_{21} & j_{22} & j_{23} \\ j_{12} & j & j_{32} \end{Bmatrix} \begin{Bmatrix} j_{31} & j_{32} & j_{33} \\ j & j_{11} & j_{21} \end{Bmatrix}. \tag{B.20}$$

These relationships will be of great advantage in the evaluation of spherical integrals.

Appendix C

Calculational Details of Electron Broadening

This appendix explains some additional background and details necessary for the understanding of chapter 8. Because electron scattering is closely related to line broadening (Baranger, 1958c,b,a; Griem et al., 1959; Fano, 1963; Griem, 1974; Griem et al., 1997), the first part of this section will introduce some of the concepts. The next section will explicitly derive the relaxation theory line broadening operator and some of its properties. Lastly, I will show the implementation details of the theory used in chapter 8, discussing the evaluation of the thermal average and the angular integrals needed.

C.1 The "T"-matrix

In the early line-shape papers (Baranger, 1958c; Kolb & Griem, 1958; Fano, 1963), correspondence was established between the line broadening operator and the scattering "T"-matrix, or the "S"-matrix.

In scattering theory, the incoming wavefunction is defined as an incoming plane-wave (along the z-direction) and an outgoing scattering wave (this process can also be written in reverse),

$$\phi^{+}(\vec{r}_p) \approx e^{ikz_p} + f(\theta_p)\frac{e^{ikr_p}}{r_p}, \tag{C.1}$$

where $f(\theta)$ is the defined as the scattering amplitude. Eq (C.1) is valid for distances large compared to the target off of which the electron is scattering.

There are two methods for solving for the scattering amplitude: finding phase shifts and the Born approximation; we will concern ourselves with the Born approximation since it has direct connection with the Relaxation theory of Fano. The solution to the free electron scattering off of some arbitrary potential obeys the following differential equation:

$$\left[\nabla_p^2 + k^2\right] \phi^+(\vec{r}_p) = V(r_p)\phi^+(\vec{r}_p). \tag{C.2}$$

The Born approximation uses a Green's function approach to find an approximate solution to ϕ^+; the derivation is in many textbooks, such as Griffiths (1995) and Mott et al. (1965) and in the review paper by Moiseiwitsch & Smith (1968). I simply outline the result, which is

$$\phi^+(\vec{r}_p) = \phi(\vec{r}_p) - \frac{1}{2\pi}\int \frac{e^{ik|\vec{r}_p - \vec{r}'_p|}}{|\vec{r}_p - \vec{r}'_p|} V(\vec{r}'_p)\phi^+(r'_p)d\vec{r}'_p, \tag{C.3}$$

where ϕ is the wavefunction solution to Eq (C.2) with the right-hand side set to zero. In this instance, the wavefunction will simply be a plane wave, $\exp(-i\vec{k}\cdot\vec{r})$. This has the same functional form as Eq (C.1), so the scattering amplitude is then

$$f \approx \frac{1}{2\pi}\int e^{ik'\vec{r}'_p} V(\vec{r}'_p) e^{-ik\vec{r}'_p} d\vec{r}'_p,$$

where the scattering amplitude is simply a matrix element, $\langle k\,|V|\,k'\rangle$.

Lippmann & Schwinger (1950) re-wrote the Born approximation in terms of state-vectors,

$$|\phi^+\rangle = |\phi\rangle + GV|\phi^+\rangle, \tag{C.4}$$

so that the scattering amplitude is just the expectation value of Λ with ϕ^+,

$$f = \left\langle \phi'\,|V|\,\phi^+\right\rangle = \langle \phi'\,|V|\,\phi\rangle + \langle \phi'\,|VGV|\,\phi\rangle + \cdots . \tag{C.5}$$

The functional form of Eq (C.5) is a Taylor series where the originating function is defined as the transition "T"-matrix

$$\langle \phi' | T | \phi \rangle = \left\langle \phi' \left| \frac{V}{1 - GV} \right| \phi \right\rangle, \tag{C.6}$$

and the "S"-matrix is related to the "T"-matrix by

$$S = 1 + T.$$

The total scattered wavefunction can be written as

$$\left| \phi^{+} \right\rangle = S \left| \phi \right\rangle$$

and the various terms can be interpreted as various vertices of interaction (see figure C.1), where the first term of the "S"-matrix has no interaction. The higher-order terms of the "S"-matrix includes more complicated types of interactions, where the second term is one interaction of the scattering electron with the potential, and the third term includes two interactions within one scattering "event".

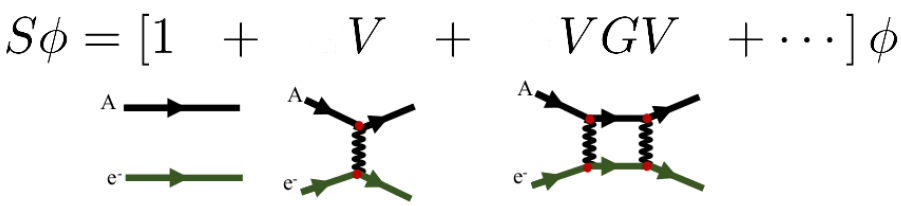

Figure C.1: Interaction diagram of the "S"-matrix

C.2 Derivation of the Relaxation Theory

This derivation is from Fano (1963). I use the Liouville notation (chapter 3.1), where Eq (3.3) can be re-written as

$$e^{-iHt} D e^{iHt} = e^{-iLt} D,$$

and start with the integration already performed on Anderson's equation (Eq 3.1),

$$I(\omega) = Im\ Tr \left\{ D \frac{1}{\omega - L_0 - L_1} D \right\}, \tag{C.7}$$

where L_0 is the isolated particle Liouville operator and L_1 is the interaction between plasma and radiator; this Fourier transform is possible because the operators L_0 and L_1 have no explicit time dependence. At this point, L_1 still contains *all* interactions as described in Eq (3.10).

C.2.1 The Scattering "T"-matrix

Manipulation of Eq (C.7) isolates the interaction of the atom with the plasma in a single term. The interaction L_1 can be removed from the denominator into a single operator, called M

$$\begin{aligned}
\frac{1}{\omega - L_0 - L_1} &= \frac{1}{\omega - L_0} \frac{1}{1 - (\omega - L_0)^{-1} L_1} \\
&= \frac{1}{\omega - L_0} \frac{1 - (\omega - L_0)^{-1} L_1 + (\omega - L_0)^{-1} L_1}{1 - (\omega - L_0)^{-1} L_1} \\
&= \frac{1}{\omega - L_0} \left[1 + \frac{(\omega - L_0)^{-1} L_1}{1 - (\omega - L_0)^{-1} L_1} \right] \\
&= \frac{1}{\omega - L_0} \left[1 + M \frac{1}{\omega - L_0} \right] && \text{(C.8)} \\
T(\omega) &= \frac{1}{1 - L_1 (\omega - L_0)^{-1}} L_1. && \text{(C.9)}
\end{aligned}$$

The operator $T(\omega)$ is the Liouville equivalent of the scattering "T"-matrix, so *this* is the equivalence with the scattering amplitude ("T"-matrix and amplitude are the same thing).

Calculating the "T"-matrix is difficult and does not lend itself to easy computation; it is therefore common practice to perform a Taylor expansion of the "T"-matrix,

$$\begin{aligned} T(\omega) &= L_1 \sum_n \left[(\omega - L_0)^{-1} L_1\right]^n \\ &\approx L_1 + L_1(\omega - L_0)^{-1} L_1 + O(L_1^3) \end{aligned} \tag{C.10}$$

The propagator, defined by the inverse of the Liouvillian, in terms two and three are evaluated by assuming that ω has both real and imaginary parts,

$$\omega = \omega' + i\epsilon,$$

then taking the limit as ϵ goes to zero. Therefore, the inverse operator is defined as

$$\lim_{\epsilon \to 0} \frac{1}{\omega' + i\epsilon - L_0^A + L_0^E} = \frac{PV}{\omega' - L_0^A + L_0^E} - i\pi\delta(\omega' - L_0^A + L_0^E), \tag{C.11}$$

where the real part of the dynamic width and shift term is evaluated with the Cauchy principal value and the imaginary part with a Dirac delta. Techniques for evaluating Eq C.11 exist: O'Brien & Hooper (1974) use a clever form of zero to evaluate the principle value, and the delta function is easily evaluated since the average over free-electron states involves multiple integrals. The delta function can eliminate an integral due to the fundamental identity

$$\int_{\infty}^{\infty} dx f(x)\delta(x - a) = f(a);$$

the integral, though, is weighted by the density matrix. It can therefore limit the number of available states and causes an exponential damping on the red side of the profile (O'Brien & Hooper, 1974, ; more in chapter 10).

C.3 The Electron-Broadening Operator

In order to write the spectral line broadening operator in the form

$$\frac{1}{\omega - L_0 - \mathcal{H}(\omega)}, \tag{C.12}$$

equation (C.9)must be transformed back after the trace is performed:

$$\begin{aligned} Tr_e\left\{\frac{1}{\omega - L_0 - L_1}\right\} &= \frac{1}{\omega - L_0^A}\left[1 + Tr_e\{T(\omega)\}\frac{1}{\omega - L_0^A}\right] \\ &= \frac{1}{\omega - L_0^A - \mathcal{H}(\omega)} \\ \mathcal{H}(\omega) &= \frac{1}{1 + Tr_e\{T(\omega)\}(\omega - L_0^A)^{-1}} Tr_e\{T(\omega)\}, \end{aligned} \tag{C.13}$$

where the trace is over electron states. The Taylor expansion of Eq (C.13) is

$$\begin{aligned} \mathcal{H}(\omega) &= Tr_e\{T(\omega)\}\sum_{n=0}^{\infty}\left[-(\omega - L_0^A)^{-1}Tr_e\{T(\omega)\}\right]^n, \\ &= Tr_e\{T(\omega)\} - Tr_e\{T(\omega)\}(\omega - L_0^A)^{-1}Tr_e\{T(\omega)\} + \cdots \end{aligned} \tag{C.14}$$

This additional transformation represents what I would call correlated collisions, or collisions in quick succession; this is different from a three-body collision, which will be discussed next. More details of this physical interpretation, including an interaction diagram is given in chapter 8.

C.3.1 Simultaneous Multiple-Particle Collisions

At this point, $T(\omega)$ contains information about all particles in the plasma. To simplify the problem, Fano does a gas-density expansion,

$$\langle T(\omega)\rangle = N\langle T_1\rangle + \frac{1}{2}N(N-1)\langle T_{12}\rangle + \cdots, \tag{C.15}$$

where $\langle T_1\rangle$ included all two-particle interactions between the plasma and the radiator (binary collisions between the radiator and electron "1"), while the second term includes three-body

interactions (interaction between radiator and electrons "1" and "2"). These terms are written explicitly as

$$\begin{aligned}
\langle T_1 \rangle &= Tr_1 \frac{1}{1 - L_{A1}(\omega - L_0^A - L_0^1)^{-1}} L_{A1} && \text{(C.16)} \\
\langle T_{12} \rangle &= Tr_1 Tr_2 \frac{1}{1 - (L_{A1} + L_{A2} + L_{12})(\omega - L_0^A - L_0^1 - L_0^2)^{-1}} (L_{A1} + L_{A2} + L_{12}) \\
&- Tr_2 \frac{1}{1 - L_{A2}(\omega - L_0^A - L_0^2)^{-1}} L_{A2} \\
&- Tr_1 \frac{1}{1 - L_{A1}(\omega - L_0^A - L_0^1)^{-1}} L_{A1}, && \text{(C.17)}
\end{aligned}$$

where for all interaction operators, I have explicitly defined which bodies are interacting.

In order to simplify the calculation, I take the second-order Taylor form of M, leading to the following gas-density expansion terms:

$$\begin{aligned}
\langle T_1 \rangle &= Tr_1\{L_{A1}\} + Tr_1\{L_{A1}(\omega - L_0^A - L_0^1)^{-1} L_{A1}\} && \text{(C.18)} \\
\langle T_{12} \rangle &= Tr_1 Tr_2\{L_{12}\} + Tr_1 Tr_2 \left\{L_{A1}(\omega - L_0^A - L_0^1 + L_0^2)^{-1} L_{A2})\right\} \\
&+ Tr_1 Tr_2 \left\{L_{A1}(\omega - L_0^A - L_0^1 - L_0^2)^{-1} L_{12}\right\} \\
&+ Tr_1 Tr_2 \left\{L_{A2}(\omega - L_0^A - L_0^1 - L_0^2)^{-1} L_{A1}\right\} \\
&+ Tr_1 Tr_2 \left\{L_{A2}(\omega - L_0^A - L_0^1 - L_0^{2)})^{-1} L_{12}\right\} \\
&+ Tr_1 Tr_2 \left\{L_{12}(\omega - L_0^A - L_0^1 - L_0^2)^{-1} L_{12}\right\}.
\end{aligned}$$

In this thesis, I am not going to concern myself with the three-body interactions. The presence of the other electrons can be included in the evaluation of T_1 by having the interaction potentials screened using Debye-Huckel theory. This screening function works well because there are also ions in the plasma which neutralizes the presence of the free electrons far from the nucleus. So these terms are only present in the slight plasma polarization in the vicinity of the atom.

C.3.2 The Matrix Structure of T & $\mathcal{H}$

Before I get into some of the details of the evaluation of M and M_c, it is important to gain some intuition about what kind of structure is to be expected of the M matrix. To illustrate this, I make some very simplifying assumptions, namely that there are only two particles where each particle has only two states, we consider only monopole and dipole transitions (since these are the dominant interactions), and that only the upper state broadening would be considered (and the frequency dependence will be neglected). I also assume that the solution of the atomic wavefunction obeys spherical harmonics and can be represented by the quantum numbers $n,\ l,\ m$, though I am neglecting the m quantum numbers.

Therefore, we can approximate L_1 as

$$\begin{pmatrix} V_{11} & 0 & 0 & V_{14} \\ 0 & V_{22} & V_{23} & 0 \\ 0 & V_{32} & V_{33} & 0 \\ V_{41} & 0 & 0 & V_{44} \end{pmatrix} \begin{pmatrix} 2sks \\ 2pks \\ 2skp \\ 2pkp \end{pmatrix} \tag{C.19}$$

To evaluate Eq C.9, a matrix inversion needs to be performed. The matrix inverse will be proportional to

$$\begin{pmatrix} b_{11} & 0 & 0 & b_{14} \\ 0 & b_{22} & b_{23} & 0 \\ 0 & b_{32} & b_{33} & 0 \\ b_{41} & 0 & 0 & b_{44} \end{pmatrix} \tag{C.20}$$

where the different elements are listed here:

$$
\begin{aligned}
b_{11} &= (1-V_{22})(1-V_{33})(1-V_{44}) - V_{23}V_{32}(1-V_{44}) \\
b_{22} &= (1-V_{11})(1-V_{33})(1-V_{44}) - V_{14}V_{41}(1-V_{33}) \\
b_{33} &= (1-V_{11})(1-V_{22})(1-V_{44}) - V_{14}V_{41}(1-V_{22}) \\
b_{44} &= (1-V_{11})(1-V_{22})(1-V_{33}) - V_{23}V_{32}(1-V_{11}) \\
b_{14} &= V_{14}V_{23}V_{32} - V_{14}(1-V_{22})(1-V_{33}) \\
b_{23} &= V_{14}V_{23}V_{41} - V_{23}(1-V_{11})(1-V_{44}) \\
b_{32} &= V_{14}V_{32}V_{41} - V_{32}(1-V_{11})(1-V_{44}) \\
b_{41} &= V_{23}V_{32}V_{41} - V_{41}(1-V_{22})(1-V_{33})
\end{aligned}
$$

To evaluate the T operator, then the matrix defined in Eq (C.20) needs to be multiplied by the interaction matrix in Eq (C.19),

$$
\left(\begin{array}{cc|cc}
b_{11}V_{11}+b_{14}V_{14} & 0 & 0 & b_{11}V_{14}+b_{14}V_{44} \\
0 & b_{22}V_{22}+b_{23}V_{32} & b_{22}V_{23}+b_{23}V_{33} & 0 \\
\hline
0 & b_{32}V_{22}+b_{33}V_{32} & b_{33}V_{33}+b_{32}V_{23} & 0 \\
b_{41}V_{11}+b_{44}V_{41} & 0 & 0 & b_{44}V_{44}+b_{41}V_{14}
\end{array}\right) \tag{C.21}
$$

In the formalism, a trace is performed over the electronic coordinates, selecting only the matrix elements in the upper left corner and lower right corner of Eq (C.21), which produces the following *diagonal* matrix,

$$
Tr_e\{T\} = \begin{pmatrix} \langle T\rangle_{11} & 0 \\ 0 & \langle T\rangle_{22} \end{pmatrix} \tag{C.22}
$$

where the matrix elements are as follows:

$$
\begin{aligned}
\langle T\rangle_{11} &= (1-V_{22})(1-V_{33})(1-V_{44})V_{11} - V_{23}V_{32}(1-V_{44})V_{11} \\
&\quad +V_{14}V_{23}V_{32}V_{14} - V_{14}(1-V_{22})(1-V_{33})V_{14} \\
&\quad +(1-V_{11})(1-V_{22})(1-V_{44})V_{33} - V_{14}V_{41}(1-V_{22})V_{33} \\
&\quad +V_{14}V_{32}V_{41}V_{23} - V_{32}(1-V_{11})(1-V_{44})V_{23} \\
\langle T\rangle_{22} &= (1-V_{11})(1-V_{33})(1-V_{44})V_{22} - V_{14}V_{41}(1-V_{33})V_{22} \\
&\quad +V_{14}V_{23}V_{41}V_{32} - (1-V_{11})(1-V_{44})V_{23}V_{32} \\
&\quad +(1-V_{11})(1-V_{22})(1-V_{33})V_{44} - V_{23}V_{32}(1-V_{11})V_{44} \\
&\quad +V_{23}V_{32}V_{41}V_{14} - (1-V_{22})(1-V_{33})V_{41}V_{14}.
\end{aligned}
$$

Already, with this simple example, it can be easily seen that the calculations to evaluate M is complicated. Therefore, a Taylor expansion in powers of V is desirable, but caution must be taken to keep the errors in such an approximation in mind. The approximate elements of $Tr_e\{M\}$ to second order are

$$
\begin{aligned}
\langle T\rangle_{11} &\approx V_{11} + V_{33} + V_{14}V_{41} + V_{32}V_{23} \\
\langle T\rangle_{22} &\approx V_{22} + V_{44} + V_{41}V_{14} + V_{23}V_{32}
\end{aligned}
$$

which are much simpler to evaluate.

Because T will be diagonal (or near enough when multiple n states are included), then it makes the evaluation of $\mathcal{H}$ quite trivial (at least for this simple case):

$$
\begin{aligned}
\langle \mathcal{H}\rangle_{11} &= \frac{1}{1+\langle T\rangle_{11}(\Delta\omega)^{-1}}\langle T\rangle_{11} \\
\langle \mathcal{H}\rangle_{22} &= \frac{1}{1+\langle T\rangle_{22}(\Delta\omega)^{-1}}\langle T\rangle_{22}
\end{aligned}
$$

C.4 Evaluation of Matrix Elements

We now examine the details of a quantum mechanical treatment of the perturbing electrons. First, we would like to discuss the exact form of the interaction potential, V, and the assumed form of the bound-electron and free-electron wavefunctions, followed then by the computational form of T under the same assumptions as Woltz & Hooper (1984). We then expand on these results by using a distorted-wave treatment for the second-order calculation of M, and finally include exchange. Since I am using the first-order gas-density expansion from Fano (1963), then I only need to solve the two-electron Hamiltonian where one electron is bound to the atom and the other electron is colliding with the atom.

C.4.1 Matrix Elements of the Coulomb Operator

Now I will go through the equations for scattering off of an atom. In this derivation, the scattering electron and atom only interact through the Coulomb interaction (for now, I assume that the atom and electron are distinguishable). Under this assumption, the total wavefunction takes the form

$$\Psi = \psi(\vec{r}_r)\phi(\vec{r}_p), \tag{C.23}$$

where the sum is over all available states which the two electrons can occupy. We define the atomic and free electrons (labeled as ψ and ϕ respectively) as:

$$\begin{aligned} \psi_{nlm} &= \frac{1}{r}R_{nl}(r_r)Y_{lm}(\theta_r,\phi_r), \\ \phi_k &= \sqrt{\frac{2}{\pi}}\sum_{l=0}^{\infty}\sum_{m=-l}^{l} i^l \frac{1}{kr}F_{kl}(r)Y^*_{lm}(\hat{k})Y_{lm}(\hat{r}). \end{aligned} \tag{C.24}$$

where R_{nl} and F_{kl} is are the radial solutions and Y_{lm} is a spherical harmonic.

The bound wavefunctions solution are known and are solutions to the following

differential equation for the isolated hydrogenic atom,

$$\left[\nabla_r^2 + 2\frac{Z}{r_r} + 2E\right]\psi(\vec{r_r}) = 0, \tag{C.25}$$

where

$$E_n = -\frac{1}{2}\frac{Z^2}{n^2}$$

is the energy of the atomic state, where n is the principle quantum number of the state. I will define the potential due to a hydrogenic atom—equivalent to V in the previous section—as

$$\Lambda_{i,j}(\vec{r}_p) \quad = \quad \int d^3\vec{r}_r \; \psi_i^*(\vec{r}_r)\left[\sum_x \frac{r_<^x}{r_>^{x+1}} P_x(\cos\theta) - \frac{\delta_{x,0}}{r_p}\right]\psi_j(\vec{r}_r), \tag{C.26}$$

where $\vec{r}_r$ is the coordinate system of the atomic electron and $\vec{r}_p$ is the coordinate of the perturbing electron. I distinguish between Λ and V: Λ is similar to an expectation value (but does not include the integration over free-electron coordinates), while V is the Coulomb operator. I have written the scattering potential in a way such that the scattering event of a single electron can induce a change in the internal state of the atom, i.e., a "transition;" this is the "T" in the "T"-matrix.

However, the potential due to the nucleus is long-range, so any charge that is not completely screened by the atomic wavefunction can be put into the solution of the free-electron; this is the thinking behind the distorted-wave treatments, but we will explore that in a later section. The wavefunction of the scattering electron is the solution to the following equation (Percival & Seaton, 1957; Moiseiwitsch & Smith, 1968; Burgess et al., 1970):

$$\left[\nabla_p^2 + 2\frac{Z-1}{r_p} + k^2\right]\phi(r_p) = 2\Lambda_{i,j}(\vec{r}_p)\phi(\vec{r}_p), \tag{C.27}$$

where k is the wavenumber of the colliding electron.

The "T"-matrix is evaluated using Eq (C.5), where the "starting" wavefunction is the solution to Eq (C.27) with the right-hand side set to zero. Such a solution would be a plane wave with $Z = 1$ or a Coulomb wave with $Z > 1$. Evaluation of the "T"-matrix requires calculation of matrix elements of the interaction potential, which is a Coulomb interaction. For the calculation of the matrix elements of the interaction between the atom and scattering wavefunction, we use Eq (C.24) and take advantage of the fact that the Legendre polynomial is built from spherical harmonics. The angular component of the integral is a spherical harmonic from the operator times two spherical harmonics from the wavefunction; this angular integral can be rewritten as a product of Wigner 3j symbols (See Eqs B.9 and B.10). Calculation of the matrix elements is done by evaluating the 3j symbols and the radial integrals:

$$\begin{aligned}\langle k_1 l_1 m_1; nlm\,|V|\,k_2 l_2 m_2; n'l'm'\rangle = \sum_{x,q}(-1)^{m_1+q+m}\sqrt{(2l_1+1)(2l_2+1)(2l+1)(2l'+1)}\times \\ \begin{pmatrix} l_1 & x & l_2 \\ 0 & 0 & 0 \end{pmatrix}\begin{pmatrix} l & x & l' \\ 0 & 0 & 0 \end{pmatrix}\begin{pmatrix} l_1 & x & l_2 \\ -m_1 & q & m_2 \end{pmatrix}\begin{pmatrix} l & x & l' \\ -m & -q & m' \end{pmatrix}\int_0^\infty dr_p F_{k_1 l_1}(r_p)F_{k_2 l_2}\times \\ \left\{ r_p^x \int_0^{r_p} dr_p \frac{1}{r_r^{x+1}} R_{nl}(r_r)R_{n'l'}(r_r) + \frac{1}{r_p^{x+1}}\int_{r_p}^\infty dr_p r_r^x R_{nl}(r_r)R_{n'l'}(r_r) \right. \\ \left. - \frac{\delta_{x,0}}{r_p}\int_0^\infty R_{nl}(r_r)R_{n'l'}(r_r)\right\} Y_{l_1 m_1}(\vec{k_1})Y^*_{l_2 m_2}(\vec{k_2}). \quad \text{(C.28)}\end{aligned}$$

I introduce a short-hand to describe the radial integrals of the xth multipole term of the *direct* interaction,

$$\hat{\Lambda}^x_{nl,n'l'}(r_p) = \int_0^\infty dr_r R_{nl}(r_p)\left[\frac{r_<^x}{r_>^{x+1}} - \frac{\delta_{x,0}}{r_p}\right] R_{n'l'}. \quad \text{(C.29)}$$

C.4.2 Distorted Wave Treatment

My calculation of the "T"-matrix will be only out to second order, in this way, we can take advantage of some nice symmetry properties to greatly simplify our calcula-

tions. Therefore the second-order calculation will only be accurate as long as the interaction between the radiator and the scattering electron is small.

In order to remedy this, we can introduce a distorting potential, U. The distorting potential can be introduced to Eq (C.27) by subtracting it from both sides of the equation (Kingston & Walters, 1980; Madison et al., 1991),

$$\left[\nabla_p^2 + 2\frac{Z-1}{r_p} + k^2 - 2U(\vec{r}_p)\right]\phi_i^{(DW)}(r_p) = 2\sum_j \left\{\Lambda_{i,j}(\vec{r}_p)\phi_j^{(DW)}(\vec{r}_p) - U(\vec{r}_p)\right\}\phi_i^{(DW)}(r_p), \quad \text{(C.30)}$$

where a good choice for the distorting potential is the monopole term of the atom,

$$U(\vec{r}_p) = \hat{\Lambda}^0_{i,i}(\vec{r}_p). \quad \text{(C.31)}$$

The "T"-matrix must then include an additional term and be modified accordingly:

$$\langle\phi_i|T|\phi_j\rangle = \left\langle\phi_i|U|\phi_j^{(DW)}\right\rangle + \left\langle\phi_i^{(DW)}|\Lambda_{i,j} - U|\phi_j^{(DW)}\right\rangle + \left\langle\phi_i^{(DW)}|(\Lambda_{i,j} - U)G(\Lambda_{i,j} - U)|\phi_j^{(DW)}\right\rangle + \cdots \quad \text{(C.32)}$$

Equation (C.32) ensures the smallness of the expansion and thus makes a second-order treatment more accurate.

C.4.3 Distorted Wave + Exchange

The treatment so far has not taken into account the indistinguishability of electrons. To remedy this, the scattering differential equation will include an exchange of coordinates; this will ensure that identical particles remain indistinguishable Bethe & Salpeter (1957).

For this derivation, we will start at the two-electron Hamiltonian where the electrons

share a common nucleus,

$$\left[-\frac{1}{2}\nabla_r^2 - \frac{1}{2}\nabla_p^2 - \frac{Z}{r_r} - \frac{Z}{r_p} + \frac{1}{|\vec{r}_r - \vec{r}_p|}\right]\Psi = E\Psi \tag{C.33}$$

where the total wavefunction includes the possibility of transitions to different states as well as the proper symmetry so that the electron can be considered indistinguishable,

$$\Psi = \sum_i \frac{1}{\sqrt{2}}\left[\psi_i(r_1)\phi_i(r_2) \pm \phi_i(r_1)\psi_i(r_2)\right], \tag{C.34}$$

where the "+" state corresponds to the spin anti-aligned singlet state, and the "-" state corresponds to the spin-aligned triplet state.

Now, inserting Eq (C.34) into Eq (C.33), and multiplying the right-hand side by $\psi_j^*(r_r)$ and assuming

$$\left[-\frac{1}{2}\nabla_r^2 - \frac{Z}{r_r}\right]\psi_i(r_r) = E_i^A\psi_i(r_r) = -\frac{1}{2}\frac{Z}{n_i}\psi_i(r_r), \tag{C.35}$$

then Eq (C.33) becomes,

$$\begin{aligned}\sum_i \quad & \psi_j^*(r)\left[-\nabla_r^2 - 2\frac{Z}{r_r}\right]\left[\psi_i(r)\phi_i(p) \pm \phi_i(r)\psi_i(p)\right] \\ & \psi_j^*(r)\left[-\nabla_p^2 - 2\frac{Z}{r_p}\right]\left[\psi_i(r)\phi_i(p) \pm \phi_i(r)\psi_i(p)\right] + \\ & \frac{2}{|\vec{r}_r - \vec{r}_p|}\left[\psi_i(r)\phi_i(p) \pm \phi_i(r)\psi_i(p)\right] \\ & = \psi_j(r)\left(2E_i^A + k^2\right)\left[\psi_i(r)\phi_i(p) \pm \phi_i(r)\psi_i(p)\right]\end{aligned}$$

then using Eq (C.35), and integrating over $\vec{r}_r$, we get the following simplification

$$\begin{aligned}\sum_i \quad & 2E_i^A\left[\phi_i(p) \pm \int d\vec{r}_r\psi_j^*(r)\phi_i(r)\psi_i(p)\right] \\ & \left[-\nabla_p^2 - 2\frac{Z}{r_p}\right]\left[\phi_i(p) \pm \int d\vec{r}_r\psi_j^*(r)\phi_i(r)\psi_i(p)\right] + \\ & \int d\vec{r}_r\psi_j^*(r)\frac{2}{|\vec{r}_r - \vec{r}_p|}\psi_i(r)\phi_i(p) \pm \int d\vec{r}_r\psi_j^*(r)\frac{2}{|\vec{r}_r - \vec{r}_p|}\phi_i(r)\psi_i(p) \\ & = \left(2E_i^A + k^2\right)\phi_i(p) \pm \left(2E_i^A + k^2\right)\int d\vec{r}_r\psi_j^*(r)\phi_i(r)\psi_i(p).\end{aligned}$$

At this point, several terms cancel, then re-arranging the equation, we get

$$\sum_i \quad \left[-\nabla_p^2 - 2\frac{Z-1}{r_p}\right]\phi_i(p) \pm 2E_i \int d\vec{r}_r \psi_j^*(r)\phi_i(r)\psi_i(p) +$$
$$2\int d\vec{r}_r \psi_j^*(r)\left(\frac{1}{|\vec{r}_r - \vec{r}_p|} - \frac{1}{r_p}\right)\psi_i(r)\phi_i(p) \pm \int d\vec{r}_r \psi_j^*(r)\frac{2}{|\vec{r}_r - \vec{r}_p|}\phi_i(r)\psi_i(p)$$
$$= k^2\phi_i(p) \pm k^2 \int d\vec{r}_r \psi_j^*(r)\phi_i(r)\psi_i(p).$$

Further re-arrangement gives the following equation:

$$\left[\nabla_p^2 + 2\frac{Z-1}{r_p} + k^2\right]\phi_j(p) =$$
$$\sum_i \left\{2\int d\vec{r}_r \psi_j^*(r)\left(\frac{1}{|\vec{r}_r - \vec{r}_p|} - \frac{1}{r_p}\right)\psi_i(r)\phi_i(p)\right.$$
$$\left. \pm 2\psi_j(p)\int d\vec{r}_r \psi_j^*(r)\left(\frac{1}{|\vec{r}_r - \vec{r}_p|} - E_i - k^2\right)\phi_i(r)\right\}. \tag{C.36}$$

For the last term, the exchange, we can use Eq (C.35) to write the energy eigenvalue in terms of the energy operators.

$$\pm 2\psi_j(p)\int d\vec{r}_r \psi_j^*(r)\left[\frac{1}{|\vec{r}_r - \vec{r}_p|} - \frac{1}{r_r} - \frac{1}{2}\left(\nabla^2 + k^2 + 2\frac{Z-1}{r_r}\right)\right]\phi_i(r). \tag{C.37}$$

Now, at this point, I want to emphasize the similarities between Eq (C.36) with Eq (C.27), the left-hand side of the equation is the same, while the first-term of the right-hand side is also the same. Now we have an additional term that takes into account the exchange interaction. One simplification to Eq (C.37) is given by Oppenheimer (1928), where

$$\frac{1}{2}\left(\nabla^2 + k^2 + 2\frac{Z-1}{r_r}\right)\phi_i(r)$$

is replaced with zero because we find the starting solution to ϕ by setting the right-hand side of Eq (C.36) to zero.

The exchange term becomes a little different under Oppenheimer's approximation when the distorted-wave treatment is used. Rather than setting the energy terms of Eq (C.37) to zero, it is set to the distorting potential,

$$\left[\nabla_p^2 + 2\frac{Z-1}{r_p} + k^2 - 2\hat{\Lambda}^0_{i,i}(\vec{r}_p)\right]\phi_i^{(DW)}(r_p) = 2\sum_j \Lambda_{i,j}(\vec{r}_p)\phi_j^{(DW)}(\vec{r}_p) - 2\hat{\Lambda}^0_{i,i}(\vec{r}_p)\phi_i^{(DW)}(r_p)$$
$$\pm 2\Xi_{i,j}(\vec{r}_p)\psi_j(\vec{r}_p) + \delta_{i,j}2\psi_j(\vec{r}_p)\int d\vec{r}_r\psi_i^*(\vec{r}_r)\hat{\Lambda}^0_{i,i}(\vec{r}_p)\phi_j(\vec{r}_r). \quad \text{(C.38)}$$

where Ξ is the exchange term, which is defined as,

$$\Xi_{i,j}(\vec{r}_p) = \int d^3\vec{r}_r\ \psi_i^*(\vec{r}_r) \times \left[\frac{1}{r_{rp}} - \frac{1}{r_r}\right]\phi_j(\vec{r}_r). \quad \text{(C.39)}$$

As with the direct term, we will use the following shorthand to denote the radial integrals of the exchange term:

$$\hat{\Xi}^x_{k_1 l_1, n' l'}(r_p) = \int_0^\infty dr_r F_{k_1,l_1}(r_r)\left[\frac{r_<^x}{r_>^{x+1}} - \frac{\delta_{x,0}}{r_r}\right]R_{n'l'}, \quad \text{(C.40)}$$

C.4.3.1 Thermal Average

For the line-broadening problem, we need to take a thermal average of the different terms of the "T"-matrix. In order to do that, we assume that the magnitude of the wave number is the same both before and after the collision (Baranger, 1958a); this guarantees that the total energy of the plasma is conserved after the collision. The density matrix of the free electron is approximately defined as

$$\rho_e = e^{-\beta H^{(e,0)}}/Tr_e\left\{e^{-\beta H^{(e,0)}}\right\} \quad \text{(C.41)}$$

As shown by O'Brien & Hooper (1974), the normalizing Trace gives an factor of the electron density times the thermal de Broglie wavelength,

$$1/Tr_e \left\{ e^{-\beta H^{(e,0)}} \right\} \approx \frac{1}{V} \lambda_T^3.$$

C.5 Spectral Line Shape Assuming Coulomb/Plane Waves

I will now take the form of the "T"-matrix that does not include the distorted wave treatment or exchange; this is the electron scattering off of a frozen atom.

C.5.1 Plasma Polarization Term

The plasma polarization term is evaluated by a thermal average over free-electron states and is simply the first term of the "T"-matrix expansion; $T^{(1)}$ will be used to denote the first-order T term. By the requirements of the thermal average, the incoming wavevector of the free electron, k, is the same as the outgoing, therefore the average is

$$T^{(1)} = n_e \lambda_T^3 \int_0^\infty d\vec{k}\ e^{-\beta \frac{1}{2} k^2} \left\langle nlm; \vec{k} \left| V \right| n'l'm'; \vec{k} \right\rangle. \tag{C.42}$$

Using the definitions for the scattering wavefunction, then the thermal average becomes a sum over the various partial waves,

$$T^{(1)} = \sum_{l_1, l_2, m_1, m_2} n_e \frac{2}{\pi} \lambda_T^3 \int_0^\infty dk d\theta_k d\phi_k\ k^2 \sin\theta\ e^{-\beta \frac{1}{2} k^2} \times \\ \langle nlm; kl_1m_1 \left| V \right| n'l'm'; kl_2m_2 \rangle\ (i)^l (-i)^l Y_{l_1 m_1}(\theta_k, \phi_k) Y^*_{l_2 m_2}(\theta_k, \phi_k) \tag{C.43}$$

Performing the angular integrals forces l_1 to be equal to l_2 and m_1 to be m_2, the imaginary components drop out and this term becomes purely real and thus contributes only to shifts of the line.

The angular integrals inside the matrix element can be evaluated using Wigner 3j symbols,

$$T^{(1)} = \sum_{x,q,l_1,m_1} \frac{2}{\pi} n_e \lambda_T^3 \int_0^\infty dk\ e^{-\beta \frac{1}{2}k^2} \left\langle kl_1 \left| \hat{\Lambda}^x_{n'l'} \right| kl_1 \right\rangle \sqrt{(2l+1)(2l'+1)}(2l_1+1)$$
$$\begin{pmatrix} l & x & l' \\ 0 & 0 & 0 \end{pmatrix} \begin{pmatrix} l_1 & x & l_1 \\ 0 & 0 & 0 \end{pmatrix} \begin{pmatrix} l & x & l' \\ -m & -q & m' \end{pmatrix} \begin{pmatrix} l_1 & x & l_1 \\ -m_1 & q & m_1 \end{pmatrix} (-1)^{m+q+m_1}. \quad \text{(C.44)}$$

By the selection rules of the 3j symbol, the only value of q that survives is zero, then using Eq (B.7) to sum over m_1, then the only value of x that survives is the $x = 0$ term, which is the monopole term,

$$T^{(1)} = \sum_{l_1} \frac{2}{\pi} n_e \lambda_T^3 \int_0^\infty dk\ e^{-\beta \frac{1}{2}k^2} \left\langle kl_1 \left| \hat{\Lambda}^x_{n'l'} \right| kl_1 \right\rangle (2l+1)(2l_1+1) \times$$
$$\delta_{ll'}\delta_{mm'} \begin{pmatrix} l & 0 & l' \\ 0 & 0 & 0 \end{pmatrix} \begin{pmatrix} l_1 & 0 & l_1 \\ 0 & 0 & 0 \end{pmatrix} \begin{pmatrix} l & 0 & l' \\ -m & 0 & m' \end{pmatrix} (-1)^{l_1+m} \sqrt{2l_1+1}. \quad \text{(C.45)}$$

Using the special value of the 3j symbol (Eq B.8), then the rest of the 3j symbols can be easily evaluated,

$$(2l+1)(2l_1+1) \begin{pmatrix} l_1 & 0 & l_1 \\ 0 & 0 & 0 \end{pmatrix} \begin{pmatrix} l & 0 & l \\ -m & 0 & m \end{pmatrix} (-1)^m \sqrt{2l_1+1}$$
$$\Rightarrow (2l+1)(2l_1+1) \begin{pmatrix} l_1 & 0 & l_1 \\ 0 & 0 & 0 \end{pmatrix} (-1)^l \frac{1}{\sqrt{2l+1}}$$
$$\Rightarrow (2l+1)$$

which equals $(2l_1 + 1)$ The final expression for the plasma polarization term is,

$$T^{(1)} = \sum_{l_1} (2l_1+1) \frac{2}{\pi} n_e \lambda_T^3 \int_0^\infty dk\ e^{-\beta \frac{1}{2}k^2} \left\langle kl_1 \left| \hat{\Lambda}^x_{n'l'} \right| kl_1 \right\rangle. \quad \text{(C.46)}$$

A similar equation to Eq (C.46) exists for the lower-state term.

I want to pause for a moment and talk about what this term means. First, the only surviving term is the monopole interaction; this means that the only contribution is

the average constant potential of the plasma. Therefore in plasmas where the atom induces little-to-no polarization of the plasma, then this term will be small, if not negligible. This term should does not affect the hydrogen spectra, but it will strongly affect more highly-charged ions, such as hydrogen-like Mg or hydrogen-like Ar, causing a significant red-shift of the line. If the dipole approximation is made, the only term of the Coulomb potential that is considered is the $x = 1$ term; since the $x = 1$ term does not survive in this approximation, then this term becomes zero.

C.5.2 Dynamic Width and Shift term

The second term of the Taylor approximation to M (derived in section C.2), is very similar to the "T"-matrix, but with Liouville generalization (and remembering that a matrix element of a product of operators is simply a matrix multiplication and that the propagator is diagonal), is

$$\begin{aligned}
\left\langle ul \left| L_1 \frac{1}{\omega - L_0} L_1 \right| u'l' \right\rangle &= \left\langle ul \left| (V^u - V^l) \frac{1}{\omega - H^u + H^l} (V^u - V^l) \right| u'l' \right\rangle \\
&= \sum_{u''l''} \left\langle ul \left| V^u - V^l \right| u''l'' \right\rangle \left\langle u''l'' \left| \frac{1}{\omega - H^u + H^l} \right| u''l'' \right\rangle \left\langle u''l'' \left| V^u - V^l \right| u'l' \right\rangle \\
&= \sum_{u''l''} \left(\langle u | V | u'' \rangle \delta_{ll''} - \delta_{uu''} \langle l | V | l'' \rangle \right) \left\langle u''l'' \left| \frac{1}{\omega - H^u + H^l} \right| u''l'' \right\rangle \times \\
&\quad \left(\langle u'' | V | u' \rangle \delta_{l''l'} - \delta_{u''u'} \langle l'' | V | l' \rangle \right) \\
&= \sum_{u''} \langle u | V | u'' \rangle \frac{1}{\omega - H^{u''} + H^l} \langle u'' | V | u' \rangle \delta_{ll'} && \text{(C.47)} \\
&\quad + \sum_{l''} \langle l | V | l'' \rangle \frac{1}{\omega - H^u + H^{l''}} \langle l'' | V | l' \rangle \delta_{uu'} && \text{(C.48)} \\
&\quad - \langle u | V | u' \rangle \frac{1}{\omega - H^{u'} + H^l} \langle l | V | l' \rangle - \langle l | V | l' \rangle \frac{1}{\omega - H^u + H^{l'}} \langle u | V | u' \rangle , && \text{(C.49)}
\end{aligned}$$

where Eqs (C.47), (C.48), and (C.49) are the upper-state broadening, lower-state broadening, and interference broadening terms.

I will denote the second-order term of $T(\omega)$ as $T^{(2)}(\omega)$. the upper-state broadening term (Eq C.47) and lower-state broadening term is defined as (using our constraints by the thermal average and using the partial-wave expansion,

$$\begin{aligned}
T^{(2)} &= \int d\vec{k}_1 \int d\vec{k}_2 e^{-\beta\frac{1}{2}k_1^2} \left\langle nlm; \vec{k}_1 \left| V \right| n''l''m''; \vec{k}_2 \right\rangle \times \\
&\quad \left\langle n''l''m''; \vec{k}_2 \left| V \right| n'l'm'; \vec{k}_1 \right\rangle \frac{1}{\Delta\omega - \frac{1}{2}(k_1^2 - k_2^2)} \\
&= \sum_{l_1,l_2,l_3,l_4} \sum_{m_1m_2m_3m_4} \int dk_1 d\theta_{k_1} d\phi_{k_1} k_1^2 \sin\theta_{k_1} \int dk_2 d\theta_{k_2} d\phi_{k_2} k_2^2 \sin\theta_{k_2} e^{-\beta\frac{1}{2}k_1^2} \times \\
&\quad \langle nlm; k_1l_1m_1 \left| V \right| n''l''m''; k_2l_2m_2 \rangle \langle n''l''m''; k_2l_3m_3 \left| V \right| n'l'm'; k_1l_4m_4 \rangle \times \\
&\quad \frac{1}{\Delta\omega - \frac{1}{2}(k_1^2 - k_2^2)} Y_{l_1m_1}(\theta_{k_1}, \phi_{k_1}) Y^*_{l_2m_2}(\theta_{k_2}, \phi_{k_2}) Y_{l_3m_3}(\theta_{k_2}, \phi_{k_2}) Y^*_{l_4m_4}(\theta_{k_1}, \phi_{k_1}).
\end{aligned}$$

As before, the angular integrals over $\vec{k}_1$ and $\vec{k}_2$ eliminate the sums over l_3, l_4, m_3, and m_4.

I will now pull out the angular components of the matrix elements:

$$\begin{aligned}
T^{(2)} &= \frac{4n_e\lambda_T^3}{\pi^2} \sum_{l_1,l_2} \sum_{m_1m_2} \sum_{x,q} \sum_{x'q'} \int dk_1 \int dk_2 e^{-\beta\frac{1}{2}k_1^2} (-1)^{m_1+m+q+m_2+q'+m''} \times \\
&\quad \langle nl; k_1l_1 \left| V \right| n''l''; k_2l_2 \rangle \langle n''l''; k_2l_2 \left| V \right| n'l'; k_1l_1 \rangle \frac{1}{\Delta\omega - \frac{1}{2}(k_1^2 - k_2^2)} \times \\
&\quad \sqrt{(2l+1)(2l''+1)(2l''+1)(2l'+1)(2l_1+1)(2l_2+1)(2l_1+1)(2l_2+1)} \times \\
&\quad \begin{pmatrix} l_1 & x & l_2 \\ -m_1 & q & m_2 \end{pmatrix} \begin{pmatrix} l & x & l'' \\ -m & -q & m'' \end{pmatrix} \begin{pmatrix} l_2 & x' & l_1 \\ -m_2 & q' & m_1 \end{pmatrix} \begin{pmatrix} l'' & x' & l' \\ -m'' & -q' & m' \end{pmatrix} \times \\
&\quad \begin{pmatrix} l_1 & x & l_2 \\ 0 & 0 & 0 \end{pmatrix} \begin{pmatrix} l & x & l'' \\ 0 & 0 & 0 \end{pmatrix} \begin{pmatrix} l_2 & x' & l_1 \\ 0 & 0 & 0 \end{pmatrix} \begin{pmatrix} l'' & x' & l' \\ 0 & 0 & 0 \end{pmatrix}
\end{aligned} \tag{C.50}$$

There are many steps to take to simplify this expression.

The first step is to take advantage of some of the 3j selection rules to eliminate the negative sign

$$\begin{aligned}
m_2 &= q' + m_1 \\
m'' &= q + m
\end{aligned}$$

then the exponent becomes $2m_1+2q+2m+2q'$; all of the numbers here are integers, which makes the exponent even, and the negative sign go to zero. Second, let's simplify some of the 3j symbol functions by using the sum rules in Appendix B (specifically Eqs B.3, B.4, and B.6),

$$\begin{aligned}
\sum_{m_1 m_2} \begin{pmatrix} l_1 & x & l_2 \\ -m_1 & q & m_2 \end{pmatrix} \begin{pmatrix} l_2 & x' & l_1 \\ -m_2 & q' & m_1 \end{pmatrix} &= \sum_{m_1 m_2} \begin{pmatrix} l_1 & x & l_2 \\ -m_1 & q & m_2 \end{pmatrix} \begin{pmatrix} l_1 & x' & l_2 \\ -m_1 & -q' & m_2 \end{pmatrix} \\
&= \frac{\delta_{x,x'}\delta_{q-q'}}{2x+1} \\
\sum_{q,m''} \begin{pmatrix} l & x & l'' \\ -m & -q & m'' \end{pmatrix} \begin{pmatrix} l'' & x & l' \\ -m'' & q & m' \end{pmatrix} &= \sum_{q,m''} \begin{pmatrix} l & x & l'' \\ -m & -q & m'' \end{pmatrix} \begin{pmatrix} l' & x & l'' \\ -m' & -q & m'' \end{pmatrix} \\
&= \delta_{l,l'}\delta_{mm'} \frac{1}{2l''+1}
\end{aligned}$$

The final equation for the upper-broadening term can be written is

$$\begin{aligned}
\left\langle nlm \left| T^{(2)}_{upper} \right| n'l'm' \right\rangle = \frac{4n_e\lambda_T^3}{\pi^2} \int dk_1 \int dk_2 e^{-\beta\frac{1}{2}k_1^2} \delta_{l,l'}\delta_{m,m'} \times \\
\sum_x \sum_{n''l''} \sum_{l_1,l_2} \frac{(2l''+1)(2l_1+1)(2l_2+1)}{(2x+1)} \begin{pmatrix} l & x & l'' \\ 0 & 0 & 0 \end{pmatrix}^2 \begin{pmatrix} l_1 & x & l_2 \\ 0 & 0 & 0 \end{pmatrix}^2 \\
\left\langle k_1 l_1 \left\| \hat{\Lambda}^x_{nl,n''l''} \right\| k_2 l_2 \right\rangle \left\langle k_2, l_2 \left\| \hat{\Lambda}^x_{n''l'',n'l} \right\| k_1 l_1 \right\rangle \frac{1}{\omega - \frac{1}{2}(k_1^2 - k_2^2)}; \quad \text{(C.51)}
\end{aligned}$$

Woltz & Hooper (1984) derived this exact equation.

These angular results can be used for either the Coulomb/plane-wave calculation or with the distorted-wave calculation. As we shall see in the next section, there will be some additional terms when Exchange is included.

C.6 Evaluation of $T(\omega)$ with Exchange

The inclusion of exchange will involve evaluation of additional terms in both the plasma polarization term and the dynamic width and shift operator. The direct term need

not be repeated since we have already derived it in the previous sections. However, I do want to point out that the formula for the dynamic width and shift term has an additional factor of one half multiplied to it compared to the direct-only calculation.

C.6.1 Plasma Polarization with Exchange

Since the direct interaction has already been solved, we need to find only the exchange term. For the exchange term, the derivation up to Eq (C.44) is the same except that in the matrix element is an exchange term,

$$\left\langle nlm \left| T_E^{(1)} \right| n'l'm' \right\rangle = - \sum_{x,q,l_1,m_1} \frac{1}{pi} n_e \lambda_T^3 \int_0^\infty dk\ e^{-\beta \frac{1}{2} k^2} \times \left\langle kl_1 \left| \hat{\Xi}^x_{nl,k_1 l_2} \right| n'l' \right\rangle \sqrt{(2l+1)(2l'+1)}(2l_1+1) \times \begin{pmatrix} l & x & l_1 \\ 0 & 0 & 0 \end{pmatrix} \begin{pmatrix} l_1 & x & l' \\ 0 & 0 & 0 \end{pmatrix} \begin{pmatrix} l_1 & x & l' \\ -m_1 & q & m' \end{pmatrix} \begin{pmatrix} l & x & l_1 \\ -m & -q & m_1 \end{pmatrix} (-1)^{m+q+m_1}. \quad \text{(C.52)}$$

We can eliminate the negative sign again by using the 3j-symbol selection rules: $m + q = m_1$, the argument in the exponent is then $2m_1$, making the term zero. I can perform the sum over q and m_1; again, we take advantage of Eq (B.6),

$$\begin{aligned} \sum_{qm_1} \begin{pmatrix} l_1 & x & l' \\ -m_1 & q & m' \end{pmatrix} \begin{pmatrix} l & x & l_1 \\ -m & -q & m_1 \end{pmatrix} &= \sum_{qm_1} \begin{pmatrix} l_1 & x & l' \\ -m_1 & q & m' \end{pmatrix} \begin{pmatrix} l_1 & x & l \\ -m_1 & q & m \end{pmatrix} \\ &= \frac{\delta_{l,l'}}{2l+1} \end{aligned}$$

This result is then diagonal in l in the atomic units, just like the direct term. The final equation for the exchange term of the plasma polarization is

$$\left\langle nlm \left| T_E^{(1)} \right| n'l'm' \right\rangle = -\delta_{ll}\delta_{mm'} \sum_{x,l_1} \frac{1}{\pi} n_e \lambda_T^3 \int_0^\infty dk\ e^{-\beta \frac{1}{2} k^2} \times \left\langle kl_1 \left| \hat{\Xi}^x_{nl,k_1 l_2} \right| nl \right\rangle (2l_1+1) \begin{pmatrix} l & x & l_1 \\ 0 & 0 & 0 \end{pmatrix}^2. \quad \text{(C.53)}$$

Interestingly, there is an allowed exchange dipole term for the plasma polarization term.

C.6.2 Dynamic Width and Shift with Exchange

There are several different processes that make up the second-order term of the M operator. Madison et al. (1990) points out that the processes are as follows:

$$\begin{gathered}\text{direct} - \text{direct}\\ \text{exchange} - \text{exchange}\\ \text{direct} - \text{exchange}\\ \text{exchange} - \text{direct}\end{gathered} \tag{C.54}$$

The different terms of T can be written as

$$\begin{aligned} T &= \frac{1}{2}\left[T_{DD} + T_{EE} + \sum_S \frac{2S+1}{4}(-1)^S \left\{T_{DE} + T_{ED}\right\}\right], \\ &= \frac{1}{2}\left[T_{DD} + T_{EE} - \frac{1}{2}\left\{T_{DE} + T_{ED}\right\}\right], \end{aligned} \tag{C.55}$$

where the sum is over the different spin orientations of the two electrons; S is the total spin of the total two-electron system. The $S = 0$ term corresponds to the spin-anti-aligned singlet (para-) state, while the $S = 1$ triplet term is the spin-aligned (ortho-) state (Bethe & Salpeter, 1957).

The first two terms of T, the direct-direct, and exchange-exchange leaves the electrons in their original positions (this idea assumes that one can actually track the electrons and know for sure that one electron is in one state or another), while the second-two processes result in an exchange of the two electrons after the collisions. Each exchange interaction is a measure of how frequently the electrons change place (Bethe & Salpeter, 1957).

The direct-direct term has already been solved, I have the final three terms to also solve. Each term will be very similar to Eq (C.50), but with exchange terms rather than direct terms.

$$
\begin{aligned}
T_{EE}^{(2)} &= \frac{4n_e\lambda_T^3}{\pi^2}\sum_{l_1,l_2}\sum_{m_1m_2}\sum_{x,q}\sum_{x'q'}\int dk_1\int dk_2 e^{-\beta\frac{1}{2}k_1^2}\times \\
&\quad \langle nl;k_1l_1|V|k_2l_2;n''l''\rangle\langle k_2l_2;n''l''|V|n'l';k_1l_1\rangle\frac{1}{\omega-\frac{1}{2}(k_1^2-k_2^2)}\times \\
&\quad \sqrt{(2l+1)(2l''+1)(2l''+1)(2l'+1)(2l_1+1)(2l_2+1)(2l_1+1)(2l_2+1)}\times \\
&\quad \begin{pmatrix} l_1 & x & l'' \\ -m_1 & q & m'' \end{pmatrix}\begin{pmatrix} l & x & l_2 \\ -m & -q & m_2 \end{pmatrix}\begin{pmatrix} l_2 & x' & l' \\ -m_2 & q' & m' \end{pmatrix}\begin{pmatrix} l'' & x' & l_1 \\ -m'' & -q' & m_1 \end{pmatrix}\times \\
&\quad \begin{pmatrix} l_1 & x & l'' \\ 0 & 0 & 0 \end{pmatrix}\begin{pmatrix} l & x & l_2 \\ 0 & 0 & 0 \end{pmatrix}\begin{pmatrix} l_2 & x' & l' \\ 0 & 0 & 0 \end{pmatrix}\begin{pmatrix} l'' & x' & l_1 \\ 0 & 0 & 0 \end{pmatrix} \qquad \text{(C.56)}
\end{aligned}
$$

Re-arranging the 3j symbols, then we can eliminate the sum over x' and q',

$$
\begin{aligned}
\sum_{m''m_1}\begin{pmatrix} l_1 & x & l'' \\ -m_1 & q & m'' \end{pmatrix}\begin{pmatrix} l'' & x' & l_1 \\ -m'' & -q' & m_1 \end{pmatrix} &= \sum_{m''m_1}\begin{pmatrix} l_1 & x & l'' \\ -m_1 & q & m'' \end{pmatrix}\begin{pmatrix} l_1 & x' & l'' \\ -m_1 & q' & m'' \end{pmatrix} \\
&= \delta_{x,x'}\delta_{qq'}\frac{1}{2x+1}
\end{aligned}
$$

then we can remove the sums over m_2 and q, and again, this term will be independent of m,

$$
\begin{aligned}
\sum_{m_2q}\begin{pmatrix} l & x & l_2 \\ -m & -q & m_2 \end{pmatrix}\begin{pmatrix} l_2 & x & l' \\ -m_2 & q & m' \end{pmatrix} &= \sum_{m_2q}\begin{pmatrix} l & x & l_2 \\ -m & -q & m_2 \end{pmatrix}\begin{pmatrix} l' & x & l_2 \\ -m' & -q & m_2 \end{pmatrix} \\
&= \delta_{ll'}\delta_{mm'}\frac{1}{2l+1}
\end{aligned}
$$

The final result for the exchange-exchange term is

$$
\begin{aligned}
\left\langle nlm\left|T_{EE}^{(2)}\right|n'l'm'\right\rangle &= \delta_{ll'}\delta_{mm'}\frac{2n_e\lambda_T^3}{\pi^2}\sum_{l_1,l_2}\sum_{x}\int dk_1\int dk_2 e^{-\beta\frac{1}{2}k_1^2}\times \\
&\quad \left\langle k_1l_1\left|\hat{\Xi}_{nl,k_2l_2}\right|n''l''\right\rangle\left\langle n''l''\left|\hat{\Xi}_{k_2l_2,n'l}\right|k_1l_1\right\rangle\frac{1}{\omega-\frac{1}{2}(k_1^2-k_2^2)}\times \\
&\quad \frac{(2l''+1)(2l_1+1)(2l_2+1)}{2x+1}\begin{pmatrix} l_1 & x & l'' \\ 0 & 0 & 0 \end{pmatrix}^2\begin{pmatrix} l & x & l_2 \\ 0 & 0 & 0 \end{pmatrix}^2 \qquad \text{(C.57)}
\end{aligned}
$$

The direct-exchange and exchange-direct terms are going to be more difficult; again, starting with the direct-exchange term

$$
\begin{aligned}
T_{DE}^{(2)} \quad = \quad & \frac{4n_e\lambda_T^3}{\pi^2}\sum_{l_1,l_2}\sum_{m_1m_2}\sum_{x,q}\sum_{x'q'}\int dk_1\int dk_2 e^{-\beta\frac{1}{2}k_1^2}(-1)^{m_1+m+q+m_2+q'+m''}\times \\
& \langle nl;k_1l_1\,|V|\,n''l'';k_2l_2\rangle\,\langle n''l'';k_2l_2\,|V|\,k_1l_1;n'l'\rangle\,\frac{1}{\omega-\frac{1}{2}(k_1^2-k_2^2)}\times \\
& \sqrt{(2l+1)(2l''+1)(2l''+1)(2l'+1)(2l_1+1)(2l_2+1)(2l_1+1)(2l_2+1)}\times \\
& \begin{pmatrix} l_1 & x & l_2 \\ -m_1 & q & m_2\end{pmatrix}\begin{pmatrix} l & x & l'' \\ -m & -q & m''\end{pmatrix}\begin{pmatrix} l_2 & x' & l' \\ -m_2 & q' & m'\end{pmatrix}\begin{pmatrix} l'' & x' & l_1 \\ -m'' & -q' & m_1\end{pmatrix}\times \\
& \begin{pmatrix} l_1 & x & l_2 \\ 0 & 0 & 0\end{pmatrix}\begin{pmatrix} l & x & l'' \\ 0 & 0 & 0\end{pmatrix}\begin{pmatrix} l_2 & x' & l' \\ 0 & 0 & 0\end{pmatrix}\begin{pmatrix} l'' & x' & l_1 \\ 0 & 0 & 0\end{pmatrix}
\end{aligned}
$$

I cannot at this point make use of the 3j sum rule (Eq B.6) in the same way, I can however, make use of an alternate definition of the 6j symbol (Eq B.12),

$$
\begin{aligned}
& \begin{pmatrix} l_1 & x & l_2 \\ -m_1 & q & m_2\end{pmatrix}\begin{pmatrix} l & x & l'' \\ -m & -q & m''\end{pmatrix}\begin{pmatrix} l'' & x' & l_1 \\ -m'' & -q' & m_1\end{pmatrix}(-1)^{m_1+m+q} \\
= \; & \begin{pmatrix} l & x & l'' \\ -m & -q & m''\end{pmatrix}\begin{pmatrix} l_1 & x' & l'' \\ m_1 & -q' & -m''\end{pmatrix}\begin{pmatrix} l_1 & x & l_2 \\ -m_1 & q & m_2\end{pmatrix}(-1)^{l_1+x'+l''}(-1)^{m_1+m+q} \\
= \; & \begin{pmatrix} l & x & l'' \\ -m & -q & m''\end{pmatrix}\begin{pmatrix} l_1 & x' & l'' \\ m_1 & -q' & -m''\end{pmatrix}\begin{pmatrix} l_1 & x & l_2 \\ -m_1 & q & m_2\end{pmatrix}(-1)^{l_1+x'+l''}(-1)^{m_1+m''+q} \\
= \; & \begin{pmatrix} l & x' & l_2 \\ -m & -q' & m_2\end{pmatrix}\begin{Bmatrix} l & x' & l_2 \\ l_1 & x & l''\end{Bmatrix}(-1)^{x'+x}.
\end{aligned}
$$

Then multiplying this last quantity by the last 3j symbol in the equation (and using the selection rule that $m_2 = q' + m$, which eliminates the minus sign)

$$
\begin{aligned}
\sum_{m_2q'}\begin{Bmatrix} l & x' & l_2 \\ l_1 & x & l''\end{Bmatrix} \quad & (-1)^{x'+x} \quad \begin{pmatrix} l & x' & l_2 \\ -m & -q' & m_2\end{pmatrix}\begin{pmatrix} l_2 & x' & l' \\ -m_2 & q' & m'\end{pmatrix} \\
& = \quad \sum_{m_2q'}\begin{Bmatrix} l & x' & l_2 \\ l_1 & x & l''\end{Bmatrix}(-1)^{x'+x}\begin{pmatrix} l & x' & l_2 \\ -m & -q' & m_2\end{pmatrix}\begin{pmatrix} l' & x' & l_2 \\ -m' & -q' & m_2\end{pmatrix} \\
& = \quad \begin{Bmatrix} l & x' & l_2 \\ l_1 & x & l''\end{Bmatrix}(-1)^{x'+x}\delta_{ll'}\delta_{mm'}\frac{1}{2l+1}.
\end{aligned}
$$

The final equation for the direct-exchange term is

$$\begin{aligned}\left\langle nlm \left| T_{DE}^{(2)} \right| n'l'm' \right\rangle &= \delta_{ll'}\delta_{mm'} \frac{4n_e\lambda_T^3}{\pi^2} \sum_{l_1,l_2} \sum_{xx'} \int dk_1 \int dk_2 e^{-\beta\frac{1}{2}k_1^2} (-1)^{x+x'} \times \\ &\left\langle k_1 l_1 \left| \hat{\Lambda}_{nl,n''l''} \right| k_2 l_2 \right\rangle \left\langle k_2 l_2 \left| \hat{\Xi}_{n''l'',k_1 l_2} \right| n'l \right\rangle \frac{1}{\Delta\omega - \frac{1}{2}(k_1^2 - k_2^2)} \times \\ &(2l+1)(2l''+1)(2l_1+1)(2l_2+1) \begin{Bmatrix} l & x & l'' \\ l_1 & x' & l_2 \end{Bmatrix} \times \\ &\begin{pmatrix} l_1 & x & l_2 \\ 0 & 0 & 0 \end{pmatrix} \begin{pmatrix} l & x & l'' \\ 0 & 0 & 0 \end{pmatrix} \begin{pmatrix} l_2 & x' & l \\ 0 & 0 & 0 \end{pmatrix} \begin{pmatrix} l'' & x' & l_1 \\ 0 & 0 & 0 \end{pmatrix} \end{aligned} \tag{C.58}$$

and using a very similar procedure for the exchange-direct term, we have

$$\begin{aligned}\left\langle nlm \left| T_{DE}^{(2)} \right| n'l'm' \right\rangle &= \delta_{ll'}\delta_{mm'} \frac{4n_e\lambda_T^3}{\pi^2} \sum_{l_1,l_2} \sum_{xx'} \int dk_1 \int dk_2 e^{-\beta\frac{1}{2}k_1^2} (-1)^{x+x'} \times \\ &\left\langle k_1 l_1 \left| \hat{\Xi}_{nl,k_2 l_2} \right| n''l'' \right\rangle \left\langle k_2 l_2 \left| \hat{\Lambda}_{n''l'',n'l} \right| k_1 l_1 \right\rangle \frac{1}{\Delta\omega - \frac{1}{2}(k_1^2 - k_2^2)} \times \\ &(2l+1)(2l''+1)(2l_1+1)(2l_2+1) \begin{Bmatrix} l & x' & l'' \\ l_1 & x & l_2 \end{Bmatrix} \times \\ &\begin{pmatrix} l_1 & x & l'' \\ 0 & 0 & 0 \end{pmatrix} \begin{pmatrix} l & x & l_2 \\ 0 & 0 & 0 \end{pmatrix} \begin{pmatrix} l_2 & x' & l_1 \\ 0 & 0 & 0 \end{pmatrix} \begin{pmatrix} l'' & x' & l \\ 0 & 0 & 0 \end{pmatrix} \end{aligned} \tag{C.59}$$

C.6.3 Interference Broadening Terms

The interference term is defined in Eq (C.49). The angular terms are, with similar manipulation as for the upper- and lower-state broadening term

C.6.3.1 Direct Term

The direct term is

$$\left\langle n_u l_u m_u; n_l l_l m_l \left| T^{(2)}_{DD} \right| n'_u l'_u m'_u; n'_l l'_l m'_l \right\rangle = -\frac{4 n_e \lambda_T^3}{\pi^2} \sum_{l_1,l_2} \sum_{xx'} \int dk_1 \int dk_2 e^{-\beta \frac{1}{2} k_1^2} \times$$

$$\sum_{x=0}^{\infty} \sum_{l_1,l_2=0}^{\infty} (2l_u+1)(2l_l+1)(2l_1+1)(2l_2+1)$$

$$\sum_q \begin{pmatrix} l_1 & x & l_2 \\ 0 & 0 & 0 \end{pmatrix}^2 \begin{pmatrix} l_i & x & l'_i \\ 0 & 0 & 0 \end{pmatrix} \begin{pmatrix} l_f & x & l'_f \\ 0 & 0 & 0 \end{pmatrix} \begin{pmatrix} l_i & x & l'_i \\ -m_i & q & m'_i \end{pmatrix} \begin{pmatrix} l_f & x & l'_f \\ -m_f & q & m'_f \end{pmatrix} \times$$

$$\left\langle k_1 l_1 \left| \hat{\Lambda}^x_{n_u l_u, n'_u l_u} \right| k_2 l_2 \right\rangle \left\langle k_2, l_2 \left| \hat{\Lambda}^x_{n_l l_l, n'_l l_l} \right| k_1 l_1 \right\rangle, \quad \text{(C.60)}$$

(C.61)

which uses the same sum-rule as the upper-state direct-direct term.

The exchange-exchange term unfortunately has no simplification, so we just evaluate all of the terms

$$\left\langle n_u l_u m_u; n_l l_l m_l \left| T^{(2)}_{EE} \right| n'_u l'_u m'_u; n'_l l'_l m'_l \right\rangle = -\frac{4 n_e \lambda_T^3}{\pi^2} \sum_{l_1,l_2} \sum_{xx'} \int dk_1 \int dk_2 e^{-\beta \frac{1}{2} k_1^2} \times$$

$$\sum_{x,x'} \sum_{l_1,l_2} (2l_u+1)(2l_l+1)(2l_1+1)(2l_2+1)$$

$$\sum_{q,q'} \sum_{m_1,m_2} \begin{pmatrix} l_1 & x & l'_i \\ 0 & 0 & 0 \end{pmatrix} \begin{pmatrix} l_i & x & l_2 \\ 0 & 0 & 0 \end{pmatrix} \begin{pmatrix} l_2 & x' & l'_f \\ 0 & 0 & 0 \end{pmatrix} \begin{pmatrix} l_f & x' & l_1 \\ 0 & 0 & 0 \end{pmatrix} \times$$

$$\begin{pmatrix} l_1 & x & l'_i \\ -m_1 & q & m'_i \end{pmatrix} \begin{pmatrix} l_i & x & l_2 \\ -m_i & -q & m_2 \end{pmatrix} \begin{pmatrix} l_2 & x & l'_f \\ -m_2 & q' & m'_f \end{pmatrix} \begin{pmatrix} l_f & x' & l_1 \\ -m_f & -q' & m_1 \end{pmatrix} \quad \text{(C.62)}$$

$$\left\langle k_1 l_1 \left| \hat{\Xi}^x_{n_u l_u, k_2 l_2} \right| n'_u l'_u \right\rangle \left\langle n_l l_l \left| \hat{\Xi}^{x'}_{k_2 l_2, n'_l l_l} \right| k_1 l_1 \right\rangle, \quad \text{(C.63)}$$

(C.64)

The direct-exchange and exchange-direct terms, on the other hand do have some

simplifications where some angular terms can be put into 6j symbols,

$$\left\langle n_u l_u m_u; n_l l_l m_l \left| T^{(2)}_{DE} \right| n'_u l'_u m'_u; n'_l l'_l m'_l \right\rangle = \frac{4 n_e \lambda_T^3}{\pi^2} \sum_{l_1,l_2} \sum_{xx'} \int dk_1 \int dk_2 e^{-\beta \frac{1}{2} k_1^2} \times$$
$$\sum_{x,x'} \sum_{l_1,l_2} (2l_u+1)(2l_l+1)(2l_1+1)(2l_2+1)$$
$$(-1)^{x+x'} \begin{pmatrix} l_1 & x & l_2 \\ 0 & 0 & 0 \end{pmatrix} \begin{pmatrix} l_i & x & l'_i \\ 0 & 0 & 0 \end{pmatrix} \begin{pmatrix} l_2 & x' & l'_f \\ 0 & 0 & 0 \end{pmatrix} \begin{pmatrix} l_f & x' & l_1 \\ 0 & 0 & 0 \end{pmatrix} \begin{Bmatrix} l_f & l'_f & x' \\ l_2 & l_1 & x \end{Bmatrix} \times$$
$$\sum_q (-1)^q \begin{pmatrix} l_f & x & l'_f \\ m_f & q & -m'_f \end{pmatrix} \begin{pmatrix} l_i & x & l'_i \\ -m_i & q & m'_i \end{pmatrix}$$
$$\left\langle k_1 l_1 \left| \hat{\Lambda}^x_{n_u l_u, n'_u l_u} \right| k_2 l_2 \right\rangle \left\langle k_2 l_2 \left| \hat{\Xi}^{x'}_{n_l l_l, k_1, l_1} \right| n'_l l_l \right\rangle \quad \text{(C.65)}$$

$$\left\langle n_u l_u m_u; n_l l_l m_l \left| T^{(2)}_{ED} \right| n'_u l'_u m'_u; n'_l l'_l m'_l \right\rangle = -\frac{4 n_e \lambda_T^3}{\pi^2} \sum_{l_1,l_2} \sum_{xx'} \int dk_1 \int dk_2 e^{-\beta \frac{1}{2} k_1^2} \times$$
$$\sum_{x,x'} \sum_{l_1,l_2} (2l_u+1)(2l_l+1)(2l_1+1)(2l_2+1)$$
$$(-1)^{x+l_1+l_2} \begin{pmatrix} l_1 & x & l'_i \\ 0 & 0 & 0 \end{pmatrix} \begin{pmatrix} l_i & x & l_1 \\ 0 & 0 & 0 \end{pmatrix} \begin{pmatrix} l_1 & x' & l_2 \\ 0 & 0 & 0 \end{pmatrix} \begin{pmatrix} l_f & x' & l'_f \\ 0 & 0 & 0 \end{pmatrix} \begin{Bmatrix} l_i & l_i & x' \\ l_2 & l_1 & x \end{Bmatrix} \times$$
$$\sum_q (-1)^q \begin{pmatrix} l_f & x' & l'_f \\ m_f & q & -m'_f \end{pmatrix} \begin{pmatrix} l_i & x' & l'_i \\ -m_i & q & m'_i \end{pmatrix}$$
$$\left\langle n_u l_u \left| \hat{\Xi}^x_{k_1 l_1, n'_u l_u} \right| k_2 l_2 \right\rangle \left\langle k_2, l_2 \left| \hat{\Lambda}^{x'}_{n_l l_l, n'_l l_l} \right| k_1 l_1 \right\rangle . \quad \text{(C.66)}$$

C.6.4 Dynamic Width and Shifts: Distorted Wave with Exchange

All of the angular parts will remain the same, the only difference between what was calculated in sections C.5.2 and C.6.2 is the argument of the radial matrix-element. Since our choice of distorting potential is the monopole term of the atom, then it should appear

accordingly in the evaluation of the matrix elements,

$$\left\langle k_1 l_1 \left| \hat{\Lambda}_{nl,n''l''} \right| k_2 l_2 \right\rangle \rightarrow \left\langle k_1 l_1 \left| \hat{\Lambda}_{nl,n''l''} - \delta_{x,0}\delta_{nl,n''l''}\hat{\Lambda}^0_{nl,n''l''} \right| k_2 l_2 \right\rangle \tag{C.67}$$

$$\left\langle k_1 l_1 \left| \hat{\Xi}_{nl,k_2 l_2} \right| n''l'' \right\rangle \rightarrow \left\langle k_1 l_1 \left| \hat{\Xi}_{nl,k_2 l_2} - \delta_{l,l_2} \frac{\langle nl|k_2 l_2\rangle}{2l+1} \delta_{x,0}\hat{\Lambda}^0_{nl,nl} \right| n''l'' \right\rangle, \tag{C.68}$$

where $\langle nl|k_2 l_2\rangle$ is simply the overlap integral, $\int_0^\infty R_{nl}(r)F_{k_2 l_2}(r)dr$.

C.7 Correlated Collisions

This is the second-term of the electron broadening operator (Eq C.13), where we subtract the term

$$\langle \mathcal{H}(\omega)\rangle = \frac{1}{\omega - H_u^{(a,0)} + H_l^{(a,0)} + \langle T(\omega)\rangle} \langle T(\omega)\rangle . \tag{C.69}$$

This term, when Taylor expanded, defines $\mathcal{H}(\omega)$ as

$$\mathcal{H}(\omega) = \langle T(\omega)\rangle \sum_{n=0}^{\infty} \left[-\frac{1}{\omega - H_u^{(a,0)} + H_l^{(a,0)}} \langle T(\omega)\rangle \right]^n . \tag{C.70}$$

Fano (1963) describes a Taylor expansion for the whole thing where he uses the projection operator of Zwanzig (1960),

$$\mathcal{H}(\omega) = (V_u - V_l) \sum_{n=0}^{\infty} \left[(1-\mathcal{P}) \frac{1}{\omega - H_u^{(a,0)} + H_l^{(a,0)}} (V_u - V_l) \right]^n , \tag{C.71}$$

where the projection operator performs a trace (or an average). The first application of the relaxation theory (Smith & Hooper, 1967) wrote down the second-order form of M_c as

$$\mathcal{H}(\omega) \approx \langle V_u - V_l\rangle + \left\langle (V_u - V_l) \frac{1}{\omega - H_u^{(0)} + H_l^{(0)}} (V_u - V_l) \right\rangle - \langle V_u - V_l\rangle \frac{1}{\omega - H_u^{(a,0)} + H_l^{(a,0)}} \langle V_u - V_l\rangle , \tag{C.72}$$

but because the dipole approximation was made (and the average electric field is zero), then the first term and (by default) the third term is zero. Because the individual operators are

already evaluated in other parts of the calculation, then the evaluation of this operator is a simple matrix multiplication.

C.8 Off-diagonal Density Matrix Elements on Plasma Polarization

In the previous sections of this chapter, I have derived the equations for the plasma polarization shift assuming that the density matrix is separable in the form

$$\rho \approx \rho_a \rho_e = e^{-\beta H^{(a,0)}} e^{-\beta H^{(e,0)}}. \tag{C.73}$$

However, Eq (C.73) is only correct when the interaction potential V is only a small perturbation. The assumption is then that the plasma polarization term can be evaluated as

$$\left\langle V_u \rho_a \rho_e \rho_a^{-1} \right\rangle,$$

while a more accurate expression would be

$$\left\langle V_u \rho_{ae} \rho_a^{-1} \right\rangle,$$

Evaluating the density matrix to all order is tedious and slow, so we will suffice ourselves with a second-order expansion of the density matrix,

$$\begin{aligned} \rho_{ae} = e^{-\beta(H^{(a,0)}+H^{(e,0)}+V)} &\approx e^{-\beta H^{(a,0)}} e^{-\beta H^{(e,0)}} \\ &- e^{-\beta H^{(a,0)}} e^{-\beta H^{(e,0)}} \int_0^\beta d\tau \; e^{\tau(H^{(a,0)}+H^{(e,0)})} V e^{-\tau(H^{(a,0)}+H^{(e,0)})}. \end{aligned} \tag{C.74}$$

Then carrying through the Liouville form of the interaction operator, the second-

order term of Eq (C.74) is

$$-\int_0^\beta d\tau\ V_u e^{-\beta H^{(a,0)}} e^{-\beta H^{(e,0)}} e^{\tau(H^{(a,0)}+H^{(e,0)})} V_u e^{-\tau(H^{(a,0)}+H^{(e,0)})} e^{\beta H^{(a,0)}} + \\ e^{-\beta H^{(a,0)}} e^{-\beta H^{(e,0)}} \int_0^\beta d\tau\ e^{\tau(H^{(a,0)}+H^{(e,0)})} V_u e^{-\tau(H^{(a,0)}+H^{(e,0)})} V_l e^{\beta H^{(a,0)}}, \quad \text{(C.75)}$$

if this is an emission process, while for an absorption process, it would be

$$-\int_0^\beta d\tau\ V_u e^{-\beta H^{(a,0)}} e^{-\beta H^{(e,0)}} e^{\tau(H^{(a,0)}+H^{(e,0)})} V_l e^{-\tau(H^{(a,0)}+H^{(e,0)})} e^{\beta H^{(a,0)}} + \\ e^{-\beta H^{(a,0)}} e^{-\beta H^{(e,0)}} \int_0^\beta d\tau\ e^{\tau(H^{(a,0)}+H^{(e,0)})} V_l e^{\beta H^{(a,0)}} e^{-\tau(H^{(a,0)}+H^{(e,0)})} V_l. \quad \text{(C.76)}$$

Let's look at the emission process for now. If we assign bra and ket vectors on the potentials and give use the eigenvalue relation for the Hamiltonians, then the problem becomes

$$-\delta_{\nu\nu'} \int_0^\beta d\tau\ \langle \mu; k_1 | V | \mu''; k_2 \rangle\, e^{-\beta(E_{\mu''}+\frac{1}{2}k_2^2)} e^{\tau(E_{\mu''}+\frac{1}{2}k_2^2)} \langle \mu''; k_2 | V | \mu' k_1 \rangle\, e^{-\tau(E_{\mu'}+\frac{1}{2}k_1^2)} e^{\beta E_{\mu'}} + \\ e^{-\beta(E_\mu+\frac{1}{2}k_1^2)} \int_0^\beta d\tau\ e^{\tau(E_\mu+\frac{1}{2}k_1^2)} \langle \mu; k_1 | V | \mu'; k_2 \rangle\, e^{-\tau(E_{\mu'}+\frac{1}{2}k_2^2)} e^{\beta E_{\mu'}} \langle \nu; k_2 | V | \nu'; k_1 \rangle \quad \text{(C.77)}$$

Then performing the integrals results in

$$-\delta_{\nu\nu'} \langle \mu; k_1 | V | \mu''; k_2 \rangle \langle \mu''; k_2 | V | \mu' k_1 \rangle\, e^{-\beta(E_{\mu''}-E_{\mu'}+\frac{1}{2}k_2^2)} \frac{e^{\beta(E_{\mu''}+\frac{1}{2}k_2^2-E_{\mu'}-\frac{1}{2}k_1^2)}-1}{E_{\mu''}+\frac{1}{2}k_2^2-E_{\mu'}-\frac{1}{2}k_1^2} + \\ \langle \mu; k_1 | V | \mu'; k_2 \rangle \langle \nu; k_2 | V | \nu'; k_1 \rangle\, e^{-\beta(E_\mu-E_{\mu'}+\frac{1}{2}k_1^2)} \frac{e^{\beta(E_\mu+\frac{1}{2}k_1^2-E_{\mu'}-\frac{1}{2}k_2^2)}-1}{E_\mu+\frac{1}{2}k_1^2-E_{\mu'}-\frac{1}{2}k_2^2} \quad \text{(C.78)}$$

And the final expression is (after a little re-arranging)

$$-\delta_{\nu\nu'} \langle \mu; k_1 | V | \mu''; k_2 \rangle \langle \mu''; k_2 | V | \mu' k_1 \rangle \frac{e^{-\beta\frac{1}{2}k_1^2} - e^{-\beta(E_{\mu''}-E_{\mu'}+\frac{1}{2}k_2^2)}}{E_{\mu''}-E_{\mu'}+\frac{1}{2}k_2^2-\frac{1}{2}k_1^2} \\ + \langle \mu; k_1 | V | \mu'; k_2 \rangle \langle \nu; k_2 | V | \nu'; k_1 \rangle \frac{e^{-\beta\frac{1}{2}k_2^2} - e^{-\beta(E_\mu-E_{\mu'}+\frac{1}{2}k_1^2)}}{E_\mu-E_{\mu'}+\frac{1}{2}k_1^2-\frac{1}{2}k_2^2}, \quad \text{(C.79)}$$

which is purely real, there is no need for using the imaginary convergence factor trick.

To finish the evaluation of this term, the average over k_1 and k_2 must be performed and weighted by the trace over k_1,

$$-n_e\lambda_T^3\int_0^\infty dk_1\int_0^\infty dk_2\left\{\delta_{\nu\nu'}\left\langle\mu;k_1\left|V\right|\mu'';k_2\right\rangle\left\langle\mu'';k_2\left|V\right|\mu' k_1\right\rangle\frac{e^{-\beta\frac{1}{2}k_1^2}-e^{-\beta(E_{\mu''}-E_{\mu'}+\frac{1}{2}k_2^2)}}{E_{\mu''}-E_{\mu'}+\frac{1}{2}k_2^2-\frac{1}{2}k_1^2}\right.$$
$$\left.-\left\langle\mu;k_1\left|V\right|\mu';k_2\right\rangle\left\langle\nu;k_2\left|V\right|\nu';k_1\right\rangle\frac{e^{-\beta\frac{1}{2}k_2^2}-e^{-\beta(E_{\mu}-E_{\mu'}+\frac{1}{2}k_1^2)}}{E_{\mu}-E_{\mu'}+\frac{1}{2}k_1^2-\frac{1}{2}k_2^2}\right\}. \quad \text{(C.80)}$$

As with the case of the dynamic width and shift operator, evaluated with exchange in section C.6.2 and the interference term is in appendix C.6.3.

Appendix D

Parabolic States

It is a common approach to solve for the atom using a spherical representation where the atom is separated into a radial function times a spherical harmonic (Bethe & Salpeter, 1957),

$$\psi(r,\theta,\phi) = \frac{1}{r} R_{nl}(r) Y_{lm}(\theta,\phi),$$

which is standard in introductory quantum physics textbooks. But spherical coordinates are not the only representation which the hydrogen atom can be easily solved.

D.1 Separation of the Schrödinger Equation in Parabolic Coordinates

It is also possible to separate the Schrödinger equation in parabolic representation (Bethe & Salpeter, 1957), where the different parabolic coordinates are

$$\begin{aligned} \xi &= r + z \\ \eta &= r - z \\ \phi &= \arctan(y/x) \end{aligned}$$

where the r coordinate can be written as

$$r = \frac{1}{2}(\xi + \eta),$$

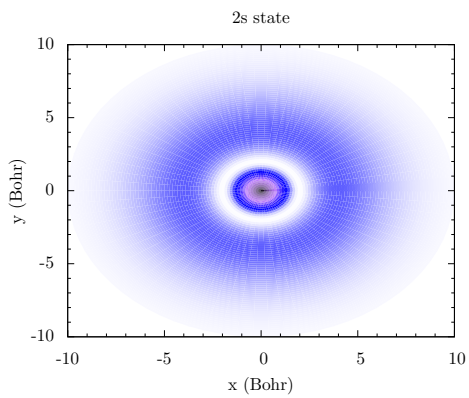

(a) $2s$ state

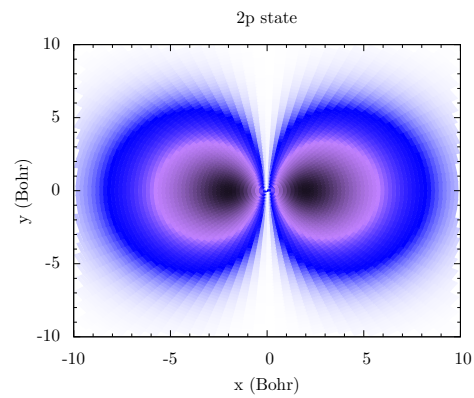

(b) $2p$ state

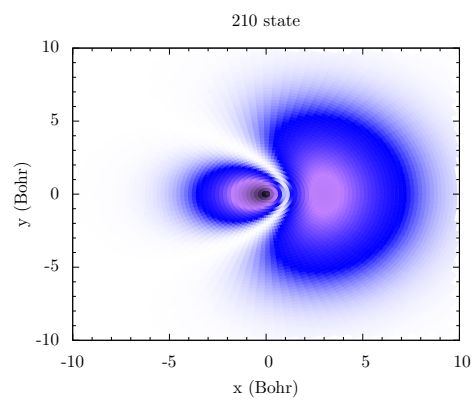

(c) Parabolic state

Figure D.1: The charge-density distribution of the $n = 2$ states of hydrogen. Panel D.1a shows the $2s$ state of hydrogen, while panel D.1b shows the $2p$ state of hydrogen; these states are the solution to the Schrödinger equation in spherical coordinates. Panel D.1c shows the solution of an $n = 2$ state in the parabolic representation, which can be built from spherical states via Eq (D.3); parabolic states have no spherical symmetry and are polarized on one side of the atom.

while the z coordinate can be written as

$$z = \frac{1}{2}(\xi - \eta), \tag{D.1}$$

which means that any perturbation along the z-direction is directly solvable in this representation. The wavefunction can separate into the following variables,

$$\psi(\xi, \eta, \phi) = F_{n_1}(\xi) G_{n_2}(\eta) e^{im\phi}, \tag{D.2}$$

where the quantum numbers n_1 denote the number of waves on the positive z side of the atom, while n_2 denote the number of waves on the negative z side of the atom. All of the quantum numbers, n, n_1, n_2, and m must satisfy the following,

$$n = n_1 + n_2 + m + 1.$$

The quantum numbers n_1 and n_2 describe the number of waves in F_{n_1} and G_{n_2} and describe the level of polarization with the quantity $q = n_1 - n_2$. Parabolic states are not spherically symmetric and the center of charge of a hydrogen atom is often not on the nucleus—contrary to the spherical representation where the center of charge is always on the nucleus (See figure D.1). It is possible to build parabolic states from the following transformation:

$$|nqm\rangle = \sum_l (-1)^{\frac{1}{2}(1+m-n-q)} \sqrt{2l+1} \begin{pmatrix} \frac{n-1}{2} & \frac{n-1}{2} & l \\ \frac{m-q}{2} & \frac{m+q}{2} & -m \end{pmatrix} |nlm\rangle. \tag{D.3}$$

The Hamiltonian is split into two differential equations, where $F_{n_1}(\xi)$, satisfies the following differential equation,

$$\left[\frac{d}{d\xi}\left(\xi \frac{d}{d\xi}\right) + \frac{1}{2}E\xi + Z_1 - \frac{m^2}{4\xi}\right] F_{n_1}(\xi) = 0 \tag{D.4}$$

$$\left[\frac{d}{d\eta}\left(\eta \frac{d}{d\eta}\right) + \frac{1}{2}E\xi + Z_2 - \frac{m^2}{4\eta}\right] G_{n_2}(\xi) = 0, \tag{D.5}$$

where $Z_1 + Z_2 = Z$, the total charge of the atom and E is the energy eigenvalue of the system.

D.2 With an Electric Field

Now, let's apply a constant electric field in the z-direction—the direction is arbitrary and would give similar answers for the x and y orientations, but the mathematics of the problem are greatly simplified if we choose the z-direction. In a spherical representation, then the electric field perturbation is

$$zF = r\cos\theta F, \tag{D.6}$$

which requires the use of matrix mechanics to solve, because the perturbations are off-diagonal,

$$zF = \begin{pmatrix} 0 & 0 & \langle 2s\,|z|\,2p\rangle\,F & 0 \\ 0 & 0 & 0 & 0 \\ \langle 2p\,|z|\,2s\rangle\,F & 0 & 0 & 0 \\ 0 & 0 & 0 & 0 \end{pmatrix} \begin{pmatrix} 2s\ m=0 \\ 2p\ m=-1 \\ 2p\ m=0 \\ 2p\ m=1 \end{pmatrix}. \tag{D.7}$$

However, in a parabolic representation, the electric field perturbation is

$$zF = \frac{1}{2}(\xi - \eta)F \tag{D.8}$$

is a (nearly) diagonal perturbation

$$zF = \begin{pmatrix} \langle 210\,|z|\,210\rangle\,F & 0 & 0 & 0 \\ 0 & \langle 2-10\,|z|\,2-10\rangle & 0 & 0 \\ 0 & 0 & 0 & 0 \\ 0 & 0 & 0 & 0 \end{pmatrix} \begin{pmatrix} 210 \\ 2-10 \\ 201 \\ 20-1 \end{pmatrix}. \tag{D.9}$$

The matrix elements of z are expressed as

$$\langle nqm\,|z|\,nqm\rangle = \frac{3}{2}\frac{n}{Z}(n_1 - n_2). \tag{D.10}$$

D.2.1 Quadratic Stark Effect

This is a second-order effect that basically accounts for the Stark effect matrix elements that connect different n states. The derivation is given in detail in Bethe &

Salpeter (1957) and the results are repeated here for convenience:

$$\left\langle nqm \left| (zF)^{(2)} \right| nqm \right\rangle = \frac{1}{16} F^2 \left(\frac{n}{Z}\right)^4 \left[17n^2 - 3q^2 - 9m^2 + 19\right] \tag{D.11}$$

D.2.2 Direct Solution

The perturbation Eq (D.8) is actually separable in ξ and η and can be solved directly by the Schrödinger equation, rather than resorting to perturbation theory (Bethe & Salpeter, 1957; Luc-Koenig & Bachelier, 1980a,b; Kilcrease et al., 1993). The differential equations for $F_{n_1}(\xi)$ and $G_{n_2}(\eta)$ are

$$\left[\frac{d}{d\xi}\left(\xi\frac{d}{d\xi}\right) + \frac{1}{2}E\xi + Z_1 - \frac{m^2}{4\xi} - \frac{1}{4}F\xi^2\right] F_{n_1}(\xi) = 0 \tag{D.12}$$

$$\left[\frac{d}{d\eta}\left(\eta\frac{d}{d\eta}\right) + \frac{1}{2}E\xi + Z_2 - \frac{m^2}{4\eta} + \frac{1}{4}F\eta^2\right] G_{n_2}(\xi) = 0 \tag{D.13}$$

The differential Eqs (D.12) and (D.13) can be solved directly. These equations are slightly different than the discussion above, for example, one will notice that in the positive η direction, the potential extends to negative infinity. This means that there are no truly bound states for this system; every state will have some behavior around the nucleus, then having a decaying exponential until the wave emerges on the other side of the potential. Therefore any value of E is acceptable for these equations. However, that does not mean that every possible value of E will exist *inside* the nucleus, this will require a very specific E and Z_1, the latter being the true eigenvalue of the problem (Bethe & Salpeter, 1957; Luc-Koenig & Bachelier, 1980a). Once Z_1 is determined, then Z_2 is determined from the property of $Z_2 = Z - Z_1$ and the solution to the free-wave part of the problem can be obtained. When the wavefunctions are obtained, then it is possible to calculate tunneling probabilities (Bethe & Salpeter, 1957; Luc-Koenig & Bachelier, 1980a) and even obtain spectral properties (Luc-Koenig & Bachelier, 1980b).

This picture of the constant electric field has been used to approximate the behavior of atoms in plasmas. As has been discussed in the body of the paper, this is not entirely the correct behavior. For example, in this picture, one can calculate the tunneling rate out the atom; this has been used to justify ionization rates in atoms (Hummer & Mihalas, 1988). But this picture has neglected the possibility that the electron can tunnel back in to the atom, nor does it account for the fact that electrons do not disappear to infinity, they still remain within the vicinity of the atom because they tunnel over to the nearest proton, so the probability of tunneling back in is larger than in the constant electric field model.

D.2.3 Selection Rules with an Electric Field

In a spherical representation, there are selection rules for dipole-allowed transitions (interaction with radiation) that are quite strict regarding the l and m quantum numbers. The parabolic representation, while it doesn't conserve the l quantum number, keeps the m quantum number. While the l quantum number is not preserved, there is a quasi-selection rule with the n_1 quantum number, where dipole matrix elements with like n_1 are the strongest.

Now, because of this selection rule, then a distinct pattern tends to arise in spectra. Let's simplify the notation and use the variable q to describe the level of polarization of the atom ($q = n_1 - n_2$). A strong dipole transition occurs when either q or m changes by one unit. The Lyα transition of hydrogen, for example has upper state quantum numbers: (nqm) 210, 2-10,201,20-1. All of these lines have strong transitions, but since 201 and 20-1 are degenerate and unshifted, then this makes for the strongest component of the line. Now, Lyβ on the other hand has the following states: 320,300,3-20, 311,3-11,31-1,3-1-1,302, and

30-2. The final two are not dipole-allowed transitions, so we will ignore them for now. The states 320 and 3-20 are $q = \pm 2$ from the ground state (100), so these, while not forbidden, will be weak; 300 ($n = 3, n_1 = 1, n_2 = 1, m = 0$), while unshifted, involves no change in q or m and by the quasi-selection rules, has no allowed dipole transition; the states 311, 31-1,3-11,3-1-1 are all shifted and are dipole-allowed. Therefore all of the transitions of the Lyβ line are shifted; it has no central component and therefore shows a double-peaked structure. This is so for all transitions; all Δn =even (2,4,6) lines have a double-peaked structure, while all Δn = odd (1,3,5) transitions have central components.

Bibliography

Alexiou, S. 2009, High Energy Density Physics, 5, 225

Alexiou, S., Dimitrijević, M., Sahal-Brechot, S., Stambulchik, E., Duan, B., González-Herrero, D., & Gigosos, M. 2014, Atoms, 2, 157

Alexiou, S., Griem, H. R., Halenka, J., & Olchawa, W. 2006, J. Quant. Spec. Radiat. Transf., 99, 238

Alexiou, S. & Lee, R. W. 2006, J. Quant. Spec. Radiat. Transf., 99, 10

Anderson, P. W. 1949, Physical Review, 76, 647

Bailey, J. E., Nagayama, T., Loisel, G. P., Rochau, G. A., Blancard, C., Colgan, J., Cosse, P., Faussurier, G., Fontes, C. J., Gilleron, F., Golovkin, I., Hansen, S. B., Iglesias, C. A., Kilcrease, D. P., Macfarlane, J. J., Mancini, R. C., Nahar, S. N., Orban, C., Pain, J.-C., Pradhan, A. K., Sherrill, M., & Wilson, B. G. 2015, Nature, 517, 56

Baranger, M. 1958a, Physical Review, 112, 855

—. 1958b, Physical Review, 111, 494

—. 1958c, Physical Review, 111, 481

Barnard, A. J., Cooper, J., & Smith, E. W. 1974, J. Quant. Spec. Radiat. Transf., 14, 1025

—. 1975, J. Quant. Spec. Radiat. Transf., 15, 429

Barstow, M. A., Bond, H. E., Holberg, J. B., Burleigh, M. R., Hubeny, I., & Koester, D. 2005, MNRAS, 362, 1134

Barstow, M. A., Joyce, S., Casewell, S. L., Holberg, J. B., Bond, H. E., & Burleigh, M. R. 2017, in Astronomical Society of the Pacific Conference Series, Vol. 509, 20th European White Dwarf Workshop, ed. P.-E. Tremblay, B. Gaensicke, & T. Marsh, 383

Bely, O. & Griem, H. R. 1970, Phys. Rev. A, 1, 97

Bergeron, P., Saffer, R. A., & Liebert, J. 1992, ApJ, 394, 228

Bergeron, P., Wesemael, F., & Fontaine, G. 1991, ApJ, 367, 253

Bethe, H. A. & Salpeter, E. E. 1957, Quantum Mechanics of One- and Two-Electron Atoms (New York: Academic Press)

Boercker, D. B. & Iglesias, C. A. 1984, Phys. Rev. A, 30, 2771

Boercker, D. B., Iglesias, C. A., & Dufty, J. W. 1987, Phys. Rev. A, 36, 2254

Bond, H. E., Schaefer, G. H., Gilliland, R. L., Holberg, J. B., Mason, B. D., Lindenblad, I. W., Seitz-McLeese, M., Arnett, W. D., Demarque, P., Spada, F., Young, P. A., Barstow, M. A., Burleigh, M. R., & Gudehus, D. 2017, ApJ, 840, 70

Burgess, A., Hummer, D. G., & Tully, J. A. 1970, Philosophical Transactions of the Royal Society of London Series A, 266, 225

Calisti, A., Khelfaoui, F., Stamm, R., & Talin, B. 1990, in American Institute of Physics Conference Series, Vol. 216, American Institute of Physics Conference Series, ed. L. Frommhold & J. W. Keto, 3–18

Carlhoff, C., Krametz, E., Schaefer, J. H., & Uhlenbusch, J. 1986, Journal of Physics B Atomic Molecular Physics, 19, 2629

Chandrasekhar, S. 1931, ApJ, 74, 81

—. 1933, MNRAS, 93, 390

Cowan, R. D. 1981, The Theory of Atomic Structure and Spectra (Los Alamos Series in Basic and Applied Sciences, Berkeley: University of California Press, 1981)

Däppen, W., Anderson, L., & Mihalas, D. 1987, ApJ, 319, 195

Davis, J., Kepple, P. C., & Blaha, M. 1976, J. Quant. Spec. Radiat. Transf., 16, 1043

Demura, A. V., Gilles, D., & Stehlé, C. 1997, in American Institute of Physics Conference Series, Vol. 386, American Institute of Physics Conference Series, 119–120

Djurović, S., Ćirišan, M., Demura, A. V., Demchenko, G. V., Nikolić, D., Gigosos, M. A., & González, M. Á. 2009, Phys. Rev. E, 79, 046402

Dufty, J. W. & Boercker, D. B. 1976, J. Quant. Spec. Radiat. Transf., 16, 1065

Ecker, G. & Kröll, W. 1963, Physics of Fluids, 6, 62

Falcon, R. E., Rochau, G. A., Bailey, J. E., Gomez, T. A., Montgomery, M. H., Winget, D. E., & Nagayama, T. 2015, ApJ, 806, 214

Falcon, R. E., Winget, D. E., Montgomery, M. H., & Williams, K. A. 2010, ApJ, 712, 585

Fano, U. 1963, Physical Review, 131, 259

Ferri, S., Calisti, A., Mossé, C., Rosato, J., Talin, B., Alexiou, S., Gigosos, M., González, M., González-Herrero, D., Lara, N., Gomez, T., Iglesias, C., Lorenzen, S., Mancini, R., & Stambulchik, E. 2014, Atoms, 2, 299

Feynman, R. P. 1949a, Physical Review, 76, 769

—. 1949b, Physical Review, 76, 749

Gell-Mann, M. & Goldberger, M. L. 1953, Physical Review, 91, 398

Gigosos, M. A. & Cardenoso, V. 1987, Journal of Physics B Atomic Molecular Physics, 20, 6005

Gigosos, M. A., Cardenoso, V., & Torres, F. 1986, Journal of Physics B Atomic Molecular Physics, 19, 3027

Gigosos, M. A., Fraile, J., & Torres, F. 1985, Phys. Rev. A, 31, 3509

Gigosos, M. A., González, M. Á., & Cardeñoso, V. 2003, Spectrochimica Acta, 58, 1489

Giuliani, G. & Vignale, G. 2008, Quantum Theory of the Electron Liquid (UK: Cambridge University Press)

Glenzer, S. & Kunze, H.-J. 1996, Phys. Rev. A, 53, 2225

Glenzer, S., Uzelac, N. I., & Kunze, H.-J. 1992, Phys. Rev. A, 45, 8795

Gomez, T. A. 2013, Master's thesis, University of Texas at Austin

Gomez, T. A., Nagayama, T., Kilcrease, D. P., Montgomery, M. H., & Winget, D. E. 2016, Phys. Rev. A, 94, 022501

Griem, H. R. 1964, Plasma spectroscopy

—. 1974, Spectral line broadening by plasmas (New York, Academic Press, Inc. (Pure and Applied Physics. Volume 39), 1974. 421 p.)

Griem, H. R., Blaha, M., & Kepple, P. C. 1979, Phys. Rev. A, 19, 2421

Griem, H. R., Halenka, J., & Olchawa, W. 2005, Journal of Physics B Atomic Molecular Physics, 38, 975

Griem, H. R., Kolb, A. C., & Shen, K. Y. 1959, Physical Review, 116, 4

Griem, H. R. & Ralchenko, Y. V. 2000, J. Quant. Spec. Radiat. Transf., 65, 287

Griem, H. R., Ralchenko, Y. V., & Bray, I. 1997, Phys. Rev. E, 56, 7186

Griffiths, D. J. 1995, Introduction to Quantum Mechanics

Gunderson, M. A., Junkel-Vives, G. C., & Hooper, C. F. 2001, J. Quant. Spec. Radiat. Transf., 71, 373

Halenka, J. 1988, J. Quant. Spec. Radiat. Transf., 39, 347

Haynes, D. A., Junkel, G. C., Gunderson, M. A., & Hooper, C. F. 2000, in American Institute of Physics Conference Series, Vol. 547, Atomic Processes in Plasmas (Twelfth), ed. R. C. Mancini & R. A. Phaneuf, 227–237

Haynes, Jr., D. A. & Hooper, Jr., C. F. 1997, J. Quant. Spec. Radiat. Transf., 58, 607

Hooper, C. J. 1968, Physical Review, 165, 215

Hubeny, I., Hummer, D. G., & Lanz, T. 1994, A&A, 282, 151

Hubeny, I. & Lanz, T. 1995, ApJ, 439, 875

Hummer, D. G. & Mihalas, D. 1988, ApJ, 331, 794

Hussey, T., Dufty, J. W., & Hooper, C. F. 1975, Phys. Rev. A, 12, 1084

Hussey, T. W., Dufty, J. W., & Hooper, Jr., C. F. 1977, Phys. Rev. A, 16, 1248

Iglesias, C. A. 2016, High Energy Density Physics, 18, 14

Inglis, D. R. & Teller, E. 1939, ApJ, 90, 439

Joyce, R. F., Woltz, L. A., & Hooper, Jr., C. F. 1987, Phys. Rev. A, 35, 2228

Junkel, G. C., Gunderson, M. A., Hooper, Jr., C. F., & Haynes, Jr., D. A. 2000, Phys. Rev. E, 62, 5584

Kepple, P. & Griem, H. R. 1968, Physical Review, 173, 317

Kepple, P. C. 1972, Phys. Rev. A, 6, 1

Kilcrease, D. P., Mancini, R. C., & Hooper, Jr., C. F. 1993, Phys. Rev. E, 48, 3901

Kingston, A. E. & Walters, H. R. J. 1980, Journal of Physics B Atomic Molecular Physics, 13, 4633

Kolb, A. C. & Griem, H. 1958, Physical Review, 111, 514

Lee, R. 1971, Journal of Physics B Atomic Molecular Physics, 4, 1640

Lippmann, B. A. & Schwinger, J. 1950, Physical Review, 79, 469

Littman, M. G., Kash, M. M., & Kleppner, D. 1978, Physical Review Letters, 41, 103

Luc-Koenig, E. & Bachelier, A. 1980a, Journal of Physics B Atomic Molecular Physics, 13, 1743

—. 1980b, Journal of Physics B Atomic Molecular Physics, 13, 1769

Luque, J. M., Calzada, M. D., & Sáez, M. 2003, Journal of Physics B Atomic Molecular Physics, 36, 1573

Madison, D. H., Bray, I., & McCarthy, I. 1990, Physical Review Letters, 64, 2265

Madison, D. H., Bray, I., & McCarthy, I. E. 1991, Journal of Physics B Atomic Molecular Physics, 24, 3861

Mancini, R. C., Kilcrease, D. P., Woltz, L. A., & Hooper, C. F. 1991, Computer Physics Communications, 63, 314

Moiseiwitsch, B. L. & Smith, S. J. 1968, Reviews of Modern Physics, 40, 238

Mott, N., Massey, H., & Massey, H. 1965, The Theory of Atomic Collisions, The International Series of Monographs on Physics (Clarendon Press)

Musielok, J., Böttcher, F., Griem, H. R., & Kunze, H.-J. 1987, Phys. Rev. A, 36, 5683

Nagayama, T., Bailey, J. E., Mancini, R. C., Iglesias, C. A., Hansen, S. B., Blancard, C., Chung, H. K., Colgan, J., Cosse, P., Faussurier, G., Florido, R., Fontes, C. J., Gilleron, F., Golovkin, I. E., Kilcrease, D. P., Loisel, G., MacFarlane, J. J., Pain, J.-C., Rochau, G. A., Sherrill, M. E., & Lee, R. W. 2016, High Energy Density Physics, 20, 17

Nguyen, H., Koenig, M., Benredjem, D., Caby, M., & Coulaud, G. 1986, Phys. Rev. A, 33, 1279

O'Brien, J. T. & Hooper, Jr., C. F. 1974, J. Quant. Spec. Radiat. Transf., 14, 479

Oks, E. 2000, J. Quant. Spec. Radiat. Transf., 65, 405

Olchawa, W. 2002, J. Quant. Spec. Radiat. Transf., 74, 417

Oppenheimer, J. R. 1928, Physical Review, 32, 361

Percival, I. C. & Seaton, M. J. 1957, Proceedings of the Cambridge Philosophical Society, 53, 654

Pillet, P., van Linden van den Heuvell, H. B., Smith, W. W., Kachru, R., Tran, N. H., & Gallagher, T. F. 1984, Phys. Rev. A, 30, 280

Pittman, T. L. & Fleurier, C. 1986, Phys. Rev. A, 33, 1291

Ralchenko, Y. V., Griem, H. R., & Bray, I. 2003, J. Quant. Spec. Radiat. Transf., 81, 371

Salpeter, E. E. 1952, ApJ, 115, 326

Seaton, M. J. 1990, Journal of Physics B Atomic Molecular Physics, 23, 3255

Smith, C. C. & Burgess, D. D. 1978, Journal of Physics B Atomic Molecular Physics, 11, 2087

Smith, E. W. 1968, Physical Review, 166, 102

Smith, E. W., Cooper, J., & Vidal, C. R. 1969, Physical Review, 185, 140

Smith, E. W. & Hooper, C. F. 1967, Physical Review, 157, 126

Stambulchik, E. 2013, High Energy Density Physics, 9, 528

Stambulchik, E., Calisti, A., Chung, H.-K., & González, M. 2014, Atoms, 2, 378

Stambulchik, E., Fisher, D. V., Maron, Y., Griem, H. R., & Alexiou, S. 2007, High Energy Density Physics, 3, 272

Stambulchik, E. & Maron, Y. 2006, J. Quant. Spec. Radiat. Transf., 99, 730

Stamm, R., Smith, E. W., & Talin, B. 1984, Phys. Rev. A, 30, 2039

Stehle, C. 1994, A&A, 292, 699

Stehle, C. & Jacquemot, S. 1993, A&A, 271, 348

Stewart, J. C. & Pyatt, Jr., K. D. 1966, ApJ, 144, 1203

Tremblay, P.-E. & Bergeron, P. 2009, ApJ, 696, 1755

Tremblay, P.-E., Ludwig, H.-G., Steffen, M., & Freytag, B. 2013, A&A, 559, A104

Uhlenbusch, J. & Vioel, W. 1989, Contributions to Plasma Physics, 29, 459

van Linden van den Heuvell, H. B. & Gallagher, T. F. 1985, Phys. Rev. A, 32, 1495

Vidal, C. R., Cooper, J., & Smith, E. W. 1971, J. Quant. Spec. Radiat. Transf., 11, 263

—. 1973, ApJS, 25, 37

Wiese, W. L., Kelleher, D. E., & Helbig, V. 1975, Phys. Rev. A, 11, 1854

Wiese, W. L., Kelleher, D. E., & Paquette, D. R. 1972, Phys. Rev. A, 6, 1132

Winget, D. E., Hansen, C. J., Liebert, J., van Horn, H. M., Fontaine, G., Nather, R. E., Kepler, S. O., & Lamb, D. Q. 1987, ApJL, 315, L77

Woltz, L. A. & Hooper, Jr., C. F. 1984, Phys. Rev. A, 30, 468

—. 1988, Phys. Rev. A, 38, 4766

Wrubel, T., Büscher, S., Kunze, H.-J., & Ferri, S. 2001, Journal of Physics B Atomic Molecular Physics, 34, 461

Zwanzig, R. 1960, J. Chem. Phys., 33, 1338

Zwanzig, R. 2001, Nonequilibrium Statistical Mechanics (OUP USA)